In-situ Investigation of the shear-induced alignment of Diblock Copolymer Melts using Rheo-SAXS, Rheo-Dielectric and FT-Rheology

Zur Erlangung des akademischen Grades eines

DOKTORS DER NATURWISSENSCHAFTEN

(Dr. rer. nat.)

Fakultät für Chemie und Biowissenschaften

Karlsruher Institut für Technologie (KIT) – Universitätsbereich

Vorgelegte

DISSERTATION

Von

Thomas Meins

Aus

Bayreuth

Die vorliegende Arbeit wurde von November 2007 bis Juni 2011 unter der Betreuung von Herrn Pof. Dr. Manfred Wilhelm am Karlsruher Institut für Technologie (KIT) - Universitätsbereich angefertigt.

„Geistreich sein heißt,

sich leicht verständlich zu machen,

ohne deutlich zu werden"

-Jean Anouilh

Für meine Familie

Duygu, Papatya, …

Contents

1. Introduction

The term polymer, derived from ancient Greek πολύς (polus "many, much") and μέρος (meros "part"), defines a class of materials which consist of several (hundreds to thousands) chemical repeating units. Most of the polymer materials used frequently in our daily life are synthesized form chemical substances, the so called monomers. The monomers originate from natural recourses mainly from fossil resources like crude oil. Common monomers are carbon compounds which obey chemical reactive functionalities for instance double bounds like styrene, ethylene, propylene or isoprene.

There are numerous polymerization methods, with different weightings for industrial and scientific applications. The prevalent techniques applied for large scale processing are the free radical polymerization, polycondensation respectively addition polymerization for the production of polyester and polyamides respectively polyurethanes and the coordinative polymerization using organo metals as catalysts for the synthesis of polyethylene and polypropylene[1]. The focus of recent scientific efforts is based on the development and improvement of controlled polymerization techniques such as the Reversible Addition-Fragmentation chain Transfer (RAFT)[2-4], nitroxide-mediated polymerization (NMP)[5, 6], Atom Transfer Radical Polymerization (ATRP)[7-9] or the anionic[10-13] respectively cationic[14, 15] polymerization. These so called "living" polymerization techniques facilitate the synthesis of well defined complex macromolecular architectures. Depending on the adopted monomer, polymerization method and experimental conditions a large variety of chemical and especially mechanical properties can be achieved. These macromolecular materials have been rapidly substituting or enhancing classical materials as steel, alumina, concrete or mineral glass.

Due to the extraordinary range of polymer properties, they are suitable for a large variety of industrial applications such as packaging, construction or health care. Polymers possess low densities combined with excellent mechanical properties as well as large scale processing capabilities with a minor cost of production. These are only some of their key advantages of polymer materials. The ubiquitous roles in everyday life range from familiar synthetic plastics, degradable biopolymers to phase separated systems with various microstructures on a nanometer length scale. From

Fig. 1 it can be seen that since the early 1950 the worldwide production of polymers has increased from approximately 1.5 million tons to more than 240 million tons in 2010 and this increase seems to be kept on[16].
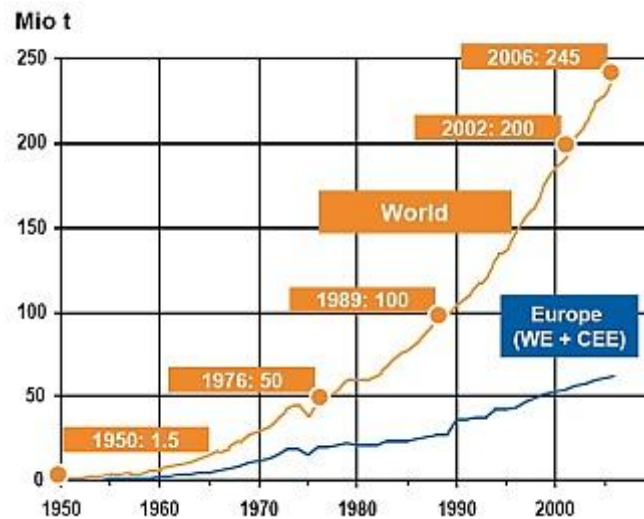
Fig. 1 World production per year of polymers.©EuropePlastics

To serve the increasing demand of polymer materials as well as to develop processes to produce advanced functional materials, it is from major importance to understand and control the mechanical properties of the polymer materials. During the modeling step the polymer melts are exposed to strong mechanical fields, affecting the melt flow behavior during processing[17-19] which affect the quality of the final product. Furthermore, hierarchical structured materials such as block copolymers are able to macroscopically align under mechanical stimulus[20, 21]. A precise understanding of these processes enables the production of new functional materials with tailored properties. Therefore the necessity derives, to precisely characterize and quantify the mechanical properties of the polymer materials, utilizing rheological techniques.

Rheology is the study of the flow of matter and is adapted to substances which have a complex molecular structure, as polymers[22]. The flow of polymer melts cannot be characterized by a single value of viscosity respectively elasticity. Moreover, the mechanical properties are a complex function depending on various factors such as temperature, mechanical deformation or the applied shear profile as well as molecular parameters like the chain architecture and the degree of polymerization.

2

Polymers obey both, viscous and elastic characteristics, therefore defined viscoelastic materials[23]. Systems which obey additional phase separation, such as block copolymers, show even more complex flow behavior, attributed to the numerous different morphologies and complex structures.

Block copolymers consist of two or more different building blocks covalently bond to each other. Driven by thermodynamic effects, these systems may undergo phase separation into self assembled microstructures. These microstructures exhibit various morphologies depending on the chemical composition of the different blocks, temperature and the volume fraction of the blocks[24-26]. It has been proven by Koppi et. al.[27], that block copolymer melts, containing randomly ordered anisotropic domains on a sub-micrometer scale, can be shear-induced aligned to an ordered structure with long range periodicity. This orientation process is of great scientific and industrial interest, as for almost all advanced applications involving block copolymers, such as ionic or photonic conductors or functional membranes, the hierarchically structured materials have to become macroscopic anisotropic[28].

In this thesis the flow behavior of complex fluids, with a particular focus on the non-linear regime, is investigated, utilizing sensitive and unique in-situ rheological combinations. For the mechanical analysis of complex fluids, several different techniques can be utilized[23, 29]. These cover a vast number of shear cell geometries and test setups from steady shear over transient to dynamic measurements.

For the macroscopic orientation of symmetric block copolymers, large amplitude oscillatory shear (LAOS) showed to be the method of choice, giving access to different orientations of the unit normal of the lamellae with respect to the shear flow direction[30]. The shear-induced alignment process causes the mechanical response of the sample melt to become a function of time with respect to its non-linear behavior. In the non-linear regime, during the LAOS experiment, the obtained signals consist of higher harmonics of the applied mechanical excitation frequency $\omega_1/2\pi$. Analyzing the mechanical raw data in terms of the concept of Fourier-Transform-Rheology (FT-Rheology)[31, 32], the resulting mechanical response can be evaluated with respect to the phase and magnitude spectra which consists of odd higher harmonics of $\omega_1/2\pi$. Utilizing FT-Rheology, the degree of mechanical non-linearity during LAOS can be followed and quantified. In this thesis the time dependence of the intensity of the third harmonics $I(3\omega_1)$ to the fundamental $I(\omega_1)$, determined from the FT-Rheology

3

magnitude spectra is used as a measure for the mechanical non-linear response, and is abbreviated throughout this thesis as $I_{3/1}$. The FT-Rheology methodology is considered to be one of the most sensitive methods for quantifying mechanical non-linearity[31, 32]. For a better understanding of the non-linear rheological behavior of complex fluids, the need of simultaneous acquisition of information on the microstructure and molecular dynamics in the sample arises.

To obtain insights to the underlying macroscopic orientation processes and to correlate structural changes to the dynamic of the polymer chains and the non-linear mechanical response, unique and specially combined methods were applied. These methods were specially designed for thorough in-situ measurements of the mechanical parameters under precise rheological conditions.

In-situ dielectric measurements carried out with a high sensitive Rheo-Dielectric setup[33, 34], permitting the investigation of polymer chain dynamics as well as the conductive behavior of hybrid polymer nano-composites under large amplitude oscillatory shear. The effect of mechanical fields on phase separated soft matter such as block copolymer melts can be studied by a combination of a rheometer and small angle X-ray scattering techniques (SAXS). To in-situ monitor the alignment process a new and unique approach was realized by combining a modified Rheometer with a strong X-ray source as provided by a synchrotron. The resulting Rheo-SAXS[35] combination located at the "Deutsches Elektronen Synchrotron" (DESY) in Hamburg, enables precise rheological measurements of polymer melts, using small sample volumes and simultaneous probing mechanical induced structural changes on a nanometer scale with high time resolution.

2. Theory

In this chapter the fundamentals of rheology are described, starting from basic principles of rheology and then discussed the response of viscoelastic fluid using simple linear models. In the latter part the response of the material in oscillatory shear flow is extensively discussed, here the linear response of the material is described using Maxwell model and to understand the non-linear viscoelasticity, recently developed FT-Rheology techniques, are introduced. Additionally, the reader is familiarized to the basic theory and applications of dielectric relaxation spectroscopy and also a short introduction to the theory of small angle X-Ray scattering is provided.

2.1. Principles in Rheology

From the invention of bronze over the manufacturing of steel to the mass production of synthetic plastics, the discovery and improvement of new materials with enhanced mechanical properties has been crucial for the promotion of human civilization. Frequently, these materials are manufactured from raw materials like copper (e.g. tin and bronze), iron oxide (e.g. steel) or fossil resources (e.g. polymers). The unique characteristics of these "synthetic" materials are their outstanding mechanical properties and the possibility to be accessible and producible in large quantities. Polymers meet these expectations, becoming one of the most important material classes in our modern life.

To derive and follow processing parameters, determining application areas and also for quality assurance, the need of a precise characterization and quantification arises. By applying rheological techniques the mechanical behavior of the material, like stiffness, maximum load and shear-induced flow, is determined. Furthermore, the knowledge about the rheological properties of a material allows conclusions about structural processes and molecular dynamics, such as polymer chain motions[22, 36].

The basic principles in Rheology are derived from each measurements conducted by Newton (viscosity) and Hook (elasticity). Based upon these two approaches the knowledge of the rheological properties of substance allows a first classification into three classes of materials[23]:

- Ideal solids show elastic strain dependence and they reversible release the stored energy after load removal. In a phenomenological model this behavior can be described by an ideal spring.

- Ideal liquids (Newtonian fluids) dissipate the deformation energy as heat which is called an inelastic deformation. The inelastic deformation can be described as a dash pot filled with an ideal liquid.

- Viscoelastic materials obey a superposition between elastic and viscous behavior showing time dependent stress behavior under constant deformation. With phenomenological models this behavior is described by combinations of ideal springs and dash pots which may be connected in series or parallel.

A detailed discussion on the mathematical description of the viscous and elastic fractions and the resulting phenomenological models is provided in following.

2.1.1. Viscosity and elasticity

To derive the Newton approach a simple shear experiment is introduced (see **Fig. 2**). A substance with the thickness d is placed between two equally sized parallel plates with a surface A, covering the whole sample plates. At the flexible upper plate a force F is applied which causes a movement of the upper plate with a velocity v.
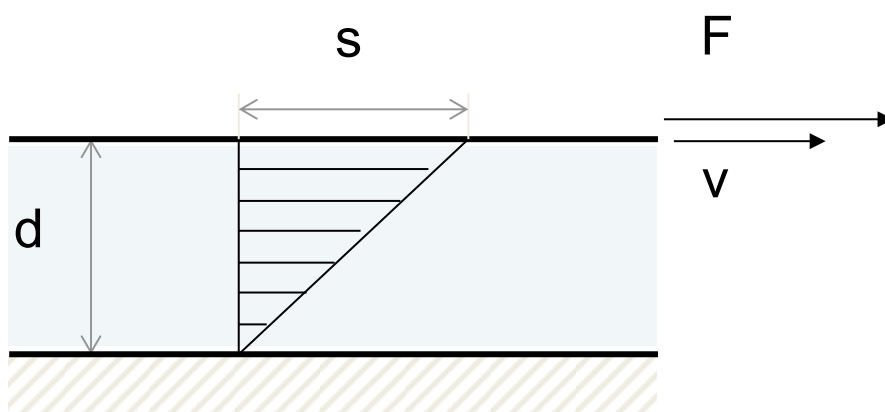
Fig. 2 Schematic sketch of a simple shear experiment. The upper plate is moved a force F with a velocity v while the lower plate is fixed. The distance between the two plates is d and the displacement is characterized by s.

The obtained deformation is quantified by the shear strain γ which is the ration between the displacement s and the gap d between the plates:

$$\gamma = \frac{s}{d} \qquad\qquad\qquad (2.\ 1)$$

The resulting shear stress ξ is defined as

$$\frac{F}{A} = \xi = \eta\left(\frac{v}{d}\right) = \eta\left(\frac{d\gamma}{dt}\right) = \eta\dot{\gamma} \qquad\qquad (2.\ 2)$$

with η [Pa*s] being the viscosity and $\dot{\gamma}$ [s^{-1}] the applied shear rate. The viscosity η is a measure for the resistivity of a fluid which is mechanically deformed. It is defined as the force which has to be applied, to deform a substance in between two parallel plates with a surface of 1 m² and a gap of 1 m with a velocity of 1 m/s[37]. For instance the viscosity of water at 20 °C is 1 mPa*s.

Newton's approach is valid for various gasses liquids, and oils whose stress versus strain rate curves is linear and passes through the origin. In **Fig. 3** the behavior of Newtonian and Non-Newtonian Fluids are represented.
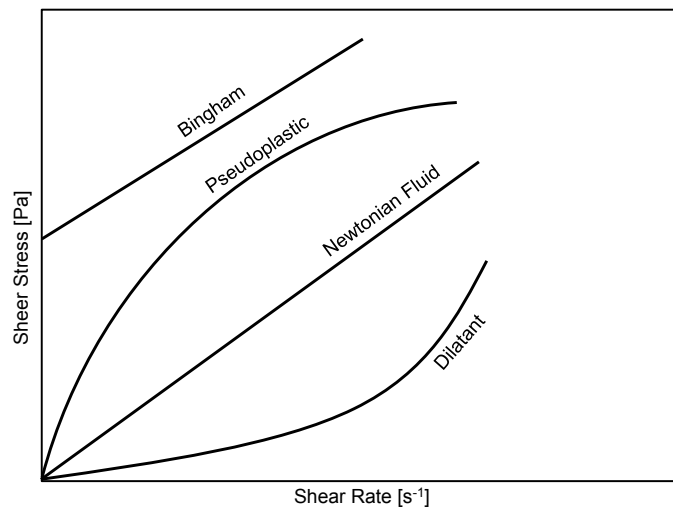
Fig. 3 Behavior of Newtonian and Non-Newtonian fluids under constant shear rate.

Fluids which obey dilatant behavior exhibit shear hardening which means their viscosity increases as the shear rate is increased (e.g. starch in water, sand). On the other hand the viscosity of pseudoplastic fluids is decreased with increasing shear rate which is defined as shear thinning (e.g. grease, paint, yoghurt). The Bingham

fluids behave like a ridged body below a critical shear stress ξ_c (yield stress) but flows as Newtonian fluid once the critical shear stress is exceeded (e.g. ketchup).

To describe the elastic behavior of a material Hooke's law of elasticity can be used which is an approximation that states, that the elastic deformation of a material is direct proportional to the applied force. Considering a spring with the cross section area A and a length L[38]. By applying a force F the spring is extended by ΔL. From Hooke's law we obtain that the extension is linear proportional to the tensile stress ξ_x:

$$\xi_x \blacksquare = -G\varepsilon_x \qquad\qquad (2.\ 3)$$

with $\varepsilon_x = \Delta L/L$ and the shear module (Young's module) G [Pa]. The Hooke's law is only valid to certain loading conditions. In this region the materials are called linear-elastic materials.

In this section the basic expression for the viscous and elastic deformation were presented. In the following two simple phenomenological models are introduced which describe the viscoelastic properties based on a superposition of elastic (spring) and viscous (dash pot) contributions.

2.1.2. Phenomenological models

Elastic materials strain instantaneously when a pulling force is applied and return back to their original state as the load is removed. Viscous material also deform under load, dissipating the applied energy as heat into the environment which causes an irreversible deformation of the system. Viscoelastic materials show a complex flow behavior which can be described as a superposition of elastic and viscous contributions[36].

The buildup blocks of phenomenological models, to describe the experimental observed viscoelasticity are represented by a combination of elastic and viscous contributions as an ideal spring respectively a dash pot filled with an ideal liquid of viscosity η. By connecting these two elements in series or parallel, several phenomenological models can be constructed which are used to adequately describe the measured mechanical response of a material[39]. From all combinations possible, here the two simplest possible combinations are presented, series and parallel phenomenological models.

The simplest parallel combinations of the spring and the dash pot, is the Kelvin Voigt model (see **Fig. 4**). This approach describes a solid like material with additional viscous properties.
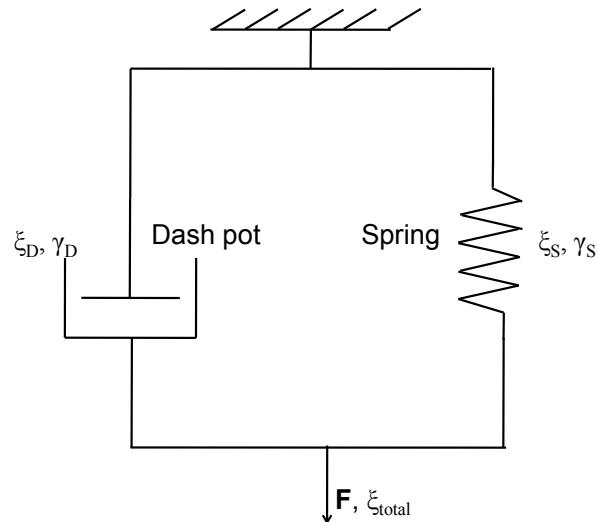
Fig. 4 The Kelvin-Voigt (parallel combination of a spring and a dash pot) element with mainly elastic response including some viscous properties.

The stress and the strain in this model are derived as follows:

$$\gamma_{total} = \gamma_s = \gamma_D$$
$$\xi_{total} = \xi_S + \xi_D .$$

(2. 4)

Materials which obey more viscous rather than elastic contributions, like polymer melts, can be described by a serial connection of a spring and a dash pot, which is referred as the Maxwell model[40] (see **Fig. 5)**. As in this thesis the entire rheological studies were performed on polymer melts, a more detailed interpretation of the Maxwell model is given.
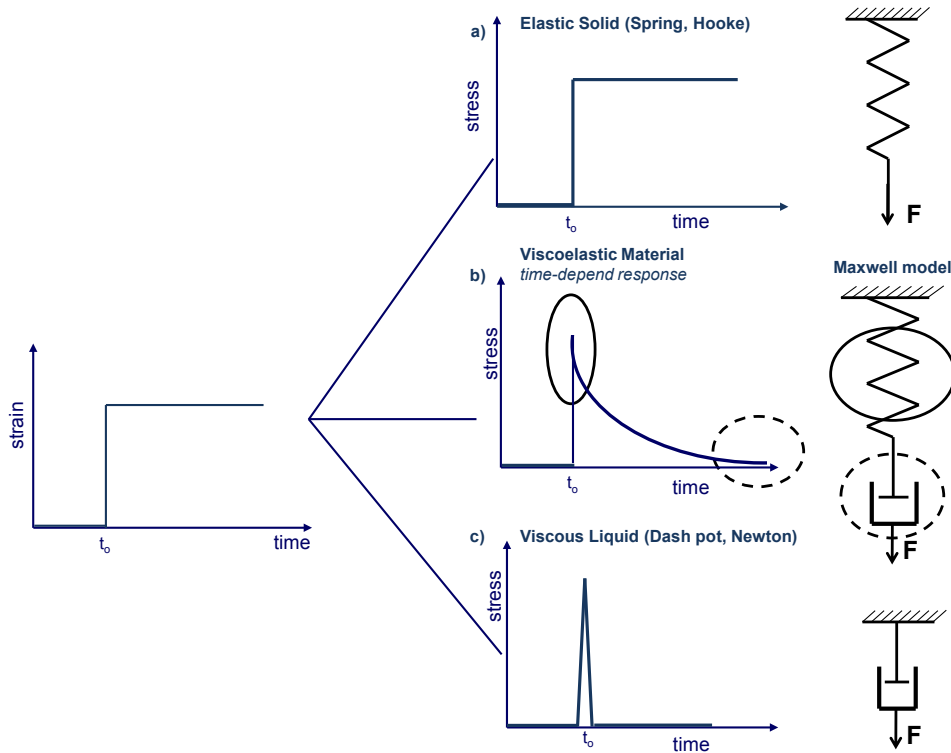
Fig. 5 Time dependent stress of a) the spring, c) the dash pot and b) the Maxwell model if subjected to constant deformation.

On the left side of **Fig. 5** the serial combination of the spring and the dash pot are schematically represented, which build up the Maxwell model. By applying a constant deformation at a time t_0 the two elements exhibit a time dependent stress response which is schematically represented on the right hand side of **Fig. 5**.

For the ideal elastic spring the applied load causes a rapid increase in the stress response which is kept constant throughout the experiment, while the dash pot rapidly dissipates the stress by viscous flow, and irreversibly elongates. Viscoelastic material possesses both, elastic and viscous properties. First the spring suddenly deforms followed by a deformation of the dash pot with a constant time rate. The total stress and the total strain in the equilibrium can be described as followed:

$$\xi_{total} = \xi_S = \xi_D$$
$$\gamma_{total} = \gamma_S + \gamma_D$$

(2. 5)

From this the shear rate for the overall Maxwell model, expressed by equation **(2.2)**, is given by:

10

$$\dot{\gamma} = \frac{1}{G} \cdot \frac{d\xi_S}{dt} + \frac{\xi_D}{\eta} = \frac{1}{G}\dot{\xi} + \frac{1}{\eta}\xi \qquad (2.6)$$

Equation **(2.6)** is the governing equation for the Maxwell model. The relaxation behavior of the system under constant strain can be derived by simply integrating equation **(2.6)** with the assumption that $\xi = \xi_0$ at t = 0, see ref.[36].

$$\xi = \xi_0 e^{-\left(\frac{G}{\eta}t\right)} \qquad (2.7)$$

The expression **(2.7)** indicates that the time dependent stress response of a viscoelastic material, described by a Maxwell model approach, exhibits exponentially decaying time behavior.

2.1.3. Oscillatory deformation

The aim of this section is to recall fundamental principles of dynamic mechanical measurements in the linear regime, where the mechanical parameters under isothermal investigation only depend on the applied excitation frequencies. It has to be kept in mind that the response to a mechanical stimulus is influenced by intermolecular forces caused by chemical and physical interactions[41]. These interactions take place on different timescales due to microstructural motions (Brownian motion, diffusion), which result from thermal or mechanical induced energy. Thus the measured linear mechanical response to a small amplitude oscillatory shear (SAOS) field will depend on the temperature and the applied excitation frequency.

If a sample is deformed sinusoidal with a constant frequency ω_1, the resulting shear stress is going to oscillate with the same frequency, but is shifted by certain phase angle δ, with respect to the strain wave. The periodic strain can be expressed as followed:

$$\gamma\ t\ = \gamma_0 \sin(\omega_1 t) \qquad (2.8)$$

Hence the shear rate is given by the time derivative of equation **2.8**:

$$\dot{\gamma} = \omega_1 \gamma_0 \cos(\omega_1 t) \qquad (2.9)$$

For a pure elastic material the stress response is in phase relative to the applied strain signal (see **Fig. 6a**) while for pure viscous materials a phase shift of 90° is observed (see **Fig. 6b**). In viscoelastic materials the mechanical response contributes to both, elasticity and viscosity, resulting in phase shift, with a phase angle δ between $0° \leq \delta \geq 90°$ (see **Fig. 6**c).
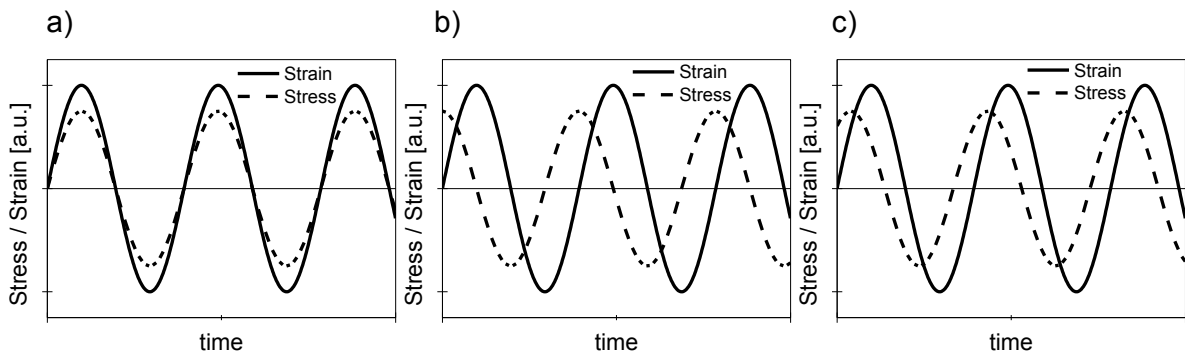
Fig. 6 Stress response (doted lines) caused by sinusoidal deformation (solid lines) for, a) ideal solid, b) ideal liquid and c) a viscoelastic material.

The time dependent stress in a viscoelastic material under small amplitude oscillatory shear (SAOS) can be expressed by:

$$\xi\ t\ =\ \xi_0 \sin(\omega_1 t + \delta)\ . \qquad (2.10)$$

By applying trigonometric addition theorems to equation **(2.10)** the shear stress can be separated into two contributions, representing an in-phase (first term in equation **(2.11)**) and an 90° outer phase part (last term in equation **(2.11)**), with respect to the excitation.

$$\xi\ t\ =\ \xi'_0 \sin(\omega_1 t) + \xi''_0 \cos(\omega_1 t) \qquad (2.11)$$

The complex modulus G* is obtained by dividing equation **(2.11)** by the shear amplitude.

12

$$G^*(\omega) = \frac{\xi^*}{\gamma_0} = G'(\omega)\sin(\omega t) + G''(\omega)\cos(\omega t) \qquad (2.\ 12)$$

Using the notation of a complex modulus

$$G^*(\omega) = \frac{\xi^*}{\gamma_0} = G' + iG'' \ , \qquad (2.\ 13)$$

and the Euler-relation ($e^{i\varphi} = \cos(\varphi) + i\sin(\varphi)$), the storage modulus G'(ω), can be received from the real part whereas the loss modulus, G''(ω), is obtained from the imaginary part:

$$G'(\omega) = \frac{\xi_0}{\gamma_0} \cdot \cos(\delta)$$
$$G''(\omega) = \frac{\xi_0}{\gamma_0} \cdot \sin(\delta) \qquad (2.\ 14)$$

The real part represents the elastic properties and the imaginary part the viscous one. The ratio of $\frac{G''}{G'}$ defines the angle between the excitation and the measured response and is defined as the loss tangent:

$$\tan(\delta) = \frac{G''}{G'} \ . \qquad (2.\ 15)$$

Considering again the in section **2.1.2** introduced Maxwell model and the derived equation **(2.6)** for the shear rate ($\frac{d\gamma}{dt} = \frac{1}{G}\dot{\xi} + \frac{1}{\eta}\xi$), but this time under an oscillating deformation the solution of the differential equation is given by:

$$\xi = \left[\frac{G \cdot \tau_M^2 \cdot \omega_1^2}{1 + \tau_M^2 \cdot \omega_1^2}\right] \cdot \sin(\omega_1 t) + \left[\frac{G \cdot \tau_M \cdot \omega_1}{1 + \tau_M^2 \cdot \omega_1^2}\right] \cdot \cos(\omega_1 t) \qquad (2.\ 16)$$

The relaxation time τ of a Maxwell element is defined as $\tau = \dfrac{\eta}{G}$. Equation **(2.16)** can be written as:

$$\xi = G' \cdot \sin(\omega_1 t) + G'' \cdot \cos(\omega_1 t) .$$ (2. 17)

It can be seen that the storage and loss modulus obey different frequency dependence of G' ~ ω^2 respectively G'' ~ ω at low frequencies. This behavior can be used to describe the experimentally observed mechanical response of viscoelastic fluid under oscillatory shear. In **Fig. 7** the frequency dependence of G'(ω) and G''(ω) (compare equation **(2.16)**) are represented, with the crossover point of G' and G'' at $\omega_1/2\pi = 1/\tau_M$ (τ_M = 10 s).
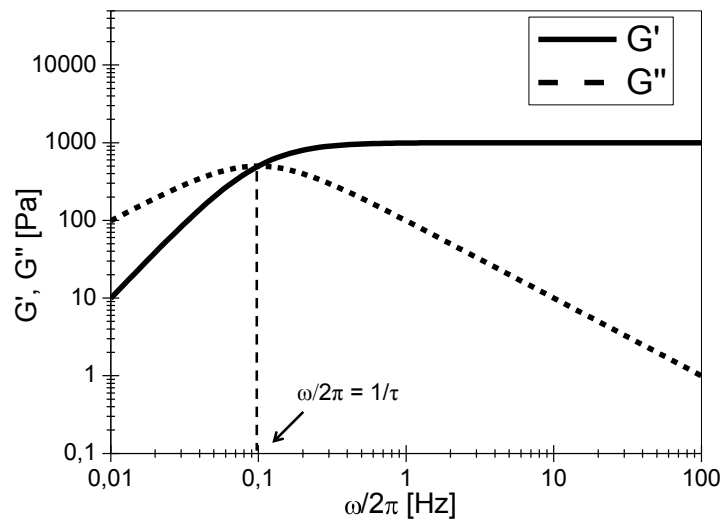
Fig. 7 Frequency dependence of the mechanical storage G' and loss G'' modulus for a Maxwell element with a relaxation time τ_M = 10 s.

It is important to notice that to describe the measured rheological data of a viscoelastic material, such as polymer melts, one Maxwell element is often insufficient. One way to account for this problem is the approximation of the frequency dependence of G' and G'' by multiple coupled models with different relaxation times[39]. These modes are expressed by:

$$G'(\omega_1) = \sum_{n=1}^{N} G_n \left[\frac{G \cdot \tau_{M,n}^2 \cdot \omega_1^2}{1 + \tau_{M,n}^2 \cdot \omega_1^2} \right]$$

$$G''(\omega_1) = \sum_{n=1}^{n} \left[\frac{G \cdot \tau_{M,n} \cdot \omega_1}{1 + \tau_{M,n}^2 \cdot \omega_1^2} \right]$$

(2. 18)

A schematic sketch of a multiple mode Maxwell model is represented in **Fig. 8**. In this model the deformation amplitude is equal to the deformation γ of each individual mode and the shear stress is given by $\xi_{multi} = \sum_{k=1}^{N} \xi_k$.
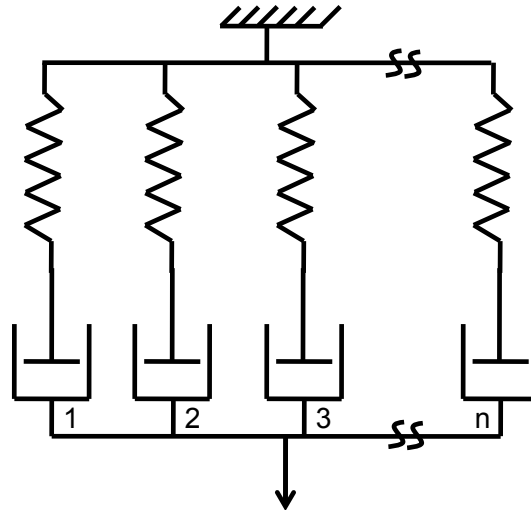
Fig. 8 Multiple mode Maxwell model, consisting of several Maxwell elements in parallel arrangement[39].

For more complex experimental data different models have been developed which are superposition of Maxwell and Kelvin-Voigt elements such as the Burger model consisting of a serial arrangement of a Kelvin-Voigt and a Maxwell[39].

2.1.4.   Time Temperature Superposition (TTS)

In the previous section the basic principles to describe the viscoelastic response observed in complex fluids were introduced. The mathematical derivations were performed for the mechanical linear regime. The mechanical linear regime is defined as the regime in which the rheological properties, G' and G" are independent on the applied deformation[23]. In this regime the mechanical stimulus is small enough that the equilibrium state of the investigated material is not influenced. Within this small

15

strain (stress) experiments a substance is deformed by a small amplitude oscillatory shear (SAOS). In the following, the fundamental viscoelastic response under SAOS of linear homopolymer melts is discussed. Furthermore the Time Temperature Superposition principle[42] is introduced which allows the construction of a master curve covering the whole mechanical accessible spectra of polymer melt dynamics.

Above the glass transition temperature, amorphous, linear homopolymer melts obey similar linear viscoelastic response[43]. Usually the frequency range in which the polymer dynamics occur exceeds the experimentally accessible frequency range (about three to four decades). Time temperature superposition (TTS) has been used to obtain the whole spectra of polymer dynamics for several properties such as creep compliance and stress compliance against time or dynamic modulus against frequency[44]. To generate a master curve the following steps are required[45]:

- A frequency sweep test is performed at isothermal conditions in the linear mechanical regime. The measured rheological properties for instance G', G'' and $tan(\delta)$ are observed double logarithmic against frequency.

- Similar frequency sweep tests are performed with the same material at different temperature levels and the dynamic modulus curves are obtained (see **Fig. 9a**).

- A reference temperature (T_R) is selected.

- All curves obtained from the frequency sweep tests at different temperature levels are shifted along the log(frequency) scale to superpose a master curve.

In **Fig. 9** the shifting process is represented for an anionic synthesized linear polystyrene (PS) with a number average molecular weight of M_w = 76,000 g/mol (76k) and a polydispersity of PDI = 1.05. The reference temperature was chosen to T_R = 160 °C.
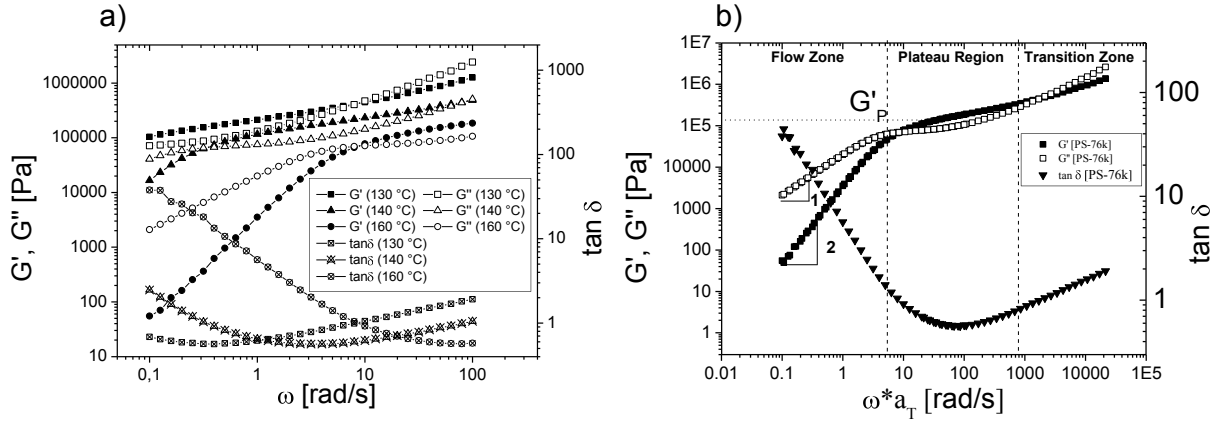
Fig. 9 a) Obtained dynamic modulus and tanδ as a function of frequency for PS-76k in the linear regime, at various temperatures. b) Master curve of G', G" and tanδ as a function of the reduced frequency ω^*a_T at T_R = 160 °C obtained from the data of (a) by TTS.

To construct accurate master curves of a polymer melt the smoothness of the overlap where two individual curves meet is an important criteria. The principal of TTS can be applied to most linear polymer melts which do not possess a phase transition in the observed temperature range. If the TTS concept is valid the master curves provides the true behavior of the polymer dynamics over a wide frequency range (approximately six decades). The factor which is needed to shift the data along the log(frequency) scale is called the shift factor a_T[23]. Williams, Landel and Ferry evaluated a semi-empirically the relationship between a_T and temperature, the so called WLF equation which can be derived by the theory of free volume[46].

$$\log(a_T) = \frac{-C_1(T - T_R)}{C_2 + (T - T_R)} \qquad . \qquad (2.\,19)$$

The constants C_1 and C_2 are universal constants with respect to the chosen reference temperature, for example for linear polystyrene C_1 = 13.7 and C_2 = 50 K, referenced to the glass transition[23].

The obtained master curve shown in **Fig. 9b** can be divided into three regimes, which correspond to specific dynamics in the polymer melt occurring on different time and length scales[36]. At low frequencies, which corresponds to high temperature behavior, the <u>flow zone</u> is observed. In this region the viscoelastic properties of the polymer melt is dominated by the viscous fraction, as G" has a higher value than G'. Therefore the overall mechanical property can be described to be liquid like. As the frequency is increased (equivalent with a decreased temperature) G' and G" cross.

17

After this crossover point the overall mechanical property of the melt is dominated by the elastic fraction obeying a rubber like behavior. This regime is called the <u>rubber plateau</u>. With increasing frequency a second crossover point is obtained, beyond, G'' again dominates the mechanical response of the melt. This region is referred as the <u>transition zone</u>. For lower temperatures respectively higher frequencies the polymer melt behaved like an elastic solid and G' dominates the mechanical response (not shown here). This regime is referred to the <u>glass zone</u>.

In the following section a brief introduction to the reptation model[22] is presented which enables to correlate molecular dynamics on different length and time scales to the observed rheological master curve.

2.1.5. The reptation model

Polymer chains are usually built up by numerous monomer units which are covalently bound to each other. Due to thermal mobility monomer units (segments) are able to perform rotational and translational motions. This enables the polymer backbone to pass through all possible conformations. The herein presented interpretations are derived for a linear homopolymer in solution and polymer melts[22, 36].

Utilizing statistical methods a relation between the chain conformations can be derived. The simplest way to describe a linear homopolymer chain is the random coil. It represents a statistical distribution of shapes over a long period of time. A key factor to describe the shape and the chain dynamics is the averaged end-to-end distance <h> (see **Fig. 10**). The relation between the average end-to-end distance and the degree of polymerization inspired experiments and simulations, suggesting a universal scaling behavior[42]:

$$\langle h \rangle \sim N^{\upsilon} \tag{2.20}$$

with the Flory exponent υ, which reflects the degree of stretching of the polymer chain. In the dense state of concentrated polymer solutions and polymer melts, where the polymer chains are highly interacting, the exponent $\upsilon = 1/2$ as derived from the ideal Gaussian random walk ("Gaussian" because the end-to-end vectors of the

polymer chains are normally distributed)[46]. In diluted solutions υ is rather larger (0.59) and for a totally elongated polymer chain the exponent becomes 1, see ref.[46].
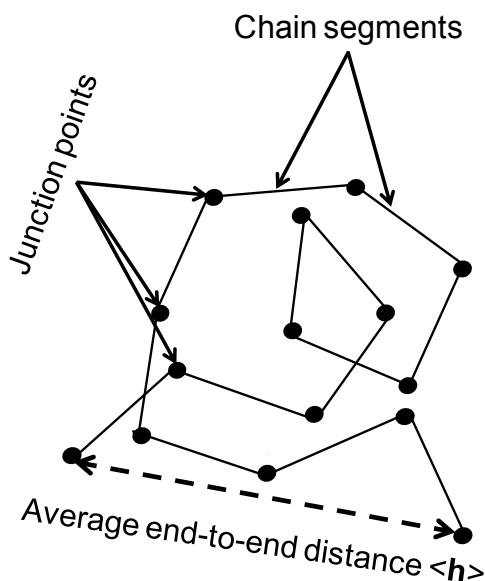
Fig. 10 Schematic representation of a polymer random coil. At the connection points the polymer segments are able to rotate around their axis.

In concentrated polymer solutions and melts, polymer chains are in close contact and interpenetrate each other. Depending on the length and the flexibility of the polymer chains, neighboring chains interpenetrate, building up entanglements. To reach a critical length to form entanglements, the polymer chain has to have a molecular weight above the entanglement molecular weight M_e, which is a characteristic value for a polymer compound, contributing to the flexibility of the polymer chain segments (e.g. M_e(PS) = 13000 g/mol[40]). These entanglements form temporary physical networks which constrain the motion of the polymer chain. This difficult many-body problem can be simplified with a single body problem in an effective field, which is a common method in theoretical physics. The single body is the polymer chain, whose viscoelastic properties is described by the Rouse model[22], embedded in the effective field which is approached as a tube like region wherein the neighboring polymer chains constrain the motion along the contour of the single chain[22].

The concept of a tube was first discussed by Doi and Edwards[47] while its influences to the dynamics were first explored by DeGennes[48]. The polymer chain is trapped inside a tube with the radius *r*, while the length of the tube is defined by the

single chain contour *L* (see **Fig. 11**). The tube radius is of the order of length of the end-to-end distance of a polymer chain with a molecular weight in the order of the entanglement molecular weight M_e[22]. Therefore polymer chains with molecular weights above the entanglement molecular weight are strongly affected by the constraining tube. The temporary tube constrains the motion of the chain perpendicular to the tube while curvilinear of the chain motion and diffusion of center of mass is permitted.
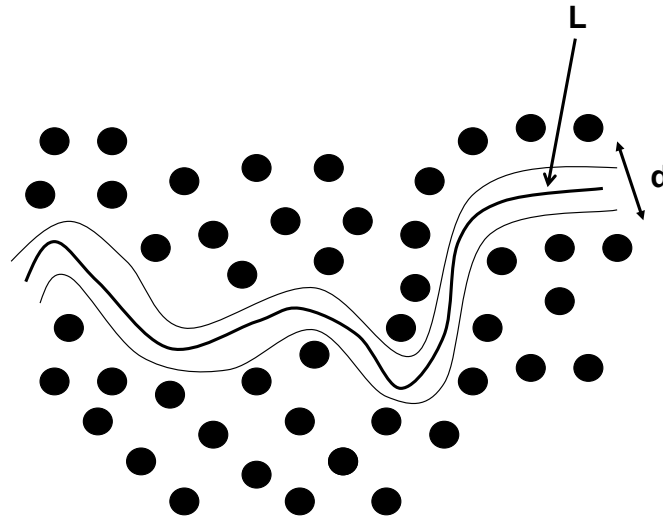
Fig. 11 Single polymer chain in a tube built up by the surrounding polymer chains. The tube is defined by the average diameter d and the contour length of the single polymer chain L.

For this simplified model the diffusion can be described by a one-dimensional diffusion constant D_c. As the chain moves along the tube, parts of the reptating chain have left the tube, leading into a new constraining effective field. Therefore, new conformations diffuse from the ends of the polymer chain inwards. The probability P(s, t) to find a chain segment at a given time *t* at a position *s* can be derived by Fick's second law[49], which is a one dimensional diffusion equation.

$$\frac{\delta P}{\delta t} = D_c \left(\frac{\delta^2 P}{\delta s^2} \right)$$

(2. 21)

with the boundary conditions

and
$$P(s,t) = \delta(0)$$
$$P(s,t) = 0 \quad \text{for} \quad s \to \pm\infty \cdot \tag{2.22}$$

Herein δ denotes the delta distribution ($\delta = 1$ for the first chain segment) and D_c the diffusion constant which fulfils Einstein's[49] law for the relation between friction coefficient ς and diffusivity:

$$D_0 = \frac{kT}{N\varsigma} \cdot \tag{2.23}$$

with N being the number of monomer units in the polymer chain.

The solution of the differential equation **(2.21)** is:

$$P(s,t) = \frac{1}{\sqrt{4\pi D_c t}} \exp\left(-\frac{s^2}{4D_c t}\right) \cdot \tag{2.24}$$

For a one dimensional system the mean square displacement of s at time t is given by

$$\langle s^2 \rangle = \int_{-\infty}^{+\infty} s^2 P(s,t) ds = 2D_c t \tag{2.25}$$

The longest time, a polymer chain needs to completely diffuse out of the original constraining tube at t = 0 (disentanglement time τ_D), can be derived by setting $<s^2>$ = L^2 and t = τ_d. It can be calculated from the following equation:

$$\tau_D = \frac{L^2}{2D_c} \tag{2.26}$$

From the relation between the one-dimensional diffusion coefficient and the polymer molecular weight ($D_c \sim M^{-1}$) the dependency of τ_d to the molecular weight can be derived.

$$\tau_D \sim M^3 \qquad\qquad\qquad\qquad (2.\,27)$$

Experimental studies revealed that the exponent slightly varies from the expected value of 3, being 3.4, see ref.[22]. The deviance from the theory to the observed values can be explained by the simplifications which have been made to derive the model. For instance the approach is not concerning the movement of the neighboring chains that built up the tube. Furthermore, other relaxation processes than chain reptation, such as contour length fluctuations[50-52], thermal constrain release[53-55] and tube dilation[56, 57] are neglected, but have to be considered for real systems. Nevertheless the tube model permits to reduce the observed mechanical response such as for linear homopolymer melts to the molecular dynamics of the polymer chains.

For example the frequency dependent mechanical response (see **Fig. 9**) as discussed in section **2.1.4** for linear homopolymer melts, can be explained by polymer chain dynamics occurring on different time scales. At low frequencies (referred as the flow zone) the mechanical response is dominated by the viscous fraction, the investigated time scale is long enough that the polymer chain can fully relax from the constraining tube. With increasing frequencies the polymer chains have less time to diffuse out of the constraining original tube.

The crossover between G' and G'' ($\tan\delta = 1$) indicates the longest disentanglement time τ_d of the polymer chains where the relation $\omega_1 / 2\pi \cdot 1 / \tau_D = 1$ is fulfilled. At frequencies beyond the cross over point the polymer chain dynamics are too slow to relax the original constraining tube on the investigated time scale ($\omega_1 / 2\pi > 1 / \tau_D$) and the entanglements which build up the tube act as a cross linked networks. In this region the physical entanglements of the melt behave on a short time scale like a rubber and the elastic modulus G' is dominating the mechanical response.

The occurrence and the extent of a rubber plateau depend only on the degree of polymerization and the specific entanglement molecular weight of the polymer. In **Fig. 12** the master curves of the dynamic storage modulus G', obtained for linear polystyrene samples with a narrow polydispersity at a reference temperature $T_R = 160\,°C$, visualizes the molecular weight dependence of the plateau zone.
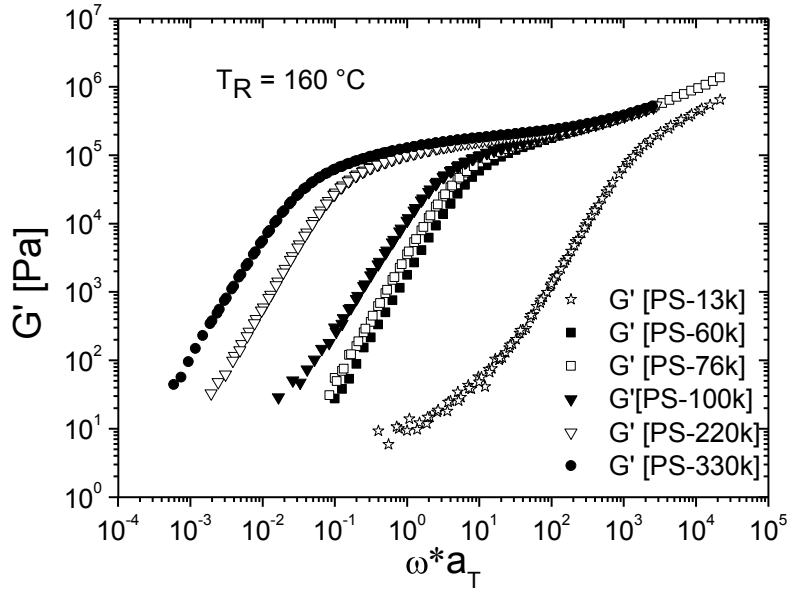
Fig. 12 Master curve obtained for linear polystyrene samples with different molecular weights at T_R = 160 °C. It can be seen that with decreasing molecular weight the rubber plateau decreases in length while for the lowest molecular weight ($M_w(Polymer) < M_c$) no plateau regime is observed.

It can be seen that the slope on the low frequency side is two for all PS samples which is predicted from the phenomenological models introduced in the section **2.1.2**. In contrast, the rubber plateau which is indicated by the nearly constant frequency dependence of G', is enlarged as the molecular weight and hence the number of entanglements increases. For the lowest molecular weight sample PS-13k (M_w = 13 000 g/mol) the polymer chains are too short to form an entangled networks. Hence the master curve of G' shows no distinct rubber plateau.

For those samples which have molecular weights above a critical weight M_c which is approximately have as large as M_e ($M_e \approx 2M_c$), the plateau value of G'_P in the rubber plateau region is approximately the same. From G'_P the entanglement molecular weight can be calculated[36]:

$$M_e = \frac{\rho_b \cdot R \cdot T}{G_P'} \qquad (2.\ 28)$$

with the bulk density ρ_b of the polymer, the ideal gas constant R and the temperature T.

2.1.6. LAOS: Introduction to the non-linear regime

In the 1960's to 1970's the basic concept of large amplitude oscillatory shear (LAOS) had been reported in literature[29, 58-60]. From the non-linear mechanical response four different classes of materials were characterized[61]. Strain thinning is the most commonly effect observed in concentrated polymer solutions and melts under LAOS, being related to shear thinning in steady shear flow[36, 62]. It originates from mechanical induced orientation of polymer chains, particles or microstructures. This alignment decomposes intermolecular constrains in the sample[29].

Directly in contrast to the strain thinning behavior is the observed strain hardening. This effect is contributed to interactions between segments of the complex fluid. For instance a polyvinal alcohol (PVA) Borax (sodium borate) solution exhibits strain hardening. This effect is expected to be contributed by shear-induced complexation between the hydroxyl group of the PVA and the borate anions which resists the undergoing shear deformation[63].

A further phenomenon, often observed for soft glassy materials such as emulsions[64] and suspensions[65], is strain overshoot. The effect may be regarded as a combination between formation and destruction of intermolecular networks. The strain overshoot can be subdivided into a weak and strong strain overshoot. The former only shows an overshoot in $G''(\gamma_0)$ while the later exhibits an overshoot in both $G'(\gamma_0)$ and $G''(\gamma_0)$[29]. A schematic representation for the above described phenomena is presented in **Fig. 13**.
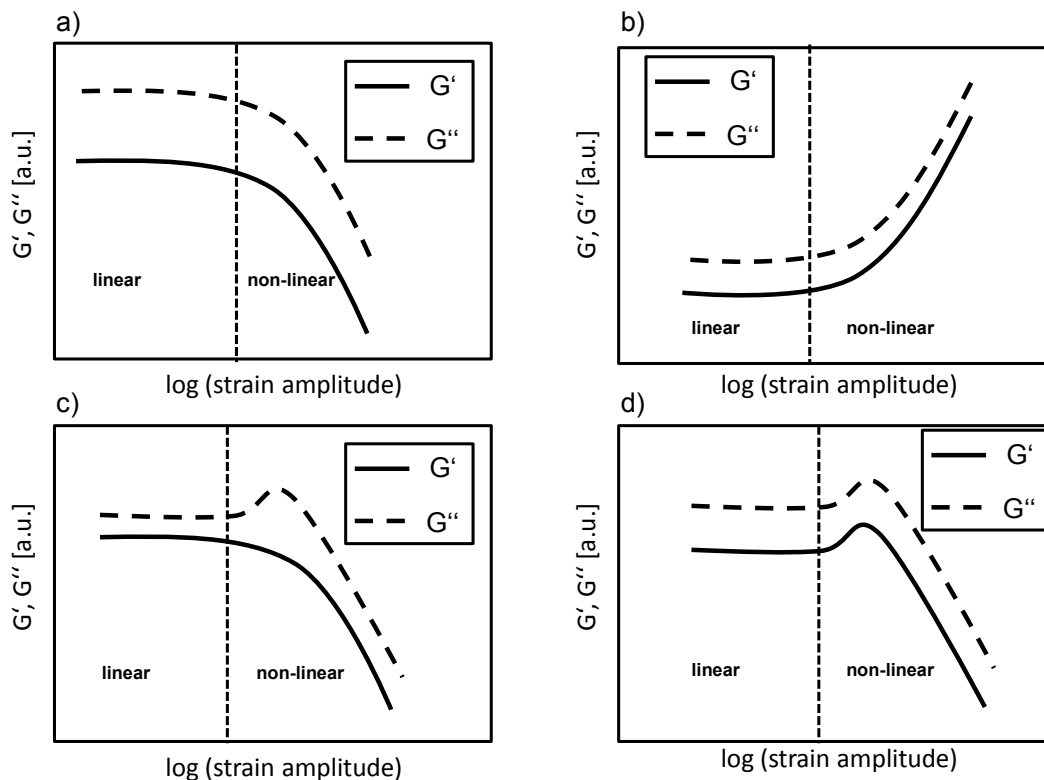
Fig. 13 Different strain dependence of complex fluids under LAOS as outlined by Hyun et al.[61]; a) strain thinning, b) strain hardening, c) weak overshoot, d) strong overshoot. The dotted vertical lines separate between linear and non-linear mechanical response.

From the strain dependence of the mechanical module, a classification into a linear regime and a regime in which the mechanical response obeys non-linear behavior can be derived. The linear regime is classically defined as the area in which the mechanical response of the sample is only a function of the applied shear frequency and do not depend on the strain amplitude. The non-linear regime begins as the mechanical module show strain dependence. The onset of the non-linear regime is roughly estimated by the dashed lines in **Fig. 13**. Typically critical strain amplitudes, above which linear homopolymer melts obey non-linear behavior, are in the range of $\gamma_0 > 0.1$[29].

As discussed above, G'(ω) and G''(ω) are based inherently on the assumption that the stress response are purely sinusoidal. For LAOS experiments, however, the resulting stress is no longer a purely sinusoidal. In **Fig. 14**a pure sinusoidal, as obtained in the linear regime and a stress response during LAOS experiment are represented for PS-100k at T = 160 °C and $\omega/2\pi$ = 1 Hz.

25
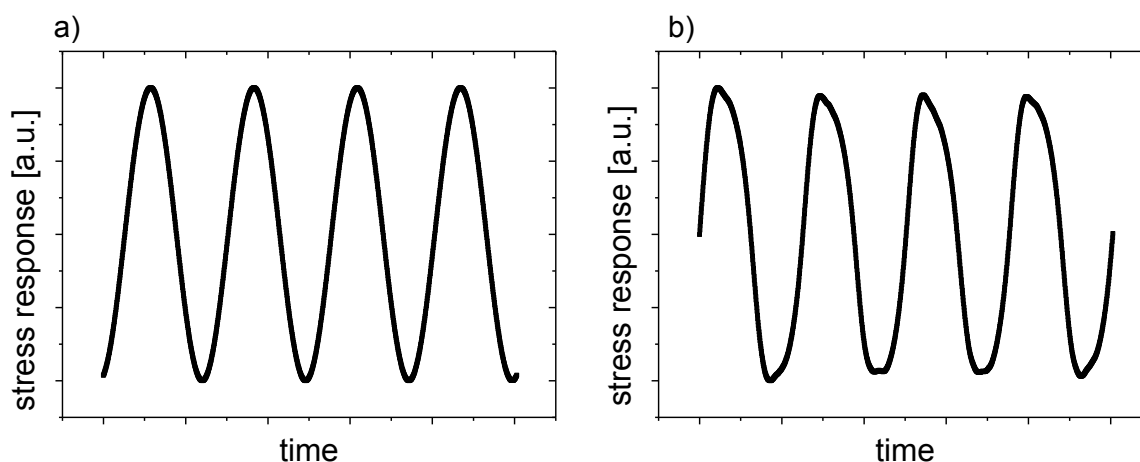
Fig. 14 Stress data of a linear polystyrene (PS-100k) sample: a) $\omega/2\pi$ = 1 Hz, T = 160 °C and γ_0 = 0.01 (linear response), b) $\omega_1/2\pi$ = 1 Hz, T = 160 °C and γ_0 = 5.8 (non-linear response)

The distortion of the periodic stress response under LAOS conditions is a clear identification for the non-linear regime even for the time dependent stress signal. As large amplitude oscillatory shear experiments are not limited to shear frequency and strain amplitude as measurements in the linear regime are, they can be applied for various viscoelastic materials. Nevertheless, often the deviance from pure sinusoidal stress response is not clearly visible from the obtained raw data. Several methods have been developed to distinguish between linear and non-linear regime, as well as to characterize and quantify the nonlinear viscoelastic response, see reference and publications cited there[29].

A graphical method which allows to rapidly and qualitatively evaluating the experimental data are the so called Lissajous curves[66]. In this representation the stress (stress rates) is plotted versus the strain (rate of strain) (see **Fig. 15**). The variety of stress waveforms, which are obtained for complex fluids, gives rise to theoretical and experimental efforts to correlate these structures to changes in the material or even to molecular dynamics.

26
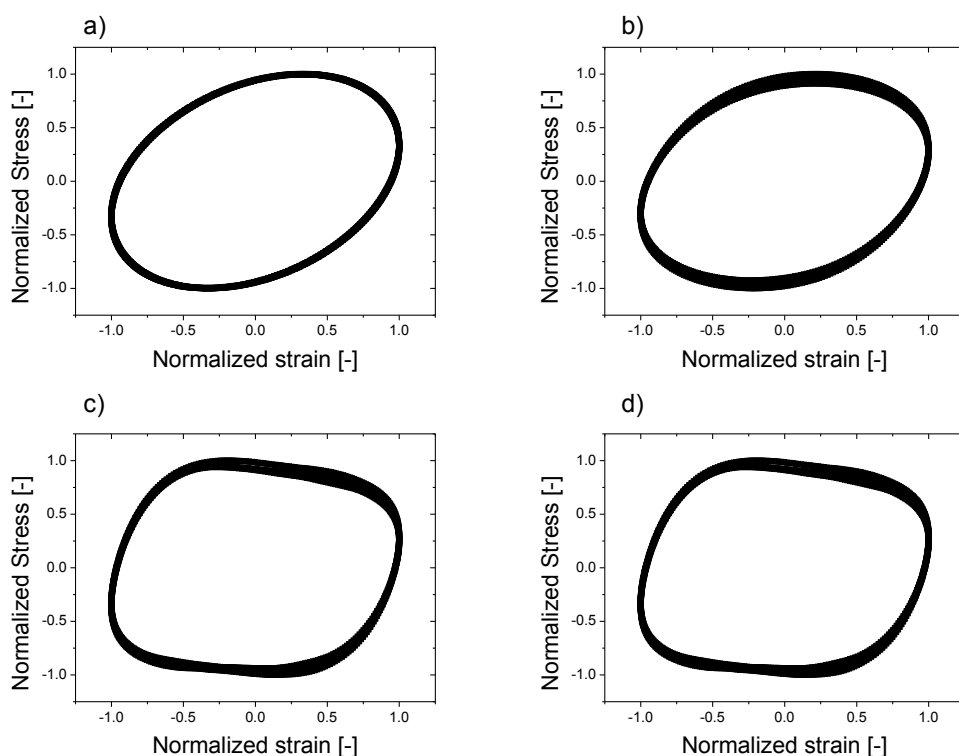
Fig. 15 Experimental obtained Lissajous curves (stress y axis) versus strain (x axis) of PS-100k for several measurement cycles ($\omega_1/2\pi$ = 1 Hz, T = 160 °C) for a) γ_0 = 0.3, b) γ_0 = 2, c) γ_0 = 4, d) γ_0 = 5.8.

In the case of linear viscoelastic behavior (not shown here) the Lissajous curves show ellipses. Deviances from this shape and symmetry (2 mirror axis, 1 point of inflection) indicate non-linear behavior. In the case of linear homopolymer melts the broadening of the ellipsoid indicates that polymer melt is dissipative at different frequencies[36], as can be seen from the obtained waveforms for PS-100k.

This visual method is helpful to distinguish between linear and non-linear viscoelastic response also providing an overview of nonlinear viscoelastic response, but is rather insufficient to quantify and directly follow non-linear mechanical flow. The in the following section presented Fourier-Transform Rheology (FT-Rheology) enables to analyze and quantify the non-linear viscoelastic response with a high sensitivity.

2.2. Fourier Transform Rheology

In the section **2.1.6** it has been mentioned that for large amplitude oscillatory shear experiments the resulting stress signal is no longer a pure sinusoidal, but a periodic function which is somehow distorted compared to the input signal. By

applying the concepts of Fourier Transformation[67] to analyze the mechanical non-linear response signal a phase spectra and magnitude spectra is obtained which consist of higher harmonics with respect to the excitation frequency ω_1[31, 32]. This method was already suggested in the early 1960's[68], but due to technical problems (specifically soft- and hardware) and experimental limitation (e.g. torque and transducer resolution), this concept had not been established for non-linear mechanical data analysis.

Principally the methodology for high sensitivity Fourier Transform rheology (FT-Rheology) designed by Wilhelm et al.[31, 32], established this concept of data analysis in the field of oscillatory non-linear rheology. Before a detailed discussion about the applications of FT-Rheology for mechanical characterization is provided, a brief introduction to the concepts of Fourier Transformation analysis is given.

2.2.1. Basic aspects of the Fourier Transformation

The Fourier Transformation is used to decompose a signal into its constituent frequencies. It is applied to continuous integrable functions which are decomposed into a series of orthogonal trigonometric functions. The Fourier Transformation transforms one complex-valued function of a real variable into another. For instance a real or complex time signal f(t) is transformed in to its frequency dependent spectrum F(ω). Furthermore, common variable transformations are impulse / space or densities of electrons are converted to the reciprocal space.

To derive the basic mathematical concepts the Fourier Transformation of time signal, f(t), into the frequency dependent spectrum F(ω) are discussed[67].

$$f(t) = \frac{1}{2\pi} \int_{-\infty}^{+\infty} F(\omega)\exp(it\omega_1)d\omega \tag{2. 29}$$

and

$$F(\omega_1) = \int_{-\infty}^{+\infty} f(t)\exp(-i\omega_1 t)dt . \tag{2. 30}$$

The prefactor $\dfrac{1}{2\pi}$ depends on the applied convention which is chosen. Equation (2.29) and (2.30) show that the Fourier Transformation is inherently complex. Thus, even for a real time-domain data set, f(t), conversion into the frequency dependent function F(ω), results in a complex spectrum, with a real $F_R(\omega)$ and an imaginary $F_I(\omega)$ part.

$$F(\omega) = F_r(\omega) + iF_i(\omega) = A(\omega)\exp(iP(\omega)) \tag{2.31}$$

Alternatively, the complex spectra can be analyzed with respect to the magnitude A(ω) and the phase P(ω). The magnitude and phase spectra are calculated as followed:

$$\left| A(\omega) \right| = \sqrt{\mathrm{Re}^2 + \mathrm{Im}^2} = \sqrt{F_r(\omega)^2 + F_i(\omega)^2} \tag{2.32}$$

and

$$P(\omega) = \arctan\left(\frac{\mathrm{Im}}{\mathrm{Re}}\right) = \arctan\left(\frac{F_i(\omega)}{F_r(\omega)}\right) \tag{2.33}$$

The connection between the different components is visualized in **Fig. 16**.
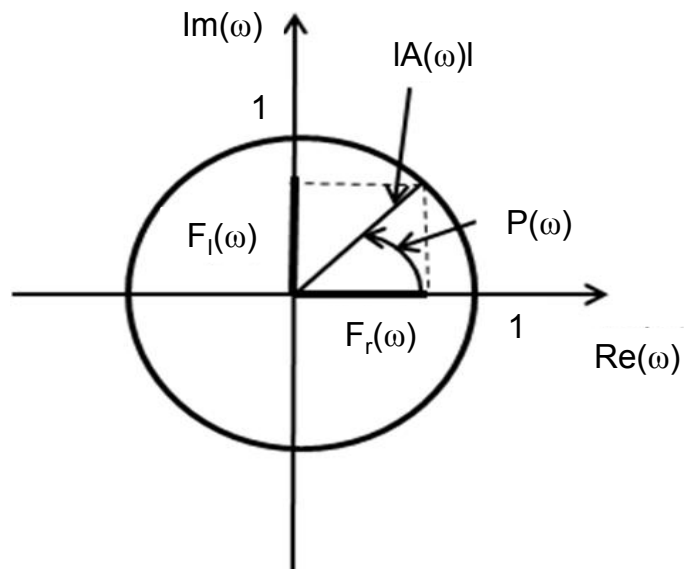
Fig. 16 Polar illustration of a complex number z = Re + i*Im to describe the connectivity between magnitude and phase.

2.2.2. Principles of FT-Rheology on the stress signal

The FT-Rheology is one of the most sensitive methods to analyze and quantify time dependent non-linear stress dependence[69, 70]. The obtained raw stress data $\zeta(t)$ are converted into the frequency dependent complex spectrum $\xi(\omega)$, which can be examined with respect to the magnitude and phase. To significantly increase the sensitivity Wilhelm et al.[31] developed the high sensitive FT-Rheology methodology, utilizing data processing techniques from NMR spectroscopy. The sensitivity, which had been one of the major problems in previous concepts of FT-Rheology, has been drastically increased (signal to noise ratio S/N ≈ 1:100,000 for a single scan), especially due to the use of oversampling with high performance Analog-to-Digital Converter (ADC) cards and a special FT algorithm. The herein presented general concept of FT-Rheology is mainly derived from the theory published by Wilhelm et al.[31, 32].

From the applied experimental conditions it is ensured, that the applied oscillating deformation occurs with a single frequency ω_1. Therefore, the higher frequencies which built up the time dependent stress response signal have to be associated with the non-linear response of the sample. To derive a mathematical explanation for the appearance of higher harmonics, the following considerations for an oscillating shear deformation have been done.

The force balance of a system with the weight m, the viscosity η and the elastic modulus G, which is stimulated by an oscillating mechanical excitation, can be described by a linear differential equation of the following type:

$$m\ddot{\gamma} + \eta\dot{\gamma} + G\gamma = A_0 \exp(i\omega t)$$

(2. 34)

The left side corresponds to the kinematic, viscous and elastic fractions, which effect the system. The solution of the differential equation **(2.34)** in the linear regime with the assumption for a single viscosity and elasticity is given by the following harmonic function:

$$\gamma(t) = \gamma_0 \exp i(\omega_1 t + \delta) \quad,$$

(2. 35)

with the characteristic phase shift δ.

As already mentioned above the non-linear regime is defined as the regime in which the viscosity η is a function of the absolute shear rate even under periodic conditions. Therefore, η is independent of the shear direction ($\eta(\dot{\gamma}) = \eta(-\dot{\gamma})$). The shear rate depended expression for $\eta(\dot{\gamma})$ can be approximated via a Taylor expansion with respect to the shear rate:

$$\eta(|\dot{\gamma}|) = \eta_0 + a|\dot{\gamma}| + b|\dot{\gamma}|^2 + ... \qquad (2.36)$$

The herein made assumption can also be assigned to oscillatory shear experiments such as LAOS while the expansion coefficients η_0, *a* and *b* might be complex numbers. This can be interpreted as induced phase shifts with respect to the excitation frequency. For an oscillating mechanical stimulus it was shown above that the deformation is given by:

$$\gamma\ t\ =\ \gamma_0 \sin(\omega_1 t) \qquad (2.8)$$

and

$$\dot{\gamma} = \omega_1 \gamma_0 \cos(\omega_1 t) \qquad (2.9)$$

The time dependence of the shear rate $|\dot{\gamma}|$ is expressed as a sum of different harmonic contributions:

$$|\dot{\gamma}| = \omega_1 \gamma_0 \left(\frac{2}{\pi} + \frac{4}{\pi} \left(\frac{\cos(2\omega_1 t)}{1 \cdot 3} - \frac{\cos(4\omega_1 t)}{1 \cdot 5} + \frac{\cos(6\omega_1 t)}{1 \cdot 7} \pm ... \right) \right)$$
$$\propto\ a' + b'\cos(2\omega_1 t) + '\cos(4\omega_1 t) + ... \qquad (2.37)$$

Equation **(2.37)** shows that higher harmonics only appear if the viscosity becomes a function of the shear rate. As the cosine function has a periodicity of π, equation **(2.37)** only consists of even higher harmonic. Extending Newton's equation with equation **(2.36**) and **(2.37)**, the shear stress is given by:

$$\xi \quad \propto \quad \eta_0 + a(a' + b'\cos(2\omega_1 t) + c'\cos(4\omega_1 t) + ...)^2 ... \cos(\omega_1 t)$$
$$\propto \quad (a'' + b''\cos(2\omega_1 t) + c''\cos(4\omega_1 t) + ...)\cos(\omega_1 t) \qquad (2.\ 38)$$

With the aid of trigonometric addition theorems, followed by the multiplication of the term in the brackets with the term $\cos(\omega_1 t)$, equation **(2.38)** can be rewritten as a sum of odd harmonics:

$$\xi \quad \propto \quad A\cos(\omega_1 t) + B\cos(3\omega_1 t) + C\cos(5\omega_1 t) + ... \qquad (2.\ 39)$$

with *A*, *B*, *C*, … being the complex coefficients.

The derivation provided above, indicates that the Fourier Transformation of a time dependent stress response for a perfect sinusoidal excitation in the mechanical non-linear regime, will lead to a magnitude spectrum which consists only of more or less pronounced odd higher harmonics with respect to the excitation frequency. It has to be noted that also even harmonics have been observed experimentally. These even harmonics may be attributed to experimental artifacts[71], but also phenomena which occur on the microscopic scale may account for[72].

2.3. Block Copolymers

The definition copolymer encloses a broad variety of macromolecular structures which all have in common, that the resulting polymer is composed of at least two different homopolymers which are covalently bond. With the aid of controlled polymerization techniques such as anionic polymerization[73], atom transfer radical polymerization (ATRP)[8] or Reversible addition fragmentation chain transfer (RAFT)[4], a broad range of different molecular architectures can be obtained[12] (see **Fig. 17**). The possibility to combine several polymer chains with different chemical, physical and mechanical properties, gives rise to tailored functional materials.

Diblock copolymer

Triblock copolymer

A-B-Graftblock copolymer

Multiblock copolymer
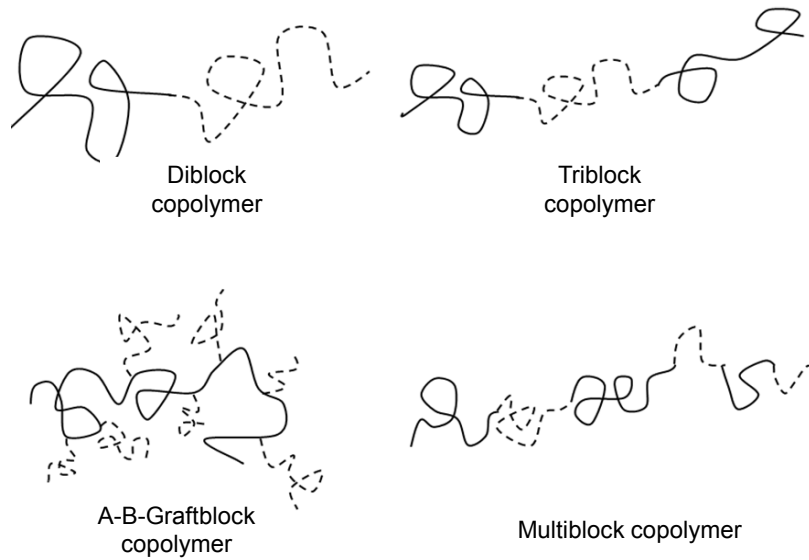
Fig. 17 Schematic representation of typical linear or branched block copolymer structures

As they main focus of this thesis deals with linear diblock copolymer melts, the attention of the following discussion is restricted to this class of block copolymers.

2.3.1. Physical properties

The chemical heterogeneity of the monomeric species (*A* and *B*), the two different polymer blocks consist of, gives rise to one of the remarkable characteristics of these material class, the "microphase separation". Three parameters control the phase behavior: the overall degree of polymerization, the overall volume fraction f and the segment-segment interaction parameter χ_{FH} (Flory-Huggins parameter)[20]. The phenomenon of phase separation, which occurs on a nanometer length scale (typically 10 – 100 nm), is governed by the two thermo dynamical effects, the enthalpy and the entropy.

For a diblock copolymer the change in the Gibbs free energy ΔG_m can be derived from the Flory-Huggins-theory[42]:

$$\frac{\Delta G_m}{k_B T} = \frac{f_i}{N_i} \ln f_i + \frac{f_j}{N_j} \ln f_j + f_i f_j \chi_{FH}$$

(2. 40)

Equation **(2.38)**, with k_B being the Boltzmann constant and T the absolute temperature, relates the change in the free energy ΔG_m, for each segment in the polymer chain, to the volume fraction f_k of the different blocks, their degree of

33

polymerization N_k and the so called Flory-Huggins interaction parameter χ_{FH}. The first two terms on the right hand side of equation **(2.40)** contributes to the entropy of mixing ΔS_m while the last term is correlated to the enthalpy of mixing ΔH_m.

The Flory-Huggins interaction parameter χ_{FH} is given by the following definition:

$$\chi_{FH} = \frac{1}{k_B T}\left(\varepsilon_{ij} - \frac{1}{2}(\varepsilon_{ii} + \varepsilon_{jj})\right).$$
(2. 41)

The parameter ε_{ij} represents the interaction energy between different and ε_{ii} respectively ε_{jj} between equal polymer segments. From equation **(2.41)** it can be seen that χ_{FH} is positive if the interaction between two different segments becomes larger than the interaction between identical polymer segments.

In the case that χ_{FH} is positive the chemical diversity of the polymer blocks causes an unfavorable energetic situation, if the two segments *A* and *B* are in contact with each other. If χ_{FH} is increased (i.e. lowering the temperature) a reduction of the *A-B* segment contact is favored[74, 75]. Depending on the overall degree of polymerization *N* the system may arrange in an equilibrium state of minimum free energy, by undergoing a phase separation in regions with enriched concentration of polymer *A* respectively *B*. This local ordering causes a loss in translational and configurationally entropy[74, 76].

The Flory-Huggins parameter can also be expressed as a function of temperature[77] via the following dependency:

$$\chi_{FH}(T) = \alpha T^{-1} + \beta$$
(2. 42)

with α ($\alpha > 0$) and β being experimentally determined parameters which are constants for a given block copolymer composition. This temperature dependence reflects the influence of the entropy to the locally compositional ordering. For increasing temperatures, χ_{FH} is becoming smaller, leading to an increased dominance of the entropy terms in equation **(2.40)**. Above a critical temperature the local segregation is energetic not stable and the system will arrange in the amorphous minimum free energy configuration (see **Fig. 18**). The critical temperature, at which the transition between the microphase separated and the amorphous state occurs, is called the ordered disordered transition temperature (T_{ODT}).

The onset of the ODT can be determined by different methods[20]. In this work the ODT was located on the one hand by rheological measurements in the linear-regime and temperature dependent SAXS measurements. From rheological measurements the ODT is identified by a drastic drop of the mechanical module obtained during a heating ramp, while for SAXS measurements the ODT is indicated by a discontinuity in the temperature behavior of both the peak intensities and the peak width.
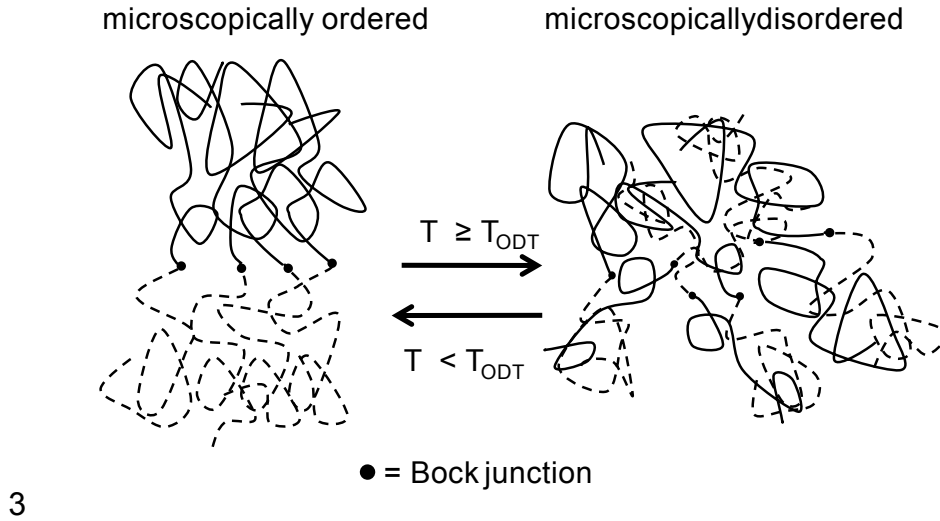
Fig. 18 Illustration of the ordered disordered phase transition in a diblock copolymer with a given overall degree of polymerization N.

For a PS-b-PI diblock copolymer system, with a major fraction of 1,4-polyisorpene in the PI-block, the α and β parameter were empirically determined by Owens et al.[78] which can be used to estimate χ_{FH}.

$$\chi_{FH} = -0.0419 + \frac{39}{T} \qquad (2.43)$$

At room temperature the Flory-Huggins parameter for a PS-b-PI is approximately χ_{FH} = 0.1. Therefore, the total degree of polymerization has to be above N > 100 to achieve a phase separated PS-b-PI diblock copolymer.

Equation **(2.40)** reveals the proportionality of the entropic terms to N^{-1} while the enthalpy term is proportional to χ_{FH}. To define a measure for the strength of the phase separation in a block copolymer, the product of χ_{FH}*N is defined, which contributes to the relation between the enthalpy and entropy energy of mixing[79].

From this definition three region can be clarified which distinguished between weak (χ_{FH}*N ≈ 10), intermediate (χ_{FH}*N ≈ 10-100) and the strong (χ_{FH}*N ≥ 100) segregation limit. For compositions with f_A = 0.5, the transition between ordered and disordered state occurs between χ_{FH}*N ≤ 10, see ref.[80]. The strength of the segregation gives information about the ordered composition profile: in the weak segregation limit (WSL) the th composition profile is approximately sinusoidal while an increase in χ_{FH}*N leads to sharper interphase between the two segments which will last in a rectangular ordered composition profile for the strong segregation limit (SSL)[79].

As the two different polymer segregate the developing microphases obey different symmetries, depending on the volume fraction f of a block copolymer segment. In **Fig. 19** the calculated phase diagram of a polystyrene-block-polyisoprene (PS-b-PI) diblock copolymer with varying volume fraction and segregation strength is shown. The calculations were carried out by Matsen et al.[81] utilizing a mean field approach. The phase diagram covers frequently occurring morphologies in binary block copolymer systems.
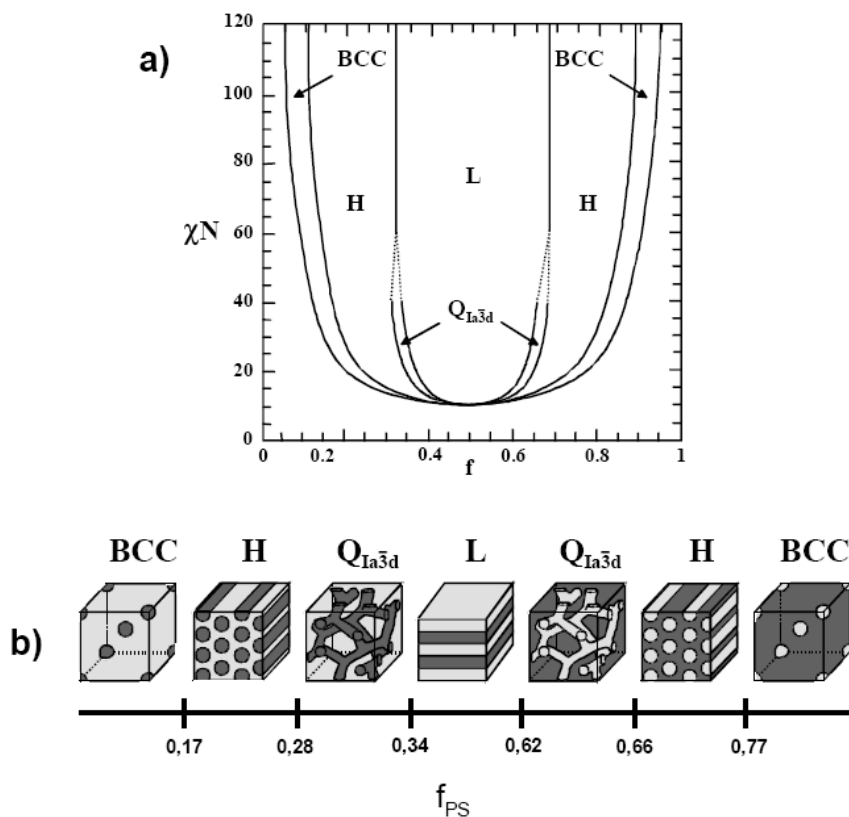
*Fig. 19 a) Calculated phase diagram for a PS-b-PI diblock copolymer with different micro phase symmetries[26]; BCC = body centered cubic, H = hexagonal, Q_{Ia3d} = gyroide and L = lamellar. b) Schematic representation of the different Morphologies at χ_{FH}*N ≈ 30 with respect to the volume fraction of the polystyrene block (dark zones).*

36

2.3.2. Mechanical response of diblock copolymers

In section **2.1.5** the dynamic viscoelastic response of a homopolymer melt was discussed with respect to the polymer chain dynamics. A master curve of a PS linear homopolymer was provided in section **2.1.4** which is subdivided into four different regimes which occur with increasing frequency as follows: the flow zone which corresponds to the full reptation of the polymer chain; the rubber plateau which is the consequence of an entangled network restricting the polymer chain to fully reptate out of the constraining tube; and the transition zone which correlates to the movement of smaller segments along the polymer chain.

For diblock copolymers the qualitative progression of the master curve has great similarities to the one of the homopolymers[82] as can be seen in **Fig. 20**. Large differences are visible in the low frequency region where a further crossover between G'' and G' occurs. Below that frequency G' dominates the mechanical response of the sample. This region is referred to the microstructure of the system which influences the mechanical response at sufficient low frequencies[82]. For higher frequencies the master curves of diblock copolymers are qualitatively similar to the one of linear homopolymer melts, with differences in the scaling behavior of G' and G'' with respect to ω_1.
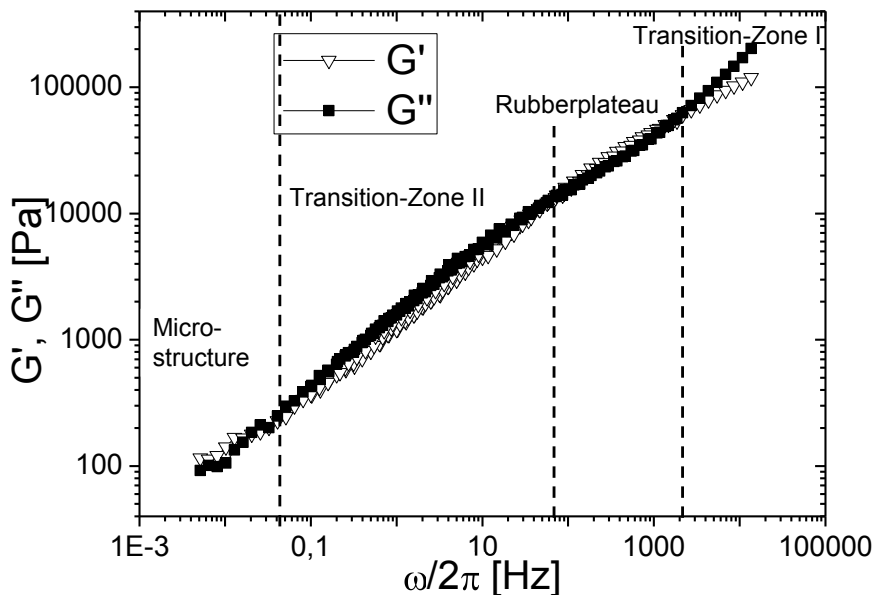
Fig. 20 Master curve of a PS-PI-20k-20k at T_R = 160 °C. Except for the low frequency region the trend of the mechanical modulii as a function of frequency are similar to the one of homopolymer melts.

2.3.3. Symmetric diblock copolymer melts under LAOS

Self assembly in block copolymer melts occurs on a nanometer length scale with various symmetries depending on the volume fraction f_i of a specific block i, as shown in **Fig. 19b** for a polystyrene-block-polyisoprene (PS-b-PI) diblock copolymer. In the following discussion only the case for f_i = 0.5 is considered as this morphology is from main interest for the investigations performed in this thesis.

Usually self assembled microstructures tend to organize into locally anisotropic ordered domains, so called grains[20]. These grains are randomly orientated in the whole sample resulting in a macroscopically isotropic material (see **Fig. 21**). These ordered domains typically have a size on the submicrometer scale. For example, Floudas et al.[83] estimated the domain sickness from the peak position and the peak width in the SAXS patterns for a PS-b-PI (M_w = 12200 g/mol, f_{PS} = 51%, PDI = 1.06) with a lamellar thickness of 12.7 nm to be approximately 70 nm.

Fig. 21 Schematic representation of a diblock copolymer sample with locally anisotropic ordered grains, which randomly orientate in the whole sample. The grain sizes are on the submicrometer scale.

By applying a large amplitude oscillatory shear, the locally anisotropic ordered domains can be macroscopically aligned with respect to the shear field becoming macroscopically anisotropic. Three different macroscopic orientations have been reported in literature for symmetric diblock copolymers under LAOS conditions (see **Fig. 22**)[30]:

- The parallel orientation, wherein the unit normal of the lamella directed along the shear gradient (*OZ* axis).
- The perpendicular orientation with the lamellar unit normal along the neutral direction (*OY* axis).
- The transverse orientation having the unit normal of the lamellar orientated along the shear direction (*OX* axis).

Macroscopic orientations:
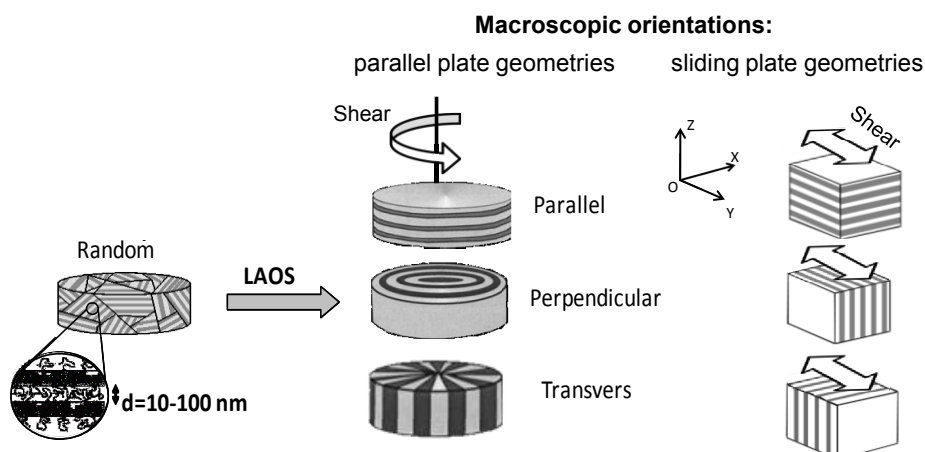
Fig. 22 Schematic representation of the observed three different types of macroscopic orientation as reported in literature[30] for parallel plate geometries and sliding plate geometries.

The schematic representation of the transverse orientation in the parallel plate geometries in **Fig. 22** cannot be adapted to real systems as the block copolymer chains at the very center of the sample disc would be highly frustrated. The frustration is caused by the narrowing distance of the lamellae spacing towards the center, which would lead to a decreasing of the lamella spacing d_{Lam}. Closer lamella spacing would result in an unfavorable compression of the polymer chains. Furthermore, the transverse orientation is a rarely observed phenomenon[30] which is also discussed in literature as a transition state during shear-induced macroscopic parallel orientation[84].

The following discussion will consequently focus only on the macroscopic parallel and perpendicular orientation. To obtain these different states of alignment with respect to the shear flow the choice of the experimental conditions (T_1, $\omega_1/2\pi$, γ_0) are of major interests. In **Fig. 23** the experimentally determined frequency and strain dependence for a polystyrene-block-polyisoprene (PS-b-PI-15k-13k) with weight average molecular weight M_w = 26;500 g/mol, f_{PS} = 51% and a polydispersity of PDI = 1.04 is represented, measured in-situ with the unique Rheo-SAXS setup located at the "Deutsches Elektronen Synchrotron" (DESY) in Hamburg[35]. It can be seen that the resulting macroscopic orientation at an arbitrary temperature (T_g < T < T_{ODT}) is a complex function of both frequency and strain amplitude. This behavior has bee investigated in detail by U. Wiesner[30].
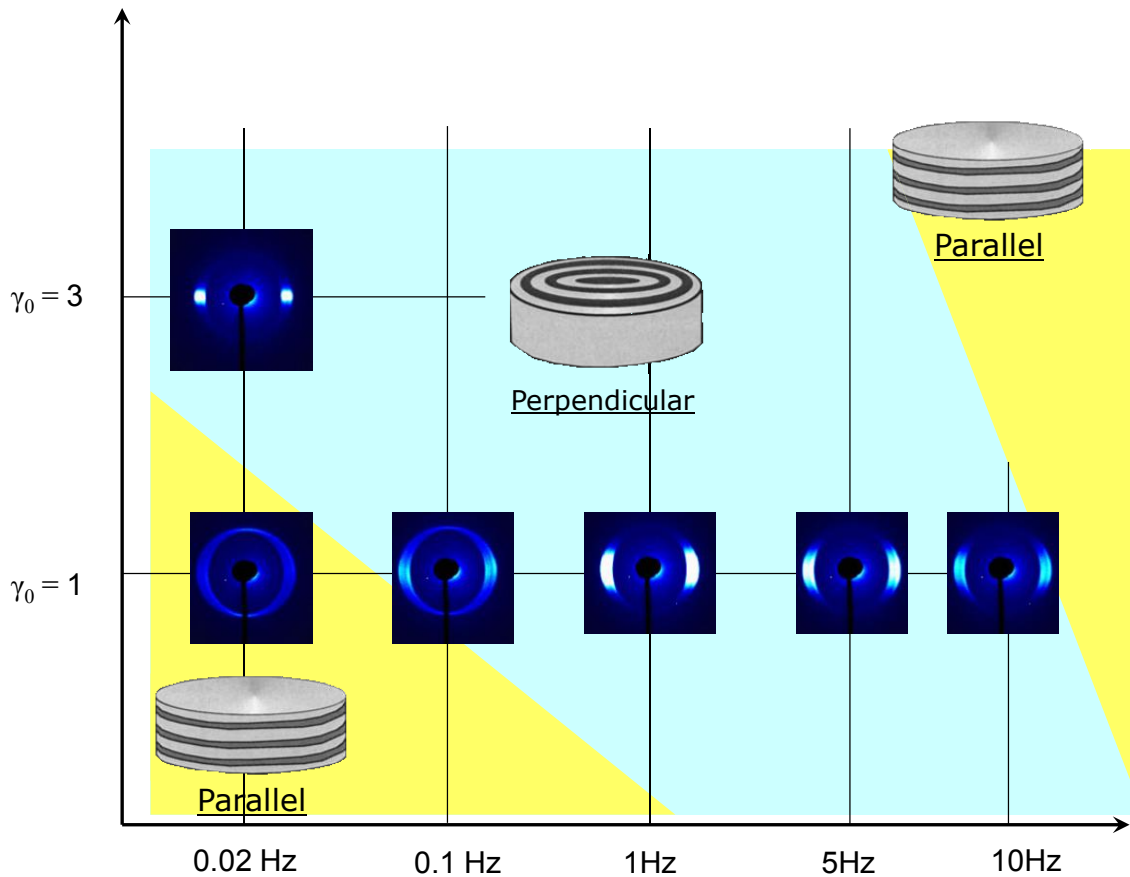
Fig. 23 Frequency and strain dependence of the stable macroscopic orientations (perpendicular and lamellar) for PS-b-PI-15k-13k at 160 °C. The measurements were performed with an unique Rheo-SAXS setup[35] at DESY.

To make predictions about the possible macroscopic alignment as a function of frequency and temperature, two methods are frequently discussed in literature[82]. Both methods focus on the frequency and temperature dependence of the linear dynamic mechanic response such as the complex viscosity and the complex modulus.

One approach considers the frequency dependence of the absolute value of the complex viscosity $|\eta^*|$, see ref.[82]. The deviance from a linear behavior along this curve is regarded as the point at which the transition between the parallel and the perpendicular alignment occurs.

Earlier work from Winey et al.[85] and Larson et al.[86] found that the master curve of mechanical modulus G' and G'' for various temperatures above and close to the T_{ODT} revealed a cross over point between the module in the amorphous and ordered state. This cross over was taken as a critical frequency $\omega_c/2\pi$ above and below the perpendicular respectively parallel alignment takes place[87]. Nevertheless, this method provides little information about the transition between perpendicular and

parallel alignment at high frequencies (low temperatures) which was assumed to occur for $\omega_1/2\pi >> \omega_c/2\pi$. In a simplified picture, without considering more complex effects being attributed to the strain amplitude, the regions for the parallel to perpendicular transition can be classified from the linear mechanical response as shown in **Fig. 23**.
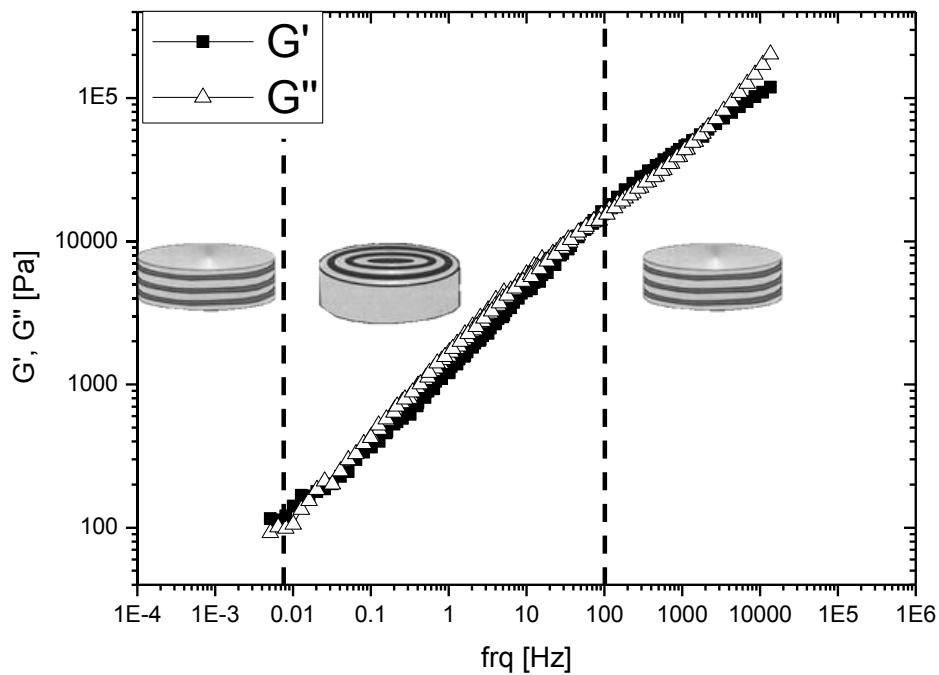
Fig. 24 Experimentally obtained Master curve for PS-b-PI-20k-20k at T = 160 °C illustrating a rough approximation of the three different regime corresponding to the macroscopic orientation under LAOS. Effects of the strain amplitude to the overall macroscopic alignment are not considered.

2.4. Dielectric Relaxation Spectroscopy

The dielectric relaxation spectroscopy (DRS) is a method to probe the dielectric properties of a material in an oscillating electric field. The important investigations of the dielectric properties contribute to a more detailed understanding of the molecular dynamics in condensed matter[88]. Furthermore, for technical applications the precise knowledge about the dielectric properties of a material is from great importance as for instance in the field of capacitors, where material with a high permittivity ε' have to be deployed. In the following a brief introduction to the basic principles of DRS and its application in the field of polymer science is provided. To derive the in the following presented basic aspects of DRS mainly the text books of F. Kremer[88] and N. G. McCrum[89] was adopted.

2.4.1. Basic considerations

The simplest setup of a dielectric measurement cell is the parallel plate capacitor. In between the parallel plates a dielectric medium is placed (see **Fig. 25**). The time dependent electric field is generated by applying an oscillating electrical voltage to the parallel plates.

$$U(t) = U_0 \sin \omega_1 t \ .$$
(2. 44)

The time dependent oscillating electric field is correlated to the voltage by the following expression, simplified by the complex notation:

$$E(t) = \frac{U(t)}{d} = E_0 \exp(-i\omega_1 t) \ .$$
(2. 45)

The electric field forces the dipole moment of the molecules (only permanent molecular dipoles) to arrange along the field vector $\vec{E}$. This molecular property results in a macroscopic polarization $\vec{P}$ of the sample:

$$\vec{P} = \varepsilon_0 (\varepsilon^* - 1) \vec{E} \ ,$$
(2. 46)

with ε_0 = 8.854*10^{-12} $\frac{A \cdot s}{V \cdot m}$ being the permittivity of the vacuum and ε^* the frequency dependent complex dielectric permittivity of the material.
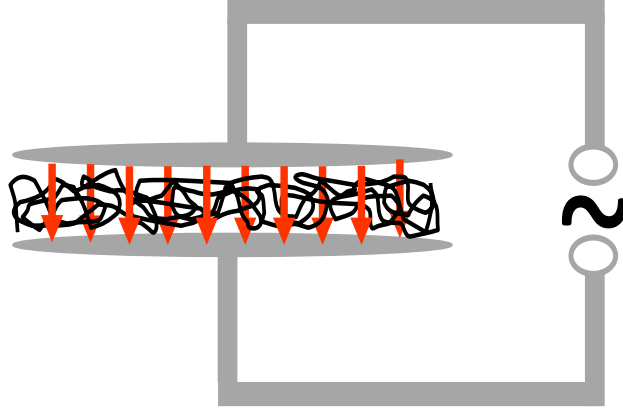
Fig. 25 Schematic representation of a dielectric medium (black solid lines) in between a parallel plate capacitor. The homogeneous electric field is indicated by the red arrows.

The total polarization of a material can be expressed as the sum over the induced polarization $\vec{P}_\infty$, which is caused by the dislocation of the electron shell, and the orientation polarization expressed by the microscopic dipole moments $\vec{\mu}_i$ per volume V:

$$\vec{P} = \frac{1}{V}\sum_i \vec{\mu}_i + \vec{P}_\infty .$$
(2. 47)

2.4.2. Dielectric Relaxation (linear response theory)

In the presented discussion of dielectric polarization the orientation polarization will be of main concern, since the induced polarization is sufficiently rapid and does not contribute to the frequency range under consideration[49] (0.1 Hz to 1 MHz).

The theory of dielectric relaxation is a special case of the "linear response theory"[88]. In the linear response theory, the time dependent polarization $\vec{P}$ which is caused by the electrical field, can be expressed as follows:

$$\vec{P}(t) = \frac{1}{V}\Sigma \vec{\mu}_i(t) + \vec{P}_\infty = \vec{P}_\infty + \varepsilon_0 \int_{-\infty}^{t} \varepsilon\left(t-t'\right)\frac{d\vec{E}\left(t'\right)}{dt'}dt' ,$$
(2. 48)

with $\varepsilon(t)$ being the time dependent dielectric function. The response of $\varepsilon(t)$ to a rapidly applied external electric field is illustrated in **Fig. 26**.

43
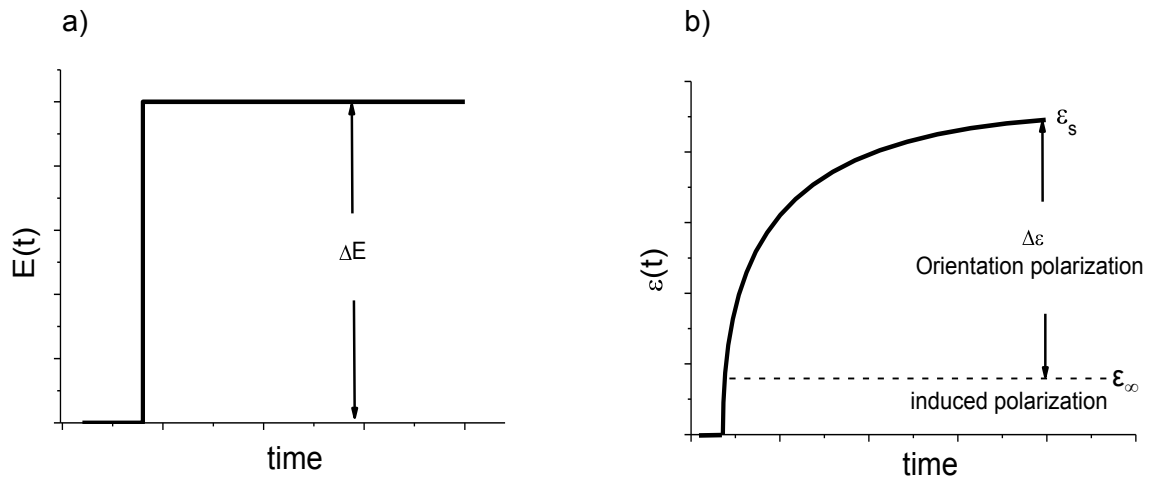
Fig. 26 a) Time dependent electrical field which is applied to a dielectric material. b) Response of the time dependent dielectric function to an rapidly applied electrical excitation (a).

In the beginning an immediate increase in the dielectric function is observed, which is caused by induced polarization. Afterwards, $\varepsilon(t)$ shows an exponential increase in time, until it reaches a plateau value. In systems which respond linearly, with respect to the amplitude of the oscillating electric field, time domain measurements can be transformed into the frequency domain via a Fourier Transformation and equation **(2.48)** becomes[89]:

$$\vec{P}(t,\omega) = \varepsilon_0 (\varepsilon^*(\omega) - 1)\,\vec{E}(t,\omega)\,, \qquad (2.\,49)$$

with the complex dielectric function

$$\varepsilon^*(\omega) = \varepsilon'(\omega) - i\varepsilon''(\omega) \qquad (2.\,50)$$

and

$$\tan \delta_e = \frac{\varepsilon''}{\varepsilon'} \qquad (2.\,51)$$

Similar to the complex modulus G* in the rheology (compare equation **(2.13)**), the real part of equation **(2.50)** corresponds to the dielectric storage modulus $\varepsilon'(\omega)$ and the imaginary part to the dielectric loss modulus $\varepsilon''(\omega)$. The dielectric loss angle δ_e is a measure for the energy which is dissipated during the dipole orientation. The time

44

dependent dielectric function is correlated with equation **(2.50)** by the following expression[88]:

$$\varepsilon^*(\omega) = \varepsilon_\infty - \Delta\varepsilon \int_0^\infty \frac{d\varepsilon(t)}{dt} \exp(-i\omega t)dt \,,$$

(2. 52)

with $\Delta\varepsilon$ being the dielectric strength and ε_∞ being the limit for very high frequencies. The dielectric strength is proportional to the dipole moment $\vec{\mu}$ directed along the electric field in the investigated system:

$$\varepsilon_s - \varepsilon_\infty = \Delta\varepsilon \sim \frac{|\vec{\mu}|^2}{k_B T} \,,$$

(2. 53)

with ε_s being the permittivity for an approximately static field:

$$\varepsilon_s = \lim_{\omega \to 0} \varepsilon'(\omega) \,.$$

(2. 54)

For a macroscopic sample the determined dipole moment is an average value[90]. Due to stochastically thermal movements of the molecules this value fluctuates around its mean value. For the stationary state the dipole moment of the sample can be expressed by the auto-correlation function of the dipole moments in the sample:

$$\vec{\mu}(\tau) = \frac{\sum_i \langle \vec{\mu}_i(0) \cdot \vec{\mu}_i(\tau) \rangle + 2\sum_i \sum_{i<j} \langle \vec{\mu}_i(0) \cdot \vec{\mu}_j(\tau) \rangle}{\left\langle \left(\sum_i \vec{\mu}_i \right)^2 \right\rangle}$$

(2. 55)

The first part in equation **(2.55)** is the dipole-dipole auto-correlation function and the second part describes the cross-correlations while in most systems under investigation the auto-correlation function is the dominant part which contributes to the dielectric response[88].

2.4.3. Relaxation models

The relaxation models presented here are mainly applied for molecular processes and dielectric relaxations in a frequency range minor than 100 GHz and are discussed in more detail in reference[88]. The models concern dielectric relaxation processes of permanent dipoles in glassy soft matter, such as polymer melts.

The non-linear time dependence of $\varepsilon(t)$ is caused by the delay (lag) of the permanent dipoles to orientate along an external electric field. The electric stimulus can be stepwise applied (time domain) or as a sinusoidal periodic stimulus (frequency domain). The molecular dynamic to retain their equilibrium state after the electric stimulus is turned off is called relaxation. The relaxation process is characterized by its relaxation time τ_e, that is a measure for the dynamic of a system to reach the equilibrium.

With the assumption that the time dependent decay of the deflection is proportional to the total deflection the relaxation process for an ideal non-interacting system with spherical molecules, can be expressed by first order differential equation[88]:

$$\frac{dP(t)}{dt} = \frac{1}{\tau_e} P(t) \, ,$$

(2. 56)

with $1/\tau_e$ being the proportional constant. Equation **(2.56)** indicates that after the electrical stimulus is turned off, the time dependent polarization shows exponential decay:

$$P(t) = P_0 \exp\left(-\frac{t}{\tau_e} \right).$$

(2. 57)

With this expression the frequency dependent complex dielectric function becomes:

$$\varepsilon^*(\omega) = \varepsilon_\infty + \frac{\Delta\varepsilon}{1 + i\omega\tau_e}$$

(2. 58)

This complex function can be decomposed into a real and an imaginary part:

$$\varepsilon'\ \omega\ = \varepsilon_\infty + \frac{\Delta\varepsilon}{1+\ \omega\tau_e^{\ 2}} \tag{2. 59}$$

$$\varepsilon''\ \omega\ = \Delta\varepsilon\frac{\omega\tau_e}{1+\ \omega\tau_e^{\ 2}} \tag{2. 60}$$

This approach was first derived from Debey, therefore, simple exponential relaxation processes which fulfill this relation are called Debey relaxations.

This model is often not sufficient to describe the observed relaxation phenomena in glassy soft matter. For example, the permanent dipoles in polymer melts cannot be approximated as spherical units. Although, the interaction of the polymer chains in the bulk (e.g. entanglements), constrain the physical dipoles to freely align to or relax from the electrical excitation. This matrix interaction can be regarded as energy barriers which have to be overcome. To adapt the Debey relaxation to the experimentally obtained relaxation processes, the model can be extended by introducing parameters, which take into account peak broadening and asymmetric shapes caused by the matrix interaction. One of these models is the Cole-Cole approach[91]:

$$\varepsilon^*(\omega) = \varepsilon_\infty + \frac{\Delta\varepsilon}{1+\ i\omega\tau_{CC}^{\ \alpha}} \tag{2. 61}$$

The Cole-Cole model, only account to peak broadening by introducing the α parameter ($0 < \alpha \leq 1$). To additionally account for an asymmetric peak shape in the frequency domain, Havriliak and Negami suggested the following semi-empirical function[92]:

$$\varepsilon^*_{HN}(\omega) = \varepsilon_\infty + \frac{\Delta\varepsilon}{1+\ i\omega\tau_{HN}^{\ \alpha\ \beta}}\ . \tag{2. 62}$$

On the one hand this function fulfils the observed peak broadening by introducing the α parameter, which causes a stronger peak broadening for small α values. On the other hand the asymmetry of the peak is accounted for by the β parameter ($0 < \beta \leq$

1). The slope of the low frequency of the dielectric loss peak ε'' is correlated with ω^{α}, while the slope on the high frequency side is determined by $\omega^{-\alpha\beta}$, with $\alpha\beta \leq 1$. **Fig.** 27 visualizes the accuracy of the above introduced models with respect to the dielectric chain relaxation mode of a 1,4-cis-polyisoprene (M_w = 20,000 g/mol, PDI = 1.03).
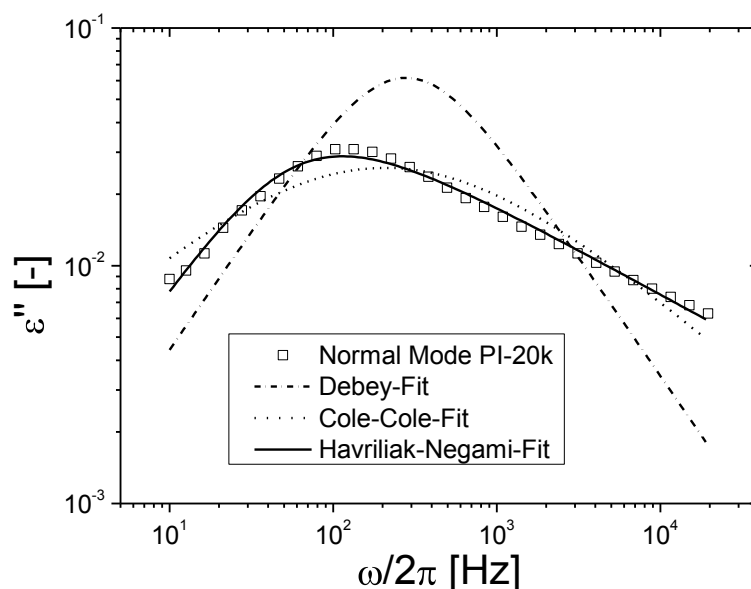
Fig. 27 Experimental dielectric normal mode (open squares) of a linear 1,4-cis-polyisoprene (M_w = 20,000 g/mol, PDI = 1.03) at T = 0 °C. The lines represent the Debey- (line+dots), the Cole-Cole (dots) and the Havriliak-Negami (solid line) relaxation functions.

2.4.4. Dipole moments in polymers

For small molecules the permanent dipole moment can be expressed by a vector $\vec{\mu}$. In contrast, polymers consist of several 100 to 1000 monomer units, each of them having one or more dipole moments. To classify the different dipole moments which appear in a polymer chain, Stockmeyer suggested a special classification[93]. This classification indexes different types of polymers into three categories (see **Fig. 28**):

- The type *A* polymers, such as 1,4-cis-polyisoprene, consist of segmental units which exhibit a molecular dipole moment along the backbone of the polymer chains. The sum over all segmental dipole moments $\vec{\mu}_i$ results in a total dipole moment $\vec{\mu}_{Sum}$, which corresponds to the end-to-end vector of the polymer chain. Therefore, it is possible to investigate polymer chain relaxations via dielectric relaxation spectroscopy. The relaxation process is designated as the normal mode.

48

- The segmental units which build up type *B* polymers posses no dipole moments directed parallel to the polymer back bone. The dipole moments of these polymers, such as polystyrene, are directed perpendicular to the back bone. This permits the detection of the relaxation processes of polymer segments, which are strongly related to the glass transition temperature of the polymer. The relaxation process is dedicated as the <u>segmental-</u> respectively the <u>α-mode</u>.

- Type *C* polymers exhibit permanent dipole moments in the side groups, for example polymethylacrylates[94] (PMA) or polymethylmetacrylates (PMMA). Usually side group relaxation occurs on a short time scale which causes a shift to higher frequencies with respect to the normal- and α-mode. The relaxation process is dedicated as the <u>β-mode</u>.

Fig. 28 Stockmeyer classification of polymer chains with different dipole moments. The arrow indicates a decrease in the relaxation time if measured at a specific temperature above the T_g.

It has to be noticed, that pure type *A* and type *C* polymers do not exist. Moreover, these types of polymers also exhibit a dipole moment perpendicular to the polymer back bone. Hence, they always appear as a combination of different types. The

relaxation times of the above mentioned three different relaxation modes, for one specific type of polymers, decreases in the order shown in **Fig. 28**.

As an example for a type A polymer, **Fig. 29** shows the experimental dielectric relaxation spectra for two 1,4-cis-polyisoprene sample with molecular weights of 10000 g/mol (PDI = 1.02) and 20000 g/mol (PDI = 1.03) at different temperatures between -30 °C $\leq$ T $\leq$ -10 °C.
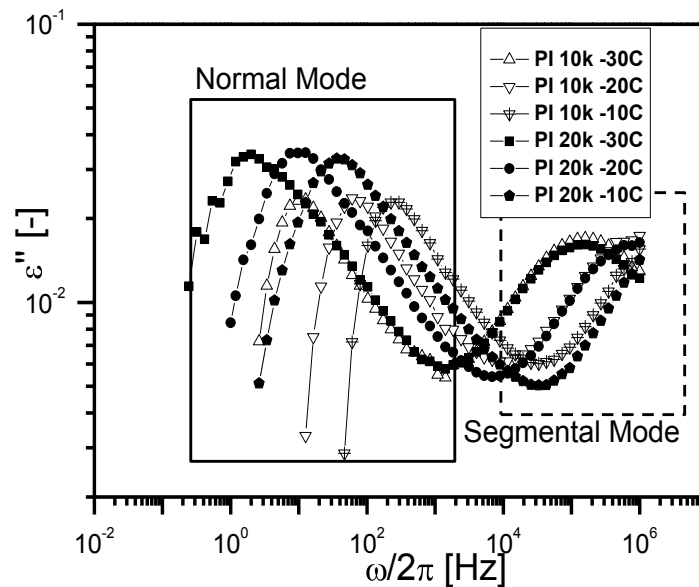
Fig. 29 Logarithmic plot of the frequency dependence of the dielectric loss ε" for PI-10k and PI-20k at different temperatures. The different relaxation modes which indicate the polymer chain relaxation (normal mode) and the segmental relaxation (segmental, α-mode) are highlighted.

An important characteristic of the normal mode is the strong molecular weight dependence on the of the polymer chains. Regarding the isothermal relaxation peaks at low frequencies (the normal mode) in **Fig. 29** for PI-10k and PI-20k it can be seen that the normal mode for PI-20k is shifted to lower frequencies. Form experimental data[95, 96] it could be shown, that above the critical molecular weight the longest relaxation time $\tau_{max-normal}$ is proportional to $\tau_{max-normal} \sim M^4$, see ref.[88]. In contrast, the segmental mode shows no significant dependence to the overall molecular weights of the polymers. The normal and segmental modes are both Arrhenius activated processes which for polymers obey a Vogel-Fulcher temperature dependence[88].

2.5. Small angle X-ray scattering

Small angle X-Ray scattering (SAXS) is a preferred method to analyze and characterize the structural properties of condensed matter on mesoscopic length scale between approximately 1 and 500 nm. As most of the macroscopic properties, for instance mechanical, magnetical, electrical or optical, are strongly influenced by the nanostructure of hierarchically ordered matter, a detailed understanding and characterization of induced structures and ordering on the nm-scale is a key factor towards new functional materials. In this section the basic principles and applications for polymer materials are presented.

2.5.1. Basic principles of scattering

An electromagnetic radiation may interfere with matter in two different ways:

- The absorption is a dissipative phenomenon and can be described quantitatively by the Lambert-Beer law (equation **(2.61)**). If an electromagnetic wave passes through a transparent substance the initial intensity I_0 is decreased depending on the extinction coefficient ε_i, the concentration of absorbing species c_i and the length L of the irradiated sample. The intensities of the transmitted light is given by[49]:

$$I_t = I_0 e^{-\varepsilon_i(\lambda) \cdot c_i \cdot L}$$

(2. 63)

- Scattering occurs if an electromagnetic wave interacts with a molecule or the electron shell of an atom, e.g. inducing an electrical dipole. This induced dipole irradiates again an electromagnetic wave in various spatial directions. The observed scattered intensities are interferences of the scattered electromagnetic wave from all scattering centers (e.g. molecules or atoms) in the irradiated volume. Scattering processes are called elastic, if the scattered electromagnetic waves have the same frequency as the incident radiation. Otherwise the scattering phenomenon is decelerated as inelastic.

The mathematical derivation introduced for the scattering phenomena are principally based on the remarks from M. Kerker[97] and C. Gerthsen[98]. The following

discussion executively gives attention to the elastic scattering phenomena, as for most SAXS experiments inelastic scattering can be neglected while absorption phenomena can be experimentally determined.

The electromagnetic wave consists of an electric and magnetic field which oscillates in phase perpendicular to each other and perpendicular to the direction of energy propagation. Usually magnetic fields are neglected in the discussion of scattering phenomena.

The time and local dependence of the electrical field vector $\vec{E}$ can be expressed by:

$$\vec{E}(x,t) = \vec{E}_0 \cdot \cos 2\pi(\nu_1 t - \frac{x}{\lambda}), \tag{2. 64}$$

with the amplitude $\vec{E}_0$, the frequency ($\nu_1 = \omega_1/2\pi$) and the wave length λ. At the point x = 0 where the molecule is located, the electric field is given by:

$$\vec{E}(0,t) = \vec{E}_0 \cdot \cos 2\pi(\nu_1 t) \tag{2. 65}$$

As already mentioned above, the oscillating electrical field interferes with matter by inducing a dipole moment $\vec{\mu}$, which oscillates with the same frequency.

$$\vec{\mu} = \alpha \vec{E} = \alpha \vec{E}_0 \cos(2\pi \upsilon_1 t) \tag{2. 66}$$

The parameter α is the polarizability which determines the response of the matter to the electric field.

The induced, oscillating dipole irradiates an electromagnetic wave with the same frequency as the incident light, which is dedicated as the elastic scattered light. The electromagnetic field scattered by the molecule is dependent on the observation distance r and angle θ.

$$\vec{E}_{Dipole} = \frac{4\alpha\vec{E}_0\pi^2\cos(2\pi\nu_1 t)}{r\lambda^2}\cdot\sin(\theta) \qquad (2.\,67)$$

The experimental accessible scattered intensity is determined by the square of the amplitude of the scattered electric field. The ratio between incident Intensity I_0 and the scattered intensity I_s is given by:

$$\frac{I_S}{I_0} = \frac{16\pi^4\alpha^2}{r^2\lambda^4}\cdot\sin^2(\theta)\,. \qquad (2.\,68)$$

Equation **(2.68)** was first derived by Lord Rayleigh from his studies about visible light scattering[49]. The derivation above was done under the assumption of polarized light. For unpolarized light, as it is also used in most SAXS studies, equation **(2.68)** is rewritten to:

$$\frac{I_S}{I_0} = \frac{8\pi^4\alpha^2}{r^2\lambda^4}\cdot(1+\cos^2(\theta))\,. \qquad (2.\,69)$$

The last term in equation **(2.69)** contributes to the polarization of the incident light. For small angle X-ray scattering with unpolarized light, the effect of polarization can be neglected[99].

2.5.2. The Bragg equation

The Bragg's law gives the angles for coherent and incoherent scattering from a crystal lattice. The scattered waves interfere with each other either constructively or destructively. This interference produces a diffraction pattern at the point of investigation. Whether, constrictive or destructive interferences are observed, is described by the Bragg equation[49]:

$$n\lambda = 2d\sin(\theta)\,, \qquad (2.\,70)$$

with the spatial periodicity of the scattering domains d, the wavelength λ and the scattering angle θ under which constructive interference occurs. From equation **(2.70)**

53

it arises that the path difference between the two scattered waves has to be an integer *n* of the applied wave length.

However, as the Bragg equation is a scalar equation, it is often useful to describe scattering in a vectorial expression. The principle of a scattering experiment is schematically shown in **Fig. 30**, while the incident and scattered beam are expressed by the wave vectors $\vec{k}_0$ respectively $\vec{k}'$.
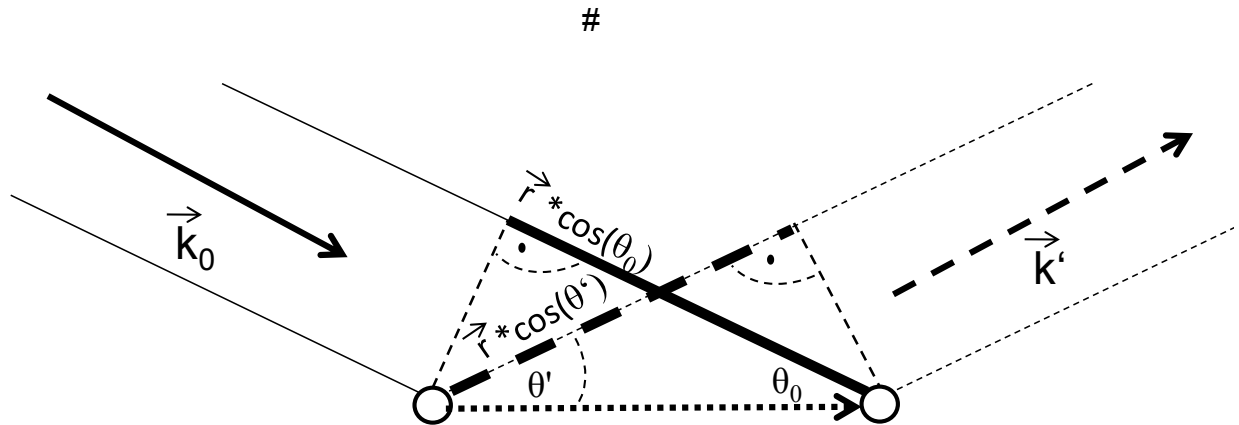
Fig. 30 Geometry of a scattering experiment.

Due to the definition of an elastic scattering process, the radiation frequency remains unchanged and the absolute values of the wave vectors are defined as:

$$\left|\vec{k}_0\right| = \left|\vec{k}'\right| = \frac{2\pi}{\lambda} \, , \tag{2.71}$$

with the definition of the wave vectors, a scattering vector $\vec{q}$ can be defined which is directed perpendicular to the scattering (see **Fig. 31**) plane and is given by:

$$\vec{q} = \vec{k}_0 - \vec{k}' \tag{2.72}$$
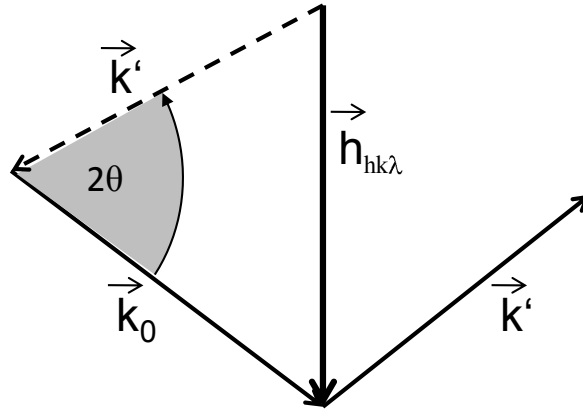
Fig. 31 Sketch of the vectorial representation of the scattering vector $\vec{q}$ which depends on the incident and the scattered wave vector $\vec{k}_0$ and $\vec{k}\,'$

The absolute value of $\left|\vec{q}\right|$ is given by:

$$\left|\vec{q}\right| = \frac{4\pi}{\lambda}\sin(\theta)\,. \tag{2.73}$$

For constructive interferences the path difference $\vec{r}$ of the wave vectors has to be:

$$\vec{q}\cdot\vec{r} = 2\pi n\,. \tag{2.74}$$

By combining equation **(2.70)** and equation **(2.73)**, the correlation between the Bragg equation and the scattering vector is derived.

$$\left|\vec{q}\right| = \frac{2\pi}{d} \tag{2.75}$$

2.5.3.   Structure and form factor

The accessible quantity in scattering experiments is the intensity of the scattered beam $I_s(\vec{q})$ which is proportional to the square of the amplitude $A_s(\vec{q})$:

$$I_s(\vec{q}) \sim I_e \cdot \left|A_s(\vec{q})\right|^2 \tag{2.76}$$

with I_e being the scattered intensity of an electron:

$$I_e = I_0 \cdot \left(\frac{e^2}{mc^2} \right) \cdot \frac{1}{r_d^2} \cdot \frac{1+\cos^2(2\theta)}{2} \; . \tag{2.77}$$

Herein, the classical electron radius is described by e^2/mc^2, with the charge e, the electron mass m and the speed of light c. The sample detector distance is described by r_d. The last term in equation **(2.77)** attributes to the polarization factor which is equal to 1 for SAXS experiments.

The amplitude of the scattered beam $A_s(\vec{q})$ derives from the Fourier Transformation of the electron density distribution within the sample.

$$A(\vec{q}) = \int_V \rho(\vec{r}) \cdot e^{i\vec{q}\vec{r}} \cdot dV \tag{2.78}$$

The electron density $\rho(\vec{r})$ is described as the number of electrons per unit volume V at the position $\vec{r}$. The electron density distribution can be regarded as a convolution of the differential electron density $\delta\rho(\vec{r})$ in a specific domain with δ-functions $\Delta(\vec{r})$ which describe the position of a domain[99, 100], for instance to describe a multi body problem or interactions of identical particles.

$$\rho(\vec{r}) = \delta\rho(\vec{r}) \otimes \Delta(\vec{r}) \; . \tag{2.79}$$

From the concepts of the Fourier Transformation[67] it follows that a FT of a convolution is equal to the product of two functions being Fourier transformed. Therefore, equation **(2.78)** can be rewritten to:

$$A(\vec{q}) = \int_V \delta\rho(\vec{r}) \cdot e^{-i\vec{q}\vec{r}} \cdot dV \cdot \int_V \Delta(\vec{r}) \cdot e^{-i\vec{q}\vec{r}} \cdot dV \; . \tag{2.80}$$

With equation **(2.76)** the scattered intensity I_S can be expressed by:

$$I_s(\vec{q}) \sim |A_s(\vec{q})|^2 \sim P(\vec{q}) \cdot S(\vec{q})$$ (2. 81)

The term $P(\vec{q})$ is dedicated as the form factor and $S(\vec{q})$ as the structure factor.

The definition of the form- and structure factor varies from the problem under examination.

- For single molecule characterization in solution the form factor is the scattering of one molecule in ideal solution while the structure factor describes the interaction.

- For colloidal particles, such as latex dispersions (see **Fig. 32**), the form factor is related to the colloidal domain, here the spherical shape, while the structure factor describes the interaction between different particles. The description of the particle as a sphere with perfect homogenous density would result in slope of the scattering of $|\vec{q}^{-4}|$ for high scattering vectors. In reality, the single chain interferes with the scattering of the particle, as a consequence of the not constant density. This phenomenon results in a liquid like scattering intensity due to the inner structure of the domain (sphere).

- In the same way, lamellae morphologies can be expressed by stacks of constant electron density (form factor) while the single stacks are arranged in perfect order (structure factor) with a periodicity L (see **Fig. 33**). In this way the scattering intensity can be derived from the product of the form factor (single lamella) and the structure factor: where the structure factor is more pronounced and becomes the dominant part of the scattering. In **Fig. 33** the experimental data for a macroscopic orientated lamella PS-b-PI-27k-32k is shown.
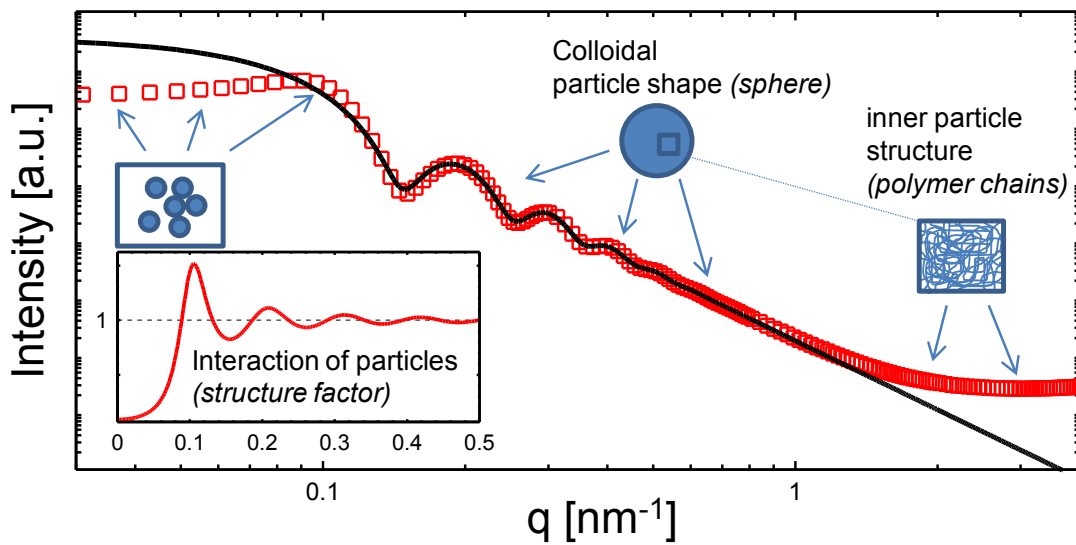
Fig. 32 Scattering intensity of colloidal latex particle (D=60 nm, σ=9%). The Black-Line is the simplified form factor, the Fourier transform of the colloidal shape. The Inset shows the structure factor of uncharged spherical particles with a volume concentration of 30% calculated according Percus-Yevick theory[101].
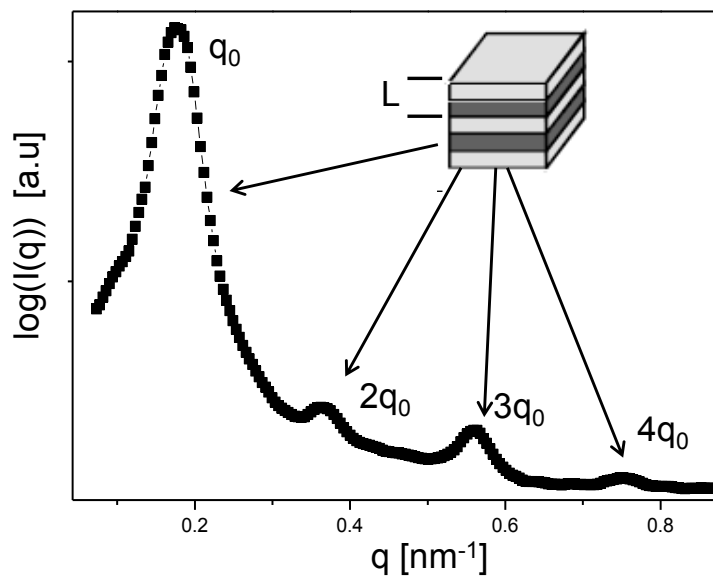
Fig. 33 Experimental data for a symmetric PS-b-PI-27k-32k (M_w=59,000 g/mol, f_{PS} = 46%, PDI = 1.06), the peaks correspond to the structure factor for an orientated lamella microsrucutre.

2.5.4. Scattering from diblock copolymers

Diblock copolymers self-assemble into a variety of ordered structures with nanoscale periodicities[20] (see **Fig. 19b**). These ordered structures gives rise to reflections in the small angle X-ray scattering patterns, as described in the previous section. It is important to notice, that the electron contrast between the different

58

blocks need to be different in order to allow the investigation of the morphology by SAXS techniques. The electron density for a specific polymer block can be calculated as followed:

$$\rho_{el} = \frac{N_A \cdot \rho_i \cdot Z_{el}}{m_i}$$ (2. 82)

.

Herein N_A denotes the Avogadro constant, ρ_{el} the electron density, ρ_i the density of the component i, Z_{el} the number of electrons of the component i and m_i the molar mass of component i.

If the phase separated systems provide long range periodicity the appearing scattering reflections provide information about the spatial distribution of the scattering objects. Each morphology has a characteristic sequence of scattering reflections which are observed in the scattering pattern. The different morphologies are classified by the appearance of higher order reflections with respect to the scattering vector $\vec{q}$ (see **Tab. 1**).

Lamellae	q_0	$2q_0$	$3q_0$	$4q_0$	$5q_0$	$6q_0$	$7q_0$
Gyroid (Bicontinous)	q_0	$3^{1/2} q_0$	$4^{1/2} q_0$	$7^{1/2} q_0$	$8^{1/2} q_0$	$10^{1/2} q_0$	$11^{1/2} q_0$
Hexagonal (Cylinders)	q_0	$3^{1/2} q_0$	$4^{1/2} q_0$	$7^{1/2} q_0$	$9^{1/2} q_0$	$11^{1/2}$	$13^{1/2}$
BCC (Spheres)	q_0	$2^{1/2} q_0$	$3^{1/2} q_0$	$4^{1/2} q_0$	$5^{1/2} q_0$	$6^{1/2} q_0$	$7^{1/2} q_0$

Tab. 1 Characteristic reflections for different microphase symmetries[20].

The spacing of the reflections is inverse related to the spacing of the lattice (see equation **(2.75)**). From the first order reflection of a lamellae morphology the long period, which is defined as the distance between two different block segments (illustrated in **Fig. 33**) can be calculated.

$$L = \frac{2\pi}{|\vec{q}|}$$ (2. 83)

3. Experimental Methods and Setups

This section provides the description of the anionic polymerization technique and the experimental setups which were mainly used in this thesis. The technical part contains the details about the three different combined methods namely the FT-Rheology setup, the optimized, high sensitive Rheo-Dielectric- and the newly developed Rheo-SAXS combination.

3.1. Anionic polymerization techniques

3.1.1. Basic considerations

The anionic polymerization had been first established in polymer science by Szwarc et al.[102] in the 1950's. This technique has the major advantaged over the conventional used free radical polymerization, that in the absence of contamination products no termination reactions occur. As the chain polymerization propagates via anionic species, termination mechanisms such as chain-chain recombination or disproportionation are suppressed, due to the Coulomb interaction between the equally charged reactive chain ends. Termination only occurs by reaction with chemical impurities or an intra- / intermolecular back biting or transfer reaction of monomers having electrophile functional groups, for instance methacrylates[12]. For this reason the anionic polymerization is defined as a controlled or "living polymerization". The living character of the anionic polymerization has the two major advantages:

- Due to the absence of termination reaction each polymer chain contains a reactive carbanion group. This functional group can be used to build up complex architectures or block copolymers by simple nucleophilic substitution reactions or by adding a new monomer to the living polymer chains[13, 103, 104].

- The absence of termination reaction also influences the kinetic of the polymerization process, which leads to a narrow molecular weight distribution indexed by the polydispersity PDI of the polymer chains. Usually a molecular weight distribution is regarded as narrow if the PDI is less than 1.1, see ref.[12].

The polydispersity is defined as[105]:

$$PDI = \frac{M_w}{M_n} , \qquad\qquad (3.\,1)$$

with

$$M_n = \frac{\sum_i n_i M_i}{n_i} = \text{first moment, number average}$$

$$\qquad\qquad (3.\,2)$$

$$M_w = \frac{\sum_i n_i M_i^2}{\sum_i n_i M_i} = \text{second moment, weight average}$$

The total molecular weight distribution can be approximated by statistical distributions. For the free radical polymerization, e.g. a Schulz-Flory- and for the controlled anionic polymerization a Poisson distribution can be derived[105].

3.1.2.   Anionic synthesis of the model compounds

All polymer compounds used in this thesis were synthesized via anionic polymerization utilizing high vacuum techniques[73]. A detailed description of the experimental procedure for the synthesis of the different polymers is provided in chapter **9**. In the following the underlying mechanism of the anionic polymerization of vinyl compounds is discussed for the example of a polystyrene-block-polyisoprene (PS-b-PI) diblock copolymer.

The reactions were carried out under argon atmosphere using secondary buthyllithium (*sec*-BuLi) as an initiator. Thoroughly dried non-polar solvents such as cyclohexane and toluene were used. However, the dissociation of the initiator in non-polar solvents is reduced compared to polar solvents such as tetrahydrofuran (THF)[12], the use of non-polar solvents is essential for the synthesis of block copolymers containing a high degree of 1,4-polyisorene. In non-polar solvents, the alkyl lithium compounds are aggregated forming three-center two-electron bonds[106]. These so called contact ion pairs are less reactive, due to the closer distance between anionic and cationic species then the solvent separated alkyllithium compounds or even the free ions which occur in polar solvents (see **Fig. 34**).

non-polar solvents $k_{\pm} \gg k_{ass}$

associated (aggregated) ion pairs   tight ion-pair (contact ion-pair)

$$1/x \quad \left[P\text{-Li} \longleftrightarrow P^- \, Li^+ \right]_n \quad \overset{K_{deass}}{\rightleftharpoons} \quad P^- , Li^+$$

$k_{ass} \downarrow + M \qquad\qquad k_{\pm} \downarrow + M$

polar solvents $k_- > k_{\pm,S} \gg k_{\pm,C}$

Solvated tight ion-pair (contact ion-pair)   solvent-separated (loose) ion-pairs   free ions

$$P^- , Li^+ . S_n \quad \overset{K_{cs}}{\rightleftharpoons} \quad P^- // S // Li^+ . S_n \quad \overset{K_{dis}}{\rightleftharpoons} \quad P^- + Li^+ . S_n$$

$k_{\pm,C} \downarrow + M \qquad k_{\pm,S} \downarrow + M \qquad k_- \downarrow + M$
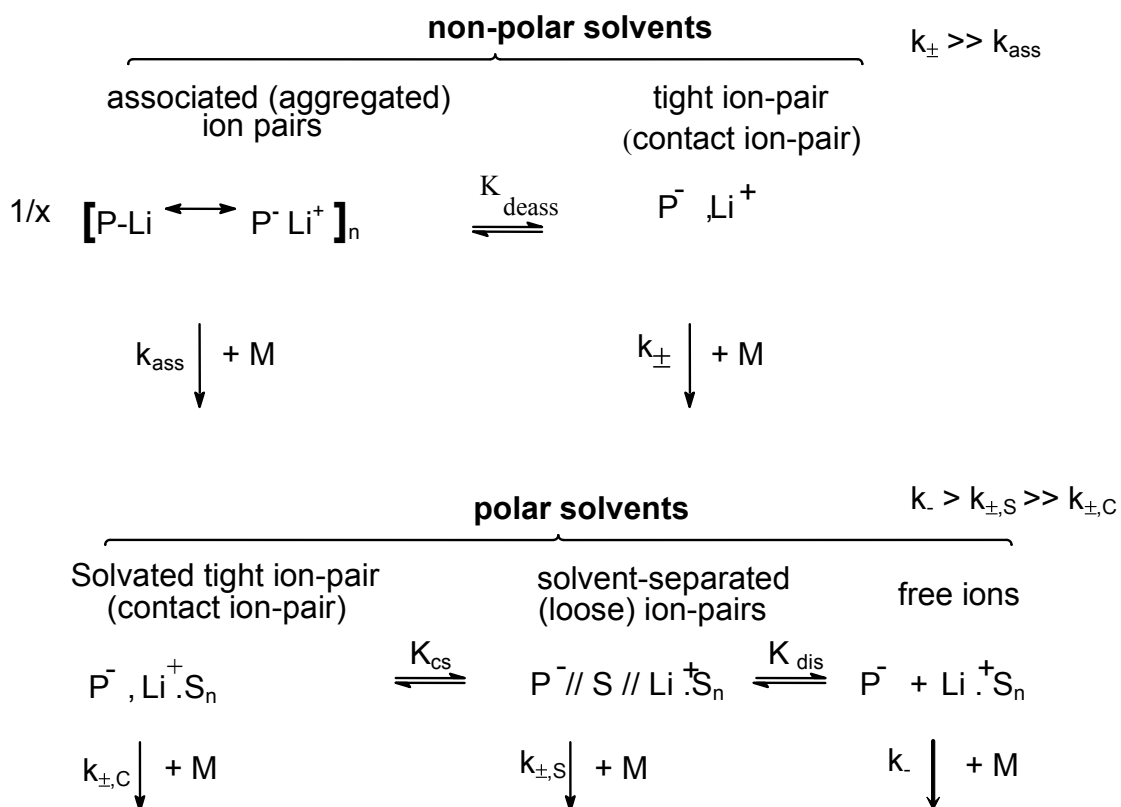
Fig. 34 States of aggregation of initiator respectively chain ends in non-polar and polar solvents[12]. The number of aggregation is n, S denotes the solvent, P the active polymer chain and M the monomer.

The regiospecific polymerization of polyisoprene with an high 1,4-fraction in non-polar solvents is explained by the absence of Lewis-bases which complex the Lithium counter ion in the polymerization process. A schematic sketch of the propagation of the polarization for both types of solvents is shown in **Fig. 35**.

Non-polar solvent

Polar solvent (e.g. 3,4-Polyisopren):
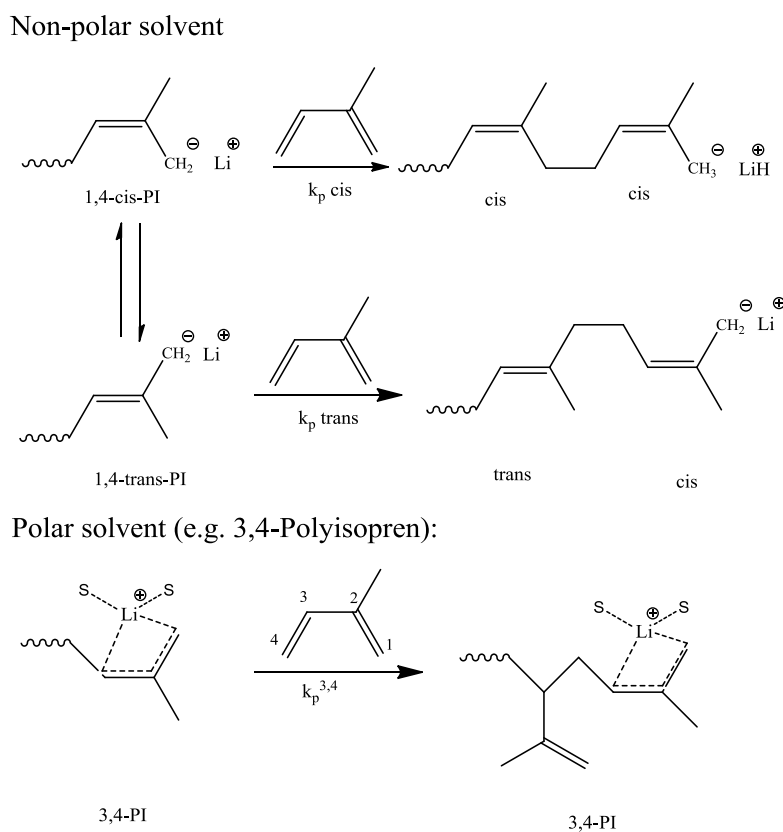
Fig. 35 Solvent depending region-selectivity of polyisoprene active centers.

The content of cis- or trans- 1,4-polyisoprene depends on the rate constant for the addition of a isoprene monomer to the active chain end and the rate of constant for an cis / trans isomerisation under the chosen conditions[12]. For the homopolymerization of isoprene at room temperature and toluene as a solvent, the ratio between cis- and trans- content is approximately 70 to 80%. As only 1,4-cis-polyisoprene possesses a dipole moment along the polymer back bone (Type *A* Polymer, see **2.4.4**), it is important to keep the 1,4-cis content as high as possible to enable precise and reliable dielectric measurements of the polymer chain dynamics.

It is worth to mention herein, that the choice of the organ metallic compounds can influence the tacticity of the polymer chain. For instance in the polymerization systems of methacrylates the polymerization initiated by lithium organic compounds (Li^+) in a polar solvent like THF leads to a high amount of syndiotactic addition, while the use of Cesium (Cs^+) as a counter ion in THF results in a predominant heterotactic addition[12].

The PS-b-PI diblock copolymers are synthesized by sequential anionic polymerization. First the purified styrene is polymerized by the addition of sec-BuLi.

Subsequently, the purified isoprene is added to the living polystyrene chains which react to a diblock copolymer with narrow polydispersity of PDI < 1.1. The reaction is terminated by adding methanol to the reaction mixture.

To receive a narrow molecular weight distribution, the sequence of the polymerization steps is important, as the addition of a polyisoprene molecule to an active polystyrene chain end, is 15 times faster then the following addition of further isoprene molecules to the polymer chain end[107]. Whereas the addition of a polystyrene molecule to an active polyisoprene chain end would be 20 times slower than the following consumption of styrene monomers, which would lead to a broadened molecular weight distribution. In **Fig. 36** a schematic sketch of the sequential polymerization of PS-b-PI is shown.

1. Polymerization of styrene
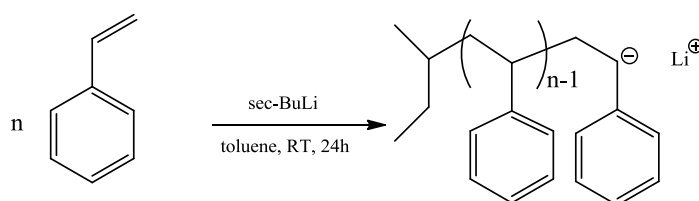
2. Copolymerization of isoprene
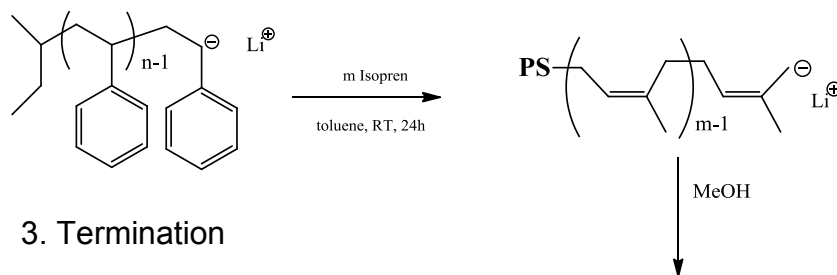
3. Termination
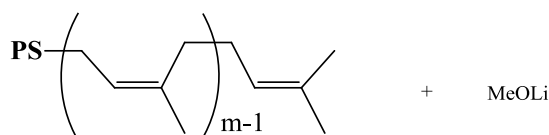
Fig. 36 Schematic sketch of the sequential anionic polymerization of styrene and isoprene to PS-b-PI.

3.1.3.   Characterization of the model compounds

The model compounds synthesized in this thesis were characterized with respect to their chemical composition by size-exclusion chromatography (SEC) and ^{1}H-nuclear magnetic resonance spectroscopy (^{1}H-NMR). The molecular weight of the

polystyrene homopolymers and precursors were characterized by SEC, which was operated with THF as solvent and calibrated to linear polystyrene. The concentrations of the polymer chains in the continuous eluent flow were analyzed by spectroscopic techniques, with a refractive index detector (RI-detector) or an ultraviolet detector (UV-detector). In addition, the polydispersity index for the whole set of model compounds, including the PS-b-PI samples, was determined from SEC measurements.

The RI- and UV- signal provides no further information than the concentration profile of the different polymer chains. Furthermore, precise molecular weight measurements are restricted to the calibration to linear polystyrene. Therefore, ^{1}H-NMR spectroscopy was applied to probe the different molecular microstructures which may occur during the polymerization of isoprene (see **Fig. 37**) and to calculate the total molecular weight of the diblock copolymers.

Cis-trans isomers Constitutional isomers

1,4-trans-PI   1,4-cis-PI   3,4-PI   1,2-PI
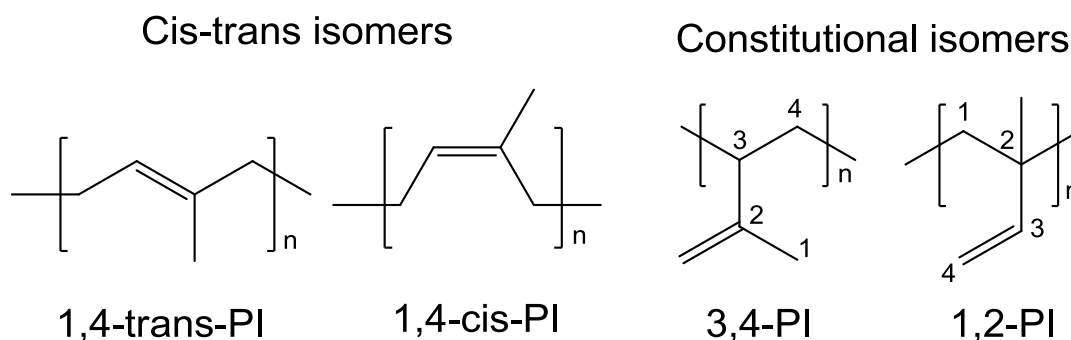
Fig. 37 Different possible microstructures of polyisoprene

In **Fig. 38** a representative ^{1}H-NMR spectra (400 MHz, CDCl$_3$) for an anionically synthesized PS-b-PI-20k-20k is shown. The diblock copolymer was polymerized in toluene, resulting in an high degree of 1,4- (5.06 ppm) rather than 3,4- (4.65 ppm) or 1,2- (5.73 ppm) polyisoprene. The content of 1,4-cis-polyisoprene for the homopolymers and the PS-b-PI diblock copolymers was calculated from the peak area of the 1,4-cis-methyl-protons at 1.61 ppm and the 1,4-trans-methyl-protons at 1.53 ppm. For all samples the content of 1,4-cis-polyisoprene was approximately 75%.
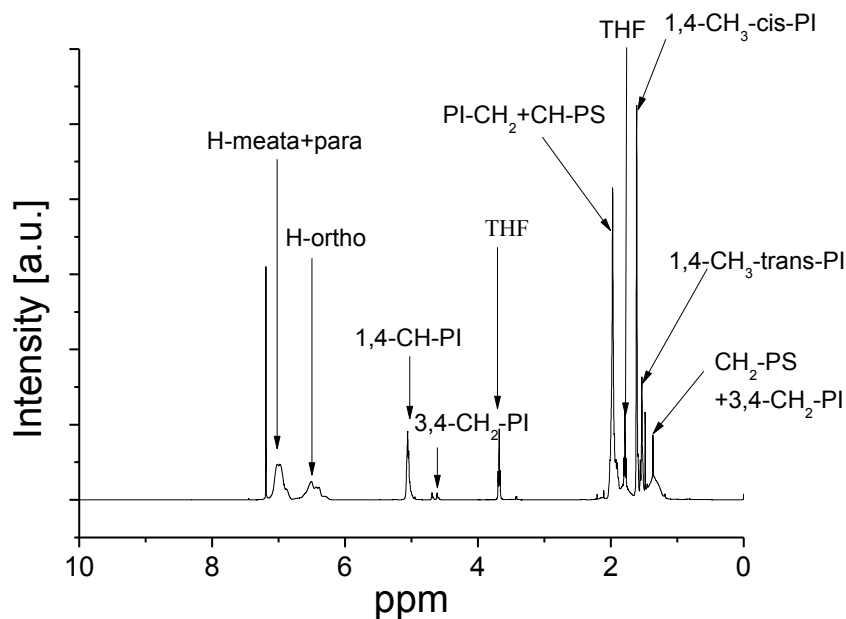
Fig. 38 400 MHz ^{1}H-NMR of an anionically synthesized PS-b-PI-20k-20k (M_w = 40,000 g/mol, f_{PS} = 50%, PDI = 1.05, T = 25 °C)

The total weight average of the molecular weight M_w and the volume fraction of the PS block f_{PS} of the PS-b-PI diblock copolymer were calculated by the following procedure:

- First a small amount of the PS precursor was taken and the molecular weight was determined by SEC.

- A ^{1}H-NMR spectra of the PS-b-PI diblock copolymer was detected. From the ratio of the peak area of the aromatic protons of the PS block and the peak area of the methylene protons of the PI block the M_w of the PI block can be calculated.

The structural properties of the diblock copolymers were characterized by small angle X-ray scattering. The morphologies were derived from the appearance of higher order reflections in the SAXS patterns, as described in section **2.5.4**. A representative scattering pattern of a macroscopic aligned PS-b-PI-22k-21k (M_w = 42,500 g/mol, f_{PS} = 52%, PDI = 1.04) is shown in **Fig. 39**. The integer periodicity of the higher order reflections indicates a lamellar morphology, as it is expected for a symmetric diblock copolymer. The spacial distribution of the lamellae dedicated as

66

the long period is correlated to the first order reflection by equation **(2.86)** ($L = \frac{2\pi}{q_0}$).

Form the first order reflection in **Fig. 39** at $q_0 = 0.21$ nm^{-1} a long period of L = 29.9 nm is calculated. This corresponds to lamella spacing of one block of d_{block} = 14.95 nm.
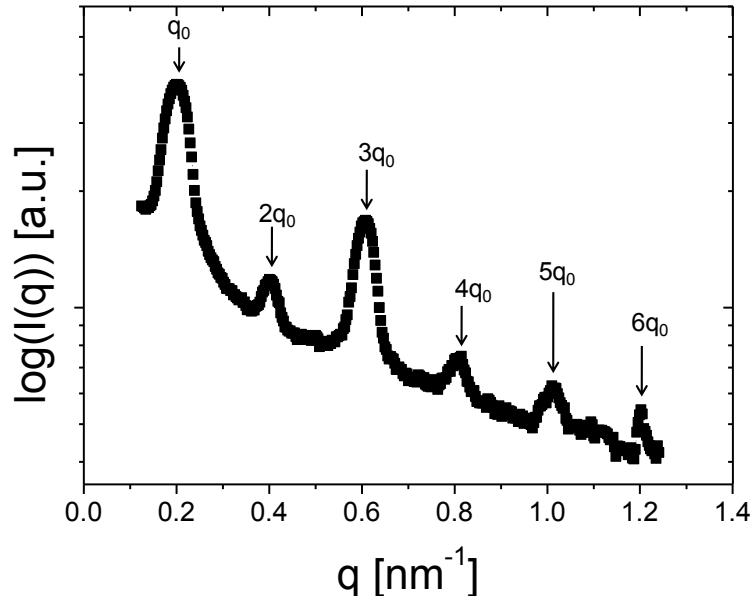
Fig. 39 SAXS pattern for a macroscopic aligned PS-b-PI-22k-21k diblock copolymer. The higher order reflections indicate a lamella morphology.

Simulations have shown[108] that the lamella spacing d_{block} is proportional to the total degree of polymerization N, the statistic segment length and the Flory-Huggins parameter χ_{FH}:

$$d_{block} \sim a \cdot N^{2/3} \cdot \chi_{FH} \tag{3.3}$$

In **Fig. 40** the double logarithmic plot of the total degree of polymerization versus the lamella spacing for symmetric diblock copolymers with different molecular weights is shown. The lowest and highest total degree of polymerization correspond to PS-b-PI-13k-13k (M_w=26,500 g/mol, f_{PS} = 51%, PDI = 1.03) respectively PS-b-PI-70k-70k (M_w = 145,000 g/mol, f_{PS} = 48%, PDI = 1.07).
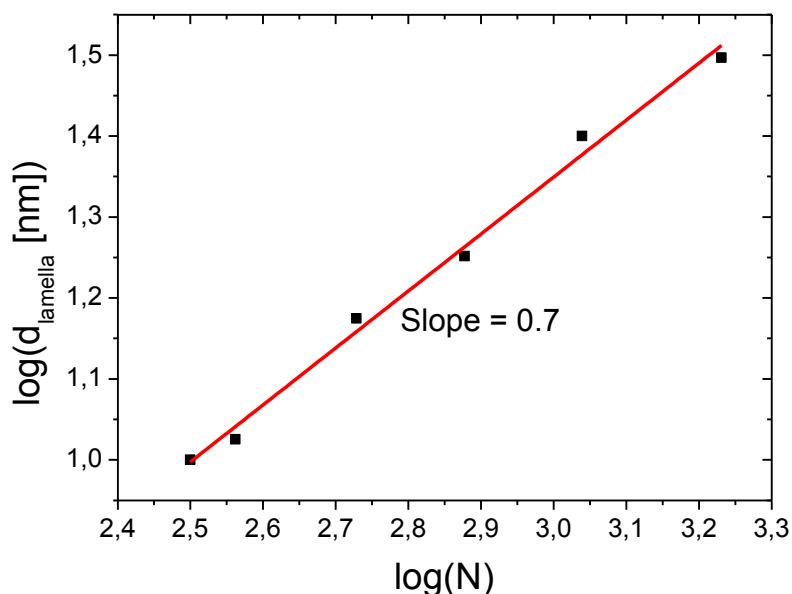
*Fig. 40 Double logarithmic plot of the total degree of polymerization N versus the lamella spacing $d_{lamellae}$ (at T = 22 °C) determined experimentally utilizing the samples summarized in **Tab. 2**.*

The deviance of the obtained slope from the predicted value of 2/3 is less than 10%. Although the relationship **(3.3)** has been derived for block copolymers in the strong segregation limit[109] (χ_{FH}*N $\geq$ 100), the investigated diblock copolymers, having segregation strength in the intermediate segregation limit (χ_{FH}*N $\approx$ 10 − 100), are in good comparison with predicted value.

The ordered disordered transition temperature was detected by a drastic decrease in the temperature dependence of the low frequency ($\omega_1/2\pi$ = 1 Hz) mechanical storage (G') and loss modulus (G'') applying a heating rate of 0.5 K/min. **Fig. 41** shows a representative temperature sweep test for PS-b-PI-15k-13k. For total molecular weights above 40,000 g/mol the T_{ODT} could not be detected in the accessible temperature range (T_{max} = 300 °C).
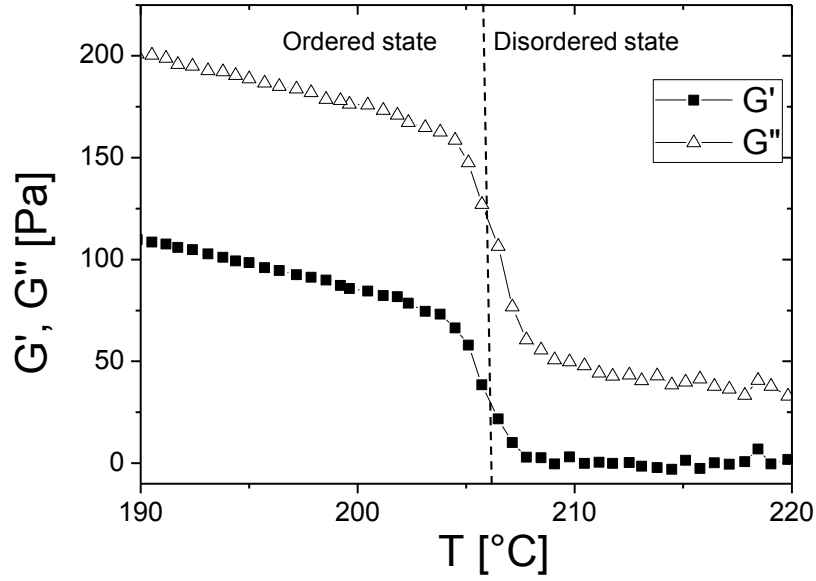
Fig. 41 Temperature sweep test for the rheological determination of the T_{ODT} for PS-b-PI-15k-13k ($\omega_1/2\pi$ = 1 Hz, Heat rate = 0.5 K/min). The T_{ODT} is determined by a drastic decrease of the low frequency modulii G' and G''.

Tab. 2 summarizes the synthesized PS-b-PI diblock copolymers and their chemical and physical properties.

Sample	M_w [g/mol]	f_{PS} [%]	Morphology	χ_{FH}*N (at 22 °C)	T_{ODT} [K]
PS-b-PI-13k-13k	26,500	51	Lamellar	29	478
PS-b-PI-15k-13k	28,000	54	Lamellar	33	480
PS-b-PI-17k-17k	35,000	49	Lamellar	37	491
PS-b-PI-22k-21k	42,500	52	Lamellar	48	x
PS-b-PI-27k-32k	59,000	46	Lamellar	68	x
PS-b-PI-40k-40k	83,000	48	Lamellar	99	X
PS-b-PI-70k-75k	144,500	49	Lamellar	154	X

Tab. 2 Summary over the synthesized PS-b-PI diblock copolymers which were mainly investigated in this thesis. PS-b-PI diblock copolymers with a T_{ODT} above the experimental accessible temperature range (250 °C) are assigned with a X.

3.2. Non-linear dynamic mechanical measurements

3.2.1. Quantitative methods

The mechanical investigation of complex fluids under large amplitude oscillatory shear (LAOS) has become of major interest in the last decades[61, 62, 70, 110-112]. With LAOS tests, mechanical non-linear properties can be studied for a large class of

materials such as polymer melts and solutions, block copolymers, biological macromolecules and polyelectrolytes. These experiments are of major interest as in most processing operations the mechanical demands are beyond the region in which the materials behave mechanically linear. In the following, a brief overview of the recent developments in the field of non-linear oscillatory shear tests is provided while the basics of experimental setups used to obtain raw stress data under LAOS are discussed in section **3.2.2**. For a more detailed discussion about non-linear oscillatory shear tests the reader is referred to the review article of Hyun et al.[29] and the publication cited there. The introduced methods were proposed to analyze non-linear stress response to deformation controlled oscillatory shear.

a) Stress decomposition

Stress decomposition[113] is one quantitative method which regards the rheological non-linear stress data as a superposition of elastic stress $\xi'(\gamma)$ and viscous stress $\xi''(\gamma)$. With the requirement that the symmetry criteria ($\xi(\dot{\gamma},\gamma)=\xi(-\dot{\gamma},-\gamma)$) is fulfilled[113], the shear stress can be composed into a term which is only a function of the strain and a term $\xi_{EO}(\dot{\gamma})$ which only contributes to the shear stress:

$$\xi(\dot{\gamma},\gamma)=\frac{\xi(\dot{\gamma},\gamma)+\xi(\dot{\gamma},-\gamma)}{2}+\frac{\xi(\dot{\gamma},\gamma)+\xi(-\dot{\gamma},-\gamma)}{2}=\xi_{OE}(\dot{\gamma},\gamma)+\xi_{EO}(\dot{\gamma},\gamma) \qquad (3.4)$$

It follows that ξ_{OE} is correlated to the elastic stress and ξ_{EO} to the viscous stress. The stress decomposition concept was extended by Ewoldt et al.[114] introducing Chebyshev polynomials, which overcome the drawback of non-orthogonality of polynomial regression fitting, to determine non-linear coefficients.

b) Characteristic functions

In recent years an interpretive method has been developed by Klein et al.[62] to model the obtained non-linear stress response. This model is based on semi empirical interpretations that the waveforms, which correspond to known rheological phenomena as shear thinning or shear hardening. These can be described by characteristic functions as follows:

- The linear response is characterized by a sine function:

$$\xi_{lin}(t) = A_{lin}\sin(\omega_1 t + \delta_{lin}) \qquad (3.5)$$

- The strain softening response is described by a rectangle function:

$$\xi_r(t) = A_r \frac{4}{\pi}(\sin(\omega_1 t + \delta_r) + \frac{\sin 3(\omega_1 t + \delta_r)}{3} + \frac{\sin 5(\omega_1 t + \delta_r)}{5} + ...) \qquad (3.6)$$

- The strain hardening response is described by a triangular function:

$$\xi_t(t) = A_t \frac{4}{\pi}(\sin(\omega_1 t + \delta_t) - \frac{\sin 3(\omega_1 t + \delta_t)}{3^2} + \frac{\sin 5(\omega_1 t + \delta_t)}{5^2} + ...) \qquad (3.7)$$

- Effects of shear band or wall slips, which are assumed to cause even harmonics, are considered by a sawtooth function:

$$\xi_{st}(t) = A_{st} \cdot 2 \cdot (\sin(\omega_1 t + \delta_{st}) - \frac{\sin 2(\omega_1 t + \delta_{st})}{2} + \frac{\sin 3(\omega_1 t + \delta_{st})}{3} + ...) \qquad (3.8)$$

With these characteristic functions the time domain signal of $\xi(t)$ can be expressed by a superposition of these function:

$$\xi(t) = \xi(t)_{lin} + \xi(t)_r + \xi(t)_t + \xi(t)_{st} . \qquad (3.9)$$

The relative contributions of these functions are capable to describe the real signal correlate with the magnitude and phase angle of the relative higher harmonics obtained by FT-Rheology[62]. Therefore, they can be used to determine non-linear mechanical phenomena such as in emulsions and suspensions.

From equation **(3.9)** it can be seen that for shear softening the intensities of the higher harmonics decay as $1/n$ (n = 1, 3, 5, …). Therefore, it is assumed that the relative intensity of the third harmonic $I_{3/1}$ will be the dominant signal in the non-linear FT-Spectra and can be regarded as a direct measure for the non-linear mechanical

response. From this expression it becomes also obvious that the maximum value of $I_{3/1}$ would be limited to 33%.

c) FT-Rheology

The basic principles of FT-Rheology were already introduced in section **2.2.2**. Herein, a new nonlinear quantitative coefficient Q[70], derived from FT-Rheology is introduced.

In the linear viscoelastic regime $I_{3/1}$ should be zero, as the stress response is only a function of frequency. However, in the non-linear regime $I_{3/1}$ becomes infinite and increases with increasing degree of mechanical non-linearity[29]. From the series expansion in equation **(2.37)** it can be derived that the n-th harmonic is proportional to:

$$I_n \sim \gamma_0^n, n = 1, 3, 5....$$

(3. 10)

Therefore, $I_{3/1}$ scales quadratically with respect to the strain amplitude:

$$I_{3/1} \sim \gamma_0^2$$

(3. 11)

For the first time, Hyun et al.[70] examined the quadratic scaling with strain amplitude of $I_{3/1}$ for various polymer melts. From these proposed a new non-linear coefficient Q had been defined[70]:

$$Q = \frac{I_{3/1}}{\gamma_0^2}.$$

(3. 12)

This new coefficient $Q(\omega, \gamma_0)$ is a function of both strain amplitude and frequency and is considered to characterize the non-linear mechanical behavior. For sufficient low strain amplitudes an asymptotic limiting value was found, similar like other rheological properties (e.g. viscosity), and defined as Q_0[70]:

$$Q_0(\omega) = \lim_{\gamma_0 \to 0} Q(\omega, \gamma_0)$$

(3. 13)

.

Recent studies revealed that Q_0 can quantify non-linearity of complex fluids as a function of frequency[115].

3.2.2. Experimental setup

All FT-Rheology measurements were performed with a strain controlled ARES Rheometer (TA-Instruments) with a separated motor and transducer technology. The rheometer is equipped with two torque transducers with different sensitivities. Transducer 1 was adopted for measurement at low viscosities with a dynamic range between $2*10^{-6}$ to $2*10^{-3}$ Nm. For higher torques, Transducer 2 was used which was capable to measure torques from $2*10^{-4}$ up to 0.2 Nm.

Additionally the rheometer was equipped with a high resolution motor with an accessible frequency range between 10^{-4} to 20 Hz and a deformation amplitude ranging from 0.005 to 500 mrad. Furthermore, the rheometer was equipped with a temperature cell enabling measurement in an accessible temperature range was between -70 and 250 °C. The low temperatures were achieved by a commercially available cooling system operated with liquid nitrogen. All measurements at elevated temperatures were performed under nitrogen to avoid degradation by oxidation.

To obtain the oscillatory raw stress data the output channels of the rheometer were connected to a computer by three BNC cables where the torque, normal force and motor displacement are available as analog voltage. The analog raw data was converted into digital signals utilizing a 16-bit analog-digital converter (ADC) card (National Instruments) with a sampling rate of 100,000 s^{-1}. The recorded time data were averaged using a home-written LabVIEW® software program[116]. With the special data processing (Over sampling), proposed by Dusschoten et al.[117], the signal to noise ratio has been further improved by factor of approximately 10. The FT-Analysis is performed with a second home-written LabVIEW® software program[116]. A schematic representation of the used setup is shown in **Fig. 42**.
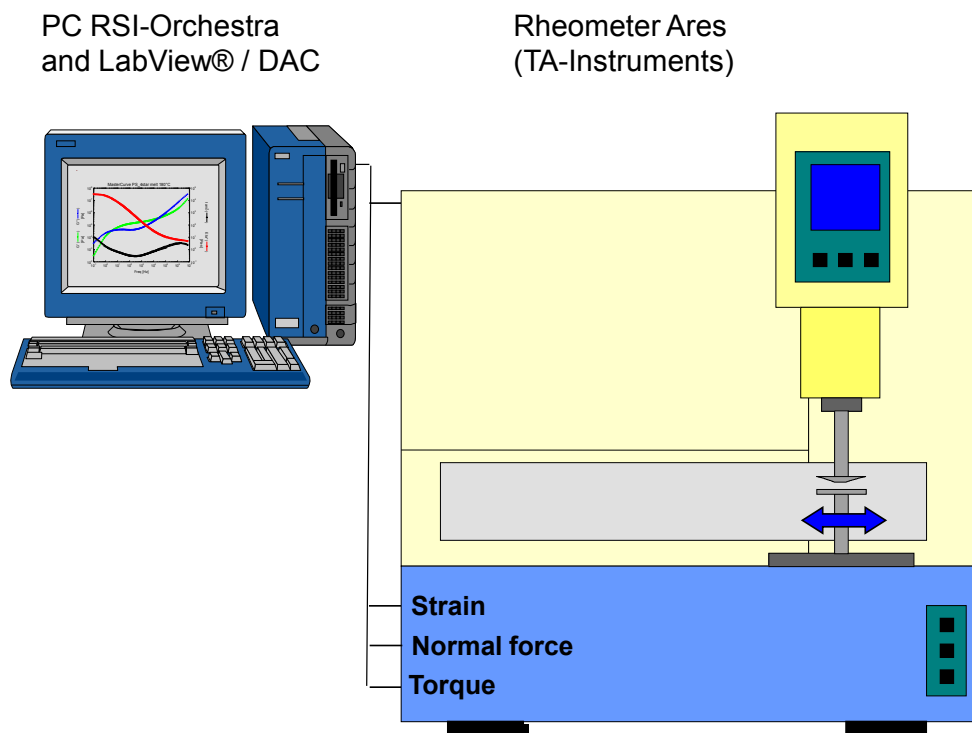
Fig. 42 Schematic representation of an experimental setup commonly used for LAOS experiments, containing a strain controlled rheometer with electronically data acquisition and analysis.

It is worth noticing that recently the method of FT-Rheology had been implied into a commercially available rheometer the Ares G2 from TA-Instruments. This feature permits the online measurement of the non-linear stress response. Additionally, the time dependence of $I_{3/1}$ can be by the ARES utilizing the NonLinear Monitoring integrated in the Orchestra® software of TA-Instruments.

3.3. Rheo-Dielectric combination

3.3.1. Recent developments / Literature review

The Rheo-Dielectric setup permits the simultaneous detection of dielectric and mechanical properties of a substance. The broadband dielectric spectroscopy usually applied for Rheo-Dielectric studies, deals with the interaction of electromagnetic waves with matter in a typical frequency range between 10^{-3} and 10^{6} Hz[88].

In this frequency range, the dielectric properties are related to collective dipolar fluctuations, polarization effects and charge transports[88]. Hence, Rheo-Dielectric measurements provide information on the relation between molecular relaxation dynamics and the corresponding mechanical response. In the following, a brief

overview of different recently in literature published Rheo-Dielectric combinations is provided.

Adachi et al.[118] introduced one of the first Rheo-Dielectric setups published in literature. The published setup consisted of a custom made coaxial cylinder-type rheometer equipped with an automatic capacitance bridge. Due to the lag of an adequate heating system this approach was limited to concentrated polymer solutions, polymers with glass transition temperatures T_g below room temperatures or emulsions and suspensions.

Crawshaw et al.[119] described a simple setup to measure the effect of shear on the electrical conductivity in pipe flow for conductive colloidal systems. Peng et al.[120] studied the influence of various processing conditions in the injection molding process of polymer melts using a specially designed plate mold geometry equipped with three-element sensor rosette. Both setups have the drawback to be inappropriate to perform LAOS experiments, as they are limited to steady shear flow experiments.

A first approach to combine a commercially available rheometer with dielectric measurement techniques was reported by Sato et al.[121]. This Rheo-Dielectric combination was based on a modified rheometer (Autoviscometer L-III, Iwamoto Seisakusho, Kyoto) to induce a mercury contact point, which enabled Rheo-Dielectric measurements without mechanical disturbance of the electrical contacts[121]. However, the mercury contact had the disadvantage of limiting elevated experimental temperature to approximately 100 °C. Therefore, this setup is principally restricted to measurements of concentrated polymer solutions or polymer melts with a glass transition temperature below the accessible temperature range. Nevertheless, important publications on the field of polymer chain dynamics have been published within the group of H. Watanabe[122-124], especially for 1,4-cis-polyisoprenes[125-127].

3.3.2. High sensitive Rheo-Dielectric combination

For the Rheo-Dielectric experiments performed in this thesis a very sensitive setup was utilized and optimized. The setup described by Hyun et al.[33] consists of a combination of an ARES (TA-Instruments) and a dielectric ALPHA-Analyzer (Novocontrol Technologies) (see **Fig. 43**). The ALPHA-Analyzer is able to measure about 12 orders of magnitude frequency range (3×10^{-5} to 1×10^7 Hz), 16 orders of

impedance range (10^{-2} to 10^{14}) and 15 orders of capacity range (10^{-15} to 1 F). These ranges exceed the capacitance bridges used in former Rheo-Dielectric measurements by several decades in each quantity. Furthermore the ALPHA-Analyzer allows a tanδ, phase shift between input voltage and output current, resolution of $\pm 3 \times 10^{-5}$ to $\pm 10^{-3}$, depending on the used capacity. The ceramic insulation (Marcor®) between the parallel plate and fixture is very brittle and has a low thermal expansion coefficient. Thus INVAR steel with an extremely low temperature coefficient of 1.3×10^{-6} K^{-1} (in comparison to 13×10^{-6} K^{-1} in conventional steel) is used as a new measuring plate and fixture. This is specifically helpful for measuring at various temperatures. The mechanical interface between the isolated parallel plate geometry and the fixture was optimized to reduce misalignments which may occur by the mechanical interface of the tool shank. The sample plates with 8, 10, 13, and 25 mm in diameter are connected to the electronic wire with a bolt, and the other end of the wire is connected with a BNC connector. An enlarged schematic representation of the mechanical interface between the electrodes and the fixture is shown in **Fig. 44**. The technical drawings of the optimized geometries are shown in the appendix. To operate at elevated temperatures a special high temperature solder was used which is temperature stable up to 300°C. The BNC connector is installed outside of the oven. All parts of the electrode are located inside the oven. This allows temperature control and electronic noise shielding environment which is from major importance to reduce the signal to noise level during the measurements.
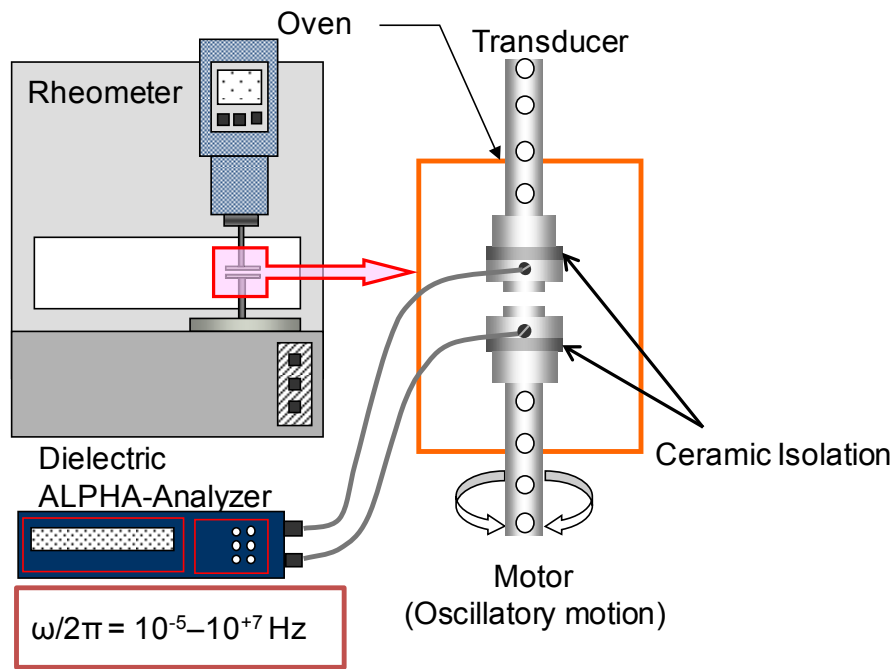
Fig. 43 Sketch of the Rheo-Dielectric setup used in this thesis.
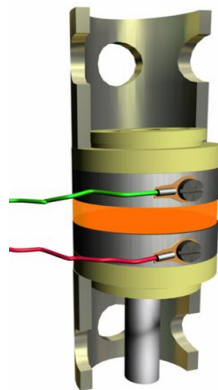
Fig. 44 Mechanical interface between the parallel plate electrodes and the fixture. The wires connect the electrodes with the Alpha analyzer and are attached to the electrodes with bolts.

With this sensitive Rheo-Dielectric combination, high viscous materials such as polymer melts can be investigated in a temperature range between -70 °C to 250 °C. The connection of the cable to the parallel plate electrodes was designed to minimize mechanical disturbance thus large amplitude oscillatory shear experiments can be performed with optimized mechanical data accuracy.

3.4. In-situ Rheo-SAXS combination

3.4.1. Recent developments / Literature review

Small angle X-ray scattering (SAXS) is a method capable to reveal ordered structural information on a nanometer length scale between 1 and 500 nm. These are typical size dimensions in polymer and colloidal systems. Therefore, SAXS experiments were shown to be the method of choice for evaluating the mechanism and kinetics of the orientation process on a length scale corresponding to the molecular dimension and for also providing an average over the representative sample volume[128].

In recent years, much effort has been devoted to online monitoring of the influence of non-linear mechanical excitations on various phase separated systems[129, 130]. Different approaches and experimental setups were developed for in-situ experiments utilizing a variety of shear cells. An example of this is the Couvette geometry[131-133], which was used to generate macroscopic orientation in block copolymer solutions under defined mechanical conditions. While this setup has the advantage of investigating the alignment along two distinct trajectories, it is limited to polymer solutions. In addition, capillary[134] and multipass[135] rheometers used high shear rates to mimic the macroscopic alignment under processing conditions.

Nevertheless, parallel plate (e.g. cone plate) geometries are preferred for examining the underlying kinetic pathway of the block copolymer melt orientation process as a function of shear frequency, strain amplitude, temperature and the duration of shear. The advantages of the here presented approach include precise dynamic mechanical measurements, simple sample preparation, ease of temperature control and the appropriate range of frequencies and strain amplitudes required for polymer melts having a glass transition temperature T_g above or below room temperature. A disadvantage of this approach is that the sample volume may become too large, resulting in an undesired abortion phenomena that may interfere with the scattering experiments. In recent years, there have been new developments using parallel plate geometries where precise rheological measurements and simultaneous characterization of mechanically induced structural changes via X-Ray scattering were obtained. With this approach, Polushkin et al.[136, 137] and Garcia-Gutierrez et al.[138] were able to investigate two distinct directions, but could only perform these experiments on a very small sample volume, which unfortunately limits

the use of large amplitude oscillatory shear (LAOS). To overcome this drawback, a new and unique Rheo-SAXS combination was developed[35] which is described in detail in the following.

3.4.2.   In-situ Rheo-SAXS combination

In-situ Rheo-SAXS measurements were carried out at the beamline BW1 of the DORIS III storage ring at HASYLAB (DESY, Hamburg, Germany)[35], at a wavelength of 0.1267 nm. In order to achieve a well defined mechanical excitation as well as precisely detecting the mechanical response, the beamline is equipped with a commercial stress controlled rheometer (Mars II, Thermo Scientific). We developed a custom made Vespel® comprised parallel plate geometry with a diameter of 36 mm containing thin windows of 0.3 mm thickness at 15.5 mm distance from the center of the plate (γ_{local} = 0.86*γ_0), to minimize scattering and absorbance effects, which reduces beam intensity. To redirect the intrinsically horizontal synchrotron X-ray beam by 90°, a diamond (004) reflection is used. The rheometer is equipped with a custom made cylindrical heating cell, operating with nitrogen as an inert gas to avoid oxidative decomposition of the polymer melts. The accessible temperature range lies between room temperature and 250 °C, with an accuracy of 0.5 °C. The scattered intensities were recorded by a 2D detector (Pilatus 100k) which can be positioned at various distances between 30 cm and 2.50 m above the sample. The acquisition time necessary for each 2D-SAXS frame was down to 11 s (10 s exposure plus 1 s delay time for data storage and triggering).

The Rheo-SAXS combination is an ideal method to characterize shear-induced structural changes on a mesoscopic length scale (1 nm to 100 nm) in-situ measuring the mechanical parameters under precise rheological conditions.
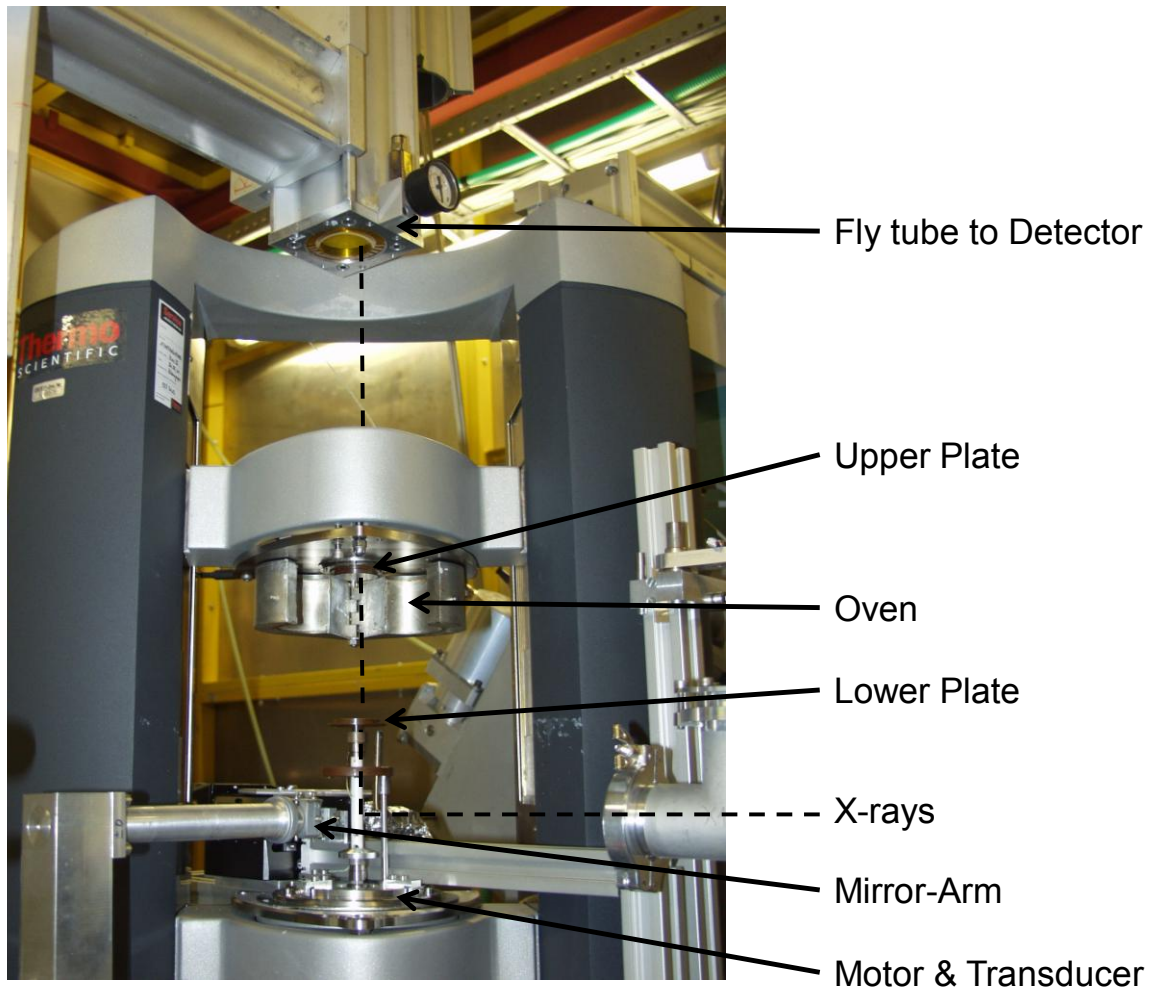
Fig. 45 Picture of the unique Rheo-SAXS setup, located at the beamline BW1 at the HasyLab.

3.5. Experimental procedure

3.5.1. Sample preparation

The PS-*b*-PI synthesized by anionic polymerization (detailed description of the anionic synthesis is provided in section 9) were freeze-dried from a cyclohexene solution (10 wt. %) under high vacuum for 10 h. The obtained pure powder was hot pressed under vacuum at 140 °C into sample discs with diameters of 13, 25 mm respectively 36 mm and a thickness of approximately 1 mm. The pressure applied to the block copolymer melt was adjusted to 10^4 Pa. The obtained discs were used without any further annealing steps.

3.5.2. Sample loading and experimental procedure

The herein described sample loading and experimental procedure concerning the rheological part was carried out for all performed LAOS experiments. For the combined methods, respectively SAXS and dielectric measurements, additional measurement protocols were carried out which will be mentioned in the corresponding sections.

The parallel plate geometries were tempered at the measurement temperature for 1 h before zero fixture was performed. The sample disc was mounted between the plates and slightly squeezed until the whole geometry surface was covered with the polymer melt and tempered between 20 min (for M_w < 40,000 g/mol) and 45 min (M_w > 40,000 g/mol).

For low molecular weight diblock copolymer melts with order-disorder transition temperatures below 250 °C, strain sweep tests were conducted to determine the mechanical linear and non-linear regimes. Afterwards, and prior to each orientation experiment, the low molecular weight block copolymer melts were heated 20 °C above the respective T_{ODT}, and then tempered for at least 20 minutes to remove all previous thermal and deformation history.

The sample was then cooled to the desired measurement temperatures while constantly adjusting the gap to control for thermal shrinkage of the sample and the sample geometries. To avoid squeeze flow induced orientation, a normal force of less than 0.05 N (~ 50 Pa) was applied.

At the measurement temperature, the samples were allowed to temper for another 20 minutes. Before and after each LAOS experiment, mechanical frequency sweeps in the linear regime were performed

3.5.3. External SAXS measurements and sample preparation

The ex-situ 2D-SAXS measurements (Hecus S3-Micro X-ray system) of the synthesized PS-*b*-PI were performed by using a point microfocus source, 2D-X-Ray mirrors and a two dimensional CCD-Detector from Photonic Science. In addition, a block collimator system was used to ensure low back ground scattering. With this system, the   vector that can be detected varies from 0.06 nm^{-1} to 4.7 nm^{-1}. It is important to note, that with the use of a block collimator system only the half 2D-SAXS pattern can be recorded (see **Fig. 52**). Nevertheless, as the 2D-SAXS patterns of the investigated symmetric diblock copolymers obey point symmetry, no relevant information is lost by this technique, but the background is reduced significantly, that no background correction have to be done.
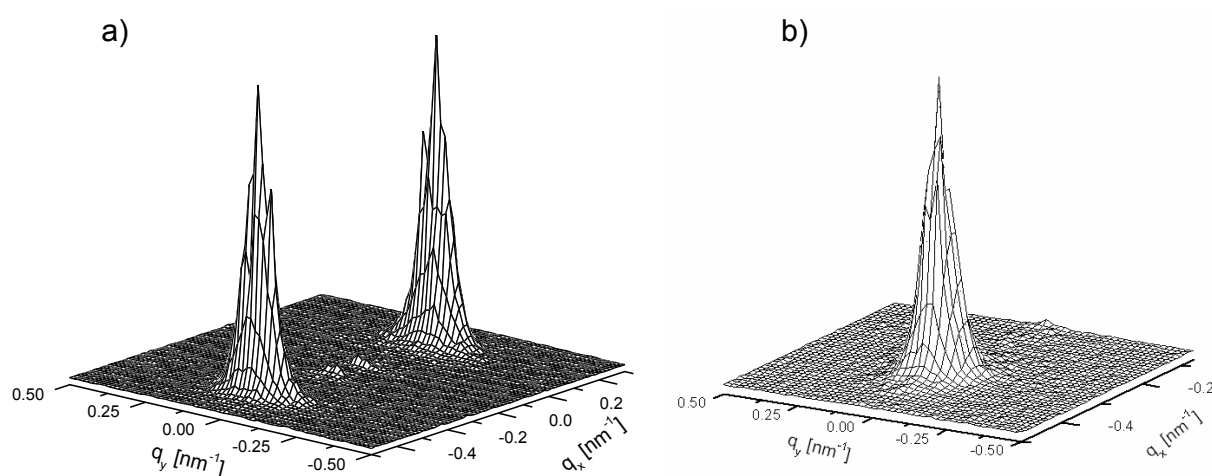
Fig. 46 2D-SAXS pattern of an macroscopic orientated symmetric block copolymer. a) Full 2D-SAXS pattern obtained by mirroring a 2D-SAXS pattern recorded with the Hecus S3-Micro X-ray b) half 2D-SAXS pattern as recorded with the block collimator system of the Hecus S3-Micro X-ray system).

To follow the time evolution of the non-linear parameter, the LAOS experiments were stopped at specific times to examine ex-situ the state of orientation. The samples were rapidly cooled to room temperature (within 10 min) and the normal force was thoroughly adjusted to compensate for thermal shrinking until the state of

orientation was frozen by the glassy PS blocks (T ≈ 80 °C). At this point, the sample was removed from the shear geometries.

For each state of orientation, the macroscopic orientation along each of the three major directions was determined at three points in the sample, i.e. at a radius of 2 mm (position c), 4 mm (position b) and 5.5 mm (position a) (see **Fig. 47**). The investigation of these three different positions revealed the influence of the strain gradient caused by the parallel plate geometry on the macroscopic orientation.
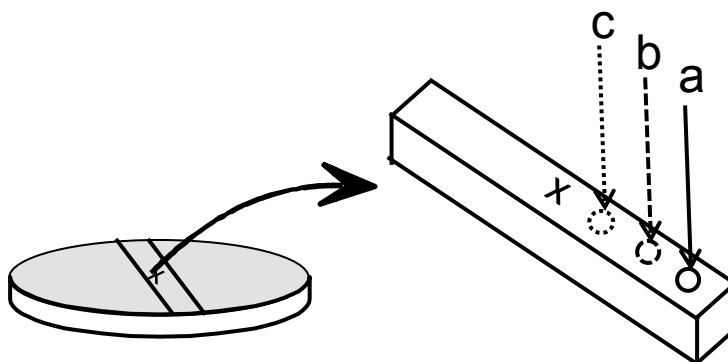
Fig. 47 Schematic sketch of the three points along the radial vector which were taken for ex-situ 2D-SAXS measurements. Position a) corresponds to r = 5.5 mm, b) to r = 4mm and c) to r = 2 mm.

3.5.4. Analysis of the 2D-SAXS pattern

The effect of LAOS to the microstructure of the self assembled diblock copolymers was probed by in-situ and ex-situ 2D-SAXS measurements. There are two different ways to average the obtained 2D-SAXS patterns and reduce the contained information to 1D-plots. This enables a better analysis of the shear induced structural changes (see **Fig. 48**):

- Azimuthally averaging the 2D-SAXS patterns in a distinct upper and lower $|\vec{q}|$ boundary along χ provides information on the orientation distribution of the unit normal of the lamellae orientated parallel to the investigated plane. To describe the time evolution of the orientation distribution during the shear-induced alignment, the time dependence of the peak width of the azimuthally averaged first order reflection is followed by the standard deviation σ_{SAXS} obtained by fitting the peak with a Gauss function. It is important to note that the full width at half maximum of the Gaussian is $2.35*\sigma_{SAXS}$.

- The peak width of the radial averaged (along $|\vec{q}|$) first order reflection in the 2D-SAXS pattern contains information about the average diblock copolymer grain size. Due the complex experimental conditions for the Rheo-SAXS setup only relative changes could be considered. The relative changes of the radial averaged peak width are determined by normalizing σ_q to the initial standard deviation σ_{q-max} obtained from the undeformed sample.
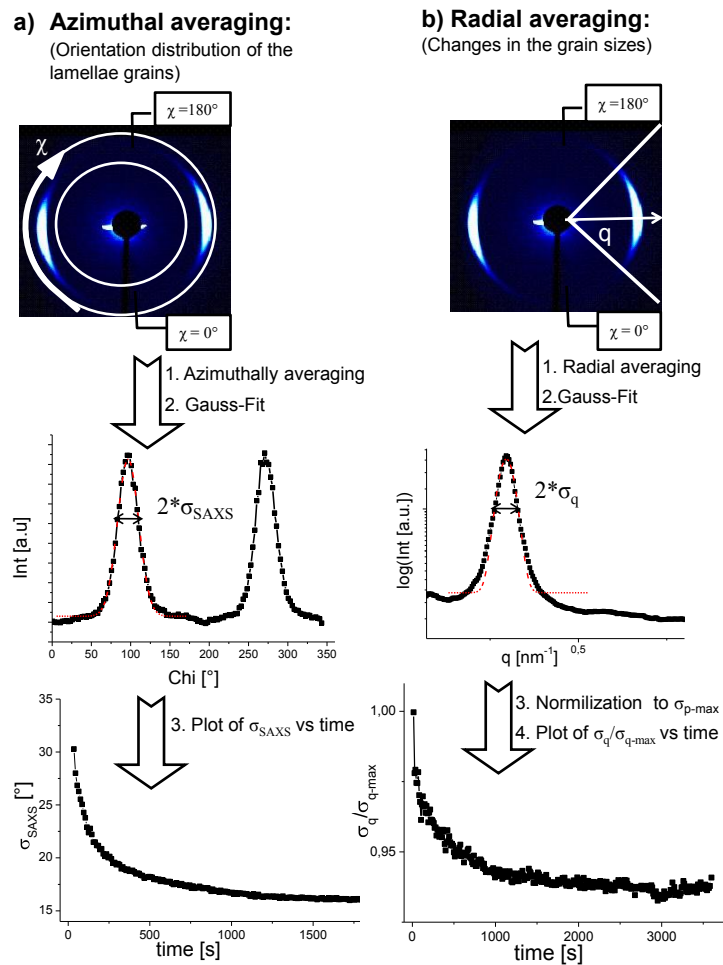
Fig. 48 Representation of the 2D-SAXS pattern evaluation. a) Azimuthally averaged first order reflection of the 2D-SAXS patterns provides information on the orientation distribution of the lamella microstructure. b) Radial averaged first order reflection of the 2D-SAXS patterns contains information about the relative change of the diblock copolymer grain sizes.

4. Shear-induced orientation of PS-b-PI-13k-13k

4.1. Literature review

Certain types of soft matter, such as liquid crystals, amphiphiles and block copolymers, self assemble into nanostructured morphologies below their order-disorder transition temperature (T_{ODT}) as a way to minimize highly unfavorable enthalpic contributions to the free energy. Self assembly usually leads to a polydomain structure with locally anisotropic ordered domains (grains) that are randomly orientated throughout the whole sample, resulting in a macroscopically isotropic material[28, 139]. However, many practical applications including functional membranes, anisotropically charged materials and photon conductors require that the final material is macroscopically anisotropic.

Application of an external stimulus, such as an electric, magnetic or mechanical field, can then be used to obtain the preferred macroscopic alignment[140-145]. As an example of this, shear flow was shown to be a feasible method for macroscopically aligning symmetric block copolymers and liquid crystals, see references[27, 146-151] and citations within.

Therefore, it is important to understand the mechanism and kinetics of mechanically induced macroscopic orientation as a way to optimize this alignment and to tailor processing conditions for specific applications. This would result in, for example, new functional materials that could be used as templates for nano-particles in certain advanced applications[76, 152, 153] as well as a way to improve non-equilibrium molecular dynamics simulations[154-157]. Furthermore, controlling the kinetic pathway of the macroscopic alignment by varying the mechanical shear field enables the exploitation of non-equilibrium or transient morphologies as first shown in a recent study[35] on low molecular weight liquid crystals. Additionally, the processing conditions can be optimized with respect to time and the achieved orientation.

For the macroscopic orientation of symmetric block copolymers, large amplitude oscillatory shear (LAOS) was shown to be the preferred method because it allows for different orientations of the unit normal of the lamellae[30]. In most studies, the morphological characterization of a shear-oriented block-copolymer was performed

ex-situ, making it difficult to study the kinetic processes involved in the alignment[82, 84, 85, 158].

It is also important to note that ex-situ measurements are more difficult to analyze due to variations caused by sample preparation, loading, thermal history of the sample and possible distortion of the aligned structures caused by cooling, unloading and trimming. Furthermore, only a limited amount of kinetic data is then available. On the other hand, these ex-situ measurements provide information about structural properties along all three directions, which is not accessible by currently available in-situ methods[159].

While birefringence is a powerful tool to follow the progress of orientation online[87, 160] enabling data processing on a microsecond scale, it unfortunately provides no direct information on nanometer length scale structural changes or molecular chain dynamics and requires ex-situ experiments to provide reliable morphological information.

Nevertheless, there is a pressing need to develop in-situ measurement techniques with adequate time resolution that can correlate induced structural changes or molecular dynamics in the melt state with the mechanical response and that can also follow the kinetic pathway of the macroscopic orientation process under precise experimental conditions. Previous in-situ experiments published in the literature mainly focused on the influence of the applied shear flow on the hierarchically structured material, but did not associate these effects with the underlying mechanical response under non-linear flow.

To overcome this drawback, a new and unique Rheo-SAXS combination was developed[35]. This setup (see **Fig. 45**) enables full rheological characterization of polymer melts while simultaneously probing mechanically induced structural changes on a nanometer length scale. In contrast to other experimental parallel plate setups where the primary x-ray beam is directed through the rheometer gap along the shear vector direction[28, 137, 161], the primary synchrotron X-Ray beam is directed through the sample along the shear gradient (*OZ* axis) (see **Fig. 52**).

Furthermore, the fluctuations of the end-to-end vector of the polyisoprene chains in the diblock copolymer melts were investigated by Rheo-Dielectric combination to reveal changes in the molecular dynamics during the alignment process. Several Dielectric studies were performed on block copolymers investigating the molecular chain dynamics[118, 122, 162, 163]. Nevertheless, this is the first time that the in-situ

86

obtained structural and molecular dynamics are correlated to each other with the aid of unique combined methods[33-35].

In the following, the shear-induced macroscopic orientation process of symmetric polystyrene-block-polyisoprene diblock copolymers will be discussed with respect to the mechanical nonlinear response and the underlying molecular dynamics and structural changes. Different experimental conditions will be provided which give rise to conclusions about the kinetic pathway of the orientation process depending on experimental parameters, such as frequency, temperature, strain amplitude, duration of shear and the molecular weight. Additionally, the discussion of the macroscopic orientation process is investigated by Rheo-Dielectric techniques.

4.2. Linear mechanical characterization

The investigated symmetric PS-b-PI-13k-13k (M_w = 26,500 g/mol, f_{PS} = 51%, PDI = 1.04) was chosen as a model compound to investigate the kinetics of shear-induced macroscopic perpendicular alignment. To achieve a macroscopic isotropic initial state, the sample was heated above the T_{ODT} before the LAOS experiments were performed.

The master curve of the mechanical linear response of the storage (G') and loss (G'') modulus as function of reduced frequency ($a_T*\omega/2\pi$) is presented for PS-b-PI-13k-13k at a reference temperature of T_{ref} = 150 °C (see **Fig. 49**). The cross over point between G' and G'' in the low frequency region ($\omega_1/2\pi \approx 0.3$ Hz) is a characteristic for self assembled block copolymer systems. In this frequency region the microstructure of the self assembled block copolymer dominates the linear mechanical response (zone A). The absence of a rubber plateau in the intermediate frequency regime indicates that the polymer chains are not entangled. Therefore, with increasing frequency the transition zone II (zone B) directly merge in the transition zone II (zone C) followed by a second junction point between G' and G'' at approximately $3*10^5$ Hz which indicates the glass transition. Beyond this critical frequency the polymer melt acts like an elastic solid (zone D).

It is important to note that for homopolymers below their T_g the storage modulus G' is approximately G' $\approx 10^9$ Pa. In contrast, in the glassy state the PS-b-PI diblock copolymers obeyed a significant lower value of the storage modulus (G' $\approx 10^7$ Pa). This can be explained by the contributions of the PI block to the linear mechanical

response of the sample. The glass transition temperature of polyisoprene is approximately $T_g(PI) \approx -60\ °C$ as determined via DSC measurements. Therefore, the PI block is still in the melt state although the PS chains are below their T_g of approximately 100 °C.
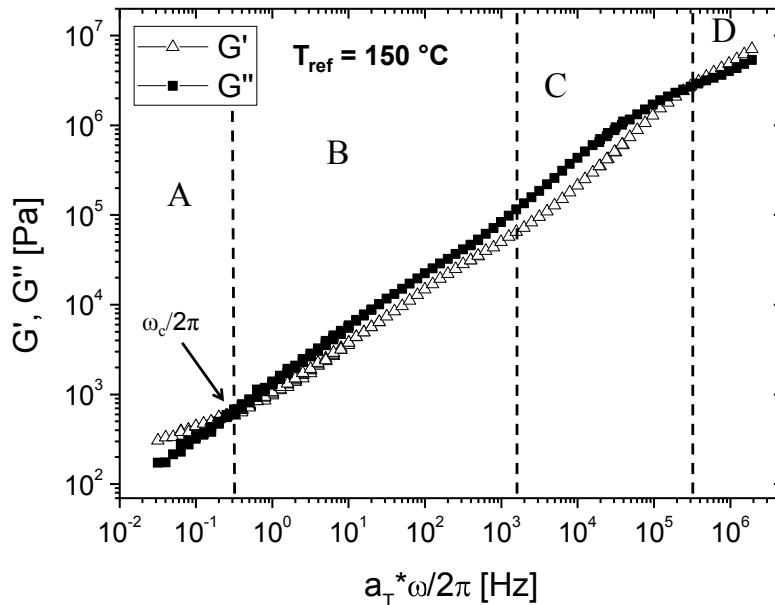
Fig. 49 Master curve of PS-b-PI-13k-13k at T_{ref} = 150 °C. The diblock copolymer shows no distinct rubber plateau which indicates that the polymer chains are not entangled.

As already mentioned in section **2.3.3** there have been two approaches to define different region in which LAOS favors either the macroscopic parallel or the perpendicular orientation[82]. These regimes were deduced from the linear viscoelastic frequency depends of the symmetric diblock copolymer melts. In the group of J. A. Kornfield[160] the critical frequency $\omega_c/2\pi$ below which the ordered structure dominates the viscoelastic behavior of the material was chosen, to distinguish between a region with preferentially parallel ($\omega_1/2\pi < \omega_c/2\pi$) respectively perpendicular orientation ($\omega_1/2\pi > \omega_c/2\pi$).

The critical frequency is determined as the junction points of the low frequency parts of the master curves of G' and G'' measured above and below the T_{ODT}. For this reason, actually two critical frequency can be obtained, one for the interception of the G' data (ω_c') and one from the interception of the G'' data (ω_c''). In **Fig. 50** the master curve for G'' is shown for temperatures above and below T_{ODT}. For G' the problem arises that the measured curves could not be superimposed because the measured data showed strong fluctuations above T_{ODT}.
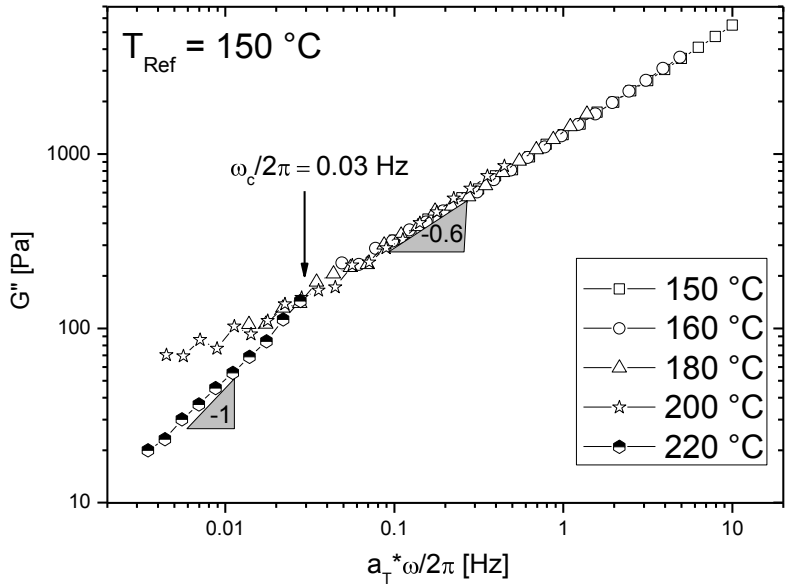
Fig. 50 The loss modulus G" versus reduced frequency at a reference temperature T$_{ref}$ = 150 °C for PS-b-PI-13k-13k. The data for G" at T = 220 °C represent the disordered melt behavior. The junction point between both curves is referred to the critical frequency $\omega''_c/2\pi$ = 0.03 Hz.

Nevertheless, Zahng et al.[82] reported differences of a factor four between ω_c' and ω_c''. Several different methods were suggested to derive the critical frequency[82]. One of them utilizes the deviation in the temperature dependence of the master curve of the absolute value of the complex viscosity $|\eta^*|$. With this method two critical frequencies in the low frequency region (ω_c) and in the high frequency region ($\omega_{d)}$ can be determined. **Fig. 51** shows the experimental determined master curve of $|\eta^*|$ as a function of the reduced frequency for PS-b-PI-13k-13k. From these findings the measurement frequencies were selected to assure shear-induced macroscopic perpendicular alignment during the LAOS experiments described in the following.
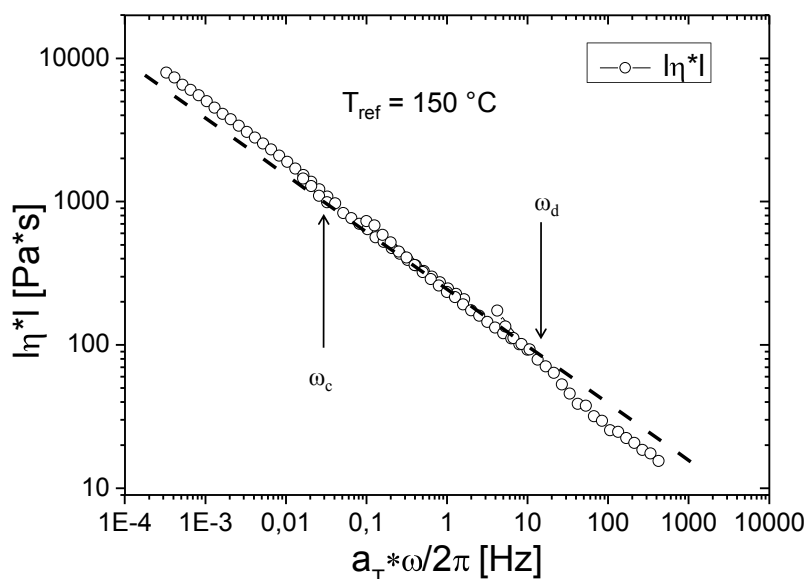
Fig. 51 Frequency dependence of Iη*I for PS-b-PI-13k-13k at T_{ref} = 150 °C. By a rough approximation two critical frequencies can be determined: $\omega_c/2\pi \approx 0.03$ Hz and $\omega_d/2\pi \approx 15$ Hz.

4.3. Strain dependent alignment kinetic

4.3.1. In-Situ Rheo-SAXS investigations

a) In-situ SAXS investigation

In this section the influence of strain amplitude is studied towards the kinetic pathway of the macroscopic perpendicular alignment. The measurement frequency and temperature were fixed to $\omega_1/2\pi$ = 1 Hz and T = 150 °C. The studies were conducted to in-situ Rheo-SAXS studies with additional ex-situ rheological and 2D-SAXS analysis. These techniques revealed a full characterization of the orientation distribution of the locally anisotropic ordered lamellae domains (grains) and helped to quantify the non-linear mechanical response caused by the shear-induced structural changes.

Different alignment kinetics were obtained depending on the applied strain amplitudes and duration of shear following a scaling law. Furthermore, an anomalous de-ordering of well aligned macroscopic perpendicular orientation was detected and characterized for strain amplitudes γ_0 > 1 being solely a function of the shear duration.

In-situ synchrotron X-ray investigations were performed to clarify the time dependent orientation evolution at varying strain amplitudes γ_0 for the macroscopic alignment process of the lamella microstructure using a 10 s time resolution for each

2D-SAXS frame. The schematic measurement setup is shown in **Fig. 52**. Additionally, SAXS images of the orientation distribution of the diblock copolymer microstructures in the melt state were recorded for the initial respectively final states.
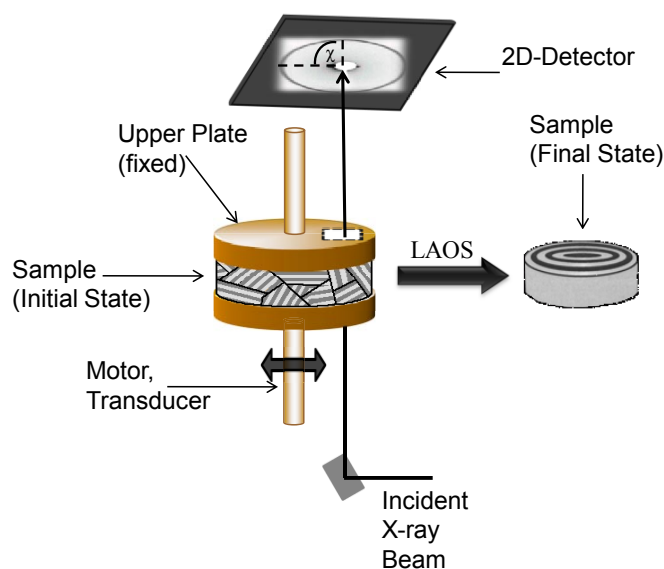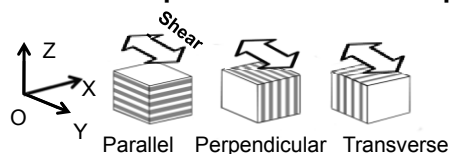
Fig. 52. Schematic representation of the Rheo-SAXS setup used in this work where a Pilatus 100k was used as a 2D-Detector.The Cartesian coordinate OXYZ is defined for a cubic sample volume similar to sliding plat geometries such that the vertically reflected X-ray beam is parallel to the OZ axis. Oscillatory shear is applied by the lower sample plate which is where the transducer is located. The upper sample plate remains fixed during the experiments.

The mechanical excitation frequency was fixed at 1 Hz for all measurements, meaning that every 2D-SAXS image averaged only 10 mechanical oscillation. According to the sample loading procedure described in the Experimental Methods (see section **3.5.2**), the following isothermal (T = 150 °C) strain amplitudes of γ_0 = 0.5, γ_0 = 1, γ_0 = 2 and γ_0 = 3 were analyzed at a constant mechanical excitation frequency of 1 Hz.

The applied experimental conditions are summarized in **Fig. 53** together with representative 2D-SAXS patterns for undeformed PS-*b*-PI and for the final state of orientation after LAOS experiments are shown (see **Fig. 53**). The initial, unaligned state shows ringlike images, which are typical for multidomain macroscopically

isotropic morphologies. However, after 1 hour of LAOS, the appearance of anisotropic SAXS patterns with pronounced reflections at 90° and 270° indicated a macroscopic perpendicular alignment of the lamellae. The azimuthally averaged SAXS patterns are displayed beneath each 2D-image where these images show a slight anisotropy in the scattering pattern even for the undeformed samples. These small amounts of pre-orientation are due to slight squeeze flow alignments, which could not be avoided even by restricting the normal force to values below 0.05 N (~ 50 Pa) and adjusting the measurement gap. As this pre-orientation is very weak compared to the strong reflections caused by the mechanical excitation, it was assumed that the effect of these pre-alignments did not dominate the experimental results of the shear orientation kinetic.
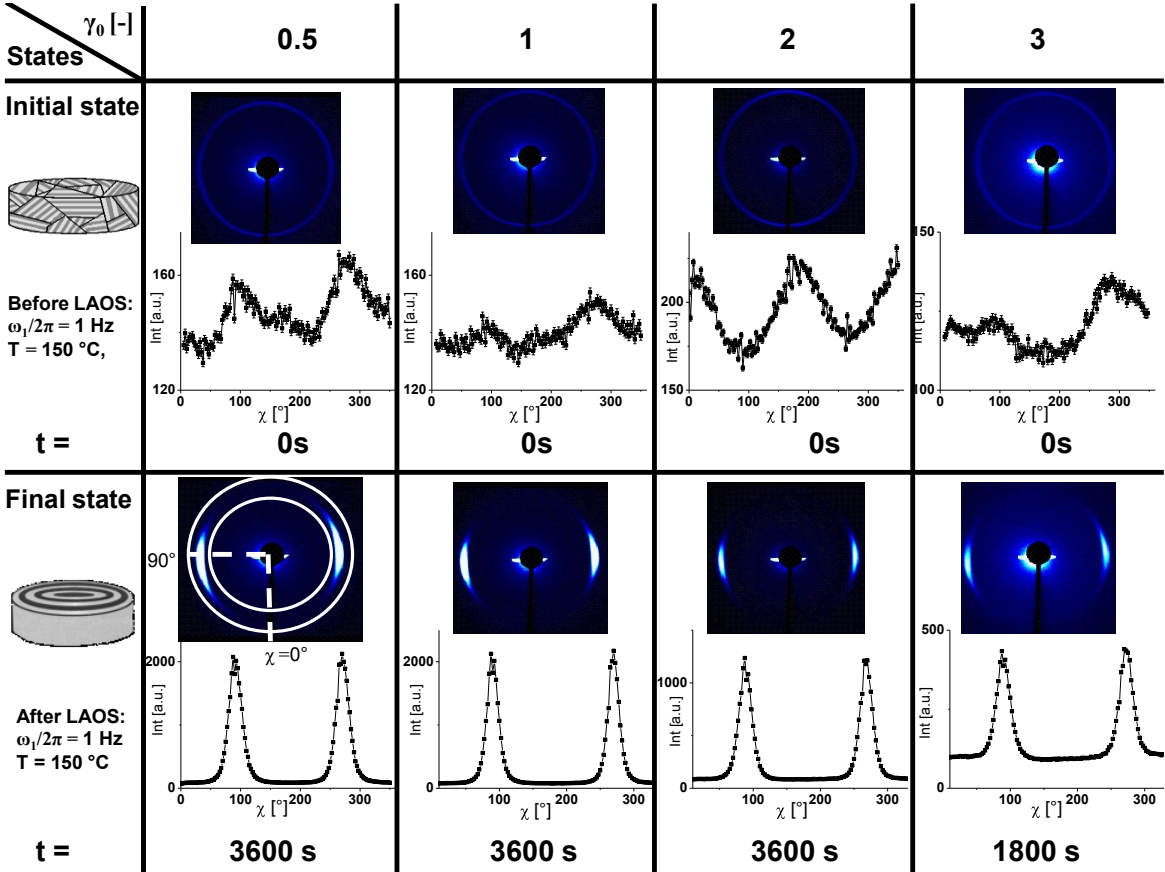
Fig. 53 Summary of the applied experimental conditions, including 2D-SAXS images and azimuthally averaged 1D-plots representing the orientation of the sample before and after shear was imposed. The peak width of the azimuthally averaged reflections at 90° and 270° were taken to monitor the alignment process during LAOS.

A representative contour plot (γ_0 = 0.5) of all 354 azimuthally averaged 2D-SAXS patterns recorded during the macroscopic orientation ($t_{experiment}$ = 3600 s) of the PS-*b*-

PI is shown in **Fig. 54**. From this representation of the data, the development of scattered reflections in an interval corresponding to a minimum scattered wave vector of $|\vec{q}|$ = 0.25 nm^{-1} and an upper boundary of $|\vec{q}|$ = 0.35 nm^{-1} is clearly seen. It is interesting to note that during the entire mechanical excitation only the scattered reflections at 90° and 270° appeared, which indicate the development of a macroscopic perpendicular orientation with the unit normal of the lamellae preferentially orientated along the OX axis. In addition, there were no detectable scattered reflections at 180° and 360° corresponding to the transverse direction.
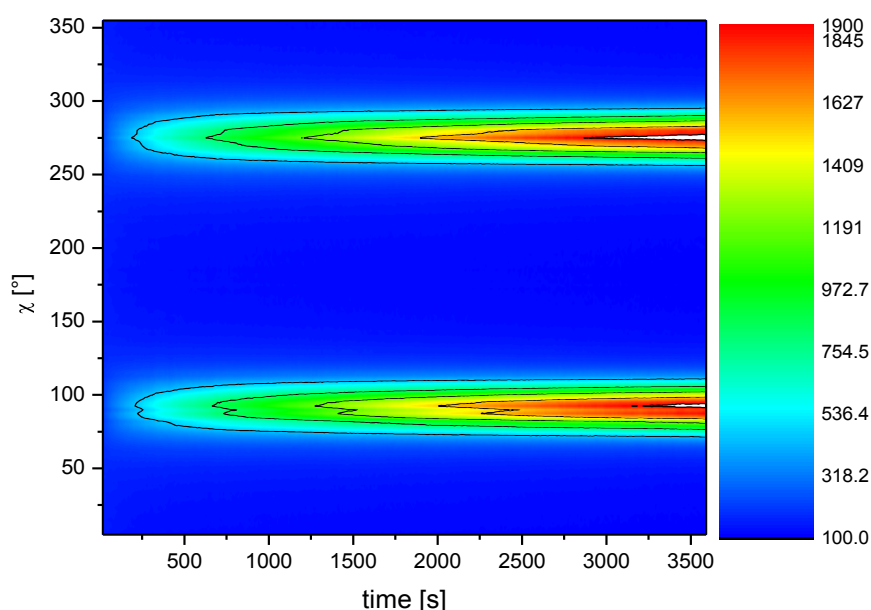
Fig. 54 Contour plot of the azimuthally averaged 2D-SAXS patterns recorded during the macroscopic orientation of PS-b-PI under large amplitude oscillatory shear (LAOS: $\omega_1/2\pi$ = 1 Hz, γ_0 = 0.5, T = 150 °C).

These results were the first obtained for block copolymer melts using our newly developed prototype Rheo-SAXS combination located at the storage ring DORIS III. At this stage of development, it was not possible to precisely determine the primary beam intensity throughout the experiment. However, selective measurements of the primary beam intensity were performed before and after each dynamic shear experiment. These measurements do not, reveal primary beam intensity fluctuations, which may also occur during the in-situ experiments, e.g. due to fluctuations in the beam-orbit.

Therefore, at this stage, the evolution of the azimuthally averaged peak width was taken as a measure for the kinetics of the alignment process. As it showed a stronger variation (by a factor of 3) between its initial and final values during the macroscopic

alignment process, the χ-dependence of the peak width was chosen for study instead of the radial averaged (θ-dependence) peak width.

By fitting the scattering reflections centered around 90° in the 2D-SAXS images for all measurement times with a Gaussian function, the standard deviation σ_{SAXS} was calculated and used to quantify the shear induced changes for the orientation distribution of the lamellae with unit normal parallel to the (*OX*, *OY*) plane.

For all four strain amplitudes used in this study, a drastic decrease in the peak width occurred in the first 100 to 250 seconds of the experiment (see **Fig. 55**). The starting values for the standard deviation vary between σ_{SAXS} = 19° for the two lowest strain amplitudes (γ_0 = 0.5 and γ_0 = 1), σ_{SAXS} = 15° for γ_0 = 2 and σ_{SAXS} = 12° for γ_0 = 3. For γ_0 = 0.5 and γ_0 = 1, the orientation process occurred throughout the whole mechanical excitation, but reached a plateau after 2000 s and 1300 s, respectively. There was only a slight deviation from the plateau value of σ_{SAXS} = 10.5° to σ_{SAXS} = 10.7° for γ_0 = 1 after 2000 s, while for γ_0 = 0.5, there was no observable deviation from the plateau value with time. The appearance of a plateau indicated that a stable macroscopic orientation was formed despite the continuing dynamic mechanical excitation.
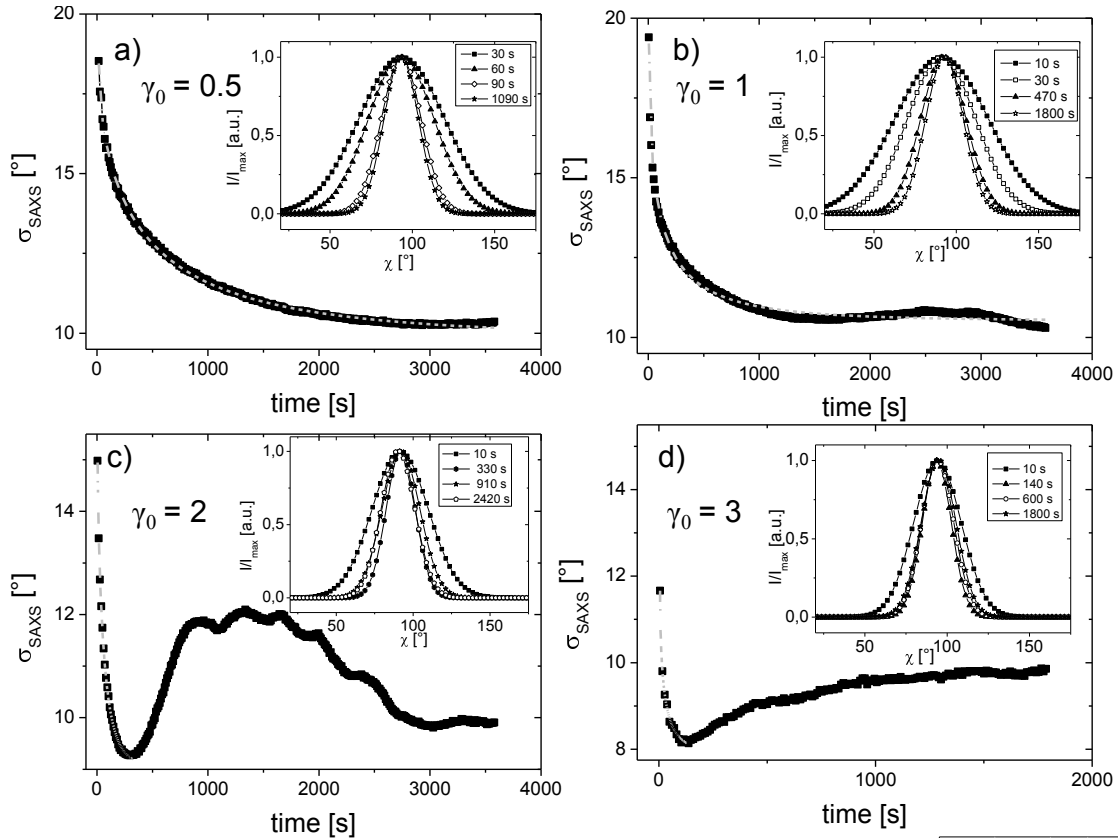
Fig. 55 Time dependence of the standard deviation σ_{SAXS} calculated by fitting the scattered reflections at 90° (2D-SAXS images) with a Gaussian function. The dotted lines represent the stretched exponential fit (see text). The insets represent the azimuthally averaged first order scattered reflections at characteristic times during the mechanical excitation. a) γ_0 = 0.5, b) γ_0 = 1, c) γ_0 = 2, d) γ_0 = 3.

The two higher strain amplitudes (γ_0 = 2 and γ_0 = 3) exhibited similar behavior in the beginning of the experiment, i.e. showed a rapid decrease in σ_{SAXS}, but, instead of reaching a plateau, formed a minimum after t = 240 s (γ_0 = 2) and t = 100 s (γ_0 = 3). This behavior was in stark contrast to the LAOS experiments at lower strain amplitudes (γ_0 ≤ 1) and indicated that this state of macroscopic orientation was not stable under continuing mechanical stimulus. For both of these strain amplitudes (γ_0 ≥ 1), the peak width began to increase from its minimum value of σ_{SAXS} = 9° (γ_0 = 2) and σ_{SAXS} = 8.2° (γ_0 = 3) at t = 350 s and t = 150 s, respectively. The insets in **Fig. 55** display the broadening of the scattering reflections, after reaching the minimum, at characteristic time intervals. For a strain amplitude of γ_0 = 3, σ_{SAXS} developed exponentially towards a stable value of σ_{SAXS} = 9.8° approximately 1000 s after passing through the minimum, while for γ_0 = 2, an overshoot was detected instead.

The de-orientation process for γ_0 = 2 began with a rapid increase in σ_{SAXS} in the first 300 s after the minimum was reached, followed by a pseudo plateau with σ_{SAXS} ≈ 12°. This state of reduced orientation was not stable and the block copolymer

lamellae began to re-orientate after 1700 s as the LAOS experiment continued. As a consequence, σ_{SAXS} decreased over the observed experimental time until a final value of $\sigma_{SAXS} \approx 10°$ was reached.

These first results obtained from the in-situ Rheo-SAXS measurements indicate that, for higher strain amplitudes ($\gamma_0 > 1$), the quality of the macroscopic orientation is a complex process, the state and degree of orientation is strongly affected by the duration of the applied mechanical field.

b) In-situ mechanical quantities (G', G")

As the goal of this study was to compare structural dynamics caused by the applied mechanical excitation with the viscoelastic response of the polymer melt, the mechanical response of the block copolymer melt was analyzed in terms of the mechanical loss modulus G" and a quantitative measure of the mechanical non-linearities via the parameter $I_{3/1}$. This non-linear parameter could only be determined accurately ex-situ, utilizing a special experimental setup[31] that included a strain controlled rheometer for the evaluation of the stress-strain raw data (see section **3.2.2**). For all rheological measurements, a data point was collected every 10 s to ensure a similar time resolution to the 2D-SAXS data.

Fig. 56 and **Fig. 57** present the data from the in-situ rheological measurements under LAOS conditions. **Fig. 56** displays the time behavior of the mechanical storage modulus G' and loss modulus G" for $\gamma_0 = 0.5$ at T = 150 °C and $\omega_1/2\pi = 1$. At the chosen experimental conditions, the in-situ measured mechanical viscoelastic behavior in the non-linear regime was dominated by the viscous (G") rather than the elastic (G') modulus ($\tan\delta$ = 3 - 4). This ratio increased at the end of the LAOS experiment where approximately $\tan\delta$ = 7. Due to the dominance of the mechanical loss modulus, G'(t) was chosen to monitor the macroscopic orientation process.
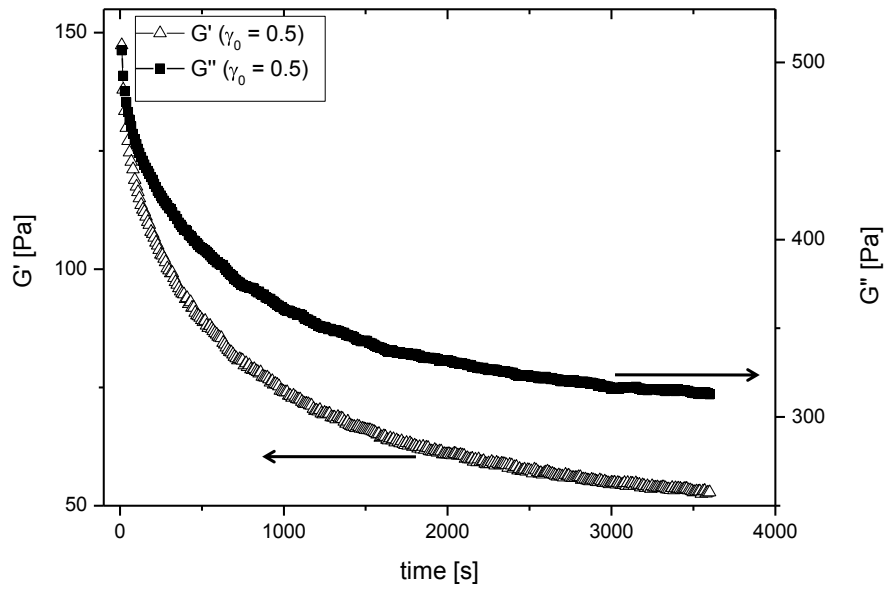
Fig. 56 Time dependence of the mechanical viscoelastic properties G' (open triangle) and G" (squares) under LAOS ($\omega_1/2\pi$ = 1Hz, γ_0 = 0.5, T = 150 °C). As the loss modulus G" dominates the mechanical response under the applied conditions, it was chosen to online monitor the alignment process.

Fig. 57a-d shows the in-situ measured mechanical loss modulus G" for all applied strain amplitudes. It can be seen that G" shifted to lower values with increasing strain amplitude, indicating that shear thinning occurred as the macroscopic orientation developed. All measurements exhibited a stretched exponential time dependence, leading to a plateau after 3000 s (γ_0 = 0.5), 1000 s (γ_0 = 1), 400 s (γ_0 = 2) and 250 s (γ_0 = 3). The plateau value for G" was strain dependent and varied between 320 Pa and 128 Pa for γ_0 = 0.5 and γ_0 = 3, respectively.
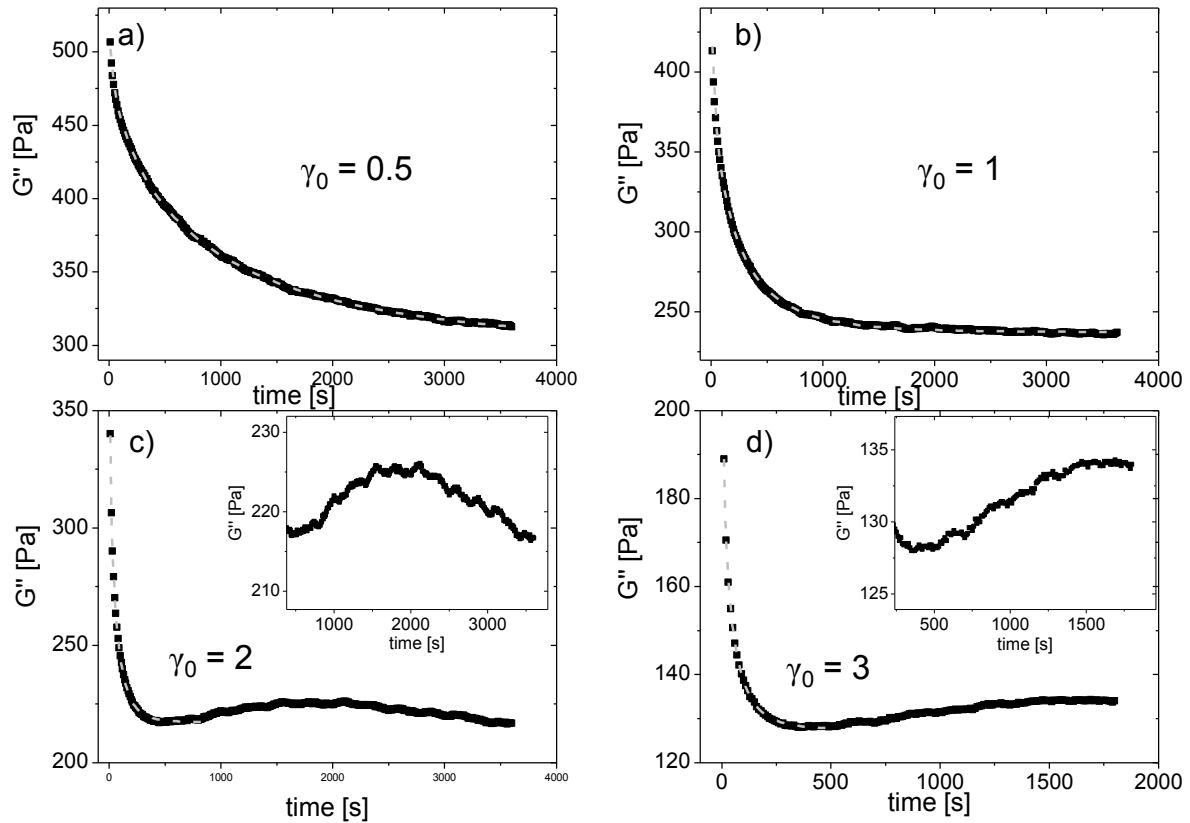
*Fig. 57 Time dependence of the in-situ measured mechanical loss modulus G″ at a) γ_0 = 05, b) γ_0 = 1, c) γ_0 = 2 and d) γ_0 = 3, with fitted stretched exponential functions (dotted lines). Insets represent the enlargement of the pseudo plateau region. The loss modulus G″ shows an astonishing similarity to the in-situ detected macroscopic orientation (see **Fig. 55**).*

From the insets in **Fig. 57c** and **Fig. 57d** it can be seen that, for the two highest strain amplitudes, the in-situ measured G″ values were not constant after the plateau was reached, but showed an increase after 600 s for γ_0 = 2 and after 500 s for γ_0 = 3. Interestingly, for all applied strain amplitudes, the time dependence of G″ was quite similar to the time progression of σ_{SAXS}, as measured by in-situ 2D-SAXS. This is especially interesting since G″ is a macroscopic linear mechanical parameter and σ_{SAXS} a much more local orientation parameter. While the two lowest strain amplitudes exhibited the same general trends for G″ as for σ_{SAXS}, the time elapsed until the plateau value was reached was significantly longer for the in-situ mechanical response G″.

For γ_0 = 2 and γ_0 = 3, G″ showed the same deviation from a stretched exponentially decreasing curve as seen in the in-situ 2D-SAXS experiments. This effect was only visible in the time progression of the G″ data, while the G′ data, which are not shown here, obeyed a simple stretched exponential decay. For a strain amplitude of γ_0 = 2, G″ increased from its plateau value of 214 Pa to 225 Pa. This

98

value then stayed nearly constant over a period of 600 s after which it decreased again to its final value of 218 Pa. However, the highest strain amplitude (γ_0 = 3) caused an increase in G" from 128 Pa to its final value of 134 Pa over a time period of 1000 s. From this data, it was clear that the major difference between the time dependence of the dynamic mechanical loss modulus and the time dependence of the structural changes as quantified by σ_{SAXS} could be mainly attributed to differences in the observed time scale. For example, the in-situ determined peak width increased after 200 s for γ_0 = 2 and after 350 s for γ_0 = 3, which is around a factor 2 faster than the increase observed in the in-situ mechanical measurements. Except for this time shift, the G" curves showed astonishing similarities to the development of the macroscopic structure as followed by 2D-SAXS. It can also be seen that a de-orientation of the orientated microstructure caused the mechanical loss modulus to increase slightly (~ 4%) during LAOS.

The linear dynamic mechanical response measured for both the un-deformed macroscopically isotropic and for the perpendicularly aligned block copolymer melt (γ_0 = 0.5) at 150 °C using a small dynamic strain amplitude of 0.02 is shown in the inset of **Fig. 58**, where the storage and loss modulii are plotted as a function of frequency.
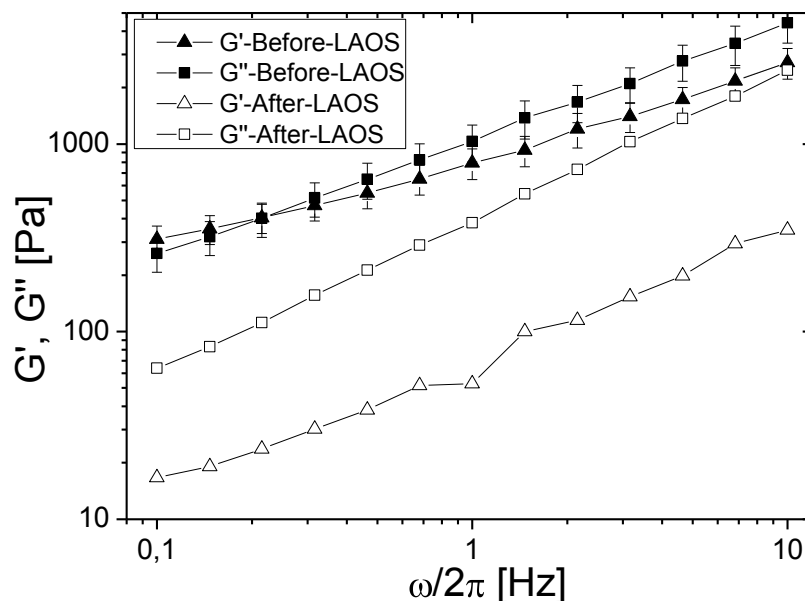
Fig. 58 Linear dynamic mechanical response at 150 °C obtained for a strain amplitude of 0.02 before (filled symbols) and after (open symbols) LAOS. After the macroscopic orientation the crossover point between G' and G" disappeared.

The data for the LAOS experiments at higher strain amplitudes were not included here as they showed similar behavior and, thus, did not seem to depend on the applied strain amplitude. For the small amplitude oscillatory shear (SAOS) experiment, a clear crossover point (tanδ = 1) at $\omega/2\pi$ = 0.2 Hz was visible for the randomly orientated sample. This crossover indicated that a transition between the mechanical response being dominated by the microstructure and the so called transition zone II occurred, which is similar to the flow behavior of linear homopolymer melts[82].

The slopes of both G' and G'' in the low frequency region of the un-deformed sample were approximately equal to 0.5. This value is typical for lamellar self-assembled block copolymers[86, 161, 164]. For the oriented sample, the slope of G'' increased to about 0.8 and the crossover point did not appear within the investigated frequency region. Furthermore, the values for the storage and loss modulii in the low frequency region were reduced by a factor of 10 (G') and 3 (G''). This reduction in the modulii for the orientated samples was verified for all achieved perpendicular alignments and was consistent with the results published in ref.[160].

From a mechanical point of view, it can be said that the shear induced transformation of a diblock copolymer melt with initially randomly orientated lamellar microdomains into an anisotropically perpendicular aligned melt led to a reduction of the linear dynamic mechanical modulii (G' and G'') with respect to the un-orientated macroscopic isotropic sample.

4.3.2. Online FT-Rheology investigations

The rheological and 2D-SAXS measurements were performed to confirm the in-situ measurements and to obtain detailed information about the macroscopic orientation of the self-assembled microdomains along the three spatial directions (*OX*, *OY* and *OZ*). Furthermore, the development of the macroscopic structure is correlated to the non-linear mechanical response. Therefore, a strain controlled rheometer was used to calculate the relative intensities of the higher harmonics $I_{n/1}$ from the raw stress data via FT-Rheology[31, 70].

a) G'' determined with the strain controlled ARES rheometer

The observed time evolutions of the mechanical loss modulus G'' during LAOS are represented for γ_0 = 0.5, 1, 2 and 3 in **Fig. 59**.
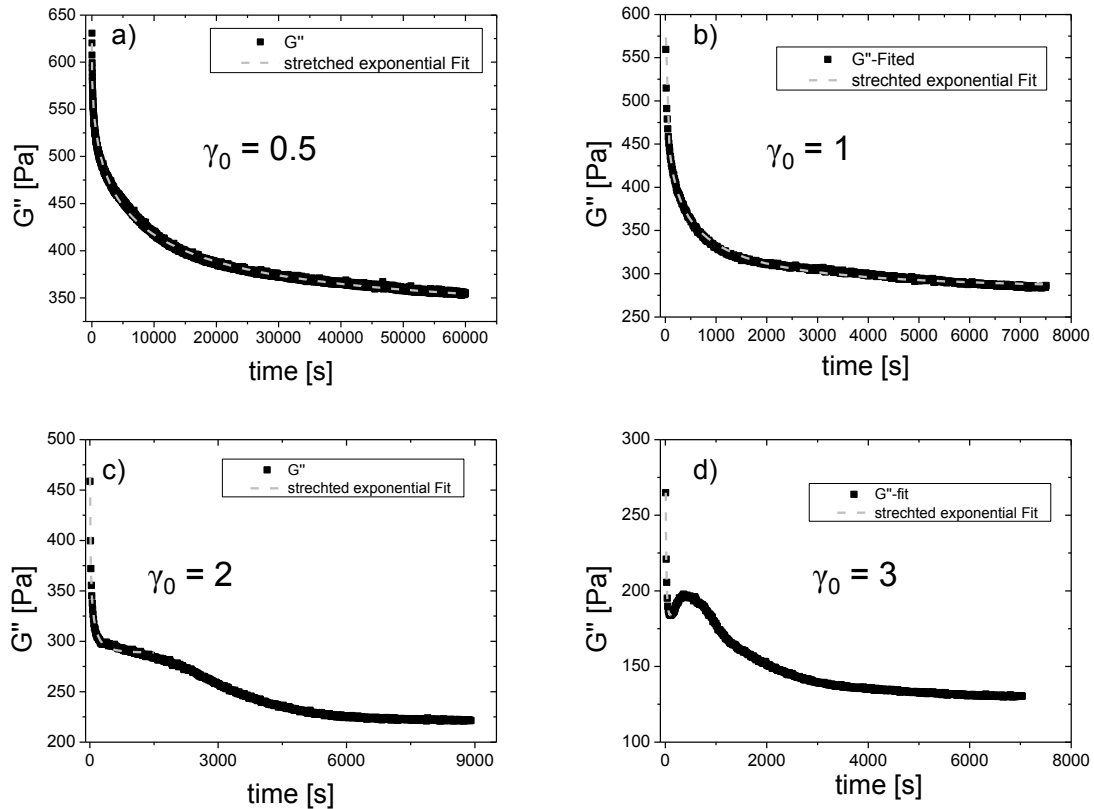
Fig. 59 Time dependence of the dynamic mechanical loss modulus G'' under LAOS measured with the strain controlled ARES rheometer for a) γ_0 = 0.5 (inset), b) γ_0 = 1, c) γ_0 = 2 and d) γ_0 =3. Dotted lines represent the stretched exponential Fit.

For the LAOS experiments with γ_0 = 0.5 and γ_0 = 1, G'' decreased monotonically. The former exhibited a rapid decrease in the first 500 s from its initial value of approximately 630 Pa to 500 Pa, followed by a less rapid decay persisting throughout the whole shear experiment, while for γ_0 = 1, a nearly constant value of 300 Pa was reached after 2500 s. With increasing strain amplitude, the time scale of the rapid drop at the start of the LAOS experiments was accelerated.

Moreover, for the two highest strain amplitudes (γ_0 = 2 and γ_0 = 3), the time evolution of G'' showed a more complex behavior that deviated from a stretched exponential decay. After a steep decrease of about 180 Pa and 120 Pa in the first 250 s and 100 s of the experiment for γ_0 = 2 and γ_0 = 3, respectively, a preliminary minimum was reached. For γ_0 = 2, this pseudo stable state stayed constant until a

less pronounced decrease from 280 Pa to 225 Pa was observed after 1800 s. Similar behavior was also seen for $\gamma_0 = 3$, with the difference that after the initial rapid drop, an overshoot between 150 s and 350 s then occurred. During this overshoot, G" increased by approximately 50 Pa in 200 s. This elevated value stayed constant for 200 s, after which it decreased over a time interval of approximately 4000 s.

By comparing the time progression of G" obtained from the stress controlled (see **Fig. 57**) and the strain controlled rheometer (see **Fig. 59**) it was clearly seen that, for the higher applied strain amplitudes $\gamma_0 > 1$, the G"(t) values have different trends in their time progression during LAOS. One of the major differences between the data sets is the fact that G" was increasing (stress controlled) and not decreasing (strain controlled) in addition to the observed overshoot for $\gamma_0 = 3$ (strain controlled). This could not be explained reasonable within our experiments. Therefore, for the further discussion of the non-linear mechanical response the non-linear parameter $I_{3/1}$ is used.

b) Non-linear response investigated by FT-Rheology

Shear-induced macroscopic alignment of the lamella self-assembled block copolymer microstructure was achieved by large amplitude oscillatory shear (LAOS). Consequently, the measured mechanical response to large deformations fell within the non-linear regime and consisted of the odd higher harmonics of the applied mechanical excitation frequency ω_1 ($\omega_1/2\pi$ = 1 Hz). By examining the mechanical raw data using the ideas developed in FT-Rheology[31, 165, 166], it was possible to analyze the resulting signal with respect to both the phase and to the higher harmonics that built up the signal.

Fig. 60 represents two calculated FT-spectra for $\gamma_0 = 3$ (T = 150 °C, $\omega_1/2\pi$ = 1 Hz) at the beginning (t = 60s, **Fig. 60a**) and the end (t = 4800 s, **Fig. 60b**) of the LAOS experiment. The frequency range of the spectra is limited to 10 Hz, as for higher frequencies no significant higher harmonics were detected.
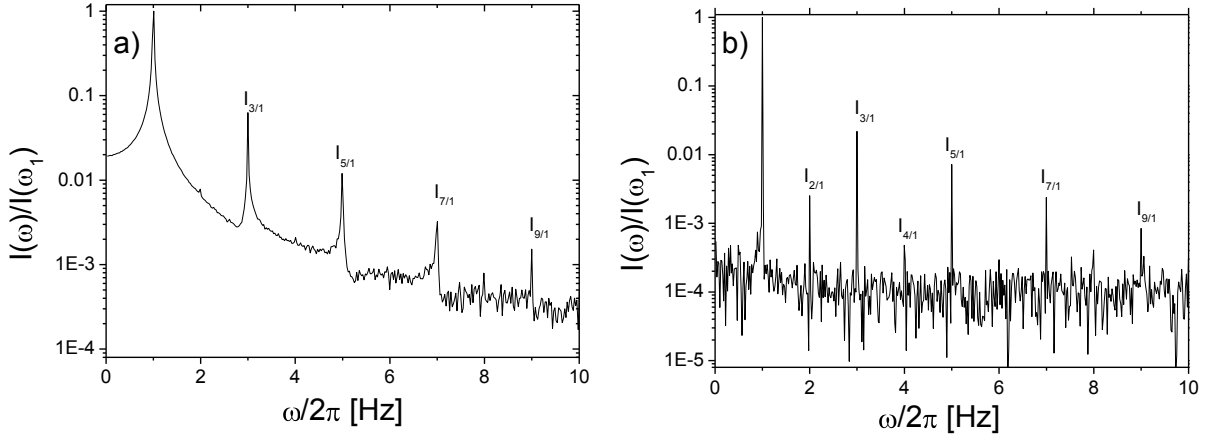
Fig. 60 FT-spectrum of the time dependent torque calculated from the mechanical raw data after 60 s (a) and 4800 s (b) for PS-b-PI-13k-13k ($\omega_1/2\pi$ = 1 Hz, γ_0 = 3 and T = 150 °C). All peaks are normalized to the fundamental peak at $\omega_1/2\pi$ = 1 Hz.

The time dependence of the magnitudes of the relative intensities of the higher harmonics $I_{n/1}$ (1 < n < 10) for the LAOS experiment with strain amplitude γ_0 = 3 is shown in **Fig. 61**.

For the odd higher harmonics it can be seen that the magnitude of $I_{n/1}$ decreases drastically in the row $I_{3/1} > I_{5/1} > I_{7/1} > I_{9/1}$. As the intensities of $I_{7/1}$ and $I_{9/1}$ are less than 1% it is questionable to use these quantities for the discussion of the mechanical non-linear response during the orientation process.

Nevertheless, for all relative intensities of the odd higher harmonics a decrease in the first 250 s is observed followed by a nearly constant value of $I_{n/1}$. After approximately 1400 s the value begins to increase again leading into a plateau after approximately 3000 s.

The time progression of the non-linear response showed similarities to the time progression of the azimuthally averaged peak width $\sigma_{SAXS}(t)$ of the first order reflection detected by the in-situ SAXS measurements for γ_0 = 3, such as the increase from the reached minimum value as LAOS proceeded (compare **Fig. 55d**). This indicates a relation between the structural development and the non-linear mechanical response during LAOS.

103
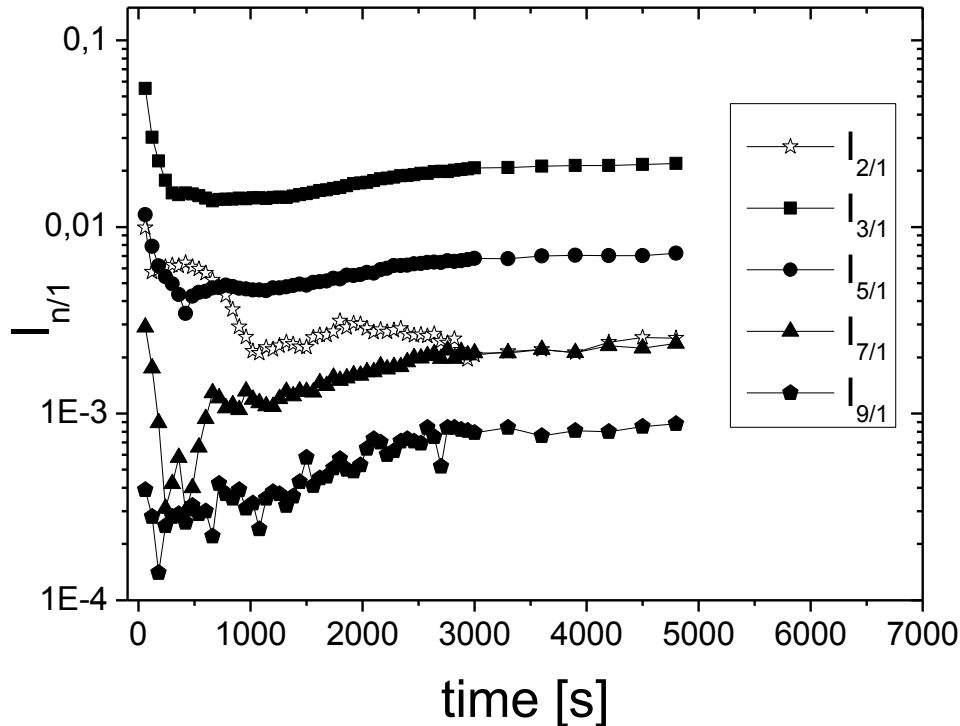
Fig. 61 Time dependence of the relative intensities of the detectable higher harmonics $I_{n/1}$ for PS-b-PI-14k-14k under LAOS ($\omega/2\pi$ = 1 Hz, γ_0 = 3, T = 150 °C)

As discussed in section **2.2.2** even harmonics are not expected for an ideal mechanical response to LAOS. However, even harmonics can be reproducible observed in the calculated FT-spectra[104]. Different approaches have been suggested to explain their appearance. Wall slip has been expected to be one of the main reasons for the appearance of even higher harmonics[167]. Wilhelm et al.[32] suggested a time dependent memory effect or a non-linear mechanical contribution in the sample. In contrast, Sagis et al.[72] proposed an approach which relates the appearance of even higher harmonics with anisotropic microstructures incorporated in the sample such as ridged particles in an elastic matrix. It is important to notice, that the appearance of even higher harmonics is still a topic of scientific interests and far away of being fully understood.

However, during the herein investigated alignment process even higher harmonics appeared (see **Fig. 60**). The time evolution of the second higher harmonic $I_{2/1}$ (open stars) for γ_0 = 3 is shown in **Fig. 61**. In contrast to the time dependence of the odd higher harmonics discussed above a pronounced overshoot in the first 1000 s of the experiment is detected for $I_{2/1}$, which leads into a nearly constant plateau with $I_{2/1}$ being approximately 0.002. However, the value for $I_{2/1}$ was very small

104

throughout all LAOS experiments performed in this thesis. Therefore, a detailed examination of the underlying effect of the appearance of even higher harmonics was neglected.

Before the time evolution of the phase difference of Φ_3 is discussed it has to be mentioned that according to literature[168, 169], phase differences of $\Phi_3 = 0°$ respectively $\Phi_3 = 360°$ indicate shear hardening while phase differences $\Phi_3 \approx 180°$ indicate shear thinning behavior. The contributions from the higher harmonics are neglected in this discussion as they dependent on the magnitude of the relative intensities of the higher harmonics which are orders of magnitudes less than the one for $I_{3/1}$ (see **Fig. 61**). Therefore, the phase difference of Φ_3 is expected to dominate the stress response.

From **Fig. 62** it can be seen that in the beginning of the experiment Φ_3 is approaching close to the values which correspond to shear thickening behavior after approximately 250 s. This time corresponds to the time at which $I_{3/1}$ reaches the minimum. After Φ_3 reached a maximum value of approximately 350° a rapid drop occurred within 100 s which leads into a plateau value of approximately 150°. Except the stark overshoot the shear-induced orientation of the PS-b-PI-13k-13k diblock copolymer showed shear thinning behavior.
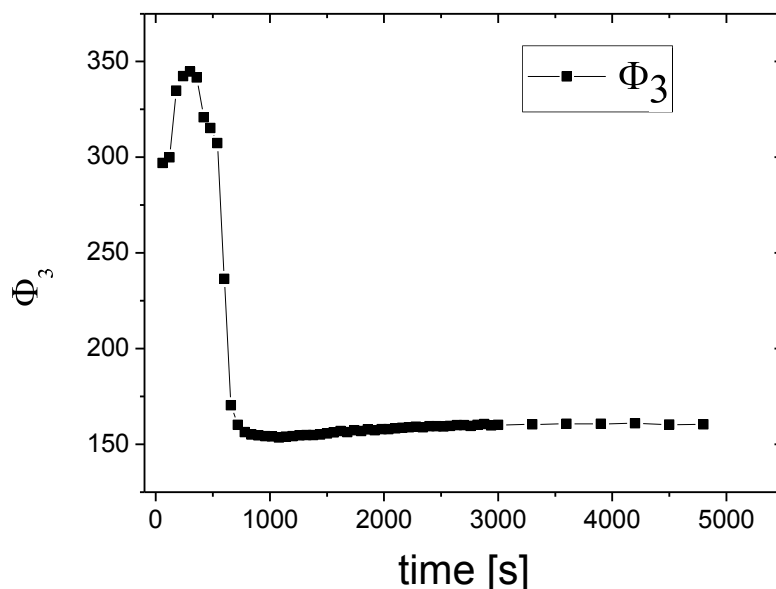
Fig. 62 Time dependence of the phase difference Φ_3. For $\Phi_3 = 0°$ respectively $\Phi_3 = 360°$ shear thickening is expected while for $0° < \Phi_3 < 360°$ shear thinning occurs.

c) *Investigation of the alignment kinetics utilizing the non-linear parameter $I_{3/1}$*

As the relative intensity of the third harmonic $I_{3/1}$ was the dominant signal in the calculated FT-Spectra (see **Fig. 61**), the time evolution of the intensity of $I_{3/1}(t)$ was used to follow the non-linear response and guide the ex-situ SAXS measurements. Previous investigations of $I_{3/1}(t)$[70, 116, 170], with respect to the mechanical excitation of block copolymers[159, 168], have shown that it is reasonable to utilize this quantity for monitoring and assessing the macroscopic orientation process.

Fig. 63 shows the time dependence of the relative intensities of the non-linear parameter $I_{3/1}(t)$ for strain amplitudes between $\gamma_0 = 0.5$ and $\gamma_0 = 3$. For all strain amplitudes, the non-linear parameter showed first a rapid stretched exponential decay in the beginning of the experiment where the magnitude and the decay constant increased with γ_0. At the two lowest strain amplitudes ($\gamma_0 = 0.5$, $\gamma_0 = 1$), G'' (compare **Fig. 59**) and $I_{3/1}$ exhibit similar behavior in that there was a rapid decrease of G'' and $I_{3/1}$ in the first 1000 s followed by a slower decay, which finally leveled off into a plateau value of $I_{3/1} = 0.02$ and $I_{3/1} = 0.16$ and G'' = 350 Pa and G'' = 300 Pa respectively.

For the two largest strain amplitudes ($\gamma_0 = 2$ and $\gamma_0 = 3$), the time dependence of $I_{3/1}$ differed from the stretched exponential trend, which is expressed by significant increase from the reached plateau value (see insets in **Fig. 63**). However, for $\gamma_0 = 2$ the increase of $I_{3/1}$ began after 1900 s and proceeded over 2900 s until it reached a final stable value of $I_{3/1} \approx 0.028$ at t = 4800 s. For the highest strain amplitude $\gamma_0 = 3$ the time elapsed until $I_{3/1}$ deviated from the minimum was approximately 900 s. After $I_{3/1}$ increased over 1300 s it led into a stable plateau at t = 2200 s for $I_{3/1} \approx 0.028$.
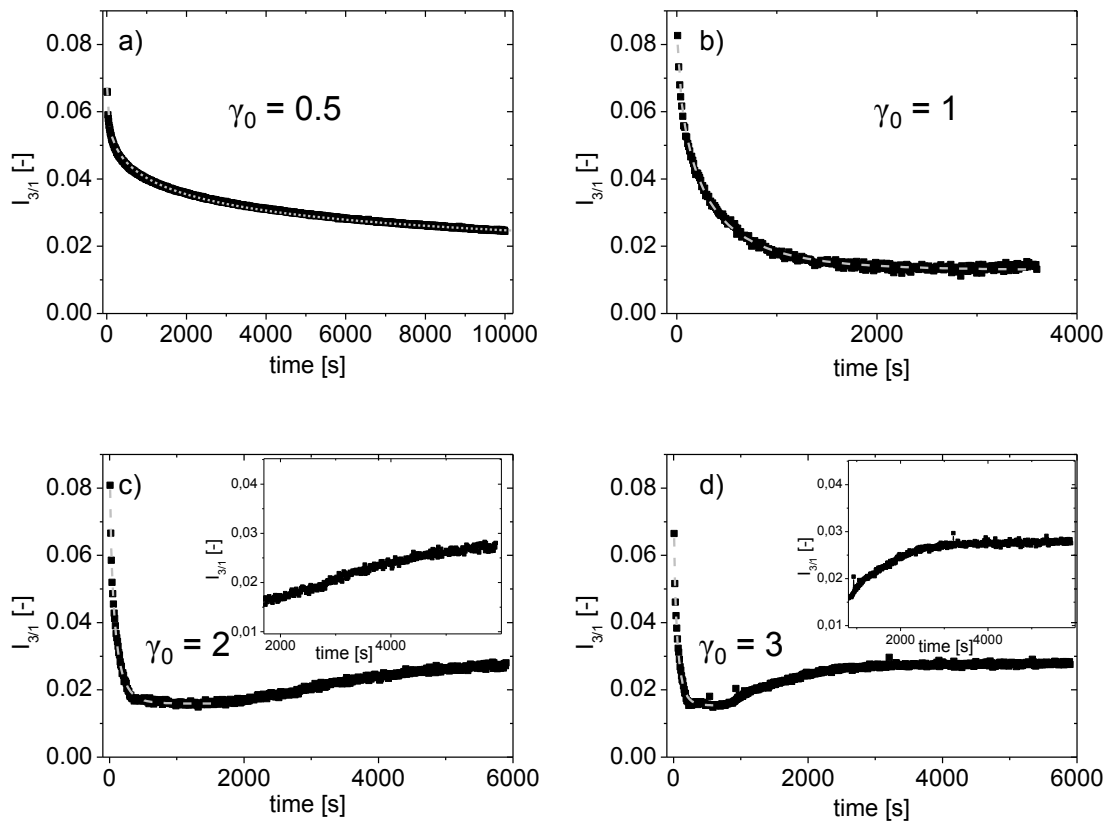
Fig. 63 Time dependence of the relative intensities of the non-linear parameter $I_{3/1}$ measured for a) γ_0 = 0.5, b) γ_0 = 1, c) γ_0 = 2 and d) γ_0 = 3. The dotted lines represent the stretched exponential fit (see text). Insets display an enlargement of the region were the de-ordering of the perpendicular alignment occurs as detected by the mechanical response.

It can be seen that the critical time t_c of shear duration at which the non-linear parameter begins to increase dependence strongly on the applied strain amplitude. To illustrate this phenomenon the time dependence of the two elevated strain amplitudes is shown in one plot (see **Fig. 64**). Interestingly, for both strain amplitudes (γ_0 = 2 and γ_0 = 2) the reached plateau value of $I_{3/1}$ after the increase is nearly equal.

107
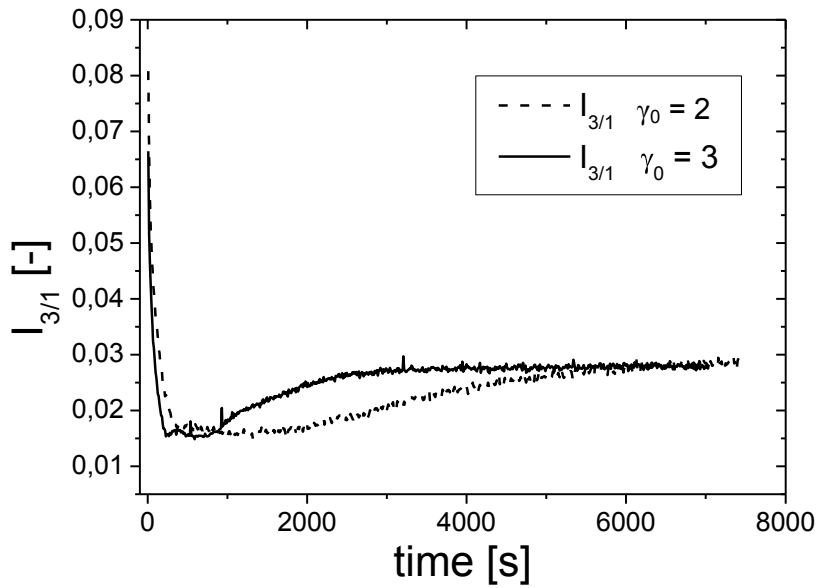
Fig. 64 Time dependence of $I_{3/1}$ for strain amplitudes γ_0 = 2 (dotted lines) and γ_0 = 3. The de-orientation also detected by an increase of $I_{3/1}$ after reaching the minimum value. For higher strain amplitudes the onset of the de-ordering occurs earlier.

4.3.3.   Ex-situ 2D-SAXS investigations

To follow the progress of macroscopic orientation during the ex-situ LAOS experiments, the non-linear parameter $I_{3/1}$ was selected as a trajectory. To examine the structure present at a specific time, the samples were removed from the shear geometries without subjecting them to any further shear. The degree of alignment for the mechanically induced anisotropic orientation distribution of the lamellae microdomains was analyzed at three different positions along the radial vector of the sample discs, as described in Experimental Methods (see **3.5.3**). For each applied strain amplitude, at least three different states of alignment were characterized by 2D-SAXS along the radial (*OY, OZ)* plane, the normal (*OX, OY*) plane and the tangential (*OX, OZ*) plane as described in the literature[159]. The experimental determined final structures for all strain dependent LAOS experiments with γ_0 = 0.5, γ_0 = 1, γ_0 = 2 and γ_0 = 3 are summarized in **Tab. 3**.

γ_0 [-] Macroscopic Orientation	0.5	1	2	3
Parallel			XX	XX
Perpendicular	X	X	XX	XX

Tab. 3 Summary of the ex-situ determined final state of macroscopic orientation for all four applied strain amplitudes at T = 150 °C and $\omega_1/2\pi$ = 1 Hz. The crosses indicate the type of macroscopic orientation observed while two crosses at a given strain amplitude indicate a biaxial orientation.

To explore the de-ordering process for $\gamma_0 > 0.5$, as first detected with in-situ 2D-SAXS measurements, mainly the data for the structural development at $\gamma_0 = 3$ were presented here because the dynamic mechanical parameters (G'' and $I_{3/1}$) showed the largest deviations from a monotonic decrease under these conditions. The times after which the LAOS measurements were stopped and the samples were taken for further ex-situ 2D-SAXS characterization are shown by arrows in **Fig. 65**. Additionally, to illustrate the reproducibility of the ex-situ mechanical measurements, the time evolution for G'' and $I_{3/1}$ for $\gamma_0 = 3$ is represented with error bars. The error bars were determined from four different measurements. It can be seen that for all dynamic mechanical measurements performed ex-situ, the statistical error was below 10%, while for $I_{3/1}$, the error was even below 3%, at least until the de-ordering process began.
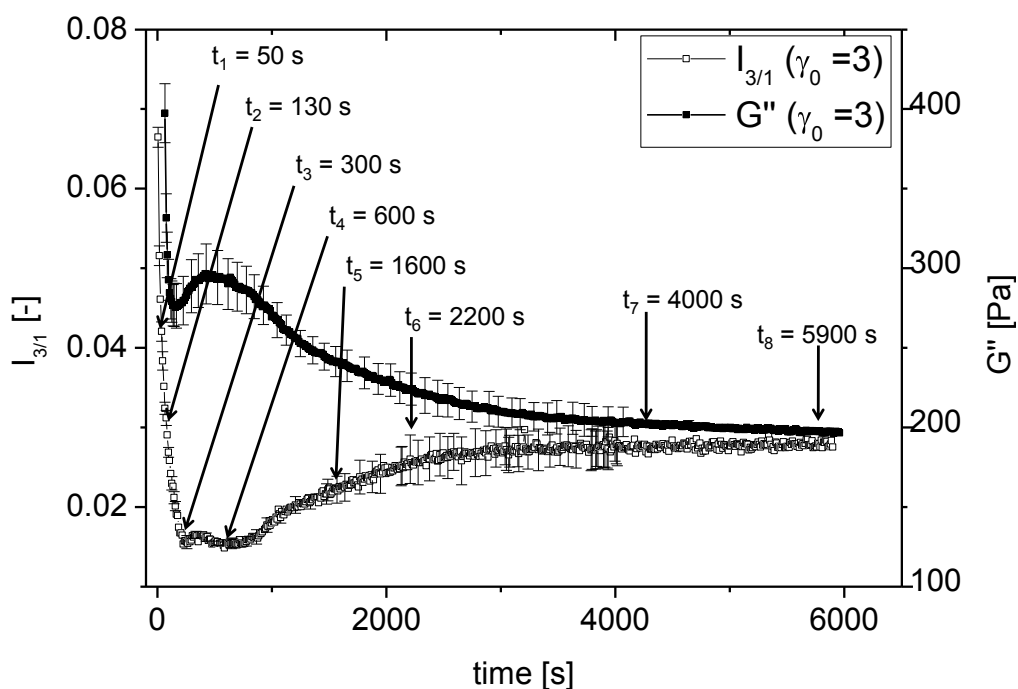
Fig. 65 G"(t) (filled squares) and $I_{3/1}(t)$ (open stars). G"(t) was shifted by 50 s to avoid an overlay of the data points. The arrows indicate the specific points that were chosen for ex-situ probing of the macroscopic structure. The error bars shown up to 2000 s were calculated from four measurements.

Apart from the initial state (t = 0), which featured the ringlike structure in all three directions expected for the isotropic initial state of the sample, an anisotropic orientation distribution was seen at all eight different pre-shear times (see **Fig. 66**) analyzed by ex-situ 2D-SAXS measurements.
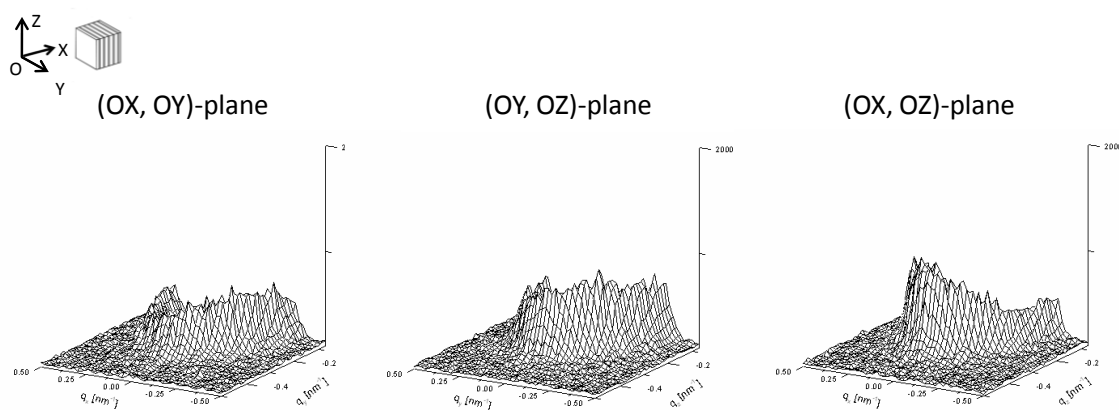
Fig. 66 2D-SAXS patterns at the initial state t_0 = 0 s along the normal (OX, OY) plane, radial (OY, OZ) plane and the tangential (OX, OZ) plane at the edge of the sample disc corresponding to position a) at r = 5.5 mm.

After 50 s, which corresponded to the regime in which G'' and $I_{3/1}$ experienced a rapid drop, a complex texture in the microstructure (see **Fig. 67**) was obtained for γ_0 > 1. At positions close to the edge of the sample geometries, the unit normal of the lamellae were orientated perpendicular (peak in the (*OX*, *OY*) plane), parallel (smaller reflection in the (*OY*, *OZ*) plane) and all orientations in between (ringlike pattern in the (*OX*, *OZ*) plane). This finding is consistent with the results reported by Chen et. al.[84].
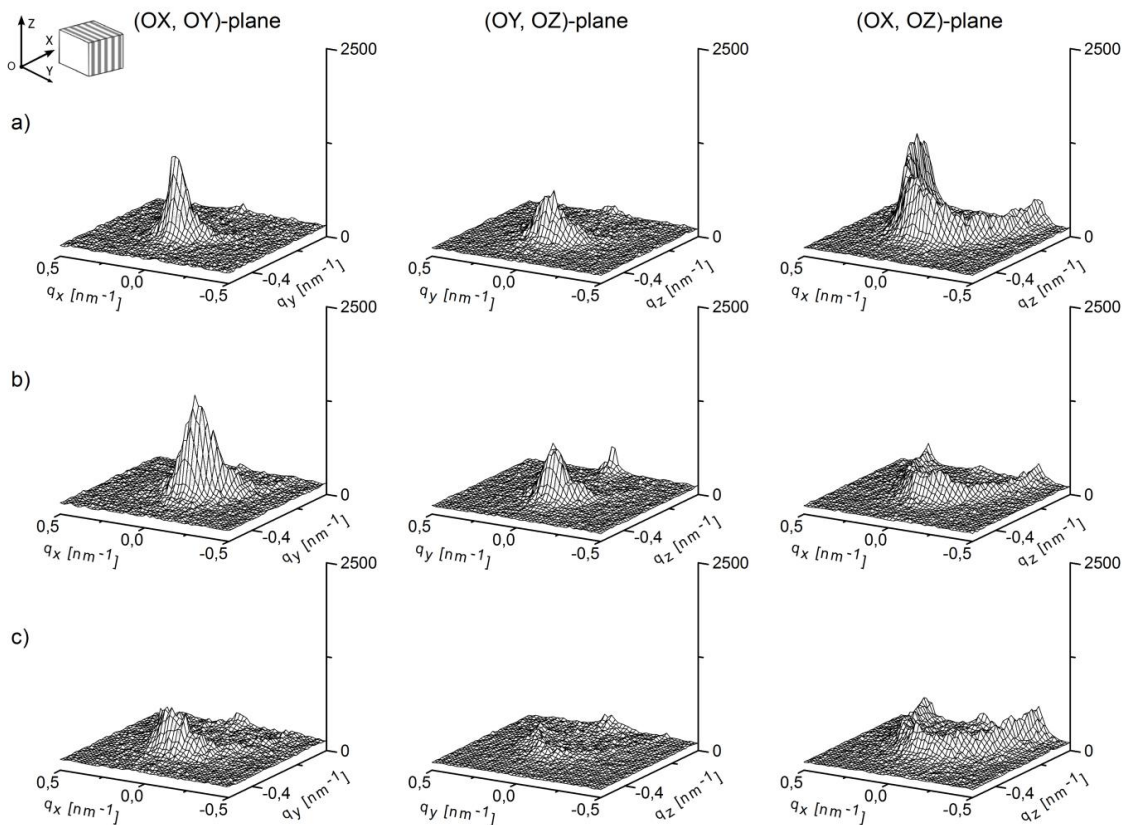
Fig. 67 2D-SAXS patterns for γ_0 = 3 after t_1 = 50 s along the normal (OX, OY) plane, radial (OY, OZ) plane and the tangential (OX, OZ) plane at three different positions with respect to the center of the sample disc: a) r = 5.5 mm, b) r = 4 mm and c) r = 2 mm. The ex-situ measured patterns indicate that the alignment of the block copolymer grains occurs in the beginning over a reduction of unfavorable transverse aligned lamellae.

After moving closer to the center of the sample geometry, the orientation distribution with its perpendicular and parallel projections decreased as the peaks in the (*OX*, *OY*) and (*OY*, *OZ*) planes broadened and decreased in intensity. This behavior is consistent with the experiments at lower strain amplitudes where the different positions along the radial vector for parallel plate geometries corresponded to lower strain amplitudes. **Fig. 68** represents the ex-situ determined 2D-scattering patterns for γ_0 = 2, γ_0 = 1 and γ_0 = 0.5 for a shear duration of approximately 50 s. It

can be seen that as γ_0 varies from 2 to 0.5, it was found that the development of the peaks became less pronounced and broader.
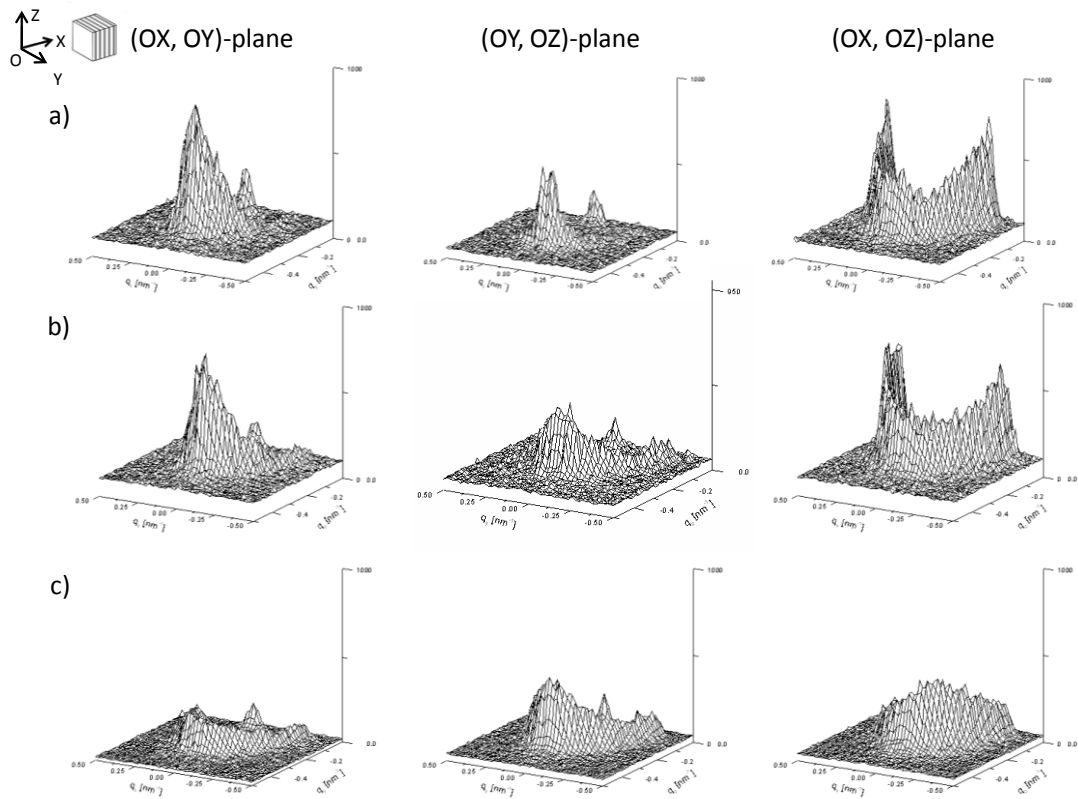
Fig. 68 2D-SAXS patterns after $t_1 = 50$ s for a) $\gamma_0 = 2$, b) $\gamma_0 = 1$ and c) $\gamma_0 = 0.5$ along the normal (OX, OY) plane, radial (OY, OZ) plane and the tangential (OX, OZ) plane at the outer positions of the sample disc (r = 5.5 mm).

As the mechanical excitation persisted, the degree of perpendicular alignment was significantly enhanced as indicated by the increased intensity and narrowed scattered peak in the (*OX*, *OY*) plane for $\gamma_0 = 3$ (see **Fig. 69**). This behavior was also obtained for the lower strain amplitudes.
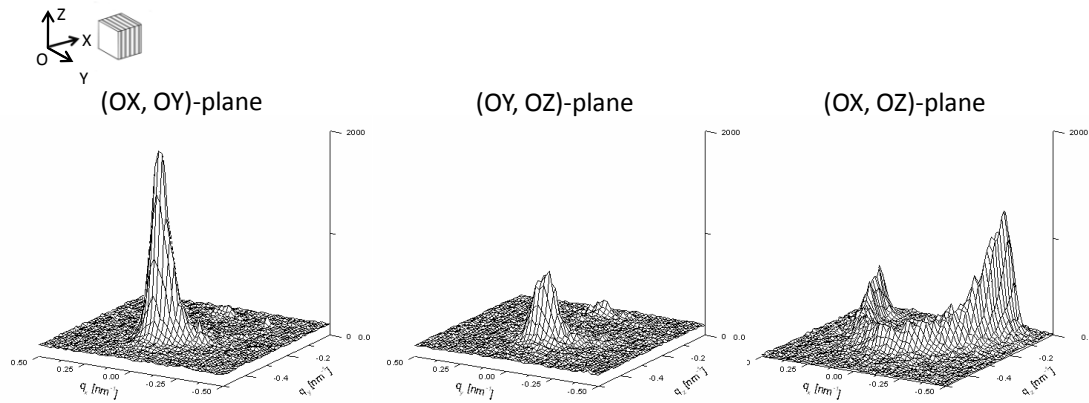
Fig. 69 2D-SAXS patterns for γ_0 = 3 after t_2 = 130 s along the normal (OX, OY) plane, radial (OY, OZ) plane and the tangential (OX, OZ) plane at the position a (r = 5.5 cm).

The scattering patterns for each state of orientation measured at different positions between the center and the edge of the sample disc (corresponding to different γ_0) clarified that the macroscopic alignment improved closer to the center of the parallel plates. At the onset of the plateau at t_3 = 300 s (γ_0 = 3), the orientation distribution was dominated by the perpendicular alignment (see **Fig. 70**) and only at a position near the edge of the parallel plate geometries (r = 5.5 mm) was there a small amount of parallel orientation ((OY, OZ)-plane) that could still be detected. Further investigation at t_4 = 700 s, indicated that the plateau region of the dynamic mechanical parameter $I_{3/1}$ corresponded to a stable state of macroscopic orientation under LAOS.
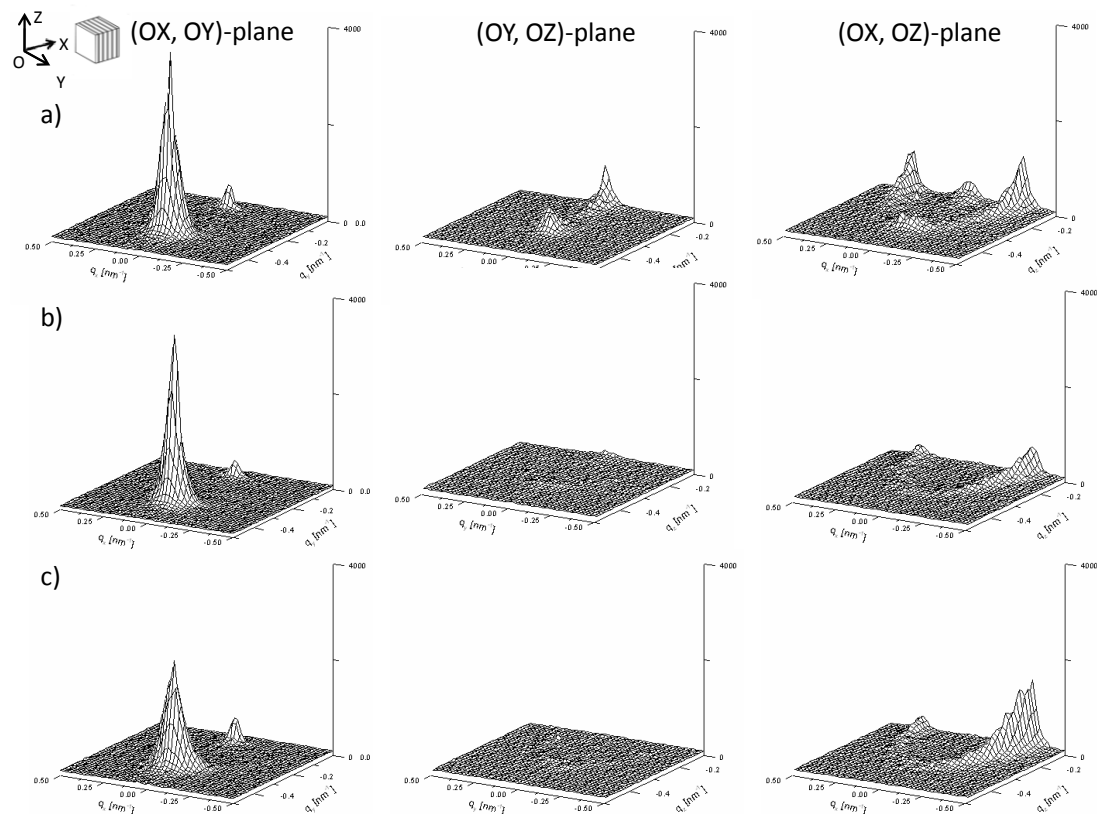
Fig. 70 2D-SAXS patterns for γ_0 = 3 after t_3 = 300 s along the normal (OX, OY) plane, radial (OY, OZ) plane and the tangential (OX, OZ) plane at three different positions with respect to the center of the sample disc: a) r = 5.5 mm, b) r = 4 mm and c) r = 2 mm. The ex-situ measured patterns indicate that at the plateau of $I_{3/1}(t)$ a nearly perfect aligned macroscopic perpendicular alignment is achieved.

For all other strain amplitudes, it was also found that at the minimum of $I_{3/1}$, the orientation distribution of the lamellae microstructures showed an overall perpendicular orientation (reflections in the (*OX, OY*)-plane). **Fig. 71** represents the ex-situ determined azimuthally averaged peak width quantified by $\sigma_{Min\text{-}SAXS}$ obtained for the four different strain amplitudes in the minimum region of $I_{3/1}$. Form the ex-situ 2D-SAXS measurements it can be seen that with increasing strain amplitude the degree of macroscopic ordering is enhanced.
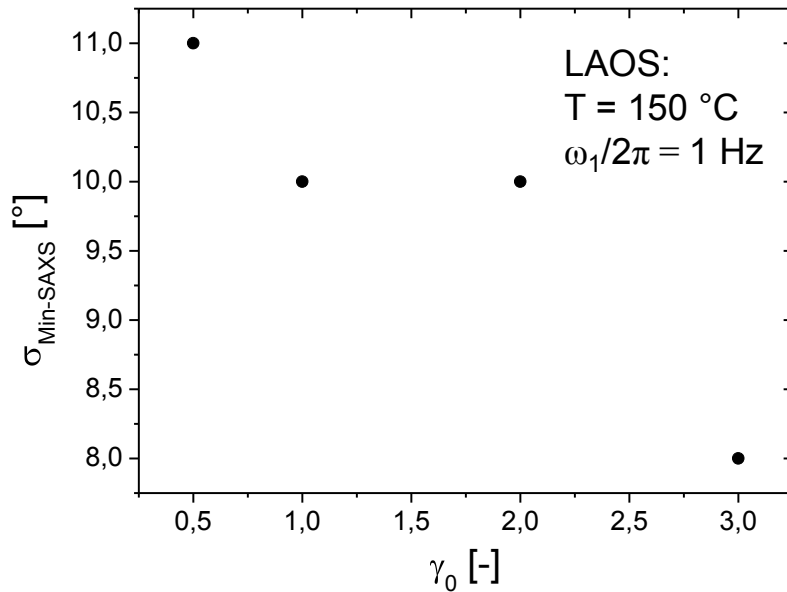
Fig. 71 Azimuthally averaged peak width of the first order reflection quantified by $\sigma_{Min\text{-}SAXS}$ at specific times at which $I_{3/1}(t)$ has reached the minimum for $\gamma_0 = 0.5$, $\gamma_0 = 1$, $\gamma_0 = 2$ and $\gamma_0 = 3$ ($\omega_1/2\pi = 1Hz$, $T = 150 °C$).

As the value of $I_{3/1}$ began to rise (only observed for $\gamma_0 > 1$ at T = 150 °C and $\omega_1/2\pi$ = 1Hz), the scattering patterns at t_5 = 1600 s indicated that the well ordered macroscopic perpendicular alignment obtained in the plateau region of $I_{3/1}$ became less ordered and showed a significant increase in the number of microdomains preferentially orientated in the parallel direction (see **Fig. 72**). It can be seen that the extent of this orientation decreased travelling from the outer edge to the center of the geometries (as γ_0 also decreases in the parallel geometries), while the perpendicular projection was the dominant orientation near the middle of the sample plates, which was a similar situation compared to the minimum of $I_{3/1}$.

115
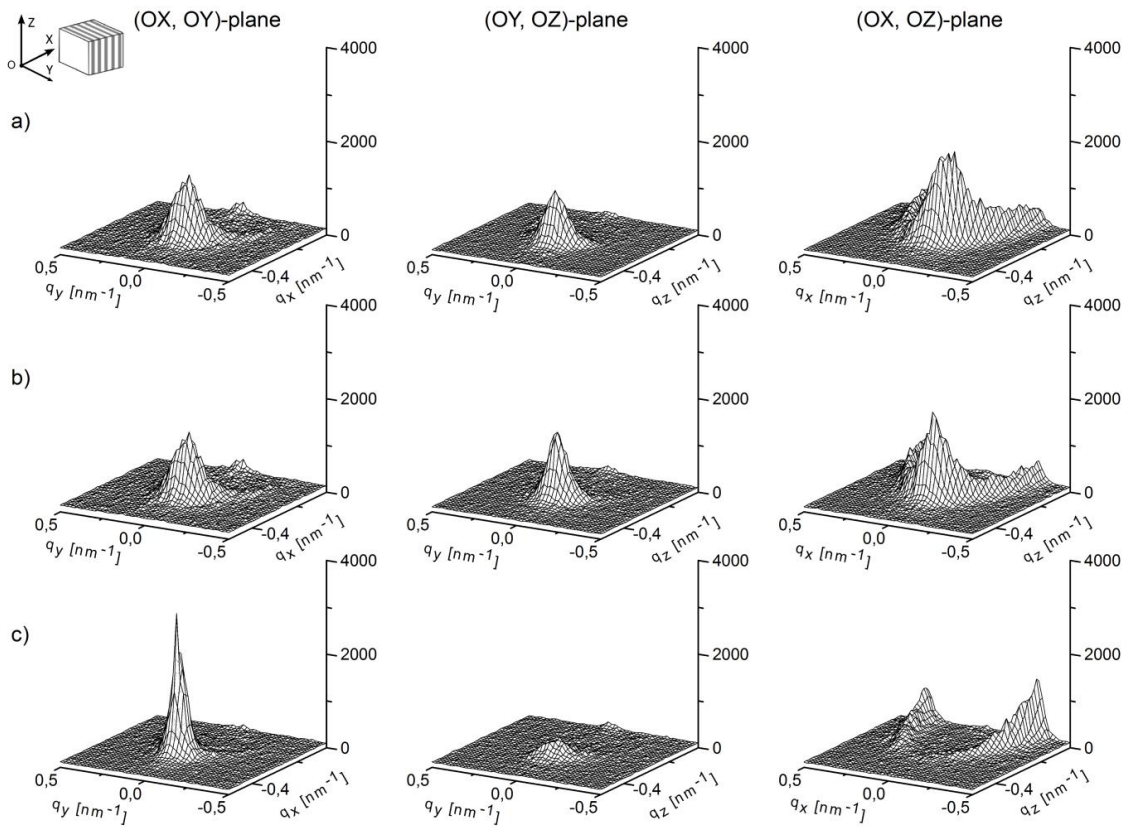
Fig. 72 2D-SAXS patterns for γ_0 = 3 after t_5 = 1600 s along the normal (OX, OY) plane, radial (OY, OZ) plane and the tangential (OX, OZ) plane at three different positions with respect to the center of the sample disc: a) r = 5.5 mm, b) r = 4 mm and c) r = 2 mm. The de-orientation process is indicated by the beginning development of a biaxial orientation with the unit normal of the lamellae being preferentially directed along the OX and OZ axis.

The de-ordering process was only detected for γ_0 > 1, while the achieved perpendicular orientation distribution remained unchanged as the mechanical stimulus proceeded for the two lower strain amplitudes. Interestingly, at the end of the experiment for γ_0 = 3 (t_8 = 5900 s), the scattering patterns in the (*OX*, *OY*) and (*OY*, *OZ*) planes showed a stable anomalous biaxial orientation with approximately similar amounts of perpendicular and parallel orientation in the region where G'' and $I_{3/1}$ exhibited constant values (see **Fig. 73**).
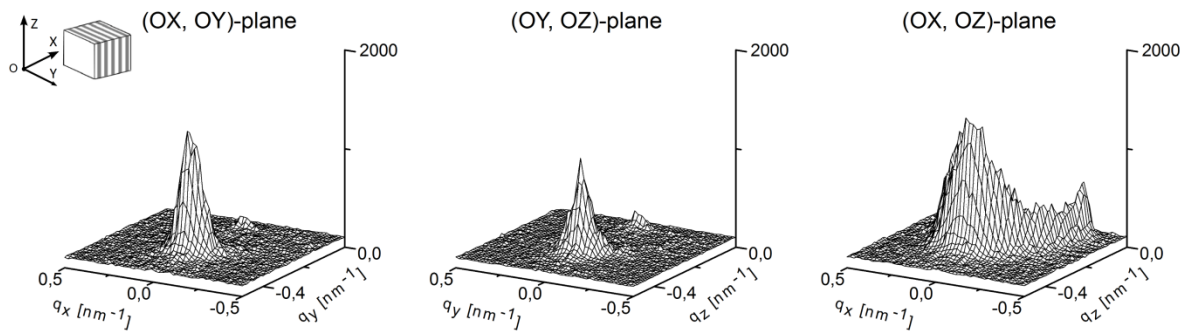
Fig. 73 2D-SAXS patterns after t_8 = 5900 s along the normal (OX, OY) plane, radial (OY, OZ) plane and the tangential (OX, OZ) plane at the edge of the sample (r = 5.5 mm) for γ_0 = 3. In the region where $I_{3/1}$ is constant, a macroscopic stable biaxial orientation is achieved.

The discovery of a stable biaxial orientation of the lamella unit normal under shear flow was first described by Okamoto et al.[161], utilizing in-situ Rheo-SAXS measurements with a custom made shear cell. This setup was, however, limited to a sawtooth type shear strain with γ_{max} = 0.5 and a time resolution of several hundred seconds. In that work[161], the specimens initially had an uniaxial parallel orientation and the biaxial alignment was achieved by re-orientating the macroscopically aligned structures. Therefore, the biaxial orientation was achieved by applying two different mechanical experimental conditions, one to initially macroscopically align the randomly orientated sample and the second to re-orientate the aligned system.

To the best of our knowledge, the results described here showed, for the first time, the development of an anomalous macroscopic biaxial orientation developed from an un-oriented macroscopic isotropic melt by applying a single set of experimental parameters ($\omega_1/2\pi$ = 1 Hz, γ_0 = 2 and γ_0 = 3, T = 150 °C) throughout the experiment. Therefore, it could be shown that under the applied conditions the appearance of a biaxial macroscopic orientation along the parallel and perpendicular directions for strain amplitudes γ_0 > 1 is only a function of the shear duration.

To summarize the ex-situ determined strain dependent structural changes for γ_0 = 3, the time dependence of the ex-situ calculated standard deviation of the azimuthally averaged first order reflection in the (OX, OY)-plane (perpendicular) and the (OY, OZ)-plane (parallel) are shown in **Fig. 74**. The measurements were performed at three different positions along the radial vector: r =5.5 mm, position b to r = 4 mm and position c to r = 2 mm. These selected positions correspond to a local strain amplitude of $\gamma_{0\text{-loc}}$ (a) = 0.81*γ_0, $\gamma_{0\text{-loc}}$ (b) = 0.67*γ_0 and $\gamma_{0\text{-loc}}$ (c) = 0.30*γ_0. It can be seen that this trend, which was also present in the time dependence of the

117

mechanical non-linear parameter $I_{3/1}$ (see doted lines in **Fig. 74a**), was reflected by the peak width of the developing macroscopic perpendicular and parallel alignments.
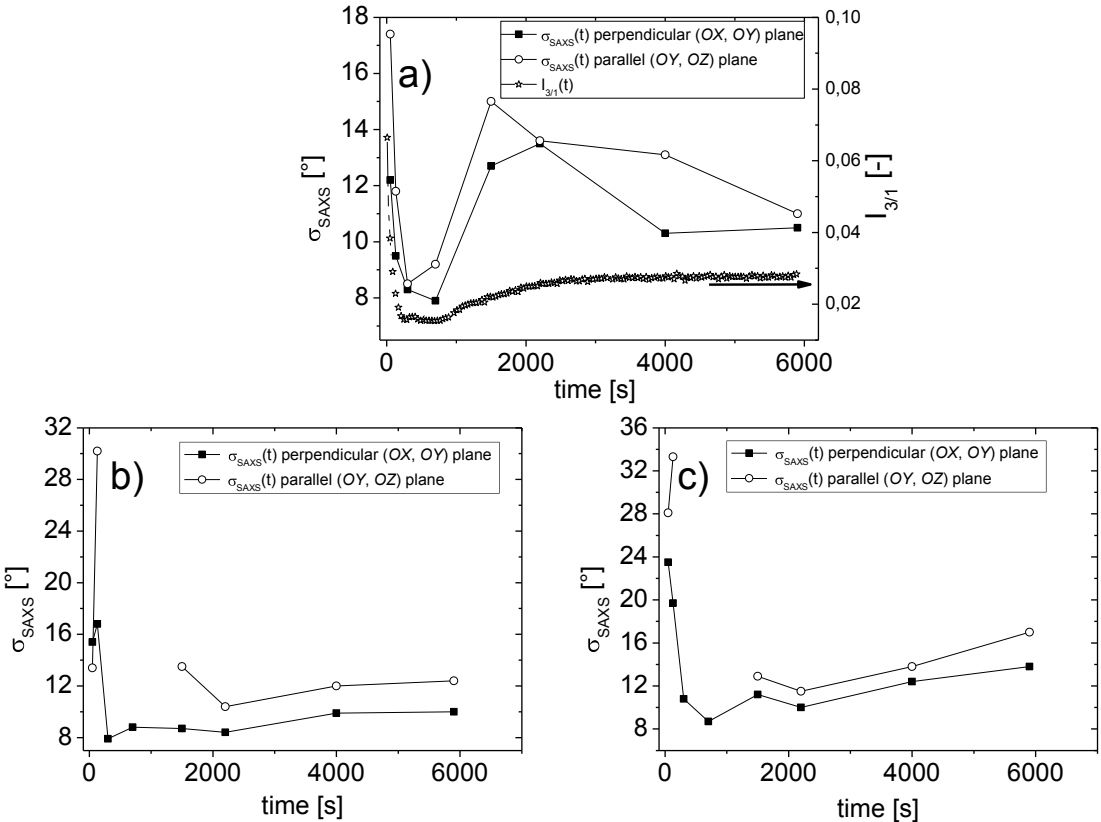
Fig. 74 Time evolution of the standard deviation as measured by ex-situ 2D-SAXS disc for the macroscopic perpendicular (filled squares) and parallel (open circles) alignments for $\gamma_0 = 3$, a) close to the edge (r = 5.5 mm), b) in the middle (r = 4 mm) and c) close to the center (r = 2 mm) of the sample. Missing points indicate that no peak was observed. The dotted lines represent the time dependence of the non-linear parameter $I_{3/1}(t)$.

Even though the orientation distribution is decreased after reaching a maximum at approximately 2000 s it is assumed that the constant elevated value of $I_{3/1} \approx 0.025$ was caused by the de-ordering of the perpendicular alignment in regions closer to the sample center.

Furthermore, no precise explanation for the correlation between the observed overshoot in the time dependence of G'' and changes in the alignment of the lamellar microdomains was found. However, the results indicate that the time progression of the non-linear response as quantified by the evolution of the non-linear parameter $I_{3/1}$, is directly correlated to the kinetic pathway of the macroscopic alignment and the following de-orientation process in the block copolymer melt.

4.4. Summary of the strain dependence orientation process

The in-situ Rheo-SAXS studies of the PS-b-PI-13k-13k model compound revealed an anomalous de-orientation during LAOS. This de-orientation was detected for $\gamma_0 > 1$ ($\omega_1/2\pi$ = 1 Hz, T = 150 °C) by a broadening of the peak width of the azimuthally averaged first order reflection quantified by σ_{SAXS}. The in-situ SAXS measurements revealed that the applied LAOS conditions first caused a well aligned perpendicular orientation of the lamellae diblock copolymer grains. However, as the applied mechanical stimulus proceeded the achieved overall orientation de-orders and the minimum value of the peak width ($\sigma_{Min\text{-}SAXS}$) increased, as detected for γ_0 =2 and γ_0 = 3.

This behavior was also seen in the time dependence of the mechanical non-linear response quantified by $I_{3/1}$ which also decreased to a minimum value ($I_{3/1} \approx$ 0.018) during the perpendicular orientation process and later increased again as the de-ordering occurred to approximately $I_{3/1}$ = 0.025.

These direct correlation of $I_{3/1}(t)$ to $\sigma_{SAXS}(t)$ was used to guide the ex-situ SAXS measurements which revealed that the during the de-ordering process a biaxial orientation distribution of the lamellae block copolymer grains occurred. In the final state, were $I_{3/1}(t)$ has reached its plateau value, the sample showed nearly equal amounts of macroscopic parallel and perpendicular aligned block copolymer grains (see **Fig. 75**). Therefore, it could be shown that $I_{3/1}(t)$ directly corresponds to the macroscopic orientation process and can be used to follow the state of alignment as well as to detect de-orientation phenomena during LAOS.
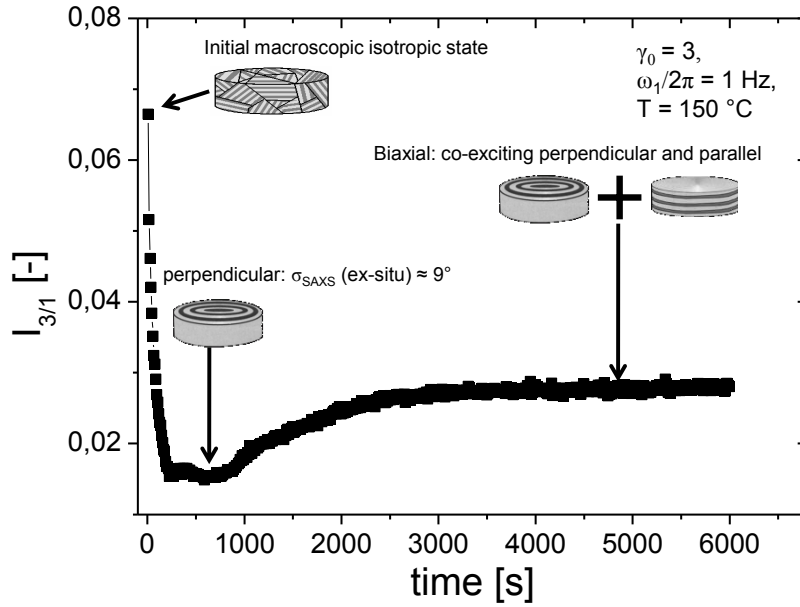
Fig. 75 $I_{3/1}(t)$ and the different states of macroscopic alignment as detected by ex-situ SAXS measurements (γ_0 = 3, $\omega_1/2\pi$ = 1 Hz, T = 150 °C).

4.5. Quantitative orientation kinetics

Based on the results above for the correlation between the non-linear mechanical response and the strain dependent structural dynamics in the sample melt, it is possible to evaluate the kinetics of the alignment process by comparing the orientation time determined for each method (2D-SAXS, G" and $I_{3/1}$). To do this, it must first be clarified how this orientation time can be calculated and to assess whether this method corresponds to a reasonable model for the experimental data.

A simple theoretical approach is presented here to deduce a mathematical expression for the underlying orientation mechanism. The main idea of this approach is to use a first order scheme for the kinetics. With the assumption that $I_{3/1}(t)$ is proportional to the number of defects $N_D(t)$ or intergrain area at a specific time, i.e. that

$$I_{3/1} \sim N_D(t) \tag{4.1}$$

the following first order kinetic expression for the time evolution under constant shear conditions (γ_0, T, $\omega_1/2\pi$) is then obtained:

$$-\frac{dN_D(t)}{dt} \sim k \cdot N_D(t) \tag{4. 2}$$

where k is proportional to the inverse of the orientation time τ (k ~ 1/τ).

It is assumed that due to heterogeneities in the size distribution of locally anisotropic ordered block copolymer domains (grains), the so called defects, the orientation times τ_o for the rotation of these grains will cover a broad range. These heterogeneities were accounted for by introducing a "heterogeneity-index" β, which broaden the single exponential. The most simple and less parameter intense description is given by a stretched exponential function. This leads to the final expression:

$$I_{3/1}(t) \sim N_D(t) \sim e^{-\left(\frac{t}{\tau}\right)^{\beta}} \tag{4. 3}$$

The latter term of equation **(4.3)** is the well known expression for the stretched exponential function, as discussed in the literature[171]. It is important to note that the stretched exponential function has already been used to describe the experimental time evolution during the shear-induced alignment process of block copolymers[168]. However, this function was used without providing further explanations for the stretched exponential time progression of the shear-induced orientation.

Using a stretched exponential provides a simple method for describing the macroscopic orientation of block copolymer grains by a rotation mechanism after taking into account that the orientation times τ posses a broad and continuous distribution than cannot be described by a single exponential decay (β = 1).

In addition to the above mentioned heterogeneity in the size distribution of the block copolymer grains, this function takes into account the appearance of a strain gradient, which in parallel plate-plate geometries, is a function of the radial distance as well as of any small pre-orientations distributed within the block copolymer melt. The broadened orientation time distribution is then expressed in terms of the deviance of β (0 < β ≤ 1) from an ideal exponential function where β = 1.

The fitted curves for time evolution of σ_{SAXS}, G'' and $I_{3/1}$ are represented by doted lines in the corresponding Figures (see **Fig. 55**, **Fig. 57**, **Fig. 59** and **Fig. 63**). Form the quality of the fitted curves it can be seen that this approach for analyzing the

kinetics of shear-induced macroscopic orientation using a rotation mechanism is reasonable. The calculated fit parameters are summarized in **Tab. 4** for all four quantities (σ_{SAXS}(in-situ), G''(stress controlled), $I_{3/1}$, G''(strain controlled)). It is clear, however, that the orientation times τ_o differ between the mechanical and 2D-SAXS measurements. This difference became strongly pronounced at the lowest strain amplitudes ($\gamma_0 = 0.5$). The stretching exponent β stayed between 0.4 and 0.8 for all measurements and exhibited, no significant strain dependence. The deviance of β from the ideal case $\beta = 1$ indicated that a broadened distribution in the dynamic orientation process occurred, which is often observed in disordered systems like polymers due to e.g. grain size distribution.

a)

Strain (SAXS in-situ Rheo-SAXS)	y_0 [°]	τ [s]	β	A [°]
0.5	10.2	430	0.58	10
1	10.5	110	0.50	10
2	9.4	60	0.80	7
3	7.7	20	0.60	4

b)

Strain (G" in-situ Rheo-SAXS)	y_0 [Pa]	τ_o [s]	β	A [Pa]
0.5	355	720	0.52	214
1	240	190	0.67	180
2	210	50	0.73	120
3	130	40	0.72	60

c)

Strain (G" ARES-Rheomter)	y_0 [Pa]	τ_o [s]	β	A [Pa]
0.5	333	6050	0.42	287
1	281	262	0.4	292
2	289	32	0.5	174
3	275	14	0.85	122

d)

Strain (I$_{3/1}$ ARES-Rheometer)	y_0 [-]	τ_o [s]	β	A [-]
0.5	0.016	2100	0.38	0.051
1	0.012	250	0.67	0.065
2	0.016	75	0.80	0.062
3	0.015	50	0.75	0.052

Tab. 4 Calculated fit parameters for all four strain amplitudes by fitting the in-situ Rheo-SAXS time data of: a) in-situ $\sigma_{SAXS}(t)$, b) G"(t), and the rheological properties obtained from a strain controlled ARES rheometer: c) G"(t) and d) I$_{3/1}$(t) with a stretched exponential fit function ($y = y_0 + A \cdot e^{-(\frac{t-t_0}{\tau})^\beta}$).

Interestingly, the plateau values γ_0 of the non-linear parameter I$_{3/1}$(t) and the peak width determined by the standard deviation σ_{SAXS} of the 2D-SAXS scattering pattern, were much less strain or method dependent compared to the plateau value of the

mechanical loss modulus G", which showed a much larger deviation. By plotting the strain amplitude as a function of the calculated orientation times for each measurement method on a double logarithmic scale, shown in **Fig. 76**, a scaling dependence of the macroscopic orientation on the applied strain amplitude was obtained.
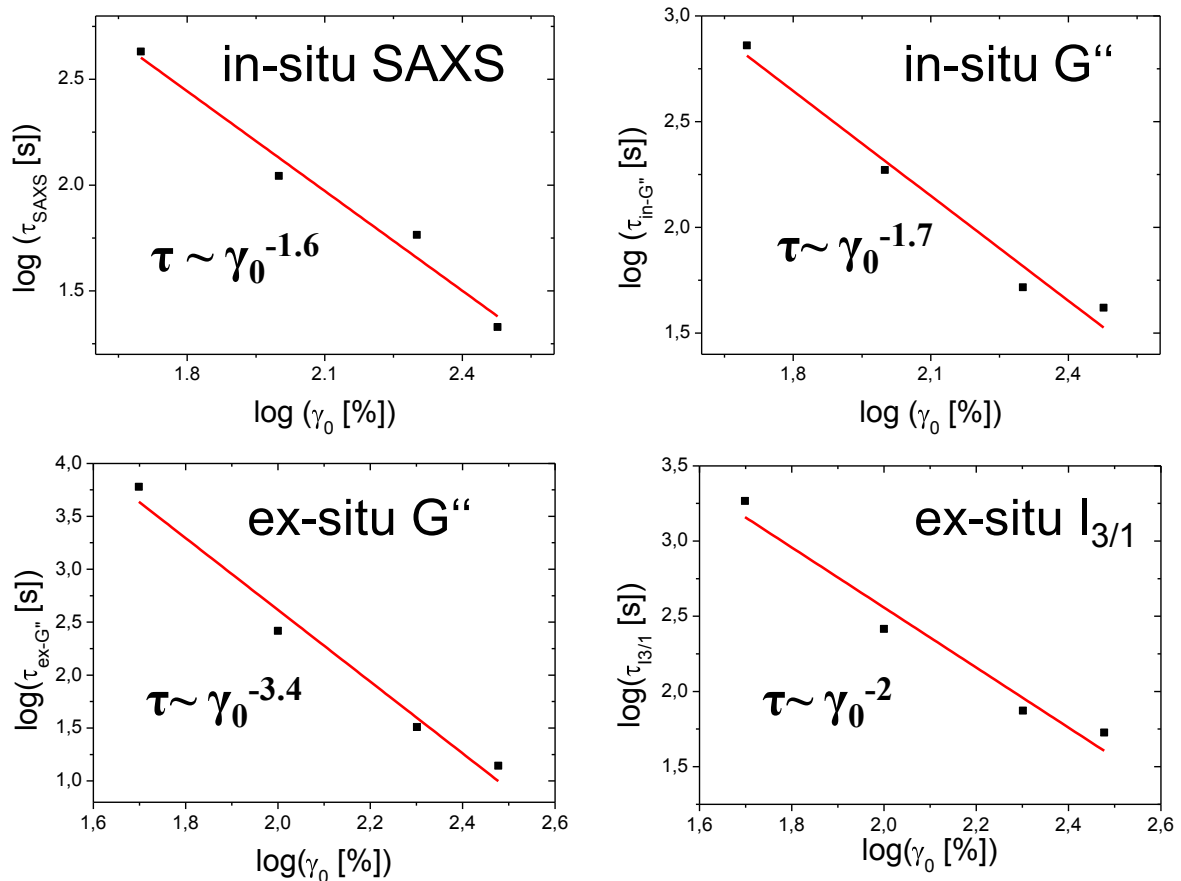
Fig. 76 Double logarithmic plot of the orientation time $\tau_o(\gamma_0)$ as a function of the strain amplitude γ_0. The solid lines represent a linear regression revealing a slope of approximately -2 for a) σ_{SAXS} (obtained from in-situ SAXS), b) G" (obtained from stress controlled rheometer) c) G" (obtained from strain controlled rheometer) and d) $I_{3/1}$ (obtained from strain controlled rheometer).

For all measurements, except the ex-situ obtained dynamic loss modulus G", it was found that the orientation time had a power law dependence on the strain amplitude ranging from $\tau \sim \gamma_0^{-1.6}$ and $\tau \sim \gamma_0^{-2}$ where this result has not been previously reported to the best of our knowledge. Unfortunately, the reason for the strong deviance for the ex-situ G" data could not be clarified within this work.

The discrepancy between the results obtained in a previous work on polystyrene-*b*-polybutadiene diblock copolymers[168] that revealed a forth power dependence ($\tau \sim$

γ_0^{-4}) on the strain amplitude, is not in contrast with the results reported here. The investigations performed by C. Oelschlaeger et al. considered the orientation of the lamella unit normal parallel to shear gradient (*OZ* axis), corresponding to a parallel overall orientation instead of a perpendicular alignment. This orientation was achieved at elevated temperatures near T_{ODT}. In this region the rheological response is dominated by the mechanical storage modulus G'' which is caused by the microstructure of the self assembled diblock copolymer. Therefore, it can be assumed that this high elasticity also affected the macroscopic orientation dynamics in the polymer melt.

4.6. Frequency and temperature dependent alignment kinetics

4.6.1. Frequency dependence of the macroscopic alignment

a) In-Situ SAXS studies

Three different shear frequencies were applied ($\omega_1/2\pi$ = 0.5 Hz, $\omega_1/2\pi$ = 1 Hz and $\omega_1/2\pi$ = 3 Hz) for γ_0 = 1 at T = 150 °C. **Fig. 77** shows the time dependence of the peak width measured by the standard deviation of the azimuthally averaged first order reflection. For all measurements a stretched exponential decrease occurred in the beginning of the experiments similar to the one obtained for the strain dependent measurements of $\sigma_{SAXS}(t)$. The magnitude of this decay was increased with decreasing frequency.
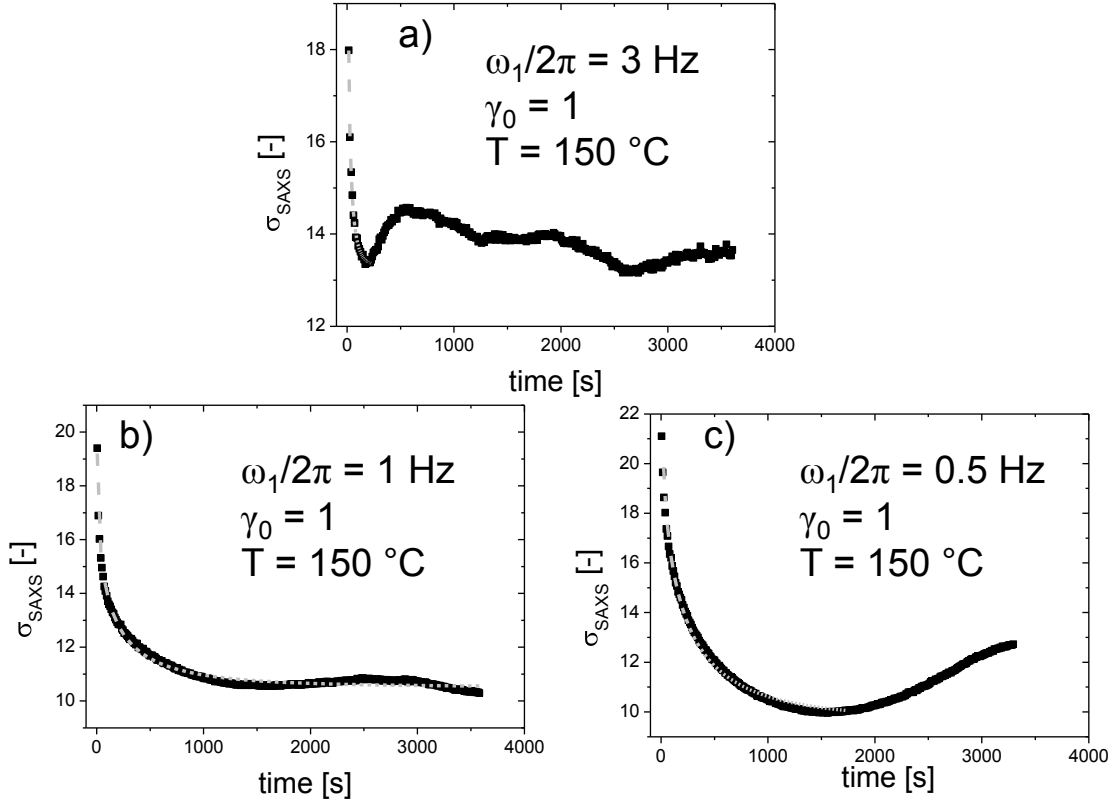
Fig. 77 $\sigma_{SAXS}(t)$ at T = 150 °C for a) $\omega_1/2\pi$ = 3 Hz, b) $\omega_1/2\pi$ = 1 Hz and c) $\omega_1/2\pi$ =0.5 Hz at T = 150 °C and γ_0 = 1. For $\omega_1/2\pi$ = 3 Hz as well as for $\omega_1/2\pi$ =0.5 Hz a pronounced de-ordering is observed while for $\omega_1/2\pi$ = 1 Hz only a slight increase in σ_{SAXS} is obtained. The dotted lines represent the stretched exponential fit function.

The obtained fit parameters are summarized in **Tab. 5**.

$\omega_1/2\pi$ (in-situ SAXS)	y_0 [°]	τ [s]	β	A [°]
0.5	9.7	170	0.56	13
1	10.5	110	0.50	10
3	13.4	30	0.75	5.5

Tab. 5 Calculated fit parameters from the in-situ determined $\sigma_{SAXS}(t)$ data for the macroscopic perpendicular orientation at T = 150 °C and γ_0 = 1 for $\omega_1/2\pi$ = 0.5 Hz, $\omega_1/2\pi$ = 1 Hz and $\omega_1/2\pi$ = 3 Hz.

Form the calculated frequency dependent orientation times τ_0, utilizing a stretched exponential fit function (see page **120**), a power law behavior is obtained with $\tau_0(\omega_1/2\pi) \sim \dfrac{1}{(\omega_1/2\pi)}$ (see **Fig. 78**). It has to be mentioned that these were the first results obtained with the unique in-situ Rheo-SAXS setup, therefore, the amount of representative data points was limited. Consequently, the provided scaling behavior may be considered as preliminary reference points which have to be further

evaluated for their universal use for low molecular weight PS-b-PI diblock copolymers.
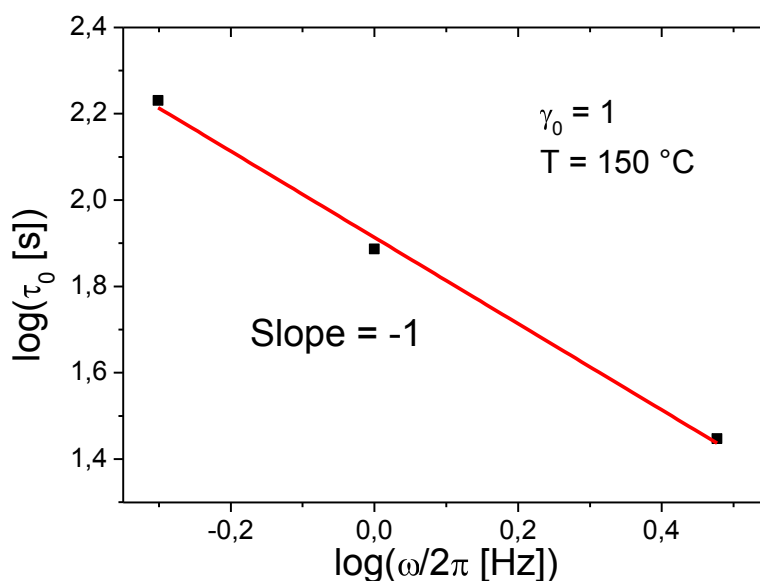
Fig. 78 Double logarithmic plot of the orientation time $\tau_0(\omega/2\pi)$ as a function of the shear frequency. An inverse proportionality is obtained, $\tau_0(\omega/2\pi) \sim (\omega/2\pi)^{-1}$.

Interestingly, strong de-orientations at t = 200 s and t = 1700 s were observed for $\omega_1/2\pi$ = 0.5 Hz and $\omega_1/2\pi$ = 3 Hz, respectively. For the intermediate frequency ($\omega_1/2\pi$ = 1 Hz) only a slight overshoot was detected at t = 2000 s. In contrast, to the monotonic increase, observed for the de-orientation at $\omega_1/2\pi$ = 0.5 Hz, the time progression of σ_{SAXS} for $\omega_1/2\pi$ = 3 Hz showed an overshoot of approximately 1.5° which finally leveled off to a slightly elevated σ_{SAXS} value of 13.6° compared to the minimum value of $\sigma_{Min\text{-}SAXS}$ = 13.4° at t = 190 s. The observed overshoot showed similarities to the in-situ investigated alignment process obtained for $\omega_1/2\pi$ = 1 Hz, γ_0 = 1 at T = 150 °C (compare **Fig. 55c**).

To illustrate the quality of the perpendicular orientation in the (*OX, OY*) plane quantified by $\sigma_{SAXS}(t)$ the three frequency dependent measurements are represented in one plot in **Fig. 79**. From the minimum value of the peak width of the azimuthally averaged first order reflection, quantified by the standard deviation $\sigma_{Min\text{-}SAXS}$, it can be seen that for increasing shear frequency the orientation distribution of the lamellae block copolymer domains became less ordered. For a shear frequency of $\omega_1/2\pi$ = 3 Hz the minimum value was $\sigma_{Min\text{-}SAXS}$ = 13.4° while for $\omega_1/2\pi$ = 0.5 Hz the sample melt became more ordered with a minimum value of $\sigma_{Min\text{-}SAXS}$ = 10°. Furthermore, it

could be shown that the minimum value $\sigma_{Min\text{-}SAXS}$ exhibited a linear dependence on the applied shear frequency (see **Fig. 80**).
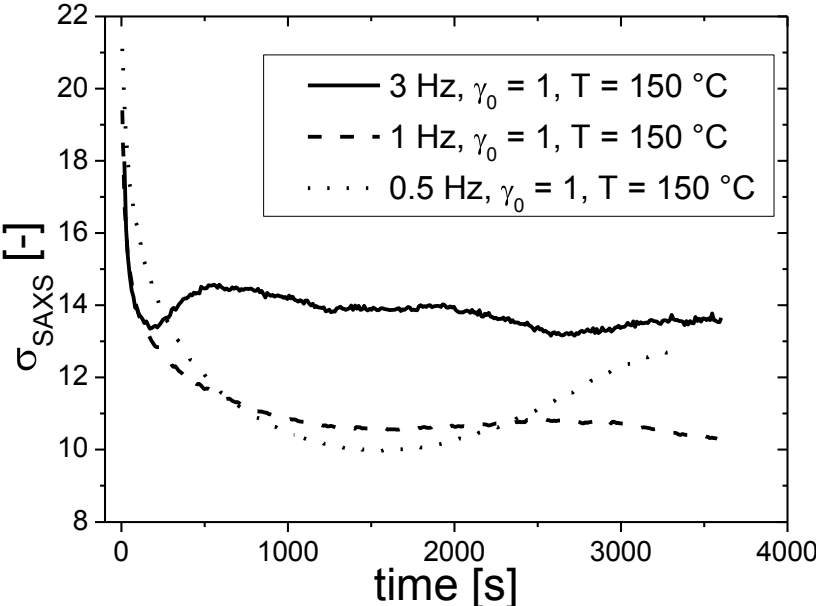
Fig. 79 Time dependence of σ_{SAXS} for the different shear frequencies [$\omega_1/2\pi$ =3 Hz (solid line), $\omega_1/2\pi$ =1 Hz (dashed line) and $\omega_1/2\pi$ =0.5 Hz (dotted line)] at T = 150 °C and γ_0 = 1 represented in one plot to illustrate the frequency dependence of the orientation distribution of the lamellae domains in the (OX, OY) plane.
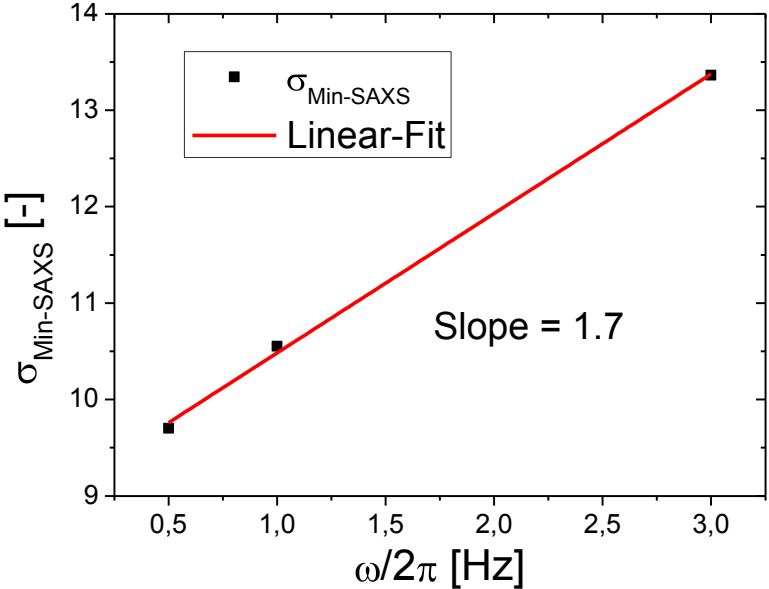
Fig. 80 Linear representation of the minimum value of $\sigma_{Min\text{-}SAXS}(\omega/2\pi)$ as a function of frequency. A linear dependence of the applied shear frequency to the quality of the perpendicular orientation of the lamellae grains was observed

b) Online FT-Rheology measurements

The effect of the shear frequency to the de-orientation process detected by the mechanical non-linear parameter $I_{3/1}$ for $\omega_1/2\pi$ = 1 Hz and $\omega_1/2\pi$ = 0.5 Hz and a strain amplitude of γ_0 = 3 is shown in **Fig. 81**. The orientation times τ_o calculated from the rapid decrease of $I_{3/1}$ was increased by more than a factor of 3 from τ_o = 50 s for $\omega_1/2\pi$ = 1 Hz to τ_o = 170 s for $\omega_1/2\pi$ = 0.5 Hz. Furthermore, the plateau region in which $I_{3/1}$ had its minimum value of approximately $I_{3/1}$ = 0.015 was enlarged by a factor of 2 from 450 s for $\omega_1/2\pi$ = 1 Hz to 900 s for $\omega_1/2\pi$ = 0.5 Hz. Additionally, the increase of $I_{3/1}$ was less steep for the lower frequency ($\omega_1/2\pi$ = 0.5 Hz) and proceeded over a time period of 7000 s until $I_{3/1}$ reached a plateau value of 0.035. In contrast, for $\omega_1/2\pi$ = 1 Hz a rapid increase during 2000 s was detected leading into a plateau of $I_{3/1}$ = 0.027 after approximately 2700 s.
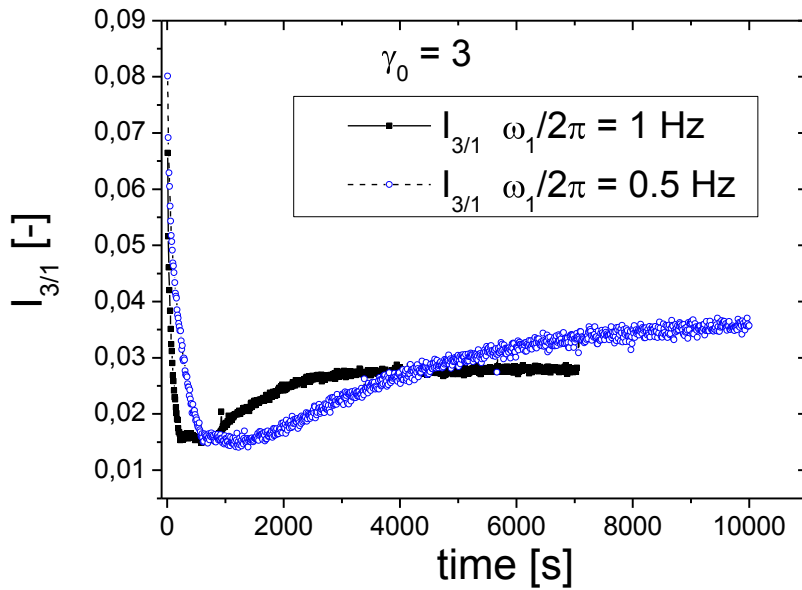
Fig. 81 Time dependence of $I_{3/1}$ for $\omega_1/2\pi$ = 1 Hz (filled squares) and $\omega_1/2\pi$ = 0.5 Hz (open circles) at T = 150 °C and γ_0 =3.

4.6.2. Temperature dependent alignment kinetics

In the discussion in section **4.3** it was shown that the strain dependent orientation time $\tau_o(\gamma_0)$ showed power law behavior of approximately $\tau_o(\gamma_0) \sim \gamma_0^{-2}$. In the following the temperature dependence of the macroscopic perpendicular orientation of PS-b-PI-13k-13k (T_{ODT} = 205 °C) at T_1 = 150 °C, T_2 = 160 °C and T_3 = 170 °C as detected

by in-situ Rheo-SAXS measurements is discussed. Three different strain amplitudes $\gamma_0 = 0.5$, $\gamma_0 = 1$ and $\gamma_0 = 2$ were applied with a fixed shear frequency of $\omega_1/2\pi = 1$ Hz.

Fig. 82a-c shows σ_{SAXS} as a function of time for specific strain amplitude at different temperatures. Form this representation it can be seen that in the beginning of the experiment the time progression of σ_{SAXS} showed a similar stretched exponentially decreasing trend for all strain amplitudes and temperatures. However, the de-ordering phenomenon exhibited complex temperature behavior.

For example, the temperature dependent trend of the de-ordering for $\gamma_0 = 2$ and for $\gamma_0 = 1$ showed different trends. For $\gamma_0 = 2$ a pronounced de-ordering at $T_1 = 150\ °C$ and $T_2 = 160\ °C$ appeared while for the highest temperature ($T_3 = 170\ °C$) no de-ordering was observed during LAOS and σ_{SAXS} decreased into a nearly constant plateau of $\sigma_{Min\text{-}SAXS} = 6°$. In contrast, for $\gamma_0 = 1$ at $T_3 = 170\ °C$ the onset of a de-ordering process was visible after 2400 s while for $T_2 = 160\ °C$ a strong overshoot of σ_{SAXS} was detected at $t \approx 1200$ s. As already shown above, no pronounced de-ordering was observed for $\gamma_0 = 1$ at $T_1 = 150\ °C$.

For $\gamma_0 = 2$ and $\gamma_0 = 1$ the minimum value of σ_{SAXS} is decreased with increasing temperature which results in a better overall perpendicular alignment for elevated temperatures. In contrast, the measurements for the lowest strain amplitude ($\gamma_0 = 0.5$) revealed a better macroscopic perpendicular orientation for $T_1 = 150\ °C$ ($\sigma_{Min\text{-}SAXS} \approx 10.2$) while for $T_2 = 160\ °C$ and $T_3 = 170\ °C$ no pronounced temperature dependence was detected and σ_{SAXS} monotonically approximates a value of $\sigma_{Min\text{-}SAXS} = 10.2°$.
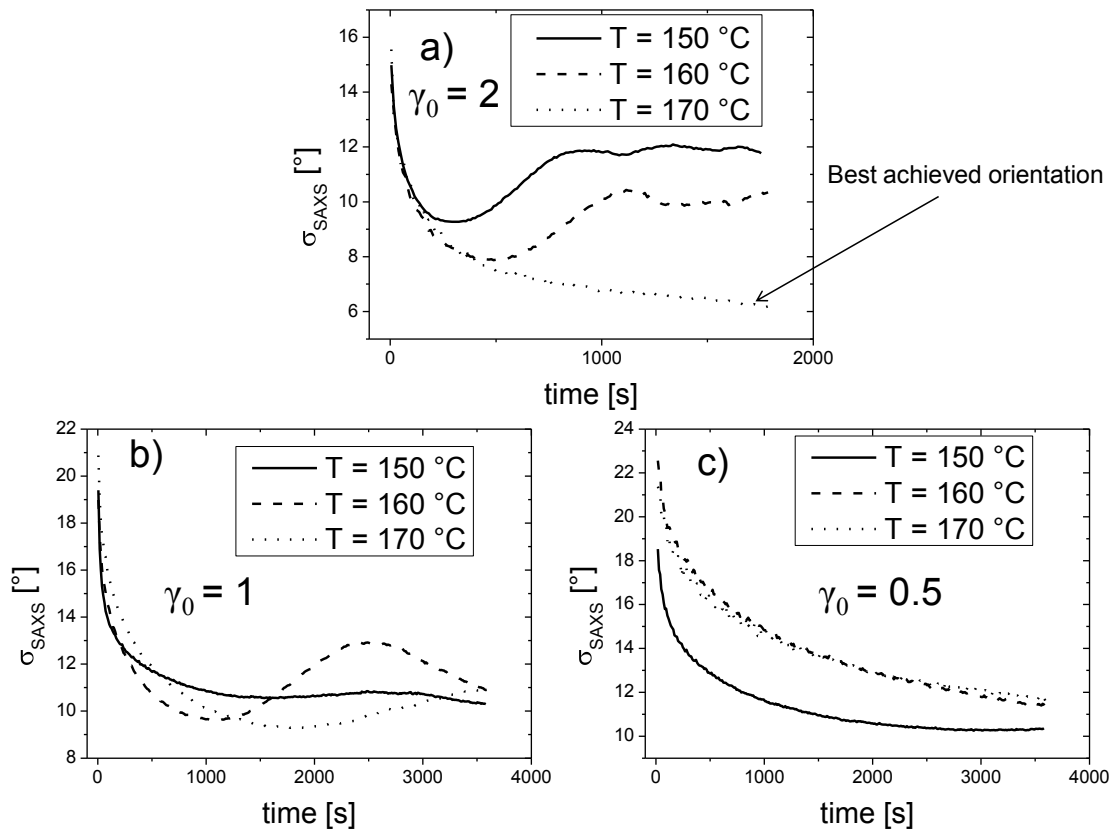
Fig. 82 $\sigma_{SAXS}(t)$ for the shear-induced macroscopic perpendicular alignment of PS-b-PI-13k-13k (T_{ODT} = 205 °C). The solid lines represent measurements at T_1 = 150 °C, the dashed lines at T_2 = 160 °C and the dotted lines at T_3 = 170 °C. The LAOS experiments were performed with a strain amplitude a) γ_0 = 2, b) γ_0 = 1, c) γ_0 = 0.5 and a shear frequency of $\omega_1/2\pi$ = 1 Hz.

To probe whether the derived power law (compare section **4.3**) of the orientation times τ_o on the strain amplitude at T = 150 °C ($\tau_o(\gamma_0) \sim \gamma_0^{-1.6}$) is also valid at different temperatures, the time dependences of σ_{SAXS} at T_1 = 150 °C, T_2 = 160 ° and T_3 = 170 °C were fitted with a stretched exponential (not shown here). The obtained fit parameters are summarized in **Tab. 6**.

a)

Strain (150 °C)	y_0 [°]	τ_o [s]	β	A [°]
0.5	10.2	430	0.58	10
1	10.5	110	0.50	10
2	9.4	60	0.80	7

b)

Strain (160 °C)	y_0 [°]	τ_o [s]	β	A [°]
0.5	11.1	989	0.81	12
1	9.4	207	0.68	11
2	7.7	97	0.76	8

c)

Strain (170 °C)	y_0 [°]	τ_o [s]	β	A [°]
0.5	10.2	1070	0.58	13
1	8.5	312	0.60	14
2	6	154	0.50	11

Tab. 6 Calculated fit parameters from the in-situ determined $\sigma_{SAXS}(t)$ data for the macroscopic perpendicular orientation at a) T_1 = 150 °C, b) T_3 = 160 °C and c) T_3 = 170 °C. All $\sigma_{SAXS}(t)$ curves were fitted with a stretched exponential function ($y = y_0 + A \cdot e^{-(\frac{t-t_0}{\tau})^\beta}$).

Fig. 83 shows the double logarithmic representation of the calculated orientation times $\tau_o(\gamma_0)$ against the strain amplitude. For T_2 = 160 °C (**Fig. 83a**) a slope of -1.7 was obtained while for the highest temperature T_3 = 170 °C the slope was slightly suppressed to -1.4. Nevertheless, it can be seen that these findings are in good agreement with the result obtained at T_1 = 150 °C (see **Fig. 76**) where $\tau_o \sim \gamma_o^{-1.6}$
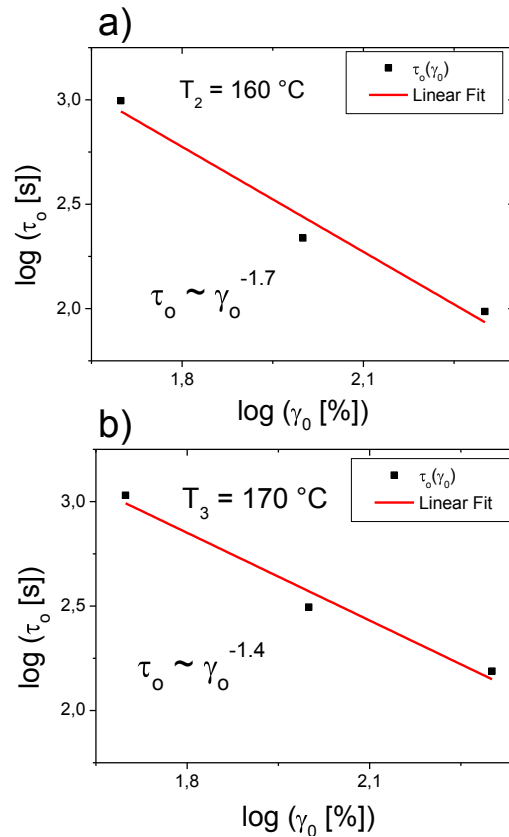
Fig. 83 Double logarithmic plot of the orientation time τ_o as a function of the strain amplitude at a) 160 °C and b) 170 °C for PS-b-PI-13k-13k (T_{ODT} = 205 °C) . The obtained power law of τ_o on the strain amplitude was in good agreement with the results obtained for T_1 = 150 °C where a slope of -1.6 was received.

It is important to note that the strain dependence of the orientation time τ_o, calculated from the non-linear parameter $I_{3/1}(t)$ showed power law dependence of $\tau_o \sim \gamma_o^{-1.6}$ at T_2 = 160 °C and $\tau_o \sim \gamma_o^{-1.7}$ at T_3 = 170 °C (not shown here).

Furthermore, the results showed that the minimum value of $\sigma_{Min\text{-}SAXS}$ decreased with increasing strain amplitude which resulted in a better macroscopic perpendicular orientation for higher γ_0 (see **Fig. 84**). This result was also obtained for T = 150 °C, if the lowest strain amplitude (γ_0 = 0.5) was neglected from the strain dependent $\sigma_{Min\text{-}SAXS}$ values.
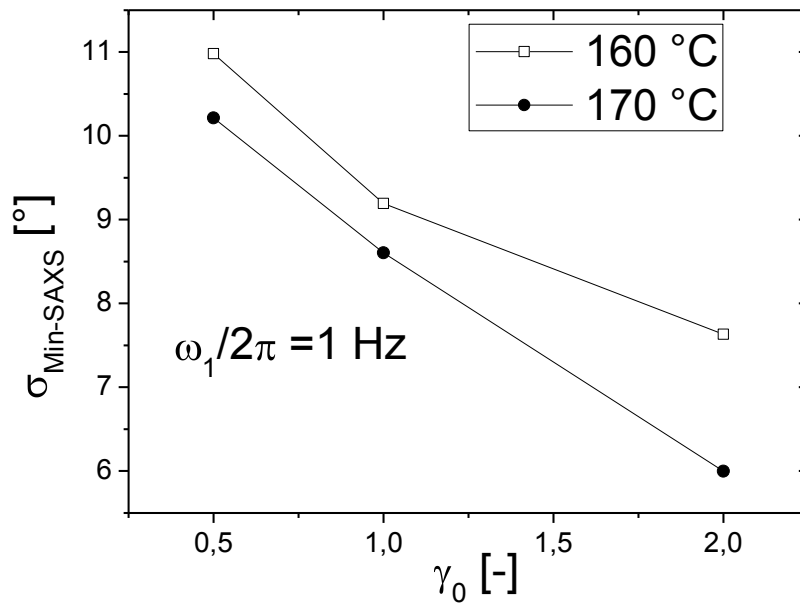
Fig. 84 Strain dependence of the minimum value $\sigma_{Min-SAXS}(\gamma_0)$ for PS-b-PI-13k-13k (T_{ODT} = 205 °C) at T = 160 °C (open squares) and T = 170 °C (filled circles) while $\omega_1/2\pi$ = 1 Hz.

4.7. Conclusion of frequency and temperature dependence

From the above performed in-situ Rheo-SAXS measurement it was found that the best degree of macroscopic orientation ($\sigma_{Min-SAXS}$ = 6°) could be achieved at T = 170 °C, γ_0 = 2 and a shear frequency of $\omega_1/2\pi$ = 1 Hz. Furthermore, it could be shown that an increase in the strain amplitude enhanced the macroscopic alignment. For T = 160 °C and T = 170 °C a linear dependence between strain amplitude and $\sigma_{Min-SAXS}$ was found while the orientation time obeyed a power law behavior to the applied strain amplitude of $\tau_o \sim \gamma_0^{-1.6}$.

However, increasing the temperature by 10 °C causes an increase in the orientation time τ_0 by approximately a factor of 1.6 for γ_0 = 1 and γ_0 = 2 while for the lowest strain amplitude γ_0 = 0.5 no specific trend was observed. Additionally, it was found that under isothermal conditions the macroscopic orientation improved with decreasing shear frequency by approximately a factor of 1.7.

The herein performed measurements on a symmetric PS-b-PI diblock copolymer melt, which was used as a model compound, clearly showed that the newly developed, unique in-situ Rheo-SAXS setup is a powerful tool to derive novel insights to the mechanism and kinetics of the shear-induced alignment.

Furthermore, it could be shown that by optimizing the mechanical excitation conditions the overall alignment can be drastically enhanced. For example, by varying the applied LAOS conditions the degree of overall orientation, quantified by

134

$\sigma_{Min-SAXS}$, was improved by more than a factor of 2, from $\sigma_{Min-SAXS}$ = 13.4° ($\omega_1/2\pi$ = 3 Hz, γ_0 = 1, T = 150 °C) to $\sigma_{Min-SAXS}$ = 6° ($\omega_1/2\pi$ = 1 Hz, γ_0 = 2, T = 170 °C).

4.8. Molecular weight dependence of the shear-induced alignment

4.8.1. Linear mechanical characterization of PS-b-PI-17k-17k

In section **4** an extensive overview of the shear induced alignment of PS-b-PI-13k-13k was provided, regarding experimental parameters like frequency, strain amplitude and temperature. In this section the influence of the molecular weight to the de-ordering process is examined. For this propose, a PS-b-PI-17k-17k with M_w = 35,000 g/mol, f_{PS} = 49% and PDI = 1.06 was probed by in-situ Rheo-SAXS and FT-Rheology. To achieve a macroscopic isotropic initial state, the sample was heated 20 °C above the order disorder transition (T_{ODT} = 215 °C) before the LAOS experiments were performed.

The master curve of the mechanical linear response of the storage (G') and loss (G'') modulus as function of reduced frequency ($a_T*\omega/2\pi$) is presented in **Fig. 85** at T_{ref} = 160 °C. In contrast to the PS-b-PI-13k-13k diblock copolymer the PS-b-PI-17k-17k showed a slight onset of a rubber plateau which is indicated by the region C.
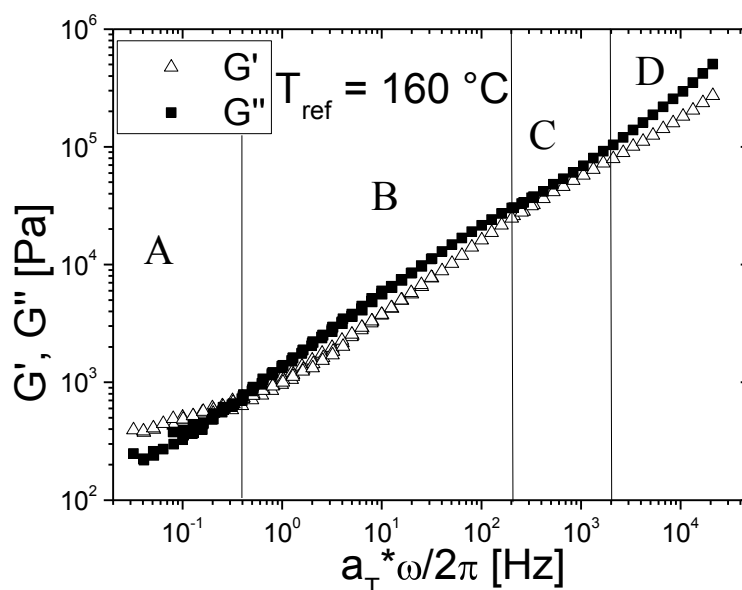
Fig. 85 Master curve of PS-b-PI-17k-17k at T_{ref} = 160 °C. The diblock copolymer shows an onset to a rubber plateau (region C) which indicates that the polymer chains are at the point to build up entanglements.

From the master curve for G" for temperatures above and below T_{ODT}, shown in **Fig. 86**, the critical frequency $\omega_c"/2\pi$ = 0.045 Hz was derived. Unfortunately, the master curve of G' and lη*l above the T_{ODT} could not be constructed as the measured data points showed strong fluctuations.

Nevertheless, form **Fig. 86** it can be seen that the chosen measurement frequency of $\omega_1/2\pi$ = 1 Hz was in the region in which LAOS generates a macroscopic perpendicular alignment.
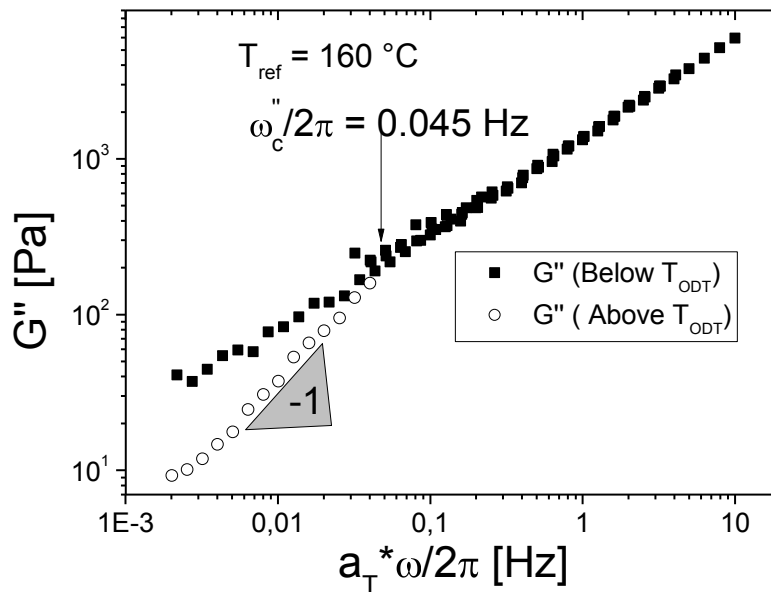
Fig. 86 Representation of the loss modulus G" versus reduced frequency at a reference temperature T_{ref} = 160 °C for PS-b-PI-17k-17k (T_{ODT} = 215 °C). The data for G" above the T_{ODT} represent the disordered melt behavior. The junction point between both curves is referred to be the critical frequency $\omega_c"/2\pi$ = 0.045 Hz.

4.8.2. In-situ Rheo-SAXS studies

Two different LAOS experiments were performed with strain amplitudes of γ_0 = 2 and γ_0 = 3 and a shear frequency of $\omega_1/2\pi$ = 1 Hz at T = 160 °C. The in-situ determined time dependent peak width of the azimuthally averaged first order reflection quantified by σ_{SAXS} is show in **Fig. 87**.

After a rapid exponential decrease in the beginning of the LAOS experiments, for both applied strain amplitudes a pronounced de-ordering was detected after a critical shear duration time of 700 s for γ_0 = 2 and 550 s for γ_0 = 3. For γ_0 = 2 the de-ordering occurred by a steep increase in σ_{SAXS} from 7.9° to σ_{SAXS} = 10.2°, followed by a region in which $\sigma_{SAXS}(t)$ increased over a period of 4500 s to approximately 11.1°. In this region the value of $\sigma_{SAXS}(t)$ showed strong undulations with varying amplitude and

wavelength. In contrast, for $\gamma_0 = 3$ the time progression of σ_{SAXS} showed a nearly monotonic rise from $\sigma_{SAXS} \approx 6°$ to $\sigma_{SAXS} = 9.7°$ over a period of 3800 s.
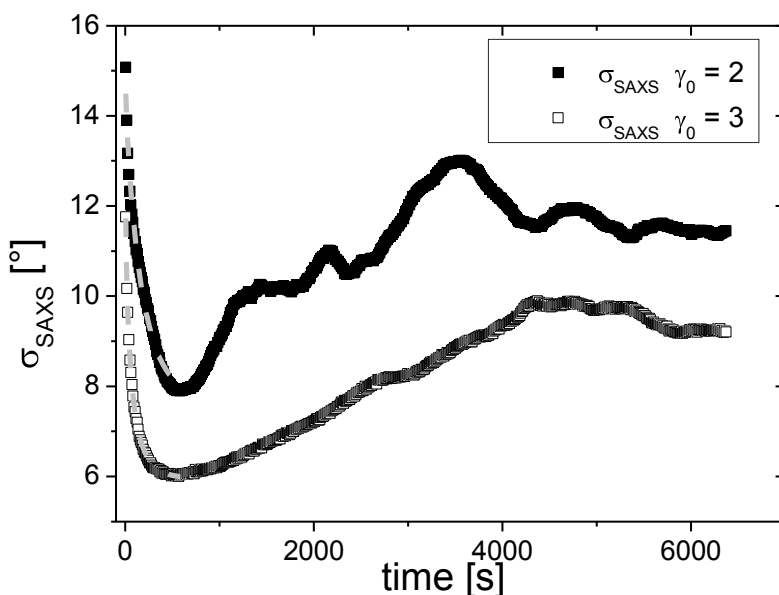
Fig. 87 Time dependence of σ_{SAXS} for the perpendicular orientation of PS-b-PI-17k-17k (T_{ODT} = 215 °C) ($\omega_1/2\pi$ = 1 Hz, T = 160 °C). The dotted lines represent the stretched exponential fit function.

The fit parameters calculated from the rapid drop of $\sigma_{SAXS}(t)$ in the beginning of the experiment are summarized in **Tab. 7**.

Strain (160 °C)	y_0 [°]	τ_o [s]	β	A [°]
2	7.7	167	0.87	8
3	5.9	63	0.71	7

Tab. 7 Calculated fit parameters from the in-situ determined time dependent σ_{SAXS} for PS-b-PI-17k-17k ($\omega_1/2\pi$ = 1 Hz, T = 160 °C) by applying a stretched exponential fit function ($y = y_0 + A \cdot e^{-(\frac{t-t_0}{\tau})^\beta}$).

4.8.3. Comparison of PS-b-PI-13k-13k and PS-b-PI-17k-17k

Before the two different molecular weight PS-b-PI diblock copolymers are compared with each other, it has to be clarified which measurement temperature of the low molecular weight PS-b-PI-13k-13k (T_{ODT} = 205 °C) corresponds to the mechanical properties of the PS-b-PI-17k-17k (T_{ODT} = 215 °C) at T = 160 °C.

To determine the corresponding experimental conditions, it seemed reasonable to compare the linear mechanical responses of both diblock copolymers, obtained at different temperatures.

Fig. 88 and **Fig. 89** represent the frequency dependence of G' and G'' for PS-b-PI-13k-13k at T = 150 °C and PS-b-PI-17k-17k at T = 160 °C respectively for PS-b-PI-13k-13k at T= 160 °C and PS-b-PI-17k-17k at T = 160 °C for small amplitude oscillatory shear. It can be seen that the linear mechanical response of PS-b-PI-13k-13k at T = 150 °C is similar to the of PS-b-PI-17k-17k at T = 160 C. In contrast, at equal temperatures the modulii of the two diblock copolymers showed significant differences. Therefore, the experimental data of PS-b-PI-13k-13k at T = 150 °C were chosen and directly compared to the shear-induced alignment of PS-b-PI-17k-17k at T = 160 C.
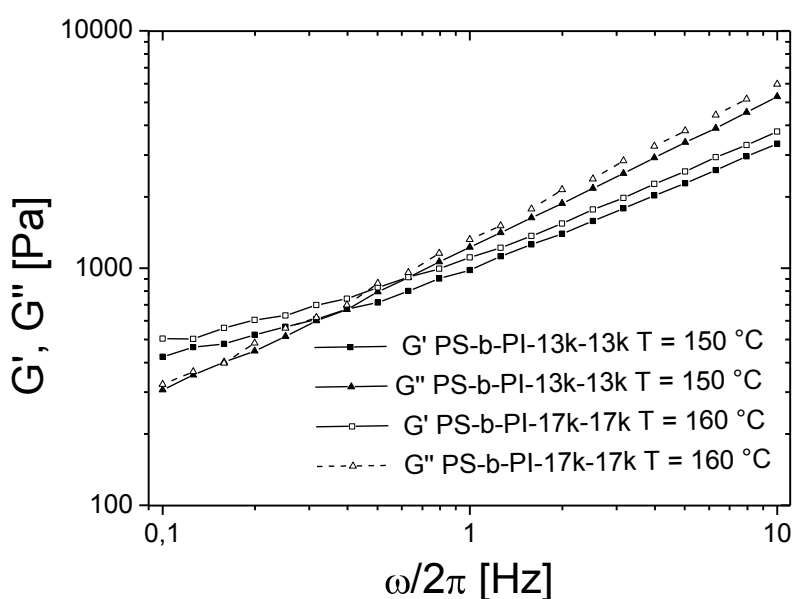
Fig. 88 Linear mechanical response of G'(square) and G''(triangle) at T = 150 °C for PS-b-PI-13k-13k (T_{ODT} = 205 °C) (filed symbols) and at 160 °C for PS-b-PI-17k-17k (T_{ODT} = 215 °C) (open symbols) obtained for γ_0 = 0.02.
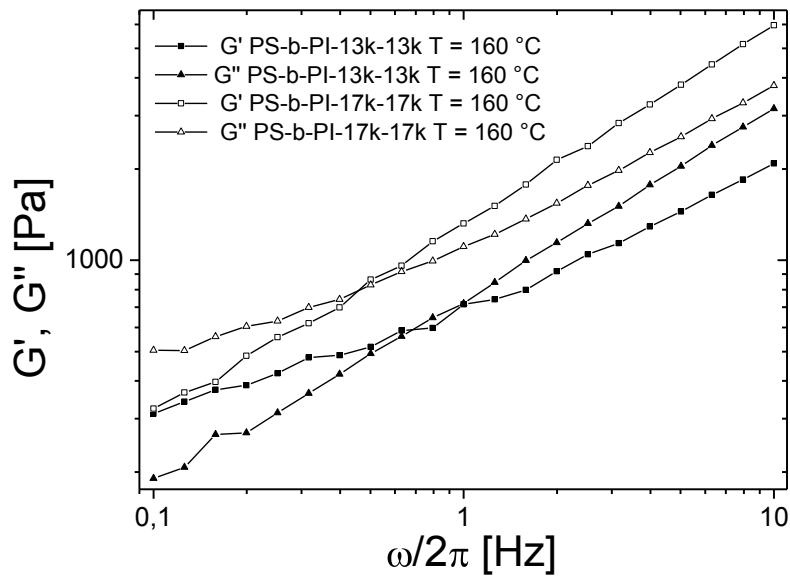
Fig. 89 Linear mechanical response of G'(square) and G"(triangle) at T = 150 °C for PS-b-PI-13k-13k (T_{ODT} = 205 °C) (filed symbols) and at 160 °C for PS-b-PI-17k-17k (T_{ODT} = 215 °C) (open symbols) obtained for γ_0 = 0.02.

Fig. 90 represents the time dependence of σ_{SAXS} for both diblock copolymers at γ_0 = 3. Both block copolymers show similar trends during LAOS. First a rapid exponential decay of $\sigma_{SAXS}(t)$ was obtained, leading into a minimum. As the mechanical stimulus proceeds a de-ordering of the well aligned perpendicular orientation was observed, indicated by an increase of $\sigma_{SAXS}(t)$.

However, the lower molecular weight diblock copolymer became less ordered, indicated by the minimum value of $\sigma_{Min-SAXS}$ = 9° for PS-b-PI-13k-13k compared to $\sigma_{Min-SAXS}$ = 7° which was obtained for PS-b-PI-17k-17k. Furthermore, the de-orientation which was observed for both polymers was delayed for PS-b-PI-17k-17k.
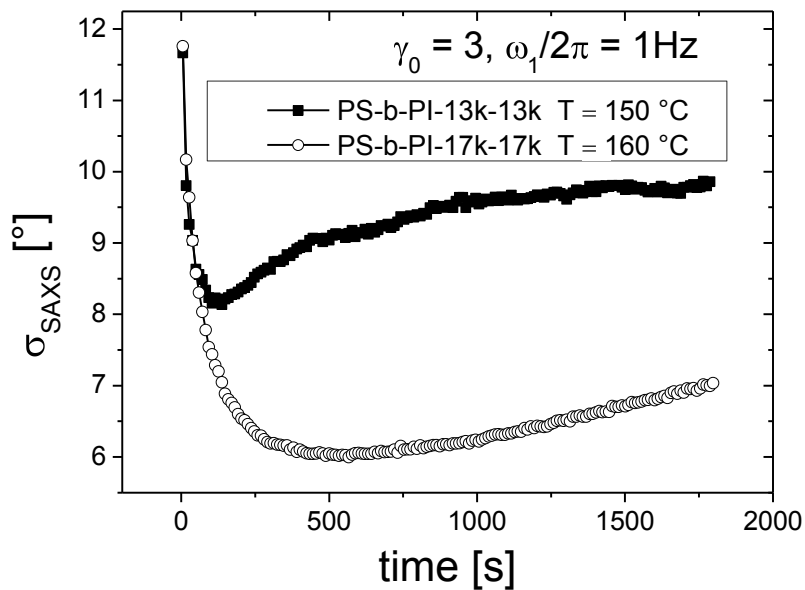
Fig. 90 Time dependence of σ_{SAXS} for PS-b-PI-13k-13k (T_{ODT} = 205 °C) (filled squares) at T = 150 °C and PS-b-PI-17k-17k (T_{ODT} = 215 °C) (open symbols) at T = 160 °C ($\omega_1/2\pi$ = 1 Hz, γ_0 = 3).

For γ_0 = 2 as shown in **Fig. 91** similar behaviors in the time progression of σ_{SAXS} were obtained. The lower molecular weight polymer became less ordered indicated by the higher $\sigma_{Min\text{-}SAXS}$ value of 9.4° while for PS-b-PI-17k-17k a value of $\sigma_{Min\text{-}SAXS}$ = 7.7° was achieved.
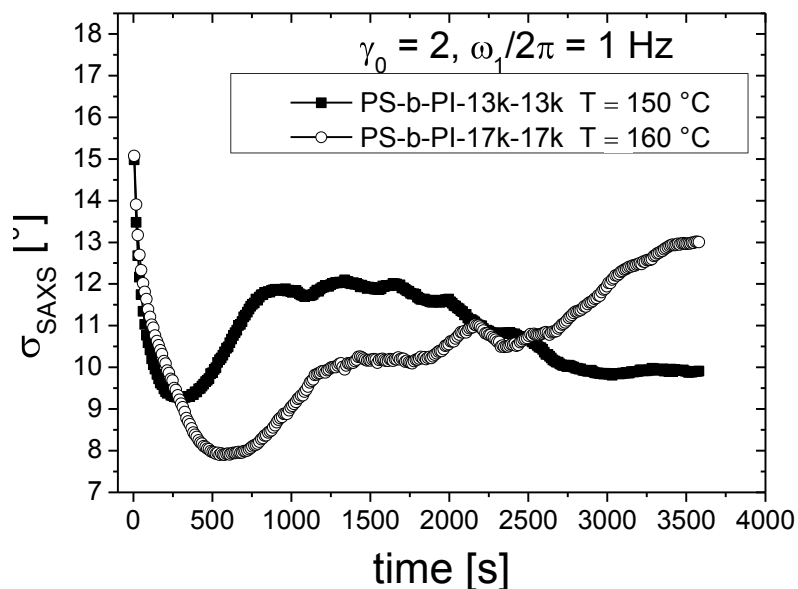
Fig. 91 Time dependence of σ_{SAXS} for PS-b-PI-13k-13k (T_{ODT} = 205 °C) (filled squares) at T = 150 °C and PS-b-PI-17k-17k (T_{ODT} = 215 °C) (open symbols) at T = 160 °C ($\omega_1/2\pi$ = 1 Hz, γ_0 = 2).

4.8.4. Molecular weight dependence detected by $I_{3/1}(t)$

For the ex-situ rheological studies three different strain amplitudes were applied ($\gamma_0 = 1$, $\gamma_0 = 2$ and $\gamma_0 = 3$) at T = 160 °C and $\omega_1/2\pi = 1$ Hz. **Fig. 92** shows the obtained time dependence of $I_{3/1}$ for the three different LAOS experiments. In the beginning of the LAOS experiments the characteristic stretched exponential drop was detected, followed by a plateau region which became more pronounced with decreasing strain amplitude. The fit parameters for the stretched exponential fit of the rapid decrease in the beginning of the experiments are summarized in **Tab. 8**.

The strain dependence of the orientation time $\tau_o(\gamma_0)$ showed the same power law dependence ($\tau_o \sim \gamma_0^{-1.6}$) as obtained from the experimental data of PS-b-PI-13k-13k.
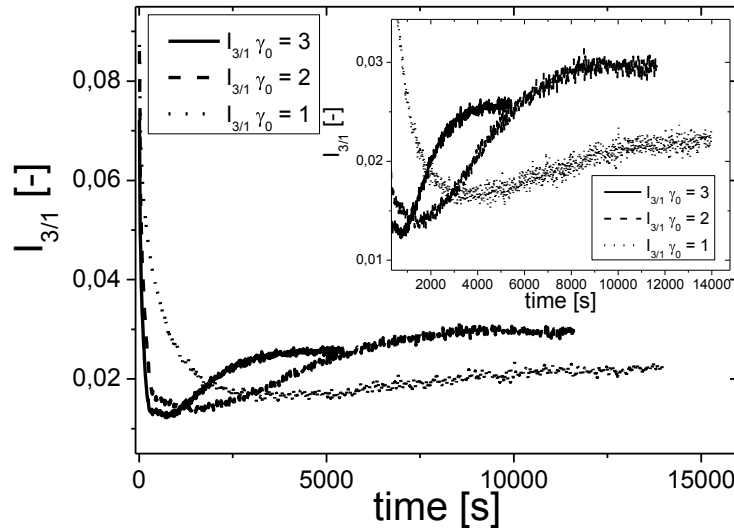
Fig. 92 $I_{3/1}(t)$ of PS-b-PI-17k-17k determined for $\gamma_0 = 1$ (dotted line), $\gamma_0 = 2$ (dashed line) and $\gamma_0 = 3$ (solid line) at T = 160 °C and $\omega_1/2\pi = 1$ Hz. Inset represent an enlargement of the onset of the de-ordering from the minimum of $I_{3/1}$.

For all applied strain amplitudes, a de-ordering process was observed, indicated by a drastic increase from the minimum value of $I_{3/1}(t)$. The critical shear duration t_c until the onset of the de-ordering process was observed, delayed with decreasing strain amplitudes ($t_c \approx 900$ s for $\gamma_0 = 3$, $t_c \approx 1400$ s for $\gamma_0 = 2$ and $t_c \approx 4000$ s for $\gamma_0 = 3$).

Strain (160 °C)	y_0 [-]	τ_o [s]	β	A [-]
1	0.015	375	0.61	0.069
2	0.014	91	0.76	0.07
3	0.012	65	0.77	0.012

Tab. 8 Calculated fit parameters from $I_{3/1}(t)$ as a function of time for PS-b-PI-17k-17k ($\omega_1/2\pi = 1$ Hz, T = 160 °C) by applying a stretched exponential fit function.

In comparison with the low molecular weight PS-b-PI-13k-13k diblock copolymer (see **Fig. 93**) $I_{3/1}(t)$ showed good similarities to the time progression of σ_{SAXS}. For higher molecular weights the minimum value of $I_{3/1}(t)$ is decreased while the onset of the de-ordering is retarded for PS-b-PI-17k-17k compared to PS-b-PI-13k-13k.
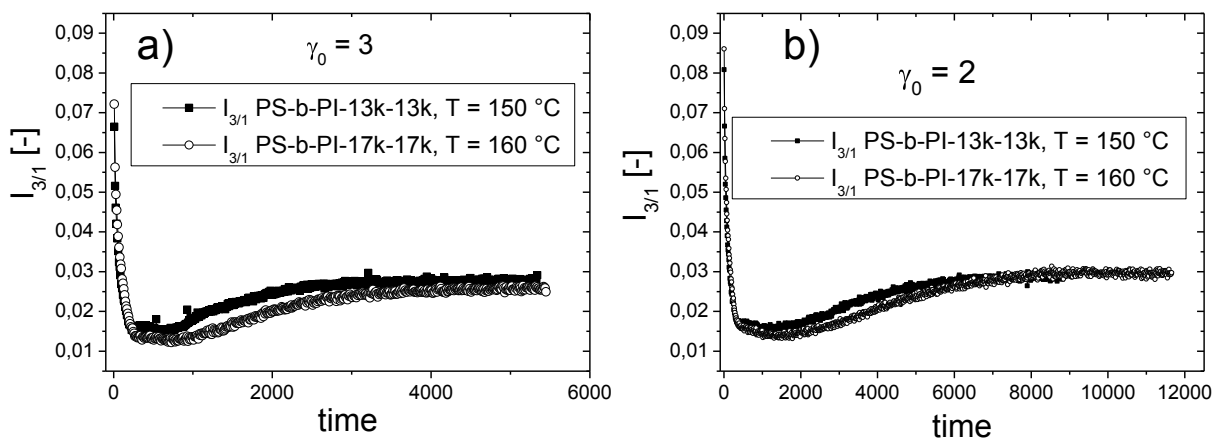
Fig. 93 Comparison of the time dependence of $I_{3/1}$ for PS-b-PI-13k-13k (filled squares) at T = 150 °C and PS-b-PI-17k-17k (open circles) at T = 160 °C for a) $\gamma_0 = 3$ and b) $\gamma_0 = 2$. The shear frequency was fixed to $\omega_1/2\pi = 1$ Hz.

4.9. Summary and discussion of the shear-induced alignment

4.9.1. Implication of the macroscopic alignment mechanism

The results obtained by in-situ Rheo-SAXS measurements indicated a significant correlation between the time dependence of the structural changes and the dynamic mechanical response of the sample melt. The former were quantified by the time evolution of the standard deviation σ_{SAXS} calculated from the azimuthally averaged first order reflection in the 2D-SAXS scattering pattern. The latter by the dominant viscoelastic property, the mechanical loss modulus G'', and the non-linear parameter $I_{3/1}$. The effect of the varying applied LAOS conditions (e.g. strain amplitude, frequency, temperature and molecular weight) to the orientation distribution of the lamellae self assembled microdomains are summarized in **Tab. 9**.

LAOS-Conditions	Impact on alignment kinetic determined by σ_{SAXS}	Impact on de-ordering determined by σ_{SAXS}	Non-linear mechanical response quantified by $I_{3/1}$
Strain dependence	➢ Power law $\tau_o \sim \gamma_0^{-1.6}$ (**Fig. 76**, **Fig. 83**) ➢ Improved alignment with increasing γ_0 (**Fig. 71**, **Fig. 84**) ➢ Linear dependence of $\sigma_{Min-SAXS}$ to γ_0 (**Fig. 84**)	➢ For $\gamma_0 > 1$ de-ordering occurred at T = 150 °C (**Fig. 55**) ➢ Final biaxial macroscopic orientation (**Fig. 73**) ➢ De-ordering occurred earlier (**Fig. 55**)	➢ Power law $\tau_o \sim \gamma_0^{-2}$(**Fig. 76**) ➢ de-ordering causes increase of $I_{3/1}$ (**Fig. 74**) ➢ Onset of de-ordering began earlier with increasing γ_0 (**Fig. 64, Fig. 92**)
Frequency dependence	➢ Inverse dependence of $\tau_o \sim \omega_1/2\pi^{-1}$ (**Fig. 78**) ➢ Lower frequencies increased the macroscopic orientation (**Fig. 80**) ➢ Linear dependence of $\sigma_{Min-SAXS}$ to $\omega_1/2\pi$ (**Fig. 80**)	➢ Complex frequency dependence (**Fig. 77**)	➢ Increased orientation times with decreasing frequency ➢ Onset of de-ordering delayed for lower frequencies (**Fig. 81**) ➢ Duration and magnitude of de-ordering extended (**Fig. 81**)
Temperature dependence	➢ Increasing temperature enhanced the alignment: $\sigma_{Min-SAXS}$ (**Fig. 82**) ➢ Orientation time τ_o increased with increasing temperature (**Tab. 6**)	➢ Temperature strongly affected de-ordering (**Fig. 82**) ➢ Higher temperatures caused a retarded de-orientation (**Fig. 82**)	➢ Orientation time τ_o increased with increasing temperature ➢ No specific dependence on the minimum value of $I_{3/1}$ was detected
Molecular weight dependence	➢ Orientation time τ_o was increased with increasing molecular weight ➢ Quality of overall orientation was enhanced with increasing molecular weight (**Fig. 90, Fig. 91**)	➢ De-ordering was retarded with increasing molecular weight (**Fig. 90**, **Fig. 91**) ➢ De-ordering increased with the molecular weight (**Fig. 91**)	➢ De-ordering was delayed (**Fig. 93**) ➢ No significant changes in the magnitude of the de-ordering process (**Fig. 93**)

Tab. 9 Summary of the different LAOS conditions and their impact on the macroscopic orientation, de-orientation and mechanical non-linear response quantified by $I_{3/1}$.

In all LAOS experiments a rapid drop in the measured quantities was detected, reflecting the increasing orientation of the lamella microstructures. With increasing strain amplitude, this process was accelerated, meaning that the rapid drop in the observed mechanical and structural parameters became even more pronounced during the LAOS experiments at higher γ_0. These findings are consistent with the results obtained by Chen et al.[84] who used in-situ birefringence and ex-situ SAXS studies to monitor the progress of macroscopic orientation. From the agreement between the shear-induced structural changes determined via 2D-SAXS and the mechanical no-linear response quantified by $I_{3/1}$, it can be seen that there is a correlation between the non-linear mechanical response and the development of the aligned macroscopic structure.

Furthermore, it was confirmed that the perpendicular orientation process began with an elimination of the orientation distribution with the unit normal of the lamellae being orientated preferentially along the transverse (*OX* axis) direction. This elimination process was more pronounced at higher strain amplitudes and was reduced travelling from the outside edge of the parallel plate to its center. Next, the remaining orientation distribution was converted into a macroscopic system with preferentially perpendicularly orientated lamellae microstructures. It could be shown that the plateau values of the non-linear mechanical parameter corresponded to a temporally stable state of macroscopic alignment that remained constant for $\gamma_0 \leq 1$ at T = 150 °C.

For the first time, it could be shown that depending on the experimental conditions the achieved degree of macroscopic orientation was not stable as the mechanical excitation continued above a certain point. This state of orientation then became de-orientated under further mechanical stimulus, resulting in a broadening of the orientation distribution and the development of a biaxial distribution with approximately equal amounts of microdomains having parallel and perpendicular orientations for $\gamma_0 > 1$ at T = 150 °C.

The ex-situ 2D-SAXS measurements revealed that $I_{3/1}$ characterized the progress of macroscopic orientation in a reasonable and reproducible way. Furthermore, $I_{3/1}(t)$ was sensitive to the de-ordering process by exhibiting a significant increase as the de-ordering takes place. It must be noted that the mechanical loss modulus G'' also showed variations from a stretched exponential decaying trend, but G'' exhibited a

different time progression for the rheological measurements carried out with the stress controlled (Mars II, Thermo Scientific) respectively the strain controlled (ARES, TA-Instruments) Rheometer which could not be explained reasonable yet.

As suggested in previous work[159, 168], it was now proven that non-linear mechanical characterization as determined via FT-Rheology was able to follow macroscopic alignment processes in real time because it is also sensitive to complex structural dynamics. This agreement inspired the idea of adopting a proposed rotational orientation mechanism instead of a selective layer melting mechanism, as a possible pathway for the perpendicular alignment and the de-ordering process[30, 155, 172]. Even though, Gupta et al.[160] concluded by the examined strain dependency of the macroscopic alignment at a fixed frequency and temperature that the kinetic pathway of the macroscopic orientation cannot be satisfactorily explained by either of the mechanisms suggested above.

For several experimental conditions (T, $\omega_1/2\pi$, γ_0) described above which caused a macroscopic perpendicular alignment a de-ordering of the well aligned macroscopic anisotropic structure was observed as the mechanical stimulus proceeded, resulting in a final biaxial orientation. This final state of overall alignment was a function of the shear duration only, which was achieved under isothermal conditions by applying a single excitation frequency and deformation amplitude. If it is assumed that the applied experimental conditions were at the vicinity of the transition point between the melting and rotation mechanisms governing the perpendicular and parallel alignment process, then the dynamic shear field would lead directly to a biaxial orientation, as neither the parallel nor the perpendicular alignment would be preferred. However, the results shown above indicate that the pathway to the biaxial orientation developed instead in two steps. First, a well-aligned perpendicular state was observed, which became unstable as the oscillating mechanical stimulus continued, and then, finally, de-ordered to create the final stable biaxial orientation which in some cases was achieved by strong undulations during the de-orientation process.

On the basis of these results, a rotation mechanism of the locally ordered block copolymer grains is proposed for these experimental conditions. In the following section, a detailed discussion on the kinetics of the rotation mechanism and its effect on the non-linear response as quantified by $I_{3/1}$ is provided. It should be noted that these assumptions are based on the results obtained by in-situ Rheo-SAXS

measurements, which confirmed that the de-ordering process occurred in the melt state and led directly to a broadening of the azimuthally averaged first order scattered reflection and was, therefore, not a result of factors necessary for ex-situ studies, such as cooling and sample preparation. On the other hand, additional FT-Rheology and ex-situ 2D-SAXS measurements provided insight into the mechanical non-linear response and structural changes along all three spatial directions.

4.9.2. Correlation between structural changes and mechanical response

A schematic sketch of the proposed macroscopic perpendicular alignment process under the applied conditions is provided in **Fig. 94**. This sketch represents the orientation process until the overall perpendicular alignment was achieved, i.e. until $I_{3/1}$ reached its minimum, not considering the de-orientation process. The direction of the unit normal of the lamellae in one locally ordered block copolymer grain is represented as a vector.

It is propose that the applied large amplitude oscillatory shear caused a rotation of the microdomains. Therefore, the various locally anisotropically ordered microdomains with their unit normal pointing statistically into all spatial directions can be regarded in terms of defects and nucleation points. Specifically, the grains possessing a lamellae unit normal with a spatial orientation that is different than the energetically favored macroscopic aligned final state, i.e. the perpendicular alignment, were considered as defects. Grains with the unit normal of their lamellae microdomains orientated in approximately the perpendicular direction (parallel to the *OX* axis) were instead regarded as nucleation points.
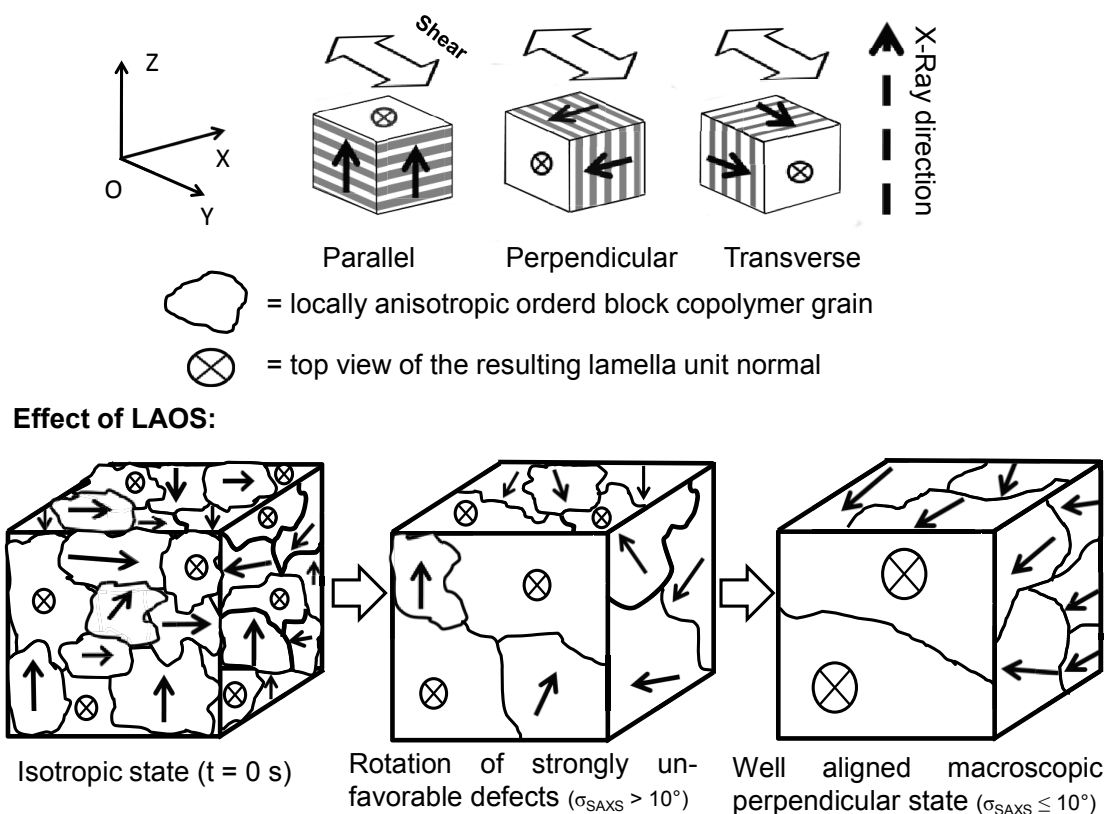
Fig. 94 Schematic representation of the shear-induced alignment of a PS-b-PI diblock copolymer melt. The unit normal of the lamellae of the locally ordered isotropic block copolymer grains are indicated by arrows and on the top view by circles with a cross. For further explanation see text.

The initial macroscopically isotropic sample melt had a randomly orientated unit normal of the locally isotropic ordered microdomain grains. Each orientation has a different energy level with respect to the shear direction, which depends on the spatial orientation of the lamella unit normal, the size and shape of the locally ordered block copolymer grain. By applying large amplitude oscillatory shear to the polymer melt, the grains which posses the most unfavorable energy levels will be rotated into the perpendicular orientation first. As the macroscopic alignment proceeds, the number of grains which do not have the favorable orientation is reduced. This process led to the final macroscopically perpendicular aligned sample melt, which was proven by in- and ex-situ 2D-SAXS studies.

As the grains were rotated into the preferred perpendicular alignment ((OX, OY) plane), some grain interfaces will vanish and larger grains will develop. The time evolution of the radial averaged first order reflection (see **Fig. 95**), indicated that the development of larger grains was not significant during the orientation process as this value varied from only 4% ($\gamma_0 = 0.5$) to 14% ($\gamma_0 = 3$) with respect to its initial and final value.

147
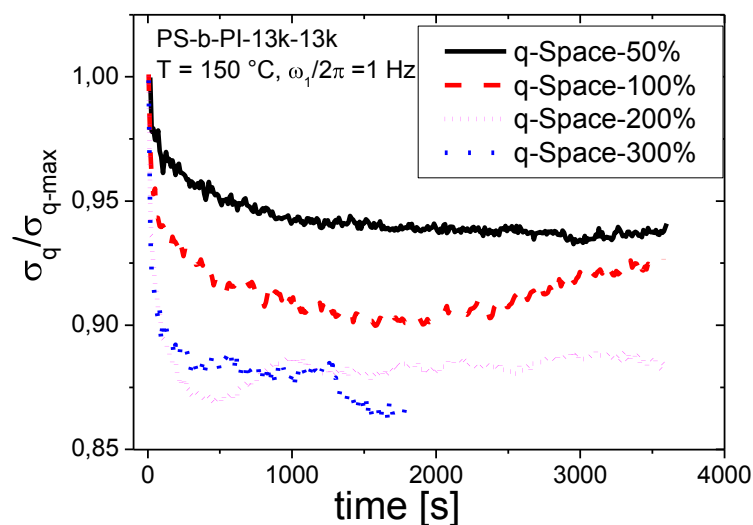
Fig. 95 Time dependence of the peak width of the radial averaged first order reflection obtained from in-situ Rheo-SAXS measurements for PS-b-PI-13k-13k at T = 150 °C, $\omega_1/2\pi$ = 1 and four different strain amplitudes.

To derive a dependency between the structural changes and the mechanical response, it was assumed that the locally ordered grains in the block copolymer melt, which have a size in the sub-micrometer range, were surrounded by an interface which separates each block copolymer grain. In a recent study, it was shown that the non linear response even for two Newtonian fluids in an emulsion is caused by interfacial tension[71, 173]. Therefore, originates as interfaces are deformed during a mechanical stimulus.

The rotation of the locally anisotropic ordered grains by LAOS will cause a deformation of the surrounding interfaces where this deformation results in a mechanical non-linear response that can be monitored and quantified using the non-linear parameter $I_{3/1}$. As the LAOS experiment proceeded, the amount of defects was reduced and, therefore, the number and extent of deformed microdomain surfaces was also reduced causing a decrease in the non-linear mechanical response. This idea is supported by the result that the observed low value plateau for $I_{3/1}$ which was evident at all LAOS experiments described above, corresponded to a well-aligned perpendicular orientation as confirmed by 2D-SAXS measurements. These results support the assumption that the non-linear response during shear-induced orientation of block copolymer melts was primarily caused by the deformation of the grain interfaces during rotational alignment and not by the interface between the two polymer constituent PS and PI.

148

The above suggested mechanism may also explain the detected increase of $I_{3/1}$ for strain amplitudes $\gamma_0 > 1$. As the in-situ Rheo-SAXS studies showed, the development of the biaxial orientation occurred by a broadening of the orientation distribution in the (OX, OY) plane. This would cause a further mechanically induced rotation of the block copolymer grains and an increase in the value of the non-linear response, which was, in fact, seen. Nevertheless, the underlying process which governs the de-orientation process is not understood, yet.

5. Re-orientation experiments of PS-b-PI diblock copolymers

All shear-induced alignment experiments introduced so far were performed with PS-b-PI diblock copolymer melts which were initially macroscopic isotropic. The isotropic initial state was achieved by heating the sample above the order disorder temperature to remove undesired pre-alignments of the lamellae microstructure. In this section a brief introduction to so called re-orientation experiments[159] of PS-b-PI diblock copolymers with different molecular weights is provided.

On the one hand re-orientation experiments are especially useful for the investigation of the shear-induced alignment of PS-b-PI diblock copolymers with high molecular weights (M_w > 40,000 g/mol). These block copolymers revealed the problem that it was not possible to reach the order disorder transition in the experimental accessible temperature range (T_{max} = 250 °C). Therefore, no uniform initial orientation could be achieved as due to shear history caused by sample preparation and loading procedures macroscopic anisotropies were already present in the sample melt (see Fig. 103). These undesired pre-alignments made it impossible to perform experiments under reproducible conditions.
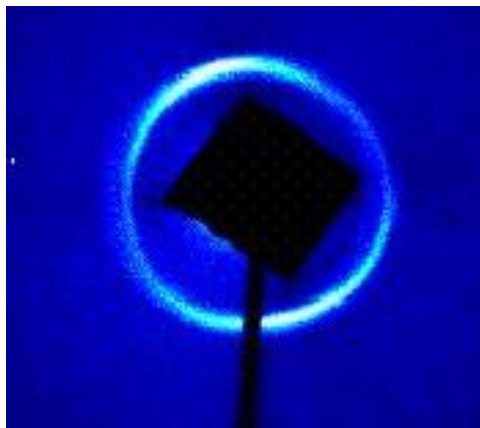
Fig. 96 2D-SAXS scattering pattern of PS-b-PI-32k-27k with induced alignments due to sample loading procedure at T = 180 °C. The T_{ODT} was higher than the experimental accessible temperature range. Therefore, no macroscopic isotropic initial state could be achieved.

To overcome this drawback a defined macroscopic alignment was generated using controlled large amplitude oscillatory shear (LAOS) conditions. Afterwards the macroscopic orientated sample melt was subjected to differing experimental conditions which were capable to re-orientate the defined initially macroscopic

ordered state into a new overall orientation with respect to the orientation of the unit normal of the lamellae to the shear flow.

On the other hand, the investigation of the re-orientation of a macroscopic well aligned sample melt reveals new insights into the stability and the re-ordering mechanism. It is important to notice that re-orientation experiments were already reported in literature utilizing in-situ[161] and ex-situ[159] structural analysis methods.

Nevertheless, with the unique Rheo-SAXS combination the re-orientation mechanism can be studied under precise rheological conditions while obtaining additional information about microstructural changes on an experimental time scale (t = 10 s) which until now has not been available. In the following four different re-orientation experiments are presented which were performed with the in-situ Rheo-SAXS setup.

The first re-orientation experiment introduced here was subjected to a PS-b-PI-20k-20k with a T_{ODT} above 250 °C. The sample melt was macroscopic perpendicular pre-aligned by applying a strain amplitude of $\gamma_0 = 3$ with $\omega_1/2\pi = 3$ Hz at T = 170 °C for two hours. The in-situ scattering pattern indicated a well aligned overall perpendicular orientation ($\sigma_{Min-SAXS} = 10.4°$) (see **Fig. 97**). Additional, no de-ordering was detected in this preliminary alignment step.

In the following re-orientation experiment the sample melt was cooled to 130 °C by thoroughly adjusting the gap to avoid squeeze flow alignments. Based on ex-situ SAXS measurements which revealed a parallel orientation at T = 130 °C for $\omega_1/2\pi = 3$ Hz and $\gamma_0 = 1$, the experimental conditions for the re-orientation from a macroscopic perpendicular orientation into a parallel orientation were set to T = 130 °C, $\omega_1/2\pi = 3$ Hz and $\gamma_0 = 0.7$. The lower strain amplitude had to be selected as for higher strain amplitudes the torque during the measurements with the Rheo-SAXS setup would have exceeded the instrumental limit.

Fig. 97 shows the in-situ measured time dependence of the orientation distribution of the lamellae microstructure with the unit normal of the lamellae parallel to the (*OX, OY*) plane for PS-b-PI-20k-20k. From the 3D-contour plot it can be seen that the initially perpendicular state was "torn apart", leading to a scattering pattern with four reflections. This four-fold scattering pattern was present throughout the LAOS experiment.

• **Perpendicular to Parallel:**

Two-fold Four-fold
(90, 270 °C, $\sigma_{Min\text{-}SAXS}$ = 11.4°)

(intermediate state)
reorientation time too short)
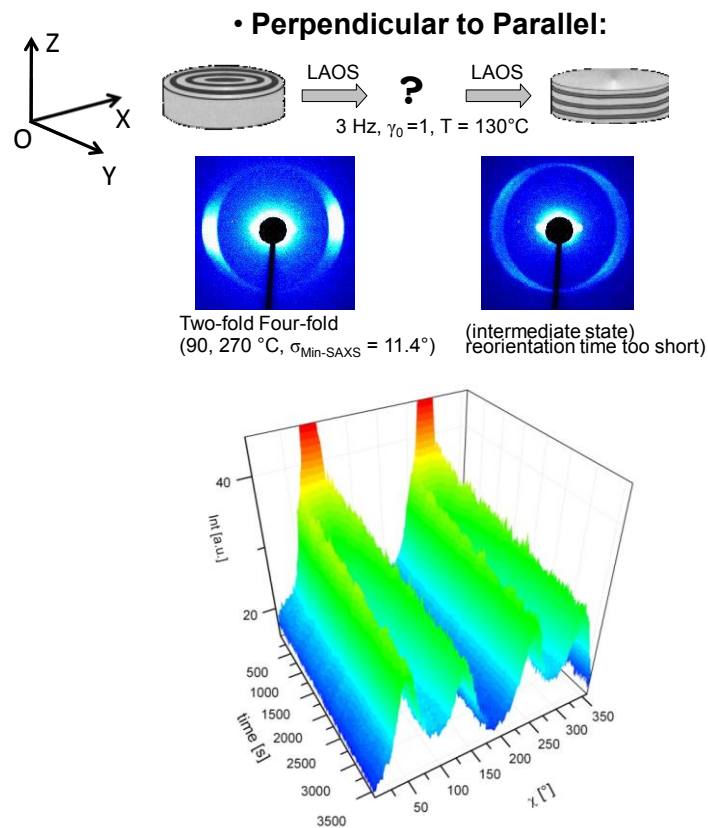
Fig. 97 Re-orientation experiment for PS-b-PI-20k-20k. The sample melt was initially perpendicular aligned ($\omega_1/2\pi$ = 3 Hz, T = 170 °C, γ_0 = 3) and afterwards subjected to different LAOS conditions (T = 130 °C, $\omega_1/2\pi$ = 3 Hz and γ_0 = 0.7) which should re-orientate the perpendicular alignment into a parallel alignment. The 3D-contour plot represents the time evolution of the 2D-SAXS patterns in the (OX, OY)-plane.

A similar re-orientation experiment was performed with a low molecular weight PS-b-PI-13k-13k which was perpendicular orientated beforehand ($\omega_1/2\pi$ = 1 Hz, γ_0 = 1, T = 150 °C). To re-orientate the macroscopic perpendicular alignment into the parallel one the experimental conditions were set to T = 120 °C, $\omega_1/2\pi$ = 3 Hz and γ_0 = 0.7. Form the in-situ detected structural development in the (*OX*, *OY*) plane (see **Fig. 98**). It can be seen that in the beginning also a four-fold scattering pattern is obtained. However, this state of alignment seemed to be unstable as the mechanical stimulus proceeded and the lamellae diblock copolymer grains were rotated again into the preferentially perpendicular orientation and the four-fold pattern merged into a two-fold scattering pattern with a preferentially perpendicular alignment.

• Perpendicular to Parallel:
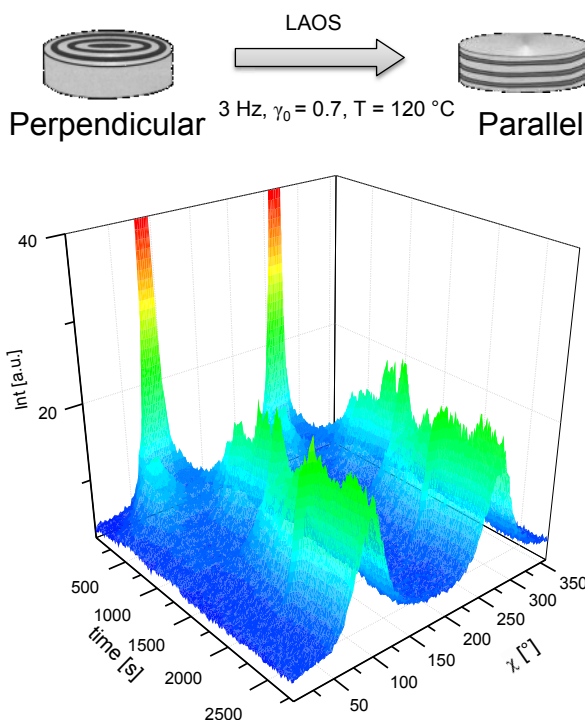
Fig. 98 Re-orientation experiment for PS-b-PI-13k-13k. The sample melt was initially perpendicular aligned ($\omega_1/2\pi$ = 1 Hz, γ_0 = 1, T = 150 °C) and afterwards subjected to different LAOS conditions (T = 120 °C, $\omega_1/2\pi$ = 3 Hz and γ_0 = 0.7) which should re-orientate the perpendicular alignment into a parallel alignment. The 3D-contour plot represents the time evolution of the 2D-SAXS patterns in the (OX, OY)-plane.

A further re-orientation experiment had the aim, to transfer a macroscopic perpendicular alignment into a parallel alignment at isothermal conditions. Therefore, a PS-b-PI-13k-13k was preliminary perpendicular aligned with $\sigma_{\text{Min-SAXS}}$ = 12.8° ($\omega_1/2\pi$ = 1 Hz, γ_0 = 1, T = 160 °C, t = 1800 s). The re-orientation was carried out at T = 160 °C, $\omega_1/2\pi$ = 0.01 Hz and γ_0 = 1. The applied shear frequency was below the critical frequency $\omega_c/2\pi$, as discussed in section **4** ($\omega_c/2\pi$ > 0.03 Hz), indicating a macroscopic parallel alignment during LAOS.

The in-situ 2D-SAXS pattern showed a oscillation in the peak intensity thorough out the LAOS experiment. The intensity of the first order reflection increased and decreased with maxima of intensity after 25 s and 75 s, respectively. These oscillation directly correlate to the applied mechanical excitation frequency of $\omega_1/2\pi$ = 0.01 Hz as schematically shown in **Fig. 100**.

• Perpendicular to Parallel:

Perpendicular 0.01 Hz, $\gamma_0 = 1$, T = 160°C

Flipping
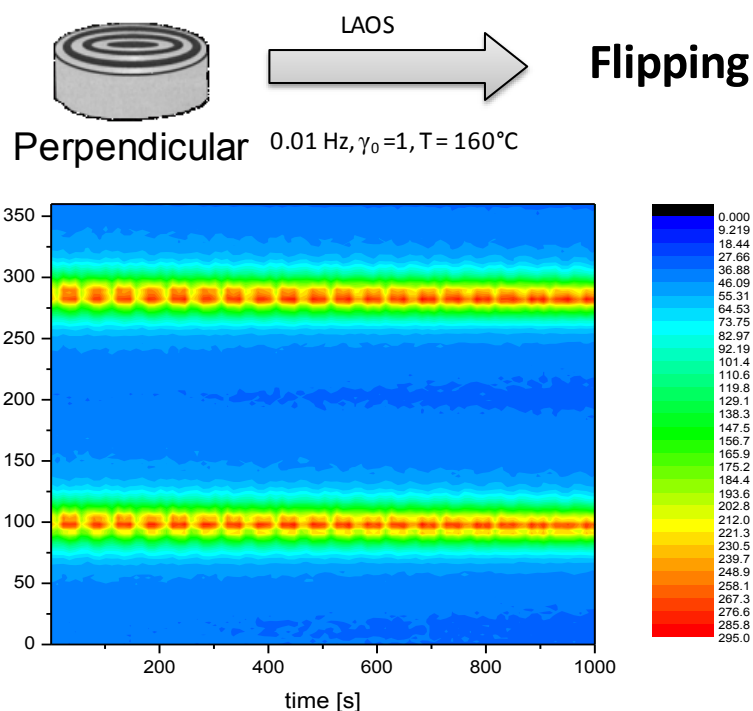
LAOS

Fig. 99 Re-orientation experiment for PS-b-PI-13k-13k. The sample melt was initially perpendicular aligned ($\omega_1/2\pi$ = 1 Hz, γ_0 = 1, T = 160 °C, $\sigma_{Min-SAXS}$ = 12.8°) and afterwards subjected to different, but isothermal LAOS conditions ($\omega_1/2\pi$ = 0.01 Hz, γ_0 = 1, T = 160 °C) which should re-orientate the perpendicular alignment into a parallel alignment. The 3D-contour plot represents the time evolution of the 2D-SAXS patterns in the (OX, OY)-plane.

Fig. 110 represents the peak width of the azimuthally averaged first order reflection quantified by σ_{SAXS} as a function of time. It can be seen that the peak width oscillates with the same frequency as the mechanical excitation frequency ($\omega_{mech}/2\pi$ = 0.01 Hz). However, the amplitude varied during one period of mechanical oscillation. Unfortunately, at the present state of investigation no reasonable explanation of this phenomenon can be provided. Nevertheless, the in-situ 2D-SAXS data clearly show that LAOS only caused a "flipping" of the lamellae microdomains with no relevant detectable re-orientation. It is important to note that the phenomenon of grain "flipping" was also detected for other PS-b-PI diblock copolymers with higher molecular weights such as PS-b-PI-20k-20k, as long the strain amplitude was sufficient high (γ_0 > 0.5) and the shear frequencies sufficient low ($\omega_1/2\pi$ < 0.1 Hz).
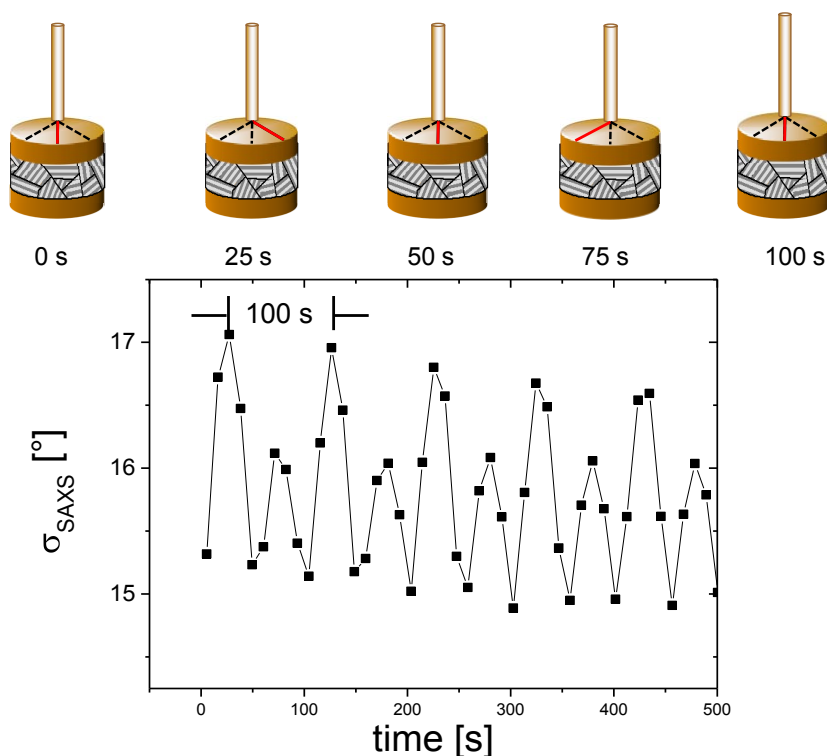
Fig. 100 $\sigma_{SAXS}(t)$ of the re-orientation of PS-b-PI-13k-13k. The sample melt was initially perpendicular aligned ($\omega_1/2\pi$ = 1 Hz, γ_0 = 1, T = 160 °C, $\sigma_{Min\text{-}SAXS}$ = 12.8°) and afterwards subjected to different, but isothermal LAOS conditions ($\omega_1/2\pi$ = 0.01 Hz, γ_0 = 1, T = 160 °C) which should re-orientate the perpendicular alignment into a parallel alignment. The sketch above illustrates the deformations of the upper geometry at specific times. The red line shows the degree of deformation during one mechanical oscillation.

The last two re-orientation experiments presented here contribute to a relatively rare macroscopic orientation, the transverse alignment (unit normal of the lamellae directed parallel to the shear direction). Throughout the LAOS experiments performed in this thesis, this orientation was only observed during the in-situ Rheo-SAXS experiments at a relatively low temperature (T = 120 °C) and high shear frequencies ($\omega_1/2\pi$ > 5 Hz) for PS-b-PI-13k-13k. The transverse alignment was indicated by reflection at χ = 0° and χ = 180°.

To re-orientate into the macroscopic parallel alignment (see **Fig. 101**) the LAOS experiment was performed at isothermal conditions (T = 120 °C) with respect to the temperature at which the initial alignment was achieved. The strain amplitude was adjusted to γ_0 = 1 and the shear frequency was set to $\omega_1/2\pi$ = 1 Hz. Form the 3D-contour plot in **Fig. 101** it can be seen that the re-orientation occurred on a time scale of minutes with a strong broadening of the initial transverse peak in the (*OX, OY*) plane.

• Transverse to Parallel:
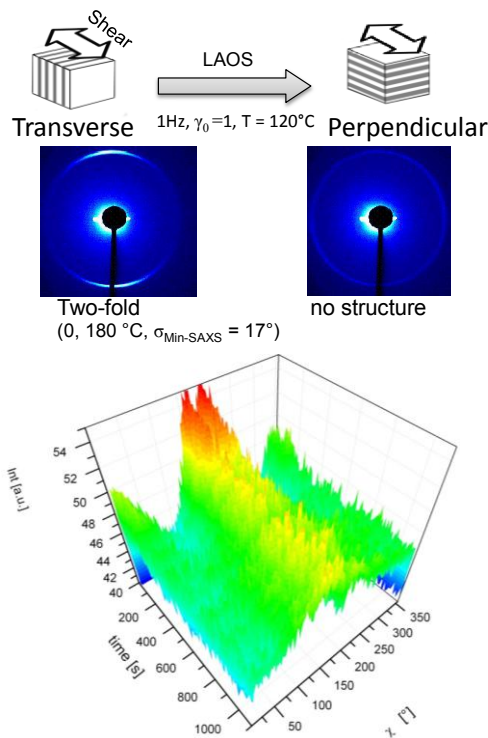
Fig. 101 Re-orientation experiment for PS-b-PI-13k-13k. The sample melt was initially transverse ($\omega_1/2\pi$ = 10 Hz, γ_0 = 0.5, T = 120 °C, $\sigma_{Min-SAXS}$ = 17°) aligned and afterwards subjected to different, but isothermal LAOS conditions (T = 120 °C, $\omega_1/2\pi$ = 1 Hz and γ_0 = 1) which should re-orientate the transverse alignment into a parallel alignment. The 3D-contour plot represents the time evolution of the 2D-SAXS patterns in the (OX, OY)-plane.

In contrast the re-orientation of a transverse alignment for PS-b-PI-13k-13k into a macroscopic perpendicular orientation performed at T = 150 °C, $\omega_1/2\pi$ = 3 Hz and γ_0 = 3 occurred in between seconds as indicated by the two strong reflections in the 2D-SAXS scattering pattern at χ = 90° and χ = 270° (see **Fig. 102**).

• Transverse to Perpendicular:

Transverse 3 Hz, $\gamma_0 = 1$, T = 150°C Perpendicular

Two-fold Two-fold

(0, 180°, $\sigma_{\text{Min-SAXS}}$ = 25°) (90°, 270°, $\sigma_{\text{Min-SAXS}}$ = 11°)

Time: 0 s 10 s
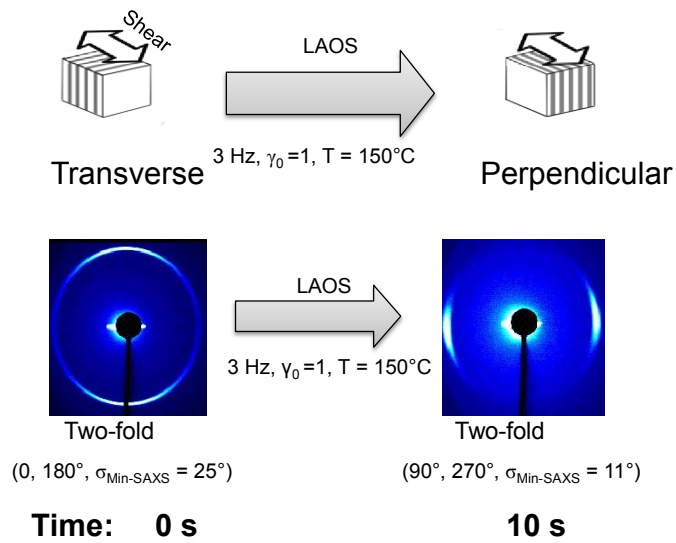
Fig. 102 Re-orientation experiment for PS-b-PI-13k-13k. The sample melt was initially transverse aligned and afterwards subjected to different LAOS conditions (T = 150 °C, $\omega_1/2\pi$ = 3 Hz and γ_0 = 3) which re-orientates the transverse alignment into a perpendicular alignment.

These were the first re-orientation experiments performed with the new and unique Rheo-SAXS setup. The herein presented results have to be examined in more details for a comprehensive understanding of the underlying mechanism of the re-orientation.

6. Rheo-Dielectric studies of the shear-induced alignment

Polyisoprene is one of the few known polymers with a non-vanishing dipole moment along the polymer backbone (type A polymer)[125]. This enables the detection of large scale chain motions, the so called normal mode which is directly correlated to the motion of the end-to-end vector. Numerous studies on the dynamics of polyisoprene chains observed by the dielectric normal mode under various conditions have been reported in literature, see ref.[88, 122, 124, 127, 174] and literature cited there. However, only little attention has been subjected to the simultaneous investigation of PS-b-PI block copolymers melts under LAOS.

The aim of the studies described below was the in-situ investigation of the macroscopic alignment process of PS-b-PI diblock copolymers with a high sensitive Rheo-Dielectric setup[33]. Therefore, the normal mode of the PI block was taken as the significant dielectric response to online follow the alignment process. Additionally, for the in-situ studies of the macroscopic alignment process a brief introduction to the dielectric relaxation of the linear homopolymers is provided.

6.1. Dielectric relaxation spectra of PS, PI and PS-b-PI

In **Fig. 103** the dielectric relaxation spectrum for a PI-20k (M_w = 19,800 g/mol, PDI = 1.03) is shown for a frequency range between 0.1 Hz and 1 MHz at different temperatures. The two different relaxation processes (normal mode and segmental mode) are highlighted by arrows. With increasing temperature the relaxation modes are shifted to higher temperatures indicating an Arrhenius activated process. It can be seen that the normal mode occurs on a time scale which is orders of magnitude lower than the segmental mode of the PI chains.
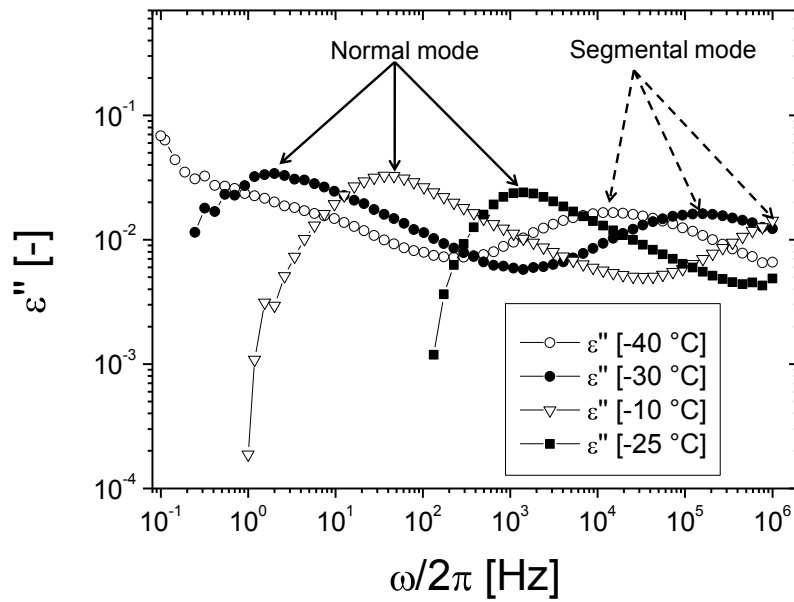
Fig. 103 Dielectric relaxation spectrum for a PI-20k at different temperatures (M_w = 19800 g/mol, PDI = 1.03).

In contrast to the dielectric loss ε'' spectra of the polyisoprene chains, the polystyrene chains (shown in **Fig. 104**) exhibit only one relaxation process in the investigated frequency range which is caused by the non-vanishing dipole moment perpendicular to the polymer backbone (segmental mode, Stockmeyer *B*). Form the frequency behavior of the dielectric loss at T = 110 °C, which is in the vicinity of the glass transition (T_g(PS-100k) $\approx$ 110 °C), it can be seen that the segmental mode is strongly broadened as the measurement temperature reaches the T_g. These finding is consistent with results observed in literature[175]. Above the glass transition the segmental mode is shifted to higher frequencies with increasing temperature. The increase on the low frequency side of the ε'' spectra is caused by charge transport effects which are related to moisture and ionic impurities. The contribution of these phenomena to the relaxation spectra become more pronounced with increasing temperature[176].
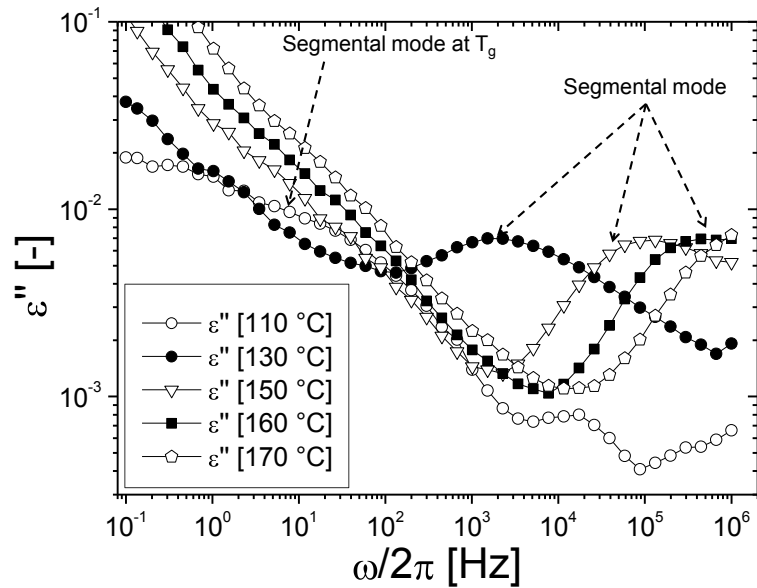
Fig. 104 Dielectric relaxation spectrum for a PS-100k (M_w = 98,000 g/ml, PDI = 1.1) at different temperatures. Close to the T_g of the PS chains the segmental mode is significantly broadened.

Diblock copolymers consist of two distinct polymer chains which both possess different dielectric properties. In the case of PS-b-PI the differences are attributed on the one hand to the different segmental relaxations which are related to the differences in the glass transition temperatures and on the other hand to the non-vanishing dipole moment along the back bone of the polyisoprene chains. It is important to note that due to the tethered polyisoprene chains and constrains caused from the polystyrene phase below the T_{ODT} the normal mode of the PI is significantly broadened, with respect to the linear homopolymer chain (see **Fig. 105**).

160
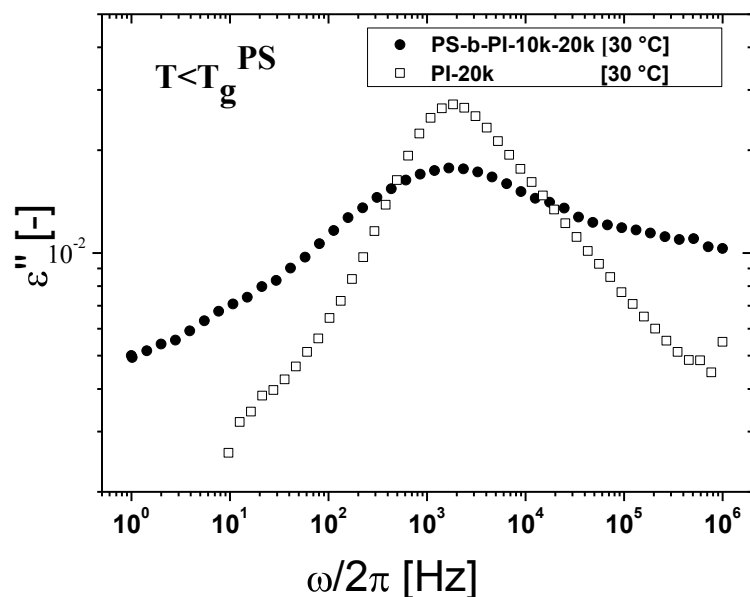
Fig. 105 Dielectric relaxation spectrum of PS-b-PI-10k-20 (filled circles) and PI-20k (open squares) at T = 30 °C. The relaxation mode of the PS-b-PI is broadened due to the tethered PI chains and the constrains of the PS blocks below the T_{ODT}.

All in-situ Rheo-Dielectric experiments presented herein were performed at elevated temperatures between 120 °C and 180 °C which is above the T_g of the polystyrene blocks. Form **Fig. 106** it becomes evident that in the frequency range under investigation also contributions of the segmental mode of the PS blocks interfere with normal mode of the polyisoprene chains. At T = 150 °C the dielectric loss spectra of the PS-b-PI-40k-40k showed two distinct relaxation processes. The one at lower frequencies is attributed to the normal mode of the PI chains while the relaxation peak at high frequencies is assumed to be associated with the segmental relaxation of the polystyrene.

This becomes even more evident by comparing the high frequency relaxation at T = 150 °C of the diblock copolymer with the segmental relaxation of PS-100k indicated by dashed lines in **Fig. 106**.

With decreasing temperature the segmental mode of the PS block and the normal mode of the PI block superimpose as both relaxation modes obey different temperature dependence. The phenomenon of superposition becomes more pronounced for lower molecular weight polyisoprene chains (see **Fig. 107**) as the relaxation time of the normal mode τ_{normal} depends on the molecular weight of the PI block ($\tau_{norma} \sim M^4$)[88].

161
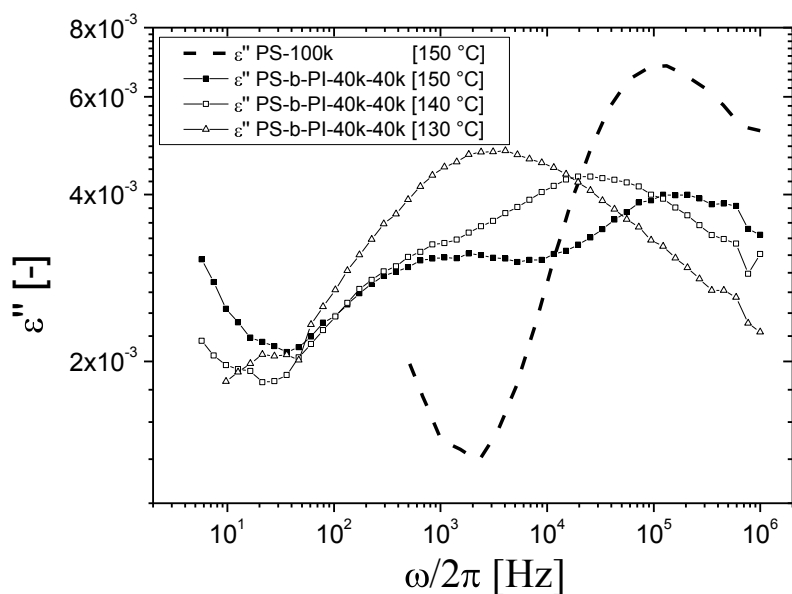
Fig. 106 Dielectric loss of PS-100k (dashed lines) and PS-b-PI-40k-40k (symbols) at various temperatures. It can be seen that with decreasing temperature the segmental mode of the PS block superimpose with the normal mode of the PI block.
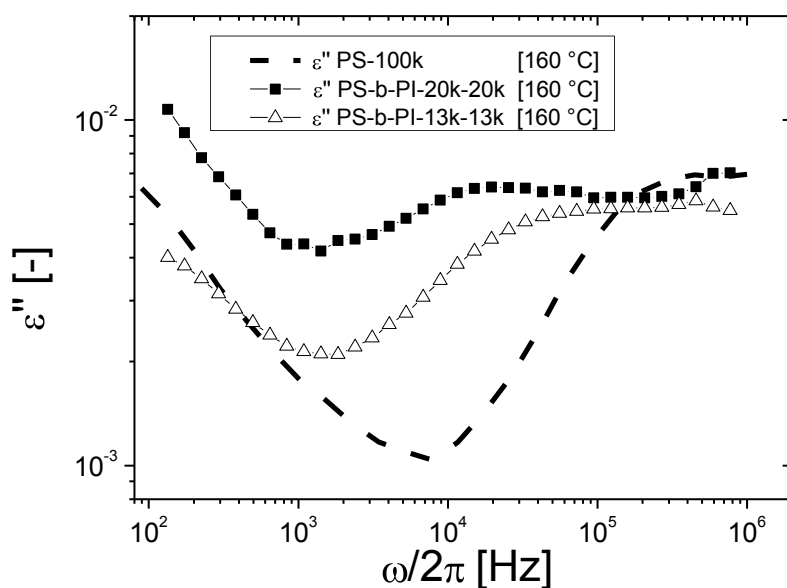
Fig. 107 Dielectric loss of PS-100k (dashed lines) and PS-b-PI-20k-20k (filled squares) and PS-b-PI-13k-13k (open triangles) at T = 160 °C.

6.2. In-situ Rheo-Dielectric studies of the shear-induced alignment

Different symmetric PS-b-PI diblock copolymers were investigated with varying molecular weights between M_w = 26,500 g/mol and M_w = 80,000 g/mol. For all measurements a dielectric frequency sweep was performed before and after each

LAOS experiment. During the LAOS experiment the dielectric response was followed at one specific frequency which was set to correspond to the frequency range in which the normal mode relaxation of the PI chains occurs. To ensure the equilibrium state of the sample melt three to five data points of $\varepsilon''(t)$ were collected without subjecting the sample to any shear. This procedure guaranteed that the observed changes in the dielectric response were attributed to the external applied mechanical stimulus. Block copolymers with T_{ODT} in the experimental accessible temperature range were heated in the disordered state to remove any shear history caused from sample preparation.

6.2.1. Macroscopic parallel orientation

A PS-b-PI-40k-40k (M_w = 83,000 g/mol, f_{PS} = 50%, PDI = 1.06) was subjected to large amplitude oscillatory shear at 160 °C, an excitation frequency of $\omega_1/2\pi$ = 1 Hz and a strain amplitude of γ_0 = 1. The 2D-SAXS patterns which were detected after the in-situ Rheo-Dielectric measurements revealed a macroscopic parallel orientation of the sample (see **Fig. 108**).
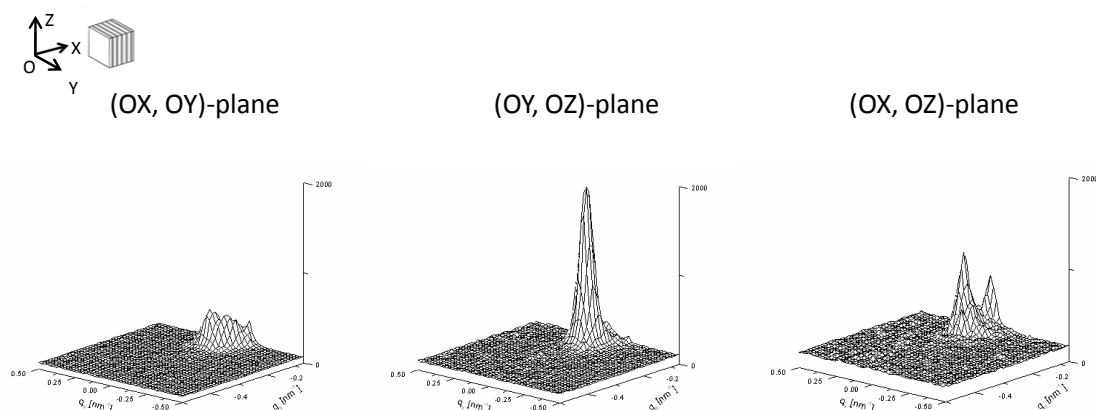
Fig. 108 2D-SAXS patterns at the final state along the normal (OX, OY) plane, radial (OY, OZ) plane and the tangential (OX, OZ) plane at r = 5.5 mm

Fig. 109 represents the static dielectric loss spectrum of PS-b-PI-40k-40k before and after. The dashed line is a superposition of a conductive contribution (low frequency relaxation) and two Havriliak-Negami relaxation processes (see section **2.4.3**) being assigned to the normal and segmental mode. The conductive contribution is described by the following expression[88]:

163

$$\varepsilon^*(\omega) = \varepsilon' + i\varepsilon'' = -i\left(\frac{\sigma(0)}{\varepsilon_0\omega}\right)^n \qquad (4.1)$$

with σ(0) being the direct current (dc) limit of $\omega \to 0$ and *n* (*n* ≤ 1) a scaling exponent.

It can be seen that after the LAOS experiment the dielectric loss of the normal mode relaxation is reduced compared to the loss spectra before LAOS. Interestingly, the segmental mode of the PS seems to be unaffected by the macroscopic alignment. **Tab. 10** summarizes the fit parameters for the dielectric loss curves of the normal mode of the PI chains before and after LAOS. No significant changes in the dielectric strength and the shape determining parameters for the assumed HN-relaxation process were detected. Only in the conductivity term a slight reduction of 12% for the exponent n occurred.
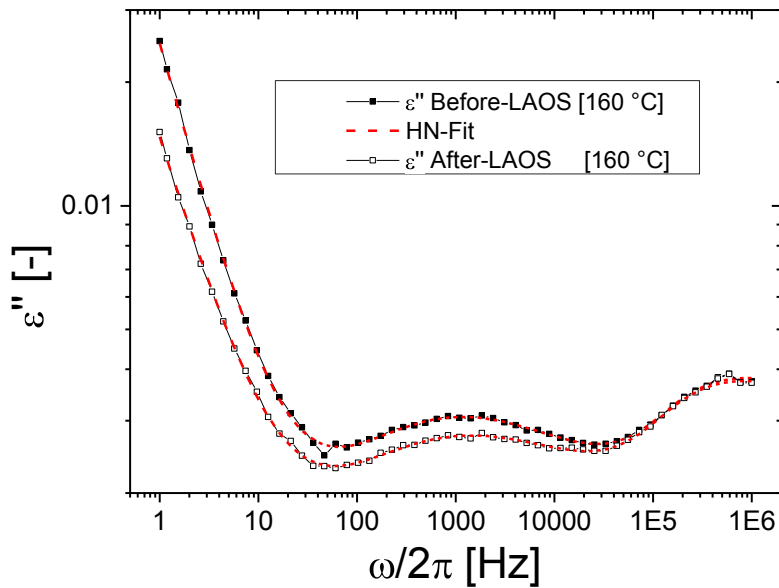
Fig. 109 Dielectric loss of PS-b-PI-40k-40k before (filled squares) and after (open squares) the LAOS experiment at T = 160 °C. The dashed line represent is a superposition of a conductive contribution (low frequency relaxation) and two Havriliak-Negami relaxation processes being assigned to the normal and segmental mode.

	σ$_0$ [S/cm]	n	Δε	τ [s]	α	β	α*β
Before	7.7*10^{-15}	0.87	0.021	6.5*10^{-4}	0.51	0.40	0.20
After	2.2*10^{-15}	0.77	0.023	6.5*10^{-4}	0.48	0.38	0.18

Tab. 10 Fit parameters obtained from the HN-Fit and a conductive contribution to the normal mode relaxation of PS-b-PI-40k-40k before and after LAOS ($\omega_1/2\pi$ = 1Hz, γ_0 = 1, T = 160 °C).

The in-situ dielectric measurements were performed with a fixed frequency of 1000 Hz while every 20 s a data point was collected. From the in-situ time dependent dielectric loss a clear decay in $\varepsilon''(t)$ is observed of approximately 14% from 0.003 to 0.0026 (see **Fig. 110**).
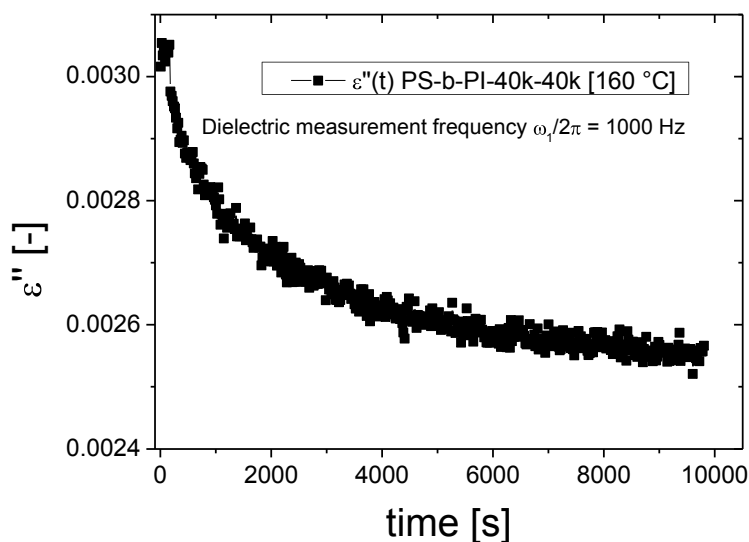
Fig. 110 In-situ detected dielectric loss at $\omega_1/2\pi$ = 1000 Hz as a function of time during the shear induced parallel alignment of PS-b-PI-40k-40k (LAOS: $\omega_1/2\pi$ = 1 Hz, γ_0 = 1, T = 160 °C).

As a further example, the Rheo-Dielectric behavior of a PS-b-PI-20k-20k during shear-induced parallel alignment is provided (T = 130 °C, $\omega_1/2\pi$ = 3 Hz and γ_0 = 1). **Fig. 111** represents the dielectric loss spectra before and after LAOS. Similar to the diblock copolymer described above a reduction of $\varepsilon''(\omega/2\pi)$ is observed which is more pronounced in the intermediate frequency range of the spectrum (between 300 Hz and 20,000 Hz) than in the high frequency limit of the spectra. It is assumed that this deviance in the peak shape is caused by the superposition of the normal mode of the polyisoprene chains and the segmental mode of the polystyrene chains as described above.

It is important to note that linear polystyrene did not show any significant decrease in the segmental mode during LAOS. From the calculated fit parameters (see **Tab. 11**) it can be seen that only the relaxation time τ of the peak was slightly affected, as all other values have been unchanged with respect to data accuracy.

165
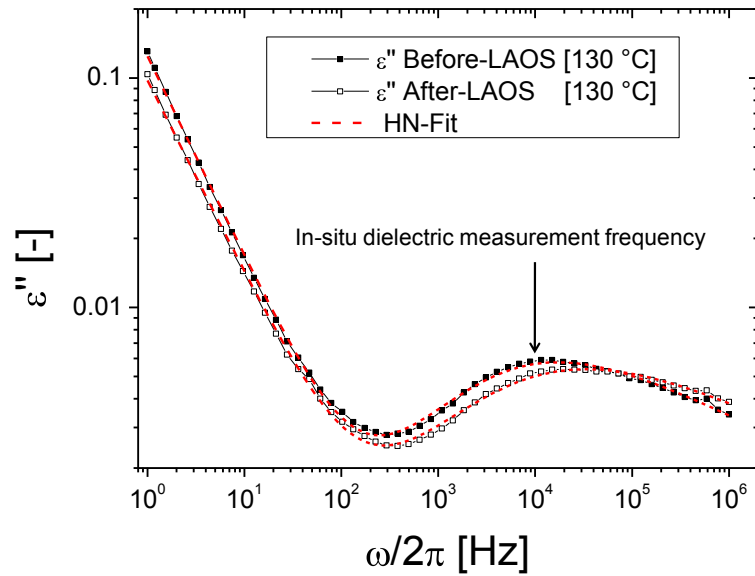
Fig. 111 Dielectric loss of PS-b-PI-20k-20k before (filled squares) and after (open squares) the LAOS experiment at T = 130 °C. The dashed line is a superposition of a conductive contribution (low frequency relaxation) and one Havriliak-Negami relaxation process being assigned to the normal mode of the PI chains.

	σ_0 [S/cm]	n	$\Delta\varepsilon$	τ [s]	α	β	$\alpha*\beta$
Before	$5.1*10^{-14}$	0.87	0.036	$4.3*10^{-5}$	0.60	0.36	0.22
After	$3.5*10^{-14}$	0.84	0.037	$2.6*10^{-5}$	0.54	0.37	0.20

Tab. 11 Fit parameters obtained from the HN-Fit and a conductive contribution to the normal mode relaxation of PS-b-PI-20k-20k before and after LAOS ($\omega_1/2\pi$ = 3Hz, γ_0 = 1, T = 130 °C).

The in-situ obtained time dependent dielectric loss data are shown in **Fig. 112** which obeyed similar time progression as the ε'' values detected for PS-b-PI-40k-40k. In the beginning a rapid dropt appeared from approximately ε'' = 0.0058 to ε'' = 0.0050 in t = 2000 s. This rapid decay is followed by region in which ε'' monotonic decreased to approximately ε'' = 0.0045.
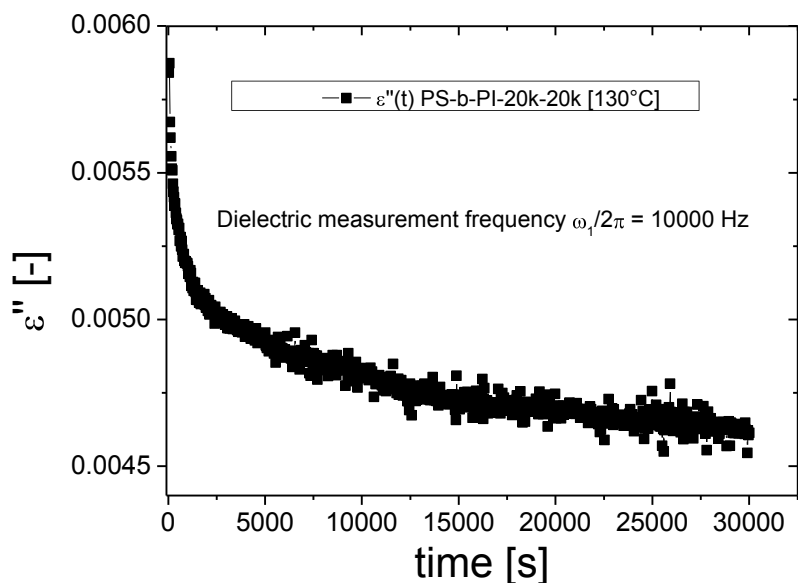
Fig. 112 In-situ detected dielectric loss at $\omega_1/2\pi$ = 10000 Hz as a function of time during the shear induced parallel alignment of PS-b-PI-20k-20k (LAOS: $\omega_1/2\pi$ = 3 Hz, γ_0 = 1, T = 130 °C).

6.2.2. Macroscopic perpendicular orientation

In contrast to the decrease of ε'' as discovered for the macroscopic parallel orientation, increasing ε''-values were obtained for the shear-induced macroscopic perpendicular alignment. As an example the Rheo-Dielectric data before and after LAOS for a lamellar PS-b-PI-15k-13k are represented in **Fig. 113**. The macroscopic orientation was achieved at T = 160 °C with $\omega_1/2\pi$ = 5 Hz and γ_0 = 1. Additionally, the fit parameters are summarized in **Tab. 12**.

It can be seen that for the perpendicular orientation the calculated relaxation time τ is retarded by more than one decade from $4.3*10^{-6}$ s to $1.8*10^{-5}$ s. Furthermore, the α and β parameters which determine the shape of the relaxation mode are changed which results in a different peak shape for the macroscopic aligned sample. However, there was a detectable change in the dielectric strength, in the order of 10%.
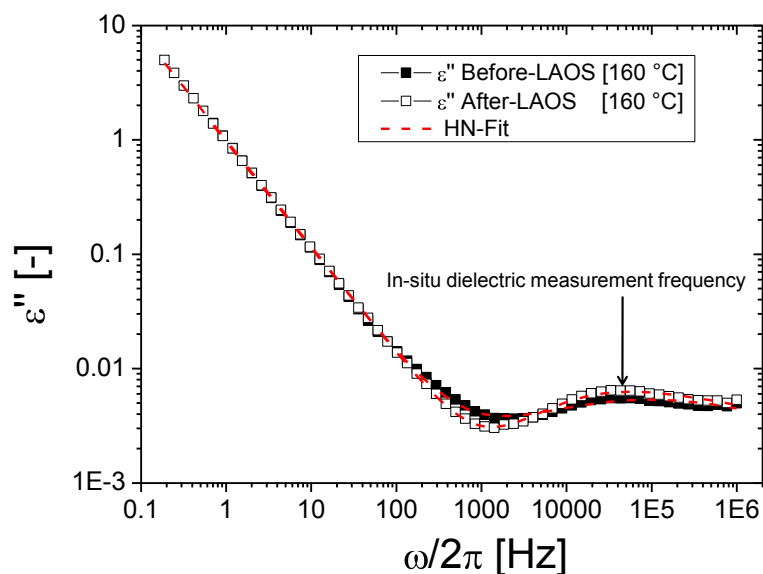
Fig. 113 Dielectric loss of PS-b-PI-15k-13k before (filled squares) and after (open squares) the LAOS experiment at T = 160 °C. The dashed line is a superposition of a conductive contribution (low frequency relaxation) and one Havriliak-Negami relaxation process being assigned to the normal of the PI chains.

	σ_0 [S/cm]	n	$\Delta\varepsilon$	τ [s]	α	β	$\alpha^* \beta$
Before	$5.3*10^{-13}$	0.93	0.037	$4.3*10^{-6}$	0.41	0.66	0.27
After	$5.5*10^{-14}$	0.93	0.042	$1.8*10^{-5}$	0.72	0.23	0.17

Tab. 12 Fit parameters obtained from the HN-Fit and a conductive contribution to the normal mode relaxation of PS-b-PI-15k-13k before and after LAOS ($\omega_1/2\pi$ = 5Hz, γ_0 = 1, T = 160 °C).

The in-situ measured time dependence of ε'' is shown in **Fig. 114** with an additional inset representing the development of the macroscopic perpendicular orientation determined by in-situ Rheo-SAXS under equal conditions. From the in-situ Rheo-SAXS data it can be seen that the dielectric loss exhibits astonishing similarities in the time progression to the structural development. For all three methods orientation times were calculated by fitting the time dependent data sets with a stretched exponential fit function. The obtained fit parameters are summarized in **Tab. 13**.

Strain (150 °C)	y_0	τ_o [s]	β	A
$\varepsilon''(t)$	0.0058	150	1	$9.1*10^{-4}$
$\sigma_{SAXS}(t)$	13°	45	0.83	20°
$I_{3/1}(t)$	0.018	30	0.35	0.078

Tab. 13 Calculated fit parameters from $\varepsilon''(t)$ determined by in-situ Rheo-Dielectric, $\sigma_{SAXS}(t)$ determined by in-situ Rheo-SAXS and $I_{3/1}(t)$ determined by FT-Rheology at T = 160 °C, $\omega_1/2\pi$ = 1 Hz and γ_0 = 1.

For the the in-situ Rheo-Dielectric measurements an orientation time $\tau_o = 150$ s was obtained while the time progression of σ_{SAXS} and $I_{3/1}$ revealed orientation times of approximately $\tau_o = 45$ s and $\tau_o = 30$ s, respectively. It is assumed that the differences in the orientation times τ_o detected by dielectric spectroscopy, SAXS and rheology are attributed to the different quantities and length scales detectable with these methods.

Small angle X-ray scattering reveals changes in the locally ordered micro domains at a specific point of the sample. The mechanical non-linear parameter $I_{3/1}(t)$ is sensitive to the rotation of the block copolymer grains as outlined in section **4.9** and reveals average information over the whole sample volume. The dielectric investigation of the polyisoprene normal mode detects fluctuation in the end-to-end vector of the polyisoprene chains averaged over the whole sample volume.

It has to be noticed that for all symmetric PS-b-PI diblock copolymers which were analyzed by Rheo-Dielectric an increase in ε'' had been detected under LAOS conditions which are attributed to generate a macroscopic perpendicular alignment.
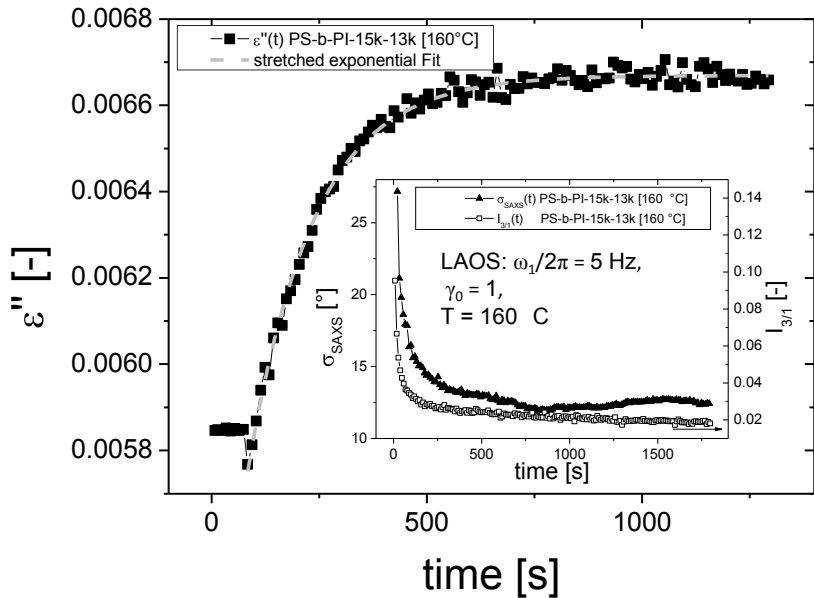
Fig. 114 In-situ detected dielectric loss at $\omega_1/2\pi = 40,000$ Hz as a function of time during the shear induced perpendicular alignment of PS-b-PI-15k-13k (LAOS: $\omega_1/2\pi = 5$ Hz, $\gamma_0 = 1$, $T = 160$ °C). Dashed lines correspond to stretched exponential fit function. The inset represents the in-situ detected orientation distribution quantified by $\sigma_{SAXS}(t)$ (filled triangle) and the non-linear parameter $I_{3/1}(t)$ (open squares) under equal rheological conditions.

6.2.3. In-situ Rheo-Dielectric investigation of PS-b-PI-13k-13k

From the results discussed above it was indicated that the macroscopic parallel respectively perpendicular orientation process can be monitored from changes in the dielectric normal mode of the polyisoprene chain relaxation. For a parallel alignment a decrease in the dielectric loss peak of the normal mode was obtained while the overall perpendicular caused an increase. In the following the de-orientation, which was discussed in detail in section **4**, was probed with the in-situ Rheo-Dielectric combination at T = 150 °C and γ_0 = 2 and γ_0 = 3 for PS-b-PI-13k-13k.

Fig. 115 and **Fig. 116** represent the in-situ measured time dependence of the dielectric loss ε'' for γ_0 = 2 and γ_0 = 3, respectively. Additionally, the time dependence of the non-linear parameter $I_{3/1}$ is included. In the beginning the dielectric loss showed a drastic stretched exponential increase in the magnitude of approximately 0.001 for both strain amplitudes. This behavior is similar to the non-linear mechanical response which showed a rapid stretched exponential decay in the beginning of the experiment. Nevertheless, the calculated orientation times of τ_o = 300 s (γ_0 = 2) and τ_o = 230 s (γ_0 = 3) for the dielectric response were significant longer than the ones obtained from the mechanical response (τ_o = 75 s for γ_0 = 2 and τ_o = 50 s for γ_0 = 3). Interestingly, short after the de-ordering occurred, indicated from an increase in $I_{3/1}$, the dielectric loss reached a maximum value. Beyond this point ε'' showed a monotonic decrease until it reached a plateau value of ε'' = 0.0056 after t ≈ 8000 s and ε'' = 0.0052 after t ≈ 6000 s for γ_0 = 2 and γ_0 = 3, respectively. For the highest strain amplitude the final ε'' was less than the initial value of ε'' = 0.0055.
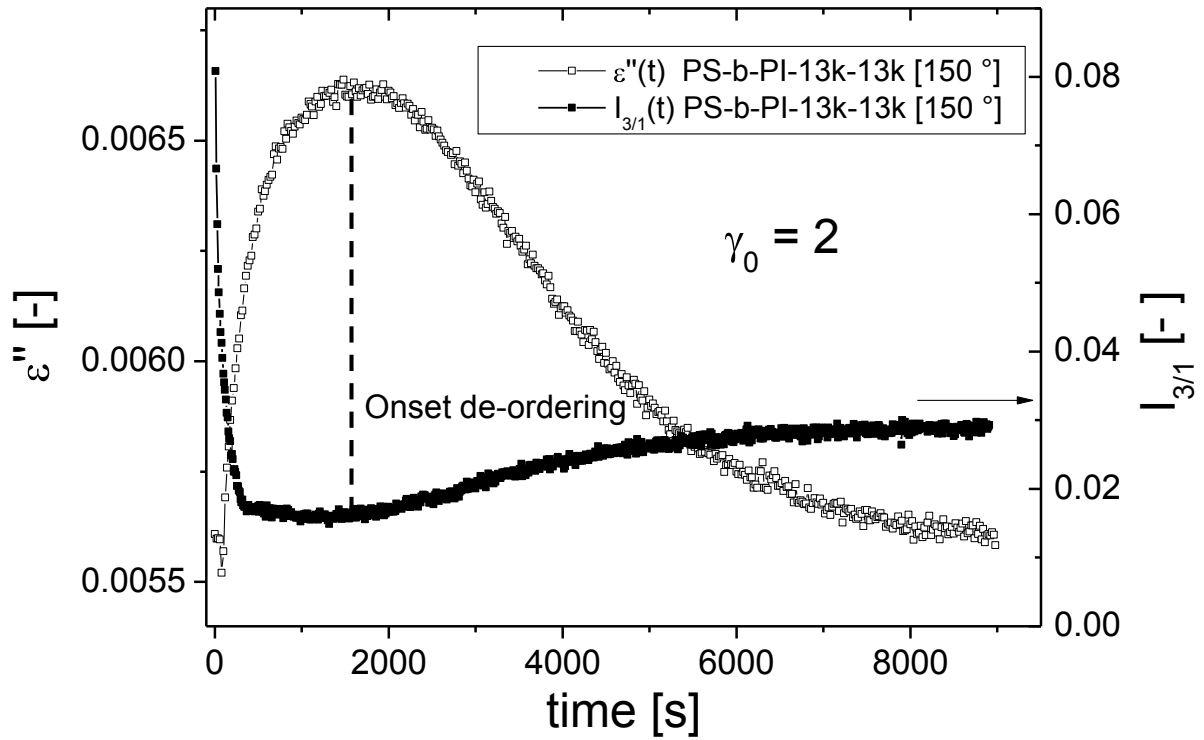
Fig. 115 In-situ detected dielectric loss ε" (open squares) as a function of time at a dielectric measurement frequency of $\omega_1/2\pi$ = 100,000 Hz and a mechanical stimulus at T = 150 °C, $\omega_1/2\pi$ = 1 Hz and γ_0 = 2. The progress of the macroscopic alignment was followed by $I_{3/1}$ (filled squares). The onset of the de-ordering is indicated by a vertical dashed line at the point where $I_{3/1}$ started to increase.
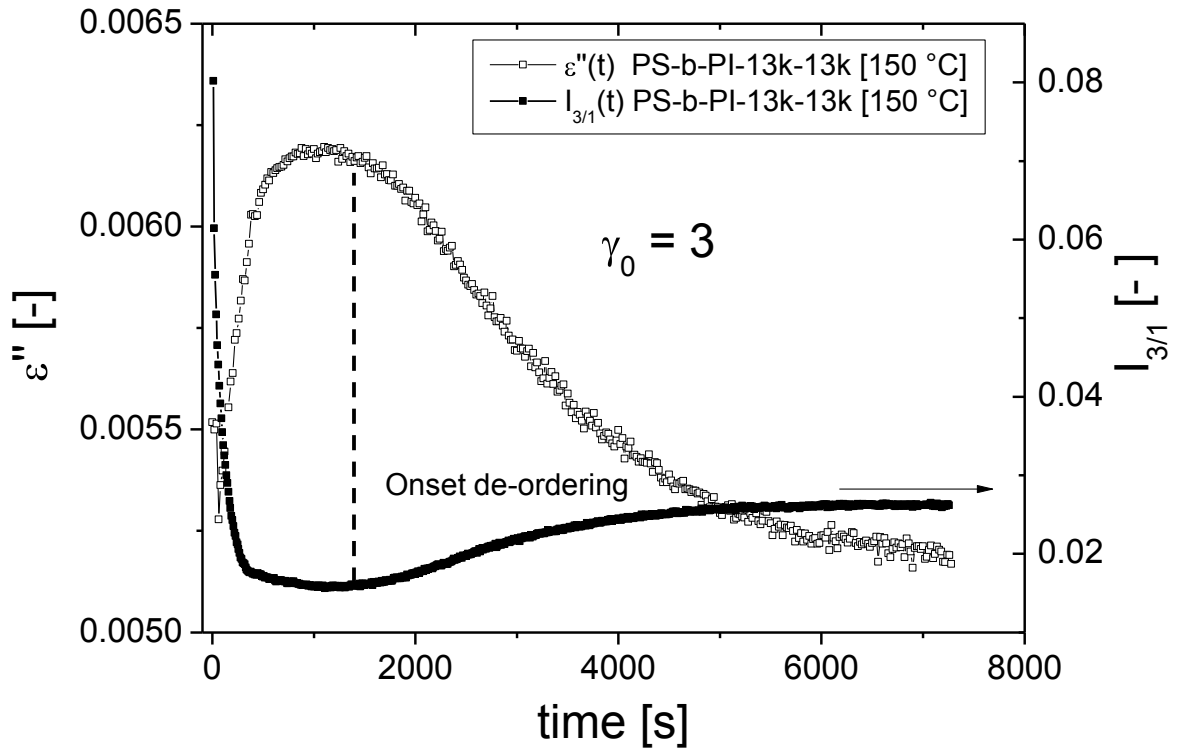
Fig. 116 In-situ detected dielectric loss ε" (open squares) as a function of time at a dielectric measurement frequency of $\omega_1/2\pi$ = 100,000 Hz and a mechanical stimulus at T = 150 °C, $\omega_1/2\pi$ = 1 Hz and γ_0 = 3. The progress of the macroscopic alignment was followed by $I_{3/1}$ (filled squares). The onset of the de-ordering is indicated by a vertical dashed line at the point where $I_{3/1}$ started to increase.

Fig. 117 represents the static dielectric loss spectra measured before and after the LAOS experiments for $\gamma_0 = 2$ and $\gamma_0 = 2$. The more likely rectangular curve shapes of the $\varepsilon''(\omega/2\pi)$ are assumed to be caused by the superposition of the normal mode of the polyisoprene chains and the segmental mode of the polystyrene chain segments as already discussed above. However, it was not possible to accurately fit the obtained relaxation peaks with a HN-relaxation process. Nevertheless, the trend which was also detected from the in-situ Rheo-Dielectric studies is clearly visible.
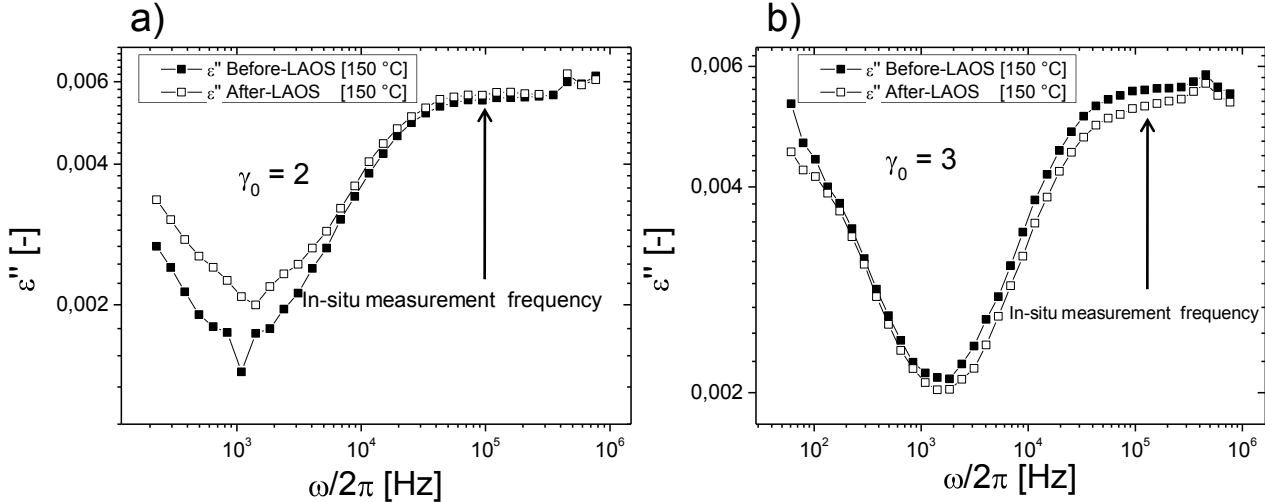
Fig. 117 Dielectric loss of PS-b-PI-13k-13k before (filled squares) and after (open squares) the LAOS experiment (T = 160 °C, $\omega_1/2\pi$ = 1 Hz and γ_0 = 3).

6.3. Summary and discussion of the in-situ Rheo-Dielectric investigations

Form the dielectric loss before and after the LAOS experiment the macroscopic orientation of the unit normal of the lamellae parallel respectively perpendicular with respect to the shear field can be distinguished (see **Tab. 14**).

Macroscopic Alignment	Dielectric loss ε''
Parallel	increased
Perpendicular	decreased

Tab. 14 Trend of the dielectric loss ε'' for the two different shear-induced macroscopic alignments.

However, it was shown that at elevated temperature above the glass transition of the polystyrene block, the dielectric normal mode may be superimposed by the segmental relaxation of the PS chain segments, depending on the molecular weight

of the PI chains. This caused further difficulties to accurately determine changes in the dielectric strength $\Delta\varepsilon$ before and after the LAOS experiment, which would give precise information about changes in the dipole moments. Nevertheless, a preliminary explanation shall be provided based on the observed increase and decrease of dielectric loss.

Form literature it is known[162, 163], that polymer chains which are tethered to an interface obey anisotropic diffusions parallel and along the normal direction of the constraining surface. The results published, indicated that the polymer chains have higher mobility parallel to the surface than in the perpendicular direction.

Based on these findings it is assumed that the polyisoprene end-to-end vector preferentially aligns parallel to the polystyrene interface as schematically illustrated in **Fig. 118**. Therefore, for the perpendicular alignment the end-to-end vector (dashed arrow) of the polyisoprene chains would preferentially orientate in the direction of the external electric field. In contrast, for the macroscopic parallel orientation, the end-to-end vector would preferentially orientate perpendicular to the applied electric field. This strongly simplified model provides an explanation to the observed increase for the perpendicular and decrease for the parallel orientation.
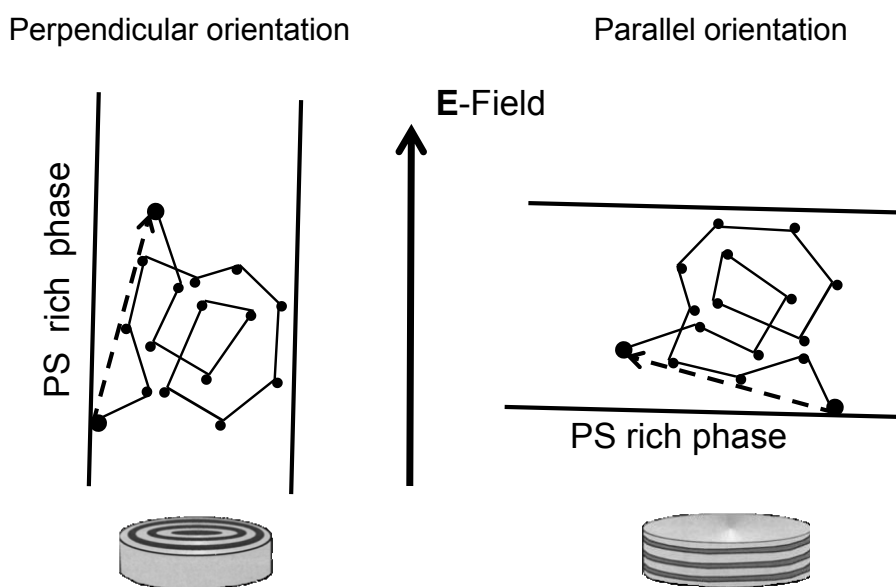
Fig. 118 Schematic sketch of the macroscopic perpendicular and parallel alignment. The dotted arrow represents the non-vanishing dipole moment along the PI- backbone which corresponds to the end-to-end vector. The polymer chain ends preferentially direct in the direction parallel to the interface between the two different blocks.

Furthermore, the in-situ time dependences of ε'' during the shear-induced alignment of PS-b-PI-13k-13k at experimental conditions under which de-ordering occurred (see section **4.3**) corresponded well with the mechanical non-linear response quantified by $I_{3/1}$. The development of the overall perpendicular alignment which was indicated by the decrease of $I_{3/1}$, resulted in an increase of the in-situ determined dielectric loss ε''.

From the assumption made above (see **Fig. 118**), the increase can be explained by the rotation of the locally ordered lamellae block copolymer grains into a macroscopic perpendicular alignment. In this state the end-to-end dipole moment would be preferentially orientated into the direction of the electric field vector and as a consequence ε'' would be increased. In the case of the de-ordering, also expected to proceed by a rotational mechanism, ε'' showed a monotonic decay until it approximately reached its initial value before the LAOS experiment was performed.

Equally, this decay can be explained from the simplified molecular picture presented in **Fig. 118** as now the well perpendicular aligned block copolymer grains are rotated out of plane into the parallel orientation in which the end-to-end dipole moments of the PI chains contribute less to the dielectric response. It is assumed that the reduction of $\varepsilon''(t)$ to approximately its initial value during the de-ordering corresponds to approximately equal amounts of block copolymer grains being parallel respectively perpendicular aligned. The point after which ε'' began to decay is in good agreement with the onset of the de-ordering as detected by $I_{3/1}$.

As a conclusion, it can be stated that the shear-induced macroscopic alignment of lamellae PS-b-PI diblock copolymers can be followed changes of the dielectric loss ε'' as a function of time. However, it is important to mention that the magnitude of these changes is relatively small ($\Delta\varepsilon'' \approx 0.0008$) which makes it challenging to precisely determine the structural changes in the sample melt. However, this clearly shows the need of this optimized high sensitive Rheo-Dielectric setup which is still able to accurately detect such small changes in the dielectric response of the sample.

7. Rheo-Dielectric of gold-hybrid diblock copolymers nano-composites

7.1. Materials and experimental procedure

In this section for the first time the influence of large amplitude oscillatory shear (LAOS) on different morphologies of Polystyrene-b-Poly(4-vinylpyridine) (PS-b-P(4VP)) gold-hybrid block copolymers was investigated. These studies were performed in collaboration with the group of Dr. Amir Fahmi from the school of Mechanical, Materials and Manufacturing Engineering University of Nottingham who provided the block copolymers under investigation.

With their ability to microphase separate giving rise to a large number of different morphologies, Block copolymer systems have gained great interest as templates and matrix for the fabrication of nano-structured hybrid materials[153, 167]. Block copolymers provide an organic matrix capable to control the shape, the dispersion, size distribution, and the alignment of nano-particles selectively incorporated in a specific domain. There are several approaches for selectively incorporate inorganic nano-particles into block copolymers: direct polymerization of a monomer-metallic complex[169] direct assembly of block copolymers with nanoscale metallic species[175] and through chemical coordination with organo metallic compounds[177].

The here presented gold hybrid PS-P(4VP) block copolymers were synthesized by C. Mendoza, using pristine PS-b-P(4VP) (from Polymer Source Inc.) as a precursor and an in situ reduction approach[152, 153] to selectively incorporate the gold nano-particles into the P(4VP) block. A schematically representation of the applied synthesis strategy is provided in **Fig. 119**. This method allowed the selectively incorporation of gold nano-particles into the P(4VP) block of the diblock copolymer.
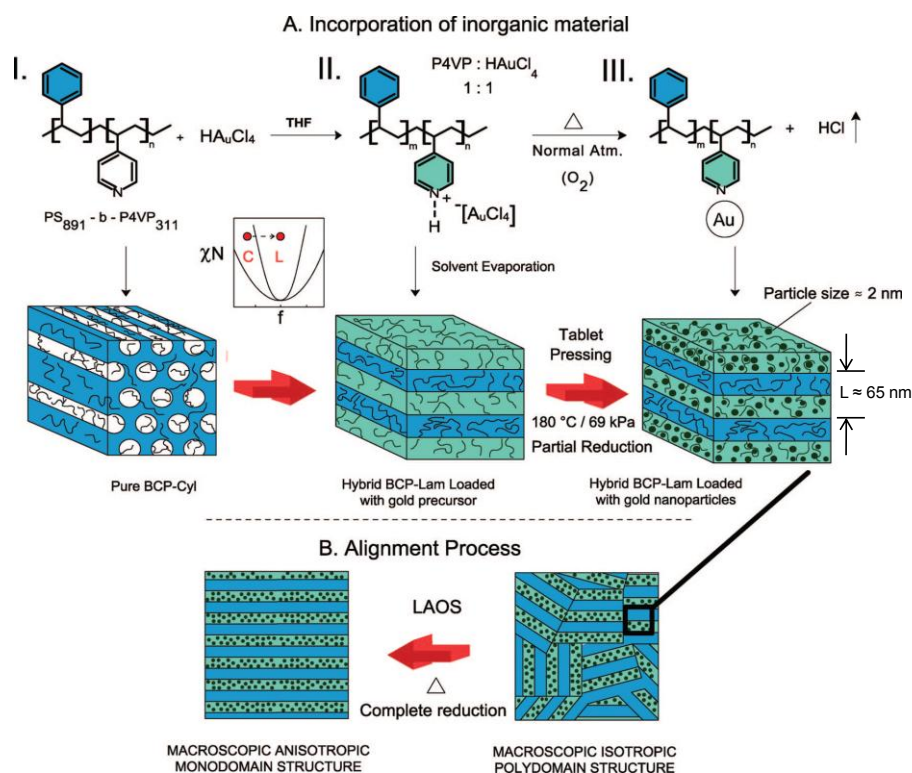
Fig. 119 *Experimental route for selectively incorporating gold nano-particles* into the P(4VP) block[152].

By applying large amplitude oscillatory shear (LAOS) the block copolymers microstructures can be macroscopically aligned resulting in highly ordered three dimensional patterns. For lamellar and hexagonal cylindrical morphologies the orientated samples become macroscopic anisotropic while for spherical morphologies the long range order is improved[20].

For the first time the shear-induced alignment of gold-hybrid PS-b-P(4VP) nano-composites was investigated with a high sensitive in-situ Rheo-Dielectric combination. The aim of this work was to probe dielectric changes especially in the conductive properties of the samples caused by the macroscopic orientation.

Three different PS-P(4VP) BCP morphologies (lamellar (lam), hexagonal cylindrical (cyl) and bcc spherical (sph)) were investigated. The microstructure of the BCP was confirmed by small angle X-Ray scattering (SAXS) and TEM measurements. The investigated pristine and hybrid BCP are listed in **Tab. 15**.

176

a)

Sample (Pristine)	M_n(PS-P(4VP)) [g/mol]	Morphology	$f_{P(4VP)}$ [%]	PDI(M_n/M_w)
PS-3917	116000-4000	Bcc-Spheres	3	1.13
PS-135	34000-2900	Bcc-Spheres	8	1.07
PS-252	93000-33000	Hex-Cylinders	26	1.13

b)

Sample (Au-Hybrid)	M_n(PS-P(4VP)) [g/mol]	Morphology	Φ_{Au} [%]	T_g(P(4VP)) [°C]
PS-3917-Au-Sph	116000-4000	Bcc-Spheres	0.30	158
PS-135-Au-Cyl	34000-2900	Hex-Cylinders	0.80	160
PS-252-Au-Lam	93000-33000	Lamellae	1	164

Tab. 15 sample details for the a) pristine and b) hybrid block copolymer gold nano-composites. Φ_{Au} is the calculated volume fraction of gold nano-particles present in the polymer systems.

The calculated volume fraction Φ_{Gold} of the gold nano particles confined in the P4VP diversifies between 4% for the lamellar morphology and 10% for the hexagonal cylindrical and the bcc spherical morphologies. The calculated distance between the particles tethered in the P(4VP) block ($r_{particle}$ = 0.9 nm) is 3 nm for the lamellar and 2 nm for the hexagonal cylindrical and the bcc spherical morphologies, assuming an ideal fcc packed lattice.

All Rheo-Dielectric experiments were performed utilizing parallel plate geometries with 10 mm in diameter. At 170 °C the zero gap was assigned after 30 min of annealing. Afterwards the sample discs were placed between the plates and slightly squeezed until the whole electrode area was covered. The sample was allowed to temper for 30 min before experiments.

Dielectric conductivity measurements at various temperatures between 130 °C and 190 °C were performed before and after LAOS. For the dielectric measurements a sinusoidal electric field in ac-mode in a frequency range from 10^{-1} to 10^6 Hz was applied to the sample. The initial temperature was 130 °C followed by increasing the temperature in 20 °C intervals. Before each frequency sweep at different temperatures the sample was annealed for 30 min.

All in-situ Rheo-Dielectric LAOS experiments were carried out at 170 °C with a mechanical excitation frequency of 1 Hz and a strain amplitude of γ_0 = 50%. The shear duration was set to 60,000 s. The in-situ dielectric measurements during LAOS were performed with a fixed dielectric frequency of 10 Hz to online monitor the dielectric response of the sample melts.

7.2. Static dielectric studies

Fig. 120 shows the real part of the complex dielectric conductivity $\sigma^*(\omega)$ as a function of frequency for a pristine and the hybrid PS-P(4VP) block copolymers at 170 °C before the LAOS experiments were performed. It is important to note that for sinusoidal electric fields the complex conductivity $\sigma^*(\omega)$ and the dielectric function $\varepsilon^*(\omega)$ are related by $\sigma^*(\omega) = i\omega\varepsilon_0\varepsilon^*(\omega)$ (ε_0 being the permittivity of free space)[88]. Samples above the percolation threshold show a frequency-independent behavior at low frequencies referred to the so called dc plateau[166, 168, 169]. As the frequency of the applied signal is increased above a certain frequency ω_c, the conductivity starts to increase from its constant dc value. The region in which $\sigma'(\omega)$ is increasing is called the ac regime.

Fig. 120 shows that all hybrid materials were above the percolation threshold indicated by the frequency independent region of σ' below 1000 Hz while the pristine block copolymers exhibited no dc plateau in the observed frequency range. For the lamellae morphology a plateau conductivity of $\sigma_0' \approx 10^{-8}$ S/cm was observed while the cylindrical morphology exhibited a plateau value of $\sigma_0' \approx 10^{-10}$ S/cm. For the spherical morphology a plateau value of $\sigma_0' \approx 10^{-11}$ S/cm was obtained. Additionally, a second relaxation process appeared in the frequency region between 10^2 and 10^5 Hz for the lamellar and cylindrical morphology. However, this relaxation process could not be explained with the herein performed experiments.
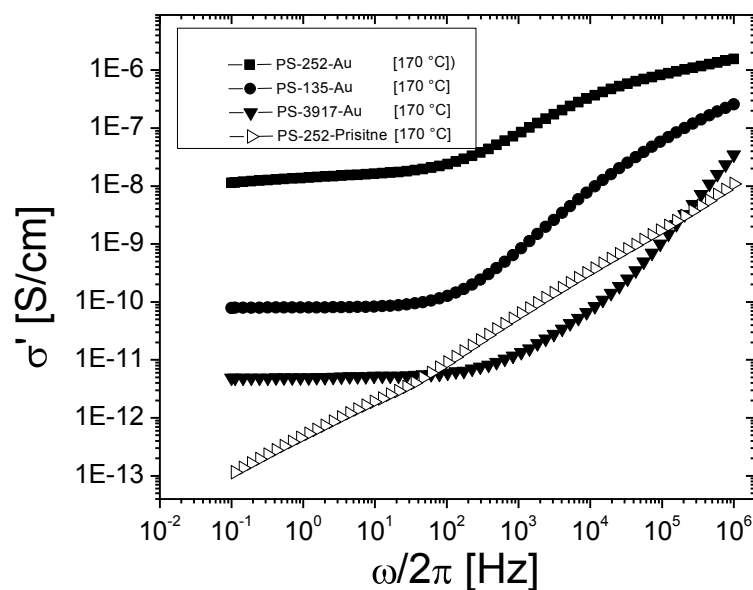
Fig. 120 Frequency dependence of real part of the complex conductivity for spherical (filled triangle), cylindrical (filled circle) and lamellar (filled squares) morphologies with gold nano-particles at 170 °C. Representative for the pristine PS-b-P(4VP) block copolymers the data for the PS-252 (open triangle) is shown. It can be seen that only for the hybrid materials a dc-plateau is observed.

TEM and STEM images were recorded for the lamellae (PS-252-Au) and spherical (PS-3917-Au) hybrid diblock copolymers to proof whether the nano-particles are confined in the PS(4VP) block (see **Fig. 121**, **Fig. 122** and **Fig. 123**). It can be seen that the particles are well located in one domain while the size of the particles differs between some nanometers and several tenth of nanometers.
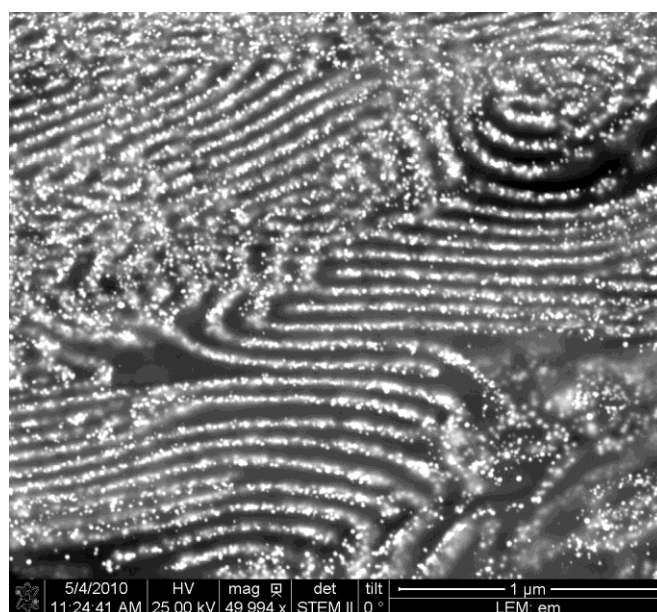
Fig. 121 STEM image of the lamellae PS-252 gold-hybrid PS-b-P(4VP). The bright spots in the image corresponds to gold nano-particles which were selectively incorporated in the P(4VP) block.
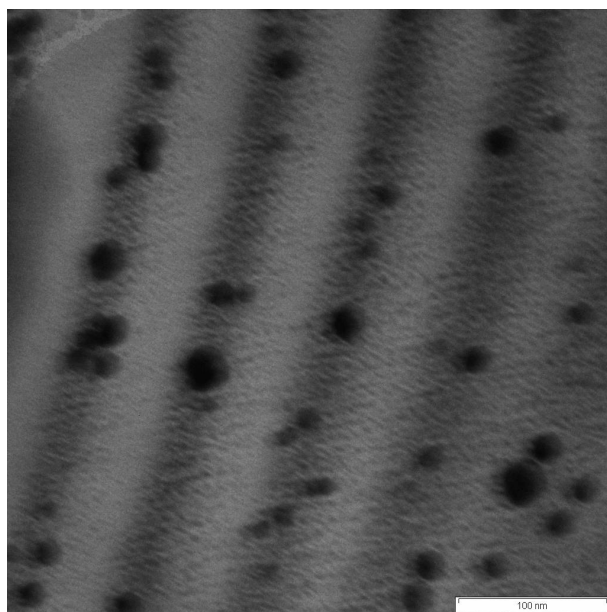
Fig. 122 TEM image of the lamellae PS-252 gold-hybrid PS-b-P(4VP). The dark spots in the image correspond to gold nano-particles which were selectively incorporated in the P(4VP) block. It can be seen that the size of the gold nano particles is broad distributed and varies between some nanometers to several tenth of nanometers.
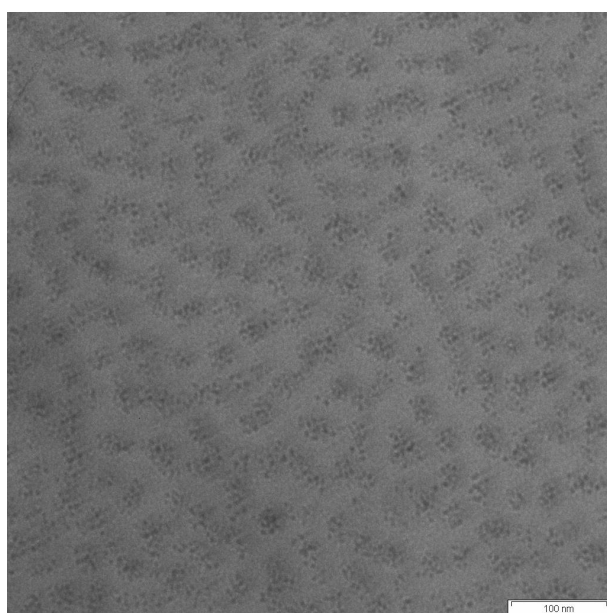
Fig. 123 TEM image of the spherical PS-3917 gold-hybrid PS-b-P(4VP). The dark spots in the image correspond to gold nano-particles which were selectively incorporated in the P(4VP) block.

Fig. 124 represents the frequency dependence of the real part σ' of the complex dielectric conductivity for the three gold hybrid diblock copolymer morphologies and a cylindrical pristine PS-b-P(4VP) diblock copolymer before and after the mechanical stimulus. For the spherical hybrid and on the cylindrical pristine PS-b-P(4VP)

180

samples, LAOS showed no significant effect to the conductivity spectra before and after the experiment. For the spherical hybrid material (PS-3917-Au) a small decrease in the dc plateau is observed after LAOS which became more pronounced for lower temperatures (T = 130 °C and T = 150 °C).

The frequency dependent conductivity spectra of the cylindrical and lamellar samples exhibited a much stronger decrease during LAOS. In both cases the plateau values of $\sigma'(\omega/2\pi)$ are significant decreased after LAOS while the magnitude of the decrease was higher for the lamellar morphology than for the cylindrical one.

From the frequency dependence of σ' the plateau value σ'_0 was calculated by fitting the data obtained at different temperatures (fit not shown) with the random free-energy barrier model developed by J. Dyre[176]. This model assumes that conductivity takes place by hopping charge carriers which are subjected to spatially randomly varying energy barrier[88]. It is solved within the Continuous-Time-Random Walk (CTRW) approximation[180] with the result[181]:

$$\sigma^*(\omega) = \sigma(0)\left[\frac{i\omega\tau_e}{\ln(1+i\omega\tau_e)}\right].$$

(5.1)

It is important to notice that the fit function could only be applied in a frequency range below the second relaxation process which occurred at higher frequencies. The theory only considers relaxation processes which are related to charge transports and does not include additional relaxation process, such as segmental relaxations in polymer chains. Nevertheless, this method allowed the precise determination of the σ'_0 values.

181
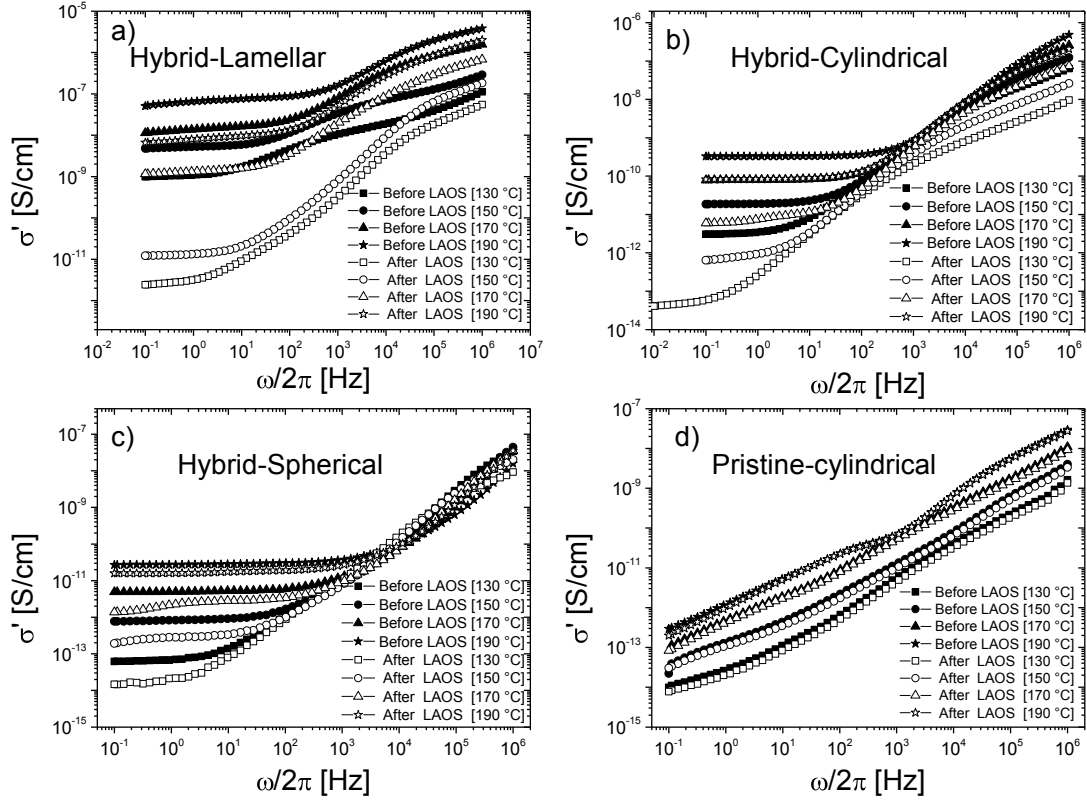
Fig. 124 Frequency dependence of the real part of the dielectric conductivity $\sigma^*(\omega/2\pi,T) = \sigma' + i\sigma'' = i\omega\varepsilon_0\varepsilon^*(\omega/2\pi,T)$ at different temperatures before (filled) and after (open) LAOS for the hybrid materials with a) lamellae, b) cylindrical, c) spherical morphologies. The data in plot d) represent the Frequency dependence of σ' for the neat PS-252 block copolymer.

By plotting the plateau value of σ_0' in an Arrhenius plot, activation energies ΔE_A before and after LAOS can be extracted (see **Fig. 125**). For the lamellar and cylindrical morphologies before LAOS the activation energies of the charge transport were in the same range of approximately $\Delta E_A \approx 1.2$ eV while for the spherical morphology the activation energy was calculated to $\Delta E_A \approx 1.6$ V. For all hybrid materials the activation energy was increased after the LAOS experiment. This increase was less pronounced for the spherical morphology with $\Delta E_A \approx 1.7$ eV (6%) while for the cylindrical morphology ΔE_A increased by approximately 50% to 1.8 eV. For the lamellae morphology the activation energy was nearly doubled to $\Delta E_A \approx$ 2.2 eV.
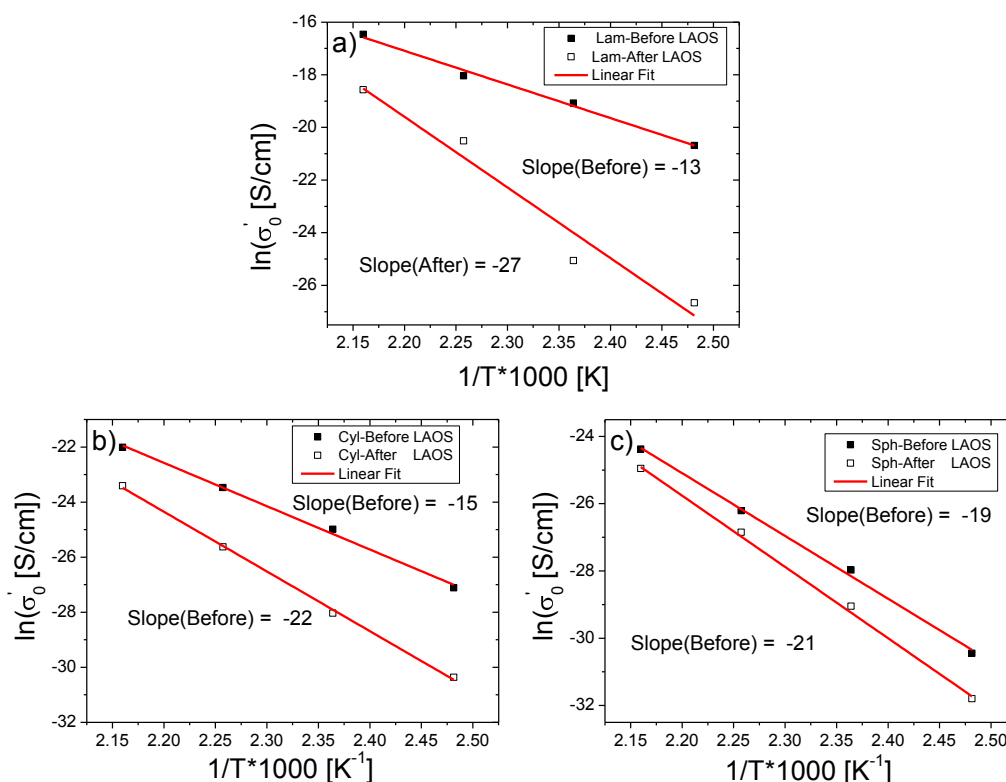
Fig. 125 Arrhenius representation of σ'_0 for a) lamellae, b) cylindrical and c) spherical gold-hybrid PS-b-P(4VP) diblock copolymers before (filled squares) and after (open squares). It can be seen that LAOS strongly affects the charge transport in the self assembled systems while this phenomenon is more pronounced for the lamellae morphology.

7.3. In-situ Rheo-Dielectric investigations

The in situ Rheo-Dielectric measurements were analyzed by the time dependence of the real part of the complex dielectric conductivity σ^*. The dielectric measurement frequency was fixed at $\omega_1/2\pi$ = 10 Hz which corresponds to the dc plateau at the measurement temperature of T = 170 °C. It is important to notice that only for spherical and cylindrical morphologies interpretable dielectric time data could be obtained.

In **Fig. 126** and **Fig. 127** the time dependence of σ' are shown for the cylindrical and the spherical morphologies of the gold-hybrid PS-b-P(4VP) diblock copolymers. For both samples LAOS caused a stretched exponential decrease of $\sigma'(t)$. The obtained curves where fitted with a stretched exponential fit function to gain information about the dielectric orientation time τ_0. It can be seen that the real part of the dielectric conductivity decayed stretched exponentially, leading into a plateau value of σ' = 1.3*10^{-11} S/cm and σ' = 2.8*10^{-12} S/cm for the cylindrical and spherical morphology, respectively. For the cylindrical morphology the observed decrease was

around 75% from σ' = 7.9*10^{-11} S/cm before to σ' = 1.3*10^{-11} S/cm after the LAOS experiment while the spherical morphology was less decreased by only 48% from σ' = 5.4*10^{-12} S/cm at the beginning to 2.8*10^{-12} S/cm. The obtained orientation times were τ_o = 2440 s for the cylindrical and τ_o = 1900 s for the spherical morphology. The fit parameters for the in-situ dielectric measurements are summarized in **Tab. 16**.
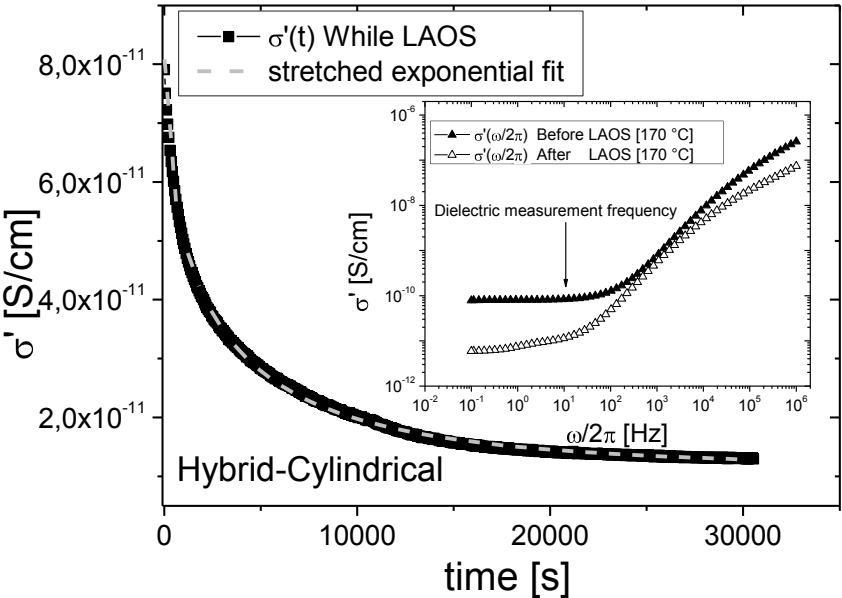
Fig. 126 Time dependence of σ' during the LAOS experiment measured at a fixed dielectric frequency of 10 Hz for the cylindrical morphology (PS-135-Au-Cyl). The inset represents the static dielectric spectra of σ'(ω/2π) before and after the LAOS experiment. The dotted lines represent a stretched exponential fit.
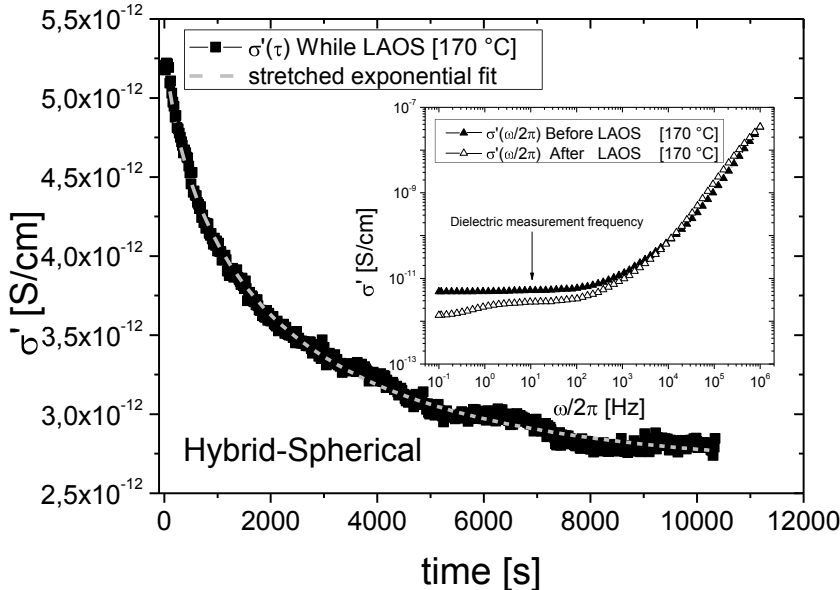
Fig. 127 Time dependence of σ' during the LAOS experiment measured at a fixed dielectric frequency of 10 Hz for the cylindrical morphology (PS-3917-Au-Sph). The inset represents the static dielectric spectra of σ'(ω/2π) before and after the LAOS experiment. The dotted lines represent a stretched exponential fit.

Sample	y_0 [S/cm]	τ [s]	β	A [S/cm]
PS-135 (Hybrid-Cylindrical)	$1.15*10^{-11}$	2440	0.55	$7.21*10^{-11}$
PS-3917 (Hybrid-Spherical)	$2.63*10^{-12}$	1900	0.65	$2.82*10^{-12}$

Tab. 16 Calculated fit parameters from $\sigma'(t)$ for the cylindrical (PS-135) and the spherical (PS-3917) gold-hybrid PS-b-P(4VP) at a constant dielectric measurement frequency of 10 Hz during LAOS ($\omega_1/2\pi$ = 1 Hz, γ_0 = 0.5 and T = 170 °C).

The in-situ measured time dependence of the non-linear parameter $I_{3/1}$ is represented in **Fig. 128** for the cylindrical (PS-135-Au-Cyl) and in **Fig. 129** for the spherical (PS-3917-Au-Sph) morphologies. In both cases $I_{3/1}(t)$ showed a strong stretched exponential increase which began at approximately 1% and reached a plateau value of approximately 30% for the spherical and of 25% for the cylindrical morphology. It is important to notice that these were the highest nonlinearities detected for polymer melts. From the basic mathematics of the non-linear parameter introduced in section **3.2.1c**), $I_{3/1}$ should be limited at a maximum value of 33%. It is assumed that this extreme high mechanical non-linear response is caused by the inorganic nano-particles which interfere with polymer dynamics during the LAOS experiments. The obtained orientation times were τ_o = 3350 s for the spherical and τ_o = 5500 s for the cylindrical morphology.

However, at the present state of investigation no precise conclusion of the underlying mechanism, governing the mechanical non-linear response, can be provided.
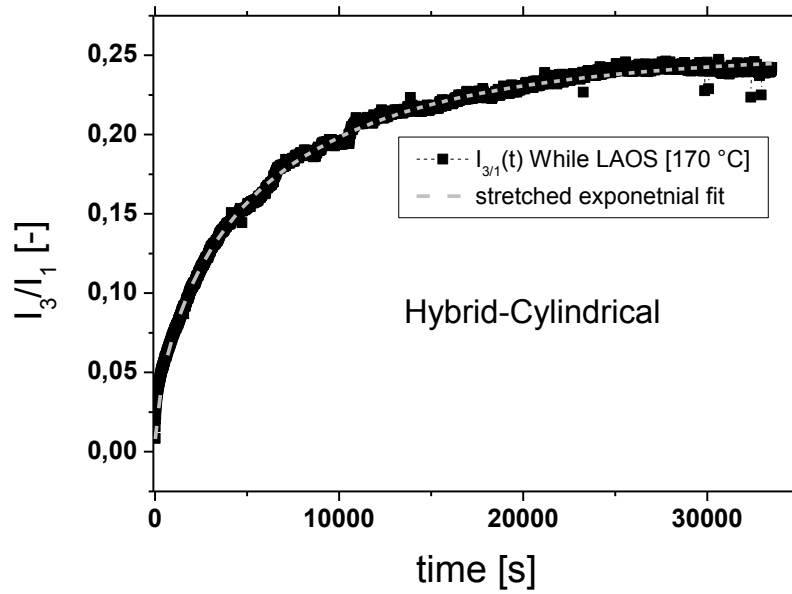
Fig. 128 In-situ measured time dependence of $I_{3/1}$ for the shear-induced alignment of the spherical gold-hybrid PS-135 block copolymer. The dotted lines represent a stretched exponential fit.
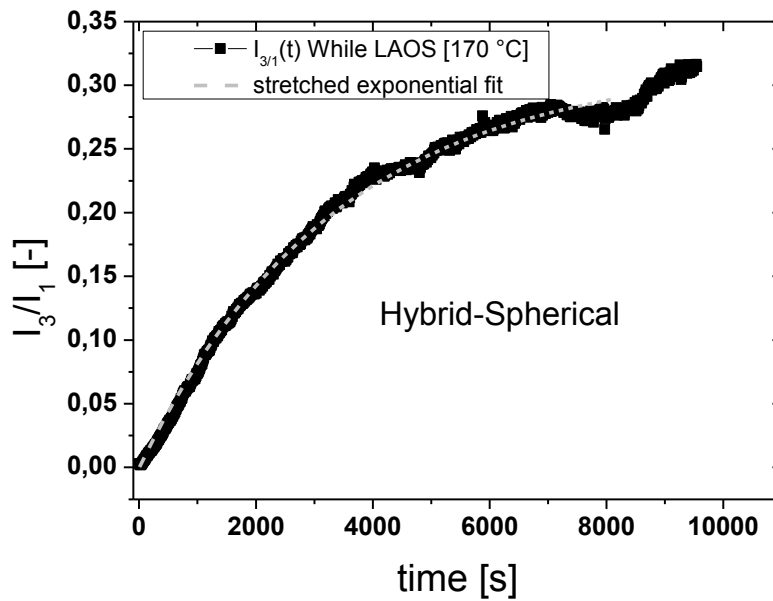
Fig. 129 In-situ measured time dependence of $I_{3/1}$ for the shear-induced alignment of the spherical gold-hybrid PS-3917 block copolymer. The dotted lines represent a stretched exponential fit.

Sample	y_0 [-]	τ [s]	β	A [-]
PS-135 (Hybrid-Cylindrical)	$8*10^{-4}$	5500	0.67	0.25
PS-3917 (Hybrid-Spherical)	$3.5*10^{-4}$	3350	1	0.32

Tab. 17 Calculated fit parameters from $I_{3/1}(t)$ for the cylindrical (PS-135) and the spherical (PS-3917) gold-hybrid PS-b-P(4VP) block copolymers during LAOS ($\omega_1/2\pi$ = 1 Hz, γ_0 = 0.5 and T = 170 °C).

7.4. Summary and discussion of the Rheo-Dielectric investigations of gold-hybrid PS-b-P(4VP)

For all investigated morphologies the gold-hybrid PS-b-P(4VP) diblock copolymers, with gold nano-particles selectively incorporated in the P(4VP) block, showed a significant frequency independent plateau in the low frequency regime of σ'. It is assumed that this so called dc-plateau appears due to charge transports along the gold nano-particles from one side of the electrode to the other. However, the measured conductivities of σ' < 10^{-7} S/cm are too small for a conductive material. Therefore, it is assumed that the charge transport occurs via a hopping mechanism between the spatial separated gold nano-particles mediated by ionic charge carriers.

Furthermore, it could be shown that LAOS affected the dielectric response of the sample melts which was reflected in a change of the activation energies calculated from the dc-plateau value of σ'($\omega_1/2\pi$). The increase in the activation energies was stronger for the morphologies which can be macroscopically anisotropic aligned, such as the cylindrical and the lamellae morphologies. For these morphologies an increase of approximately 50% to more than 100% was detected.

In contrast, the spherical morphology was less affected by LAOS (less than 10%). It is assumed that the decrease of the dc-plateau is affected by the macroscopic alignment of the diblock copolymer microstructures. Recent investigations of Mendoza et al.[152], performed under similar LAOS conditions (70%, 1 Hz, 170 °C) with the same lamellar gold-hybrid PS-P(4VP) block copolymer (PS-252-Au-Lam), revealed a perfect macroscopic parallel orientation. Based on these results it is assumed that the herein applied LAOS conditions (50%, 1 Hz, 170 °C) caused a macroscopic parallel orientation for the lamella sample as well. This would explain the drastic increase of activation energies for the charge transport after LAOS.

In this case the orientation of the unit normal of the lamellae preferentially parallel to the external electric field would disturb the percolation path which leads to inferior conductivity. This would also explain the decrease in the conductivity for the cylindrical morphology under the assumption that the P(4VP) blocks which form the cylinders are orientated along the shear direction.

The in-situ Rheo-Dielectric measurements showed for the first time that it is possible to online monitor dielectric changes of hybrid polymer materials under mechanical stimulus. Furthermore, it was shown that the mechanical non-linear

response is drastically affected by the incorporated nano-particles resulting in a high degree of nonlinearity which gives rise to further detailed investigation. These first results presented herein, revealed an insight to the time evolution of the conductivity under mechanical shear fields.

8. Concluding Remarks

The combination of a rheometer for precise mechanical measurements and a powerful X-Ray source, provided by the German Synchrotron in Hamburg (DESY), enabled the in-situ analysis of the overall mechanical alignment of hierarchical ordered systems on a nanometer length scale. With the unique Rheo-SAXS-combination, located at the beam line BW1 at HasyLab, it was possible to online monitor, with a time resolution of 10 s, the structural evolution during shear-induced alignment of a symmetric diblock copolymer. Different large amplitude oscillatory shear (LAOS) experiments were applied to study the kinetic pathway of the orientation process of diblock copolymers.

For the first time, it was shown that, for high strain amplitudes (γ_0 = 2 and 3) at T = 150 °C, an optimal degree of macroscopic orientation was achieved at short mechanical excitation times (less than 1 hour). For the first time, it could be shown that as the LAOS experiment continued after reaching a primary minimum of σ_{SAXS}, a less ordered overall orientation developed. This was indicated by a broadening of the azimuthally averaged scattered peak in the (*OX*, *OY*) plane detected by in-situ Rheo-SAXS measurements and was also confirmed by ex-situ SAXS studies, which revealed a heterogeneous biaxial distribution with both parallel and perpendicular fractions.

By comparing the structural changes with the mechanical responses, it was found that the de-orientation process was also visible in the time evolution of the mechanical properties G'' and $I_{3/1}$. The time progression of the mechanical response for G'' measured by the in-situ Rheo-SAXS setup and $I_{3/1}$, both showed a similar stretched exponential decay in the beginning of the mechanical excitation as well as an increase in G'' and $I_{3/1}$ from their plateau values at higher strain amplitudes. This increase in the mechanical properties indicated that de-ordering of the unit normal of the lamellae in the block copolymer melt occurred. Therefore, it was assumed that a higher degree of disorder in the sample caused a higher non-linear response as measured by FT-Rheology. From these findings, an orientation mechanism was proposed that is mainly dominated by the rotation of the locally ordered lamellae block copolymer grains.

Based on these results a simple model was developed which is consistent with experimental findings. This model explains the mechanical non-linear response

during the shear-induced alignment process by a rotational mechanism of the locally anisotropic aligned lamellae diblock copolymer. This causes a deformation of the grain interfaces during rotational alignment due to the interfacial tension between the locally anisotropic ordered microdomain grains.

Furthermore, different processing parameters for the herein presented model compounds were obtained for various different conditions (see **Tab. 9**). For example, the kinetics of the orientation process as measured by 2D-SAXS revealed that the overall orientation of the lamellae is a function of the applied mechanical strain amplitude γ_0 where the orientation time τ_o had a power law dependence ranging between $\tau \sim \gamma_0^{-1.6}$ and γ_0^{-2}. By comparing the in-situ time data calculated from the 2D-SAXS patterns with the measured mechanical response quantified by the non-linear parameter $I_{3/1}$, the same power law dependence for the orientation time was confirmed. Additionally, it was proven that the observed de-ordering phenomenon also occurred for higher molecular weight PS-b-PI diblock copolymers.

These first results obtained by our unique Rheo-SAXS setup demonstrate the connectivity between structural dynamics in PS-b-PI diblock copolymer melts and the mechanical non-linear response of the sample under large amplitude oscillatory shear.

From high sensitive in-situ Rheo-Dielectric measurements of the shear-induced alignment of PS-b-PI diblock copolymers it was found that dielectric measurements of the polyisoprene chain dynamics are capable to distinguish between the parallel and perpendicular alignments, respectively. For the overall parallel orientation with unit normal of the lamellae directed parallel to the external electric field, a decrease in the dielectric loss ε'' was detected. In contrast, the dielectric loss was increased for the macroscopic perpendicular alignment with the unit normal of the lamellae directed perpendicular to the external electric field. It was assumed that these phenomena were attributed to anisotropic diffusion of the tethered polymer chains parallel and perpendicular to the interface between the polyisoprene and the polystyrene block[163].

Additionally, the re-orientation process of the PS-b-PI-13k-13k diblock copolymer was also observed by in-situ dielectric measurements. It was proven that the dielectric and non-linear mechanical response quantified by $I_{3/1}$ showed astonishing similarities in their time progression.

For the first time the shear-induced alignment of gold-hybrid PS-P(4VP) nano-composites was investigated via in-situ Rheo-Dielectric techniques. It could be

shown that LAOS causes a drastically decrease of the initial conductivity. The magnitude of this effect depended on the respective morphology of the diblock copolymer. Morphologies which are capable to become macroscopically anisotropic during shear-induced alignment showed a more pronounced decrease of the conductivity after LAOS.

9. Experimental Part

9.1. High vacuum polymerization techniques

All polymers used in this thesis were synthesized using a special high vacuum line. In general, anionic polymerization techniques are very sensitive to impurities which are capable of deactivating the initiator and the propagating chain ends[73] (e.g. water, oxygen, …). All manipulations were performed in glass reactors which were connected to the vacuum line and evacuated as well as thoroughly heat dried at 500 °C under continuous pumping. Afterwards, the glass ware was allowed to cool down to room temperature before purging with dry argon (5.0) which additionally was dried over activated NaA-zeolites molecular sieves (3 Å). This procedure was repeated at least three times to remove volatile contaminants present in the inner surface of the glass. The syntheses were performed under inert atmosphere using argon. The addition of purified monomers and reactants was done via glass ampoules which were directly connected to the polymerization reactor. The initiator was added under argon counterflow via a flame dried syringe. The purified toluene respectively tetrahydrofuran, which were used as reaction solvents, were added by vacuum distillation into the polymerization reactor, which was cooled with liquid nitrogen.

9.2. Purification of solvents and monomers

9.2.1. Purification of Toluene

Toluene was refluxed under argon atmosphere in a round bottom flask containing grounded CaH_2. It was stirred for 24 hours for the reaction of CaH_2 with moisture. For further usage it was transferred into a solvent container connected to the vacuum line under inert atmosphere for further usage. The solvent container contained living Polystyrene of low molecular weight (around 1 kg/mol). The bright orange color of PSLi was used as an indicator for the purity of the solvent.

9.2.2. Purification of Tetrahydrofuran (THF)

THF was pre-dried over CaH_2 for 24 hours under inert gas before distillation. It was additionaly refluxed over sodium (Na) under an argon atmosphere in the presence of benzophenone as indicator until a bright deep purple color was attained, The THF was then distilled into the solvent container which additionally contained a small amount of Na and benzophenone to indicate the purity of the solvent. The solvent container was connected to the vacuum line for further usage.

9.2.3. Purification of Styrene (bp: 145 °C at T = 22 °C)

The purification of Styrene (Aldrich) was carried out in two steps. In the first step the monomer was dried overnight, on the vacuum line, over CaH_2 in a short path distillation apparatus and subsequently distillated into a head dried round-bottom flask for further purification over dibutylmagnesium (1 M in n-heptane). For 10 ml monomer 1 ml DBMg solution was used. The solution was stirred under argon atmosphere for 24 hours. Afterwards, the n-heptane was removed under low pressure and the purified monomer was distilled under reduced pressure into a dried and precalibrated glass ampoules. The purified monomer was stored under argon atmosphere at -20 °C further usage.

9.2.4. Purification of Isoprene (bp: 34 °C at T = 22 °C)

Isoprene was first dried over CaH_2 overnight to remove initial amounts of moisture. The pre-dried monomer is distilled at the vacuum line into a round-bottom flask containing n-BuLi, (1.3 M in cyclohexane,V(monomer)/V(n-BuLi solution) = 10/1) while the cyclohexane was removed under low pressure before the distillation was performed. The n-BuLi was allowed to react with present contaminants for 30 min. at room temperature. After a light yellow color was obtained, the monomer was distilled into dried and precalibrated glass ampoules. The monomer was stored under argon atmosphere at -20 °C.

9.2.5. Degassing

Before the solvents and monomers were used for anionic polymerization contaminations of oxygen and other gases which are dissolved in the liquids had to

be removed be degassing. The flask containing the purified liquid is connected to the vacuum line through a stopcock. The stopcock was opened until bubbles appeared. The liquid is then frozen with the stopcock closed using liquid nitrogen. Afterwards, full vacuum is applied to the frozen bulk. After high vacuum is attained, the stopcock is closed and the liquid is thawed. This so called freeze-thaw cycle was repeated for three times until no bubbles occurred in the liquid during the thaw step.

9.3. Synthesis of the homopolymers and diblock copolymers

The basic reactor used for the synthesis of the polymers is shown in **Fig. 130**. Despite the initiator, the ampoules which were directly connected to the reactor contained all necessary reagents and solvents. The reactor is attached to the vacuum line. The solvents used for the polymerization were directly distilled from the solvent container into the reactor and afterwards degassed as described above. The monomers were degassed at the vacuum line before the ampoules were equipped to the polymerization reactor. All polymerizations were initiated with sec-butyllithium (s-BuLi) (Aldrich, 1.4 M in cyclohexane) which was used without further purification.
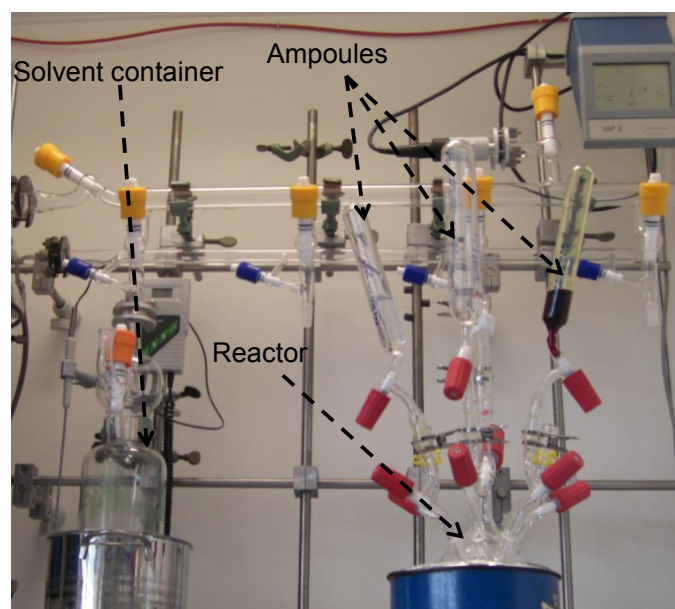
Fig. 130 Pictures of one high vacuum line equipped with a polymerization reactor which was used for the synthesis of the polymers.

9.3.1. Synthesis of Polystyrene

The polymerization of styrene was carried out in THF (V(THF)/V(monomer) = 15/1) which was cooled to -78 °C using an acetone/dry-ice cooling bath. The initiator was added under argon counter flow with a syringe. The monomer was slowly added to the initiator solvent mixture which became bright red as the polymerization started. After the total addition of monomer, the reaction was stirred for 20 min to ensure full conversion. The living polymer solution was terminated by adding a small amount of degassed MeOH to the solution. The terminated polymer solution was precipitated in MeOH (V(MeOH)/V(polymer solution) = 10/1) and the resulting crude product was freeze dried from a 10 wt.% cyclohexane solution for 10 hours under high vacuum. The powdered product was stored at room temperature.

9.3.2. Synthesis of Polyisoprene

To achieve a high degree of 1,4-Polyisoprene the polymerization was carried out in toluene at room temperature. The monomer was added to the toluene and stirred for 5 minutes before the initiator was added to the solution. After the addition of the initiator the reaction solution maintained colorless. The reaction was stirred for 24 hours to ensure full conversion before the polymerization was terminated by adding a small amount of MeOH. The synthesized polymer was stabilized with 2,6-di-*tert*-butyl-4-methylphenol to avoid crosslinking due to the unsaturated PI block. The terminated diblock copolymer was precipitated in methanol (V(MeOH)/V(polymer solution) = 10/1). The crude polymer was dried under high vacuum at 70 °C for 10 hours. The final product was stored at -20 °C.

9.3.3. Synthesis of Polystyrene-block-Polyisoprene diblock copolymers

The polystyrene-*block*-polyisoprene diblock copolymer was synthesized via sequential anionic polymerization of styrene followed by isoprene under high vacuum at room temperature using toluene as the solvent and sec-butyllithium as the initiator. The polymerization of styrene was carried out for 10 hours. Before the addition of isoprene aliquots of the PS precursor were taken for molecular characterization under argon counter flow via a syringe. After the addition of isoprene the dark red solution turned into a slight yellow color indicating the addition of isoprene to the

living polystyrene chain ends. The reaction was stirred for another 10 hours before terminating the living anions by addition of MeOH. The synthesized polymer was stabilized with 2,6-di-*tert*-butyl-4-methylphenol to avoid crosslinking due to the unsaturated PI block. The terminated diblock copolymer was precipitated in methanol (V(MeOH)/V(polymer solution) = 10/1). The resulting crude product was freeze dried from a 10 wt.% cyclohexane solution for 10 hours under high vacuum. The powdered product was stored at -20 °C until needed.

10. Bibliography

1. Odian, G. G., *Principles of polymerization*. Wiley-Interscience: Hoboken, N.J., 2004; p 812.

2. Barner-Kowollik, C.; Davis, T. P.; Heuts, J. P. A.; Stenzel, M. H.; Vana, P.; Whittaker, M. *J. Polym. Sci. Part A: Polym. Chem.* **2003,** 41, 365.

3. Zhao, Y. L.; Wang, L.; Xiao, A. G.; Yu, H. J. *Prog. Polym. Sci.* **2010,** 35, 1195.

4. Barner-Kowollik, C., *Handbook of RAFT polymerization*. Wiley-VCH: Weinheim, 2008; p 543.

5.   Georges, M. K.; Veregin, R. P. N.; Kazmaier, P. M.; Hamer, G. K. *Macromolecules* **1993,** 26, 2987.

6. Hawker, C. J.; Bosman, A. W.; Harth, E. *Chem. Rev.* **2001,** 101, 3661.

7. Wang, J. S.; Matyjaszewski, K. *J. Am. Chem. Soc.* **1995,** 117, 5614.

8. Matyjaszewski, K.; Xia, J. H. *Chem. Rev.* **2001,** 101, 2921.

9. Kato, M.; Kamigaito, M.; Sawamoto, M.; Higashimura, T. *Macromolecules* **1995,** 28, 1721.

10. Lutz, J. F. *J. Polym. Sci. Part A: Polym. Chem.* **2008,** 46, 3459.

11. Müller, A. H. E.; Hogenesch, T. E. *Macromolecules* **1988,** 21, 2336.

12. Müller, A. H. E.; Matyjaszewski, K., *Controlled and living polymerizations : methods and materials*. Wiley-VCH: Weinheim, 2009; p 612.

13. Kempf, M.; Barroso, V. C.; Wilhelm, M. *Macromol. Rapid Commun.* **2010,** 31, 2140.

14. Higashimura, T.; Sawamoto, M. *Adv. Polym. Sci.* **1984,** 62, 49.

15. Crivello, J. V. *Adv. Polym. Sci.* **1984,** 62, 1.

16. PlasticEurope, Plastics – the Facts 2010. In *PlasticEurope*, 2010.

17. Tomita, Y.; Adachi, T.; Tanaka, S. *Arch. Comput. Method. E* **1998,** 5, 167.

18. Palza, H.; Filipe, S.; Naue, I. F. C.; Wilhelm, M. *Polymer* **2010,** 51, 522.

19. Palza, H.; Reznik, B.; Kappes, M.; Hennrich, F.; Naue, I. F. C.; Wilhelm, M. *Polymer* **2010,** 51, 3753.

20. Hamley, I. W., *The physics of block copolymers*. Oxford University Press: Oxford ; New York, 1998; p 424

21. Hamley, I. W., *Developments in block copolymer science and technology*. J. Wiley: Chichester, West Sussex ; Hoboken, NJ, 2004; p 367.

22. McLeish, T. C. B. *Adv. Phys.* **2002,** 51, 1379.

23. Mezger, T. G., *The rheology handbook* Vincentz Network: Hannover, 2011; p 432.

24. Matsen, M. W. *J. Chem. Phys.* **2000,** 113, 5539.

25. Matsen, M. W.; Schick, M. *Phys. Rev. Lett.* **1994,** 72, 2660.

26. Khandpur, A. K.; Forster, S.; Bates, F. S.; Hamley, I. W.; Ryan, A. J.; Bras, W.; Almdal, K.; Mortensen, K. *Macromolecules* **1995,** 28, 8796.

27. Koppi, K. A.; Tirrell, M.; Bates, F. S.; Almdal, K.; Colby, R. H. *J. Phys. II* **1992,** 2, 1941.

28. Laiho, A.; Ikkala, O. *Rev. Sci. Instrum.* **2007,** 78.

29. Hyun, K.; Wilhelm, M.; Klein, C. O.; Cho, K. S.; Nam, J. G.; Ahn, K. H.; Lee, S. J.; H., E. R. *Prog. Polym. Sci.* **2011**, doi:10.1016/j.progpolymsci.2011.02.002.

30. Wiesner, U. *Macromol. Chem. Phys.* **1997,** 198, 3319.

31. Wilhelm, M. *Macromol. Mater. Eng.* **2002,** 287, 83.

32. Wilhelm, M.; Maring, D.; Spiess, H. W. *Rheol. Acta* **1998,** 37, 399.

33. Hyun, K.; Hofl, S.; Kahle, S.; Wilhelm, M. *J. Non-Newtonian Fluid Mech.* **2009,** 160, 93.

34. Hofl, S.; Kremer, F.; Spiess, H. W.; Wilhelm, M.; Kahle, S. *Polymer* **2006,** 47, 7282.

35.   bel, G. *Langmuir* **2011**, 2880.

36. Larson, R. G., *The structure and rheology of complex fluids*. Oxford Univ. Press: New York, 1999; p 663

37. Hirschfelder, J. O.; Curtiss, C. F.; Bird, R. B., *Molecular theory of gases and liquids*. Wiley: New York, 1964; p 1249

38. Tipler, P. A.; Gerlich, D., *Physik*. Spektrum Akad. Verl.: Heidelberg, 2004; p 1522

39. Dealy, J. M.; Wissbrun, K. F., *Melt rheology and its role in plastics processing*. Kluwer Academic: Boston, Mass., 1999; p 665.

40. Brandrup, J., *Polymer handbook*. 4. ed.; Wiley: Hoboken, N. J., 1999.

41. Neidhöfer, T., *Fourier transform rheology on anionically synthesised polymer melts and solutions of various topology*. Dissertation: Johannes Guttenberg-Universität 2003.

42. Flory, P. J., *Principles of polymer chemistry*. Cornell Univ. Press: Ithaca, NY, 2006; p 672

43. Young, R. J.; Lovell, P. A., *Introduction to polymers*. Thornes: Cheltenham, 2000; p 443.

44. Ferry, J. D., *Viscoelastic properties of polymers*. Wiley: New York, 1980; p 641

45. Alwis, K. G. N. C.; Burgoyne, C. J. *Applied Composite Materials* **2006,** 13, 249.

46. Lechner, M. D.; Gehrke, K.; Nordmeier, E. H.; Heering, R., *Makromolekulare Chemie ein Lehrbuch für Chemiker, Physiker, Materialwissenschaftler und Verfahrenstechniker*. Birkhäuser: Basel, 2003; p 536

47. Doi, M.; Edwards, S. F. *J. chem. Soc. Faraday Trans* **1978,** 74, 1789.

48. De Gennes, P. G. *J. Chem. Phys.* **1971,** 55, 572.

49. Wedler, G., *Lehrbuch der physikalischen Chemie*. Wiley-VCH: Weinheim, 2007; p 1072

50. Chavez, F. V.; Saalwachter, K. *Macromolecules* **2011,** 44, 1549.

51. Wang, S. Q. *Journal of Polymer Science Part B-Polymer Physics* **2003,** 41, 1589.

52. Milner, S. T.; McLeish, T. C. B. *Phys. Rev. Lett.* **1998,** 81, 725.

53. Wang, Z. W.; Larson, R. G. *Macromolecules* **2008,** 41, 4945.

54. Zamponi, M.; Wischnewski, A.; Monkenbusch, M.; Willner, L.; Richter, D.; Likhtman, A. E.; Kali, G.; Farago, B. *Phys. Rev. Lett.* **2006,** 96.

55. Wagner, M. H.; Rubio, P.; Bastian, H. *J. Rheol.* **2001,** 45, 1387.

56. Likhtman, A. E.; Sukumaran, S. K.; Ramirez, J. *Macromolecules* **2007,** 40, 6748.

57. Watanabe, H. *Prog. Polym. Sci.* **1999,** 24, 1253.

58. Harris, J. *Nature* **1965,** 207, 744.

59. Tee, T. T.; Dealy, J. M. *T. Soc. Rheol.* **1975,** 19, 595.

60. Komatsu, H.; Mitsui, T. *T. Soc. Rheol.* **1973,** 17, 351.

61. Hyun, K.; Kim, S. H.; Ahn, K. H.; Lee, S. J. *J. Non-Newtonian Fluid Mech.* **2002,** 107, 51.

62. Klein, C. O.; Spiess, H. W.; Calin, A.; Balan, C.; Wilhelm, M. *Macromolecules* **2007,** 40, 4250.

63. Storm, C.; Pastore, J. J.; MacKintosh, F. C.; Lubensky, T. C.; Janmey, P. A. *Nature* **2005,** 435, 191.

64. Mason, T. G.; Weitz, D. A. *Phys. Rev. Lett.* **1995,** 75, 2770.

65. Bossard, F.; Moan, M.; Aubry, T. *J. Rheol.* **2007,** 51, 1253.

66. Skoog, D. A.; Holler, F. J.; Crouch, S. R., *Principles of instrumental analysis*. Thomson Brooks/Cole: Belmont, Calif., 2007; p 1039

67. Ramirez, R. W., *The FFT : fundamentals and concepts*. Prentice-Hall: Englewood Cliffs, N.J., 1985; p 178

68. Philippoff, W. *Trans. Soc. Rheol.* **1966,** 10, 317.

69. Hyun, K.; Wilhelm, M. *Xvth International Congress on Rheology - the Society of Rheology 80th Annual Meeting, Pts 1 and 2* **2008,** 1027, 369.

70. Hyun, K.; Wilhelm, M. *Macromolecules* **2009,** 42, 411.

71. Carotenuto, C.; Grosso, M.; Maffettone, P. L. *Macromolecules* **2008,** 41, 4492.

72. Sagis, L. M. C.; Ramaekers, M.; van der Linden, E. *Phys. Rev. E* **2001,** 6305.

73. Hadjichristidis, N.; Iatrou, H.; Pispas, S.; Pitsikalis, M. *J. Polym. Sci. Part A: Polym. Chem.* **2000,** 38, 3211.

74. Matsen, M. W. *J. Phys.: Condens. Matter* **2002,** 14, 21.

75. Thomas, E. L.; Anderson, D. M.; Henkee, C. S.; Hoffman, D. *Nature* **1988,** 334, 598.

76. Bates, F. S.; Rosedale, J. H.; Fredrickson, G. H. *J. Chem. Phys.* **1990,** 92, 6255.

77. Roe, R. J.; Fishkis, M.; Chang, J. C. *Macromolecules* **1981,** 14, 1091.

78. Owens, J. N.; Gancarz, I. S.; Koberstein, J. T.; Russell, T. P. *Macromolecules* **1989,** 22, 3380.

79. Bates, F. S. *Science* **1991,** 251, 898.

80. Matsen, M. W.; Bates, F. S. *Macromolecules* **1996,** 29, 1091.

81. Matsen, M. W.; Bates, F. S. *Macromolecules* **1996,** 29, 7641.

82. Zhang, Y. M.; Wiesner, U. *Macromol. Chem. Phys.* **1998,** 199, 1771.

83. Floudas, G.; Fytas, G.; Hadjichristidis, N.; Pitsikalis, M. *Macromolecules* **1995,** 28, 2359.

84. Chen, Z. R.; Issaian, A. M.; Kornfield, J. A.; Smith, S. D.; Grothaus, J. T.; Satkowski, M. M. *Macromolecules* **1997,** 30, 7096.

85. Winey, K. I.; Patel, S. S.; Larson, R. G.; Watanabe, H. *Macromolecules* **1993,** 26, 2542.

86. Larson, R. G.; Winey, K. I.; Patel, S. S.; Watanabe, H.; Bruinsma, R. *Rheol. Acta* **1993,** 32, 245.

87. Gupta, V. K.; Krishnamoorti, R.; Chen, Z. R.; Kornfield, J. A.; Smith, S. D.; Satkowski, M. M.; Grothaus, J. T. *Macromolecules* **1996,** 29, 875.

88. Kremer, F., *Broadband dielectric spectroscopy*. Springer: Berlin 2003; p 729.

89. McCrum, N. G.; Read, B. E.; Williams, G., *Anelastic and dielectric effects in polymeric solids*. Dover: New York 1991; p 617

90. Watanabe, H.; Urakawa, O.; Kotaka, T. *Macromolecules* **1993,** 26, 5073.

91. Cole, R. S.; Cole, R. H. *J. Chem. Phys.* **1941,** 9, 341.

92. Havriliak, S.; Negami, S. *Polymer* **1967,** 8, 161.

93. Stockmayer, W. H.; Burke, J. J. *Macromolecules* **1969,** 2, 647.

94. Garwe, F.; Schonhals, A.; Lockwenz, H.; Beiner, M.; Schroter, K.; Donth, E. *Macromolecules* **1996,** 29, 247.

95. Adachi, K.; Kotaka, T. *Macromolecules* **1985,** 18, 466.

96. Boese, D.; Kremer, F. *Macromolecules* **1990,** 23, 829.

97. Kerker, M., *The scattering of light and other electromagnetic radiation*. Acad. Press: New York, 1969; p 666.

98. Gerthsen, C.; Meschede, D.; Vogel, H., *Physik : die ganze Physik zum 21. Jahrhundert*. Springer: Berlin 2002; p 1288.

99. Guinier, A.; Fournet, G. r., *Small-angle scattering of x-rays*. Wiley Chapman Hall: New York, NY, 1955; p 268.

100. Feigin, L. A.; Svergun, D. I.; Taylor, G. W., *Structure analysis by small-angle X-ray and neutron scattering*. Plenum Press: New York, 1987; p 335.

101. Cummings, P. T.; Perram, J. W.; Smith, E. R. *Mol. Phys.* **1976,** 31, 535.

102. Szwarc, M. *Nature* **1956,** 178, 1168.

103. Cernohous, J. J.; Macosko, C. W.; Hoye, T. R. *Macromolecules* **1997,** 30, 5213.

104. Hong, K. L.; Uhrig, D.; Mays, J. W. *Current Opinion in Solid State & Materials Science* **1999,** 4, 531.

105. Cowie, J. M. G., *Chemie und Physik der synthetischen Polymeren* Vieweg: Braunschweig 1997; p 489.

106. Riedel, E.; Alsfasser, R., *Moderne anorganische Chemie*. de Gruyter: Berlin 2007; p 560.

107. Prud'homme, J.; Bywater, S., Block Copolymers of Styrene and Isoprene: Experimental Desgin and Product Analysis. In *Plenum Press*, New York, 1970; p 339.

108. Semenov, A. N. *Soviet Physics JETP* **1985,** 61, 733.

109. Helfand, E.; Wasserman, Z. R. *Macromolecules* **1976,** 9, 879.

110. Papon, A.; Montes, H.; Lequeux, F.; Guy, L. *J Polym Sci Pol Chem* **2010,** 48, 2490.

111. Ravindranath, S.; Wang, S. Q. *J. Rheol.* **2008,** 52, 341.

112. Kallus, S.; Willenbacher, N.; Kirsch, S.; Distler, D.; Neidhofer, T.; Wilhelm, M.; Spiess, H. W. *Rheol. Acta* **2001,** 40, 552.

113. Cho, K. S.; Hyun, K.; Ahn, K. H.; Lee, S. J. *J. Rheol.* **2005,** 49, 747.

114. Ewoldt, R. H.; Hosoi, A. E.; McKinley, G. H. *J. Rheol.* **2008,** 52, 1427.

115. Wagner, M. H.; Rolon-Garrido, V. H.; Hyun, K.; Wilhelm, M. *J. Rheol.* **2011,** 55, 495.

116. Klein, C., *Rheology and Fourier-Transform Rheology on water-based systems*. Dissertation: 2005.

117. van Dusschoten, D.; Wilhelm, M. *Rheol. Acta* **2001,** 40, 395.

118. Adachi, K.; Fukui, F.; Kotaka, T. *Langmuir* **1993,** 10, 126.

119. Crawshaw, J.; Meeten, G. *Rheol. Acta* **2006,** 46, 183.

120. Peng, Y. Y.; Li, H. M.; Turng, L. S. *Polym. Eng. Sci.* **2010,** 50, 61.

121. Sato, T.; Watanabe, H.; Osaki, K. *Macromolecules* **1996,** 29, 6231.

122. Watanabe, H.; Sato, T.; Matsumiya, Y.; Inoue, T.; Osaki, K. *Nihon Reoroji Gakkaishi* **1999,** 27, 121.

123. Matsumiya, Y.; Balsara, N. P.; Kerr, J. B.; Inoue, T.; Watanabe, H. *Macromolecules* **2004,** 37, 544.

124. Watanabe, H.; Sato, T.; Hirose, M.; Osaki, K.; Yao, M. L. *Rheol. Acta* **1998,** 37, 519.

125. Matsumiya, Y.; Watanabe, H.; Inoue, T.; Osaki, K.; Yao, M. L. *Macromolecules* **1998,** 31, 7973.

126. Uneyama, T.; Masubuchi, Y.; Horio, K.; Matsumiya, Y.; Watanabe, H.; Pathak, J. A.; Roland, C. M. *J. Polym. Sci. Part B: Polym. Phys.* **2009,** 47, 1039.

127. Watanabe, H.; Chen, Q. A.; Kawasaki, Y.; Matsumiya, Y.; Inoue, T.; Urakawa, O. *Macromolecules* **2011,** 44, 1570.

128. Reimers, W., *Neutrons and synchrotron radiation in engineering materials science : from fundamentals to material and component characterization*. Wiley-VCH: Weinheim, 2008; p 436.

129. Abuzaina, F. M.; Garetz, B. A.; Mody, J. U.; Newstein, M. C.; Balsara, N. P. *Macromolecules* **2004,** 37, 4185.

130. Hamley, I. W.; Pople, J. A.; Booth, C.; Derici, L.; Imperor-Clerc, M.; Davidson, P. *Phys. Rev. E* **1998,** 58, 7620.

131. Di Cola, E.; Fleury, C.; Panine, P.; Cloitre, M. *Macromolecules* **2008,** 41, 3627.

132. Berghausen, J.; Zipfel, J.; Diat, O.; Narayanan, T.; Richtering, W. *Phys. Chem. Chem. Phys.* **2000,** 2, 3623.

133. Wang, H.; Kesani, P. K.; Balsara, N. P.; Hammouda, B. *Macromolecules* **1997,** 30, 982.

134. Carreras, E. S.; Piau, J.-M.; El Kissi, N.; Pignon, F.; Panine, P. *J. Rheol.* **2006,** 50, 803.

135. Stasiak, J.; Mackley, M. R.; Squires, A. M.; Castelletto, V.; Hamley, I. W.; Moggridge, G. D. *Soft Matter* **2010,** 6, 1941.

136. Polushkin, E.; van Ekenstein, G. A.; Ikkala, O.; ten Brinke, G. *Rheol. Acta* **2004,** 43, 364.

137. Polushkin, E.; Bondzic, S.; de Wit, J.; van Ekenstein, G. A.; Dolbnya, I.; Bras, W.; Ikkala, O.; ten Brinke, G. *Macromolecules* **2005,** 38, 1804.

138. Garcia-Gutierrez, M. C.; Hernandez, J. J.; Nogales, A.; Pantine, P.; Rueda, D. R.; Ezquerra, T. A. *Macromolecules* **2008,** 41, 844.

139. Hamley, I. W., *The physics of block copolymers*. Oxford Univ. Press: Oxford 2003; p 424

140. Chen, Z. R.; Kornfield, J. A.; Smith, S. D.; Grothaus, J. T.; Satkowski, M. M. *Science* **1997,** 277, 1248.

141. Wang, J. Y.; Leiston-Belanger, J. M.; Sievert, J. D.; Russell, T. P. *Macromolecules* **2006,** 39, 8487.

142. Boker, A.; Knoll, A.; Elbs, H.; Abetz, V.; Muller, A. H. E.; Krausch, G. *Macromolecules* **2002,** 35, 1319.

143. Sanger, J.; Gronski, W.; Leist, H.; Wiesner, U. *Macromolecules* **1997,** 30, 7621.

144. Schmidt, K.; Schoberth, H. G.; Ruppel, M.; Zettl, H.; Hansel, H.; Weiss, T. M.; Urban, V.; Krausch, G.; Boker, A. *Nat. Mater.* **2008,** 7, 142.

145. Olszowka, V.; Hund, M.; Kuntermann, V.; Scherdel, S.; Tsarkova, L.; Boker, A. *ACS Nano* **2009,** 3, 1091.

146. Winter, H. H.; Scott, D. B.; Gronski, W.; Okamoto, S.; Hashimoto, T. *Abstr. Pap. Am. Chem. Soc.* **1993,** 206, 407.

147. Sakurai, S. *Polymer* **2008,** 49, 2781.

148. Mori, K.; Hasegawa, H.; Hashimoto, T. *Polymer* **2001,** 42, 3009.

149. Colby, R. H. *Curr. Opin. Colloid Interface Sci.* **1996,** 1, 454.

150. Darling, S. B. *Prog. Polym. Sci.* **2007,** 32, 1152.

151. Hamley, I. W. *J. Phys.: Condens. Matter* **2001,** 13, 643.

152. Mendoza, C.; Pietsch, T.; Gutmann, J. S.; Jehnichen, D.; Gindy, N.; Fahmi, A. *Macromolecules* **2009,** 42, 1203.

153. Mendoza, C.; Pietsch, T.; Gindy, N.; Fahmi, A. *Adv. Mater.* **2008,** 20, 1179.

154. Chen, P. L. *Phys. Rev. E* **2005,** 71.

155. Frederickson, G. H. *J. Rheol.* **1994,** 38, 1045.

156. Fredrickson, G. H.; Helfand, E. *J. Chem. Phys.* **1987,** 87, 697.

157. Guo, H. X. *J. Chem. Phys.* **2006,** 125.

158. Winter, H. H.; Scott, D. B.; Waddon, A. J.; Lin, Y. G.; Karasz, F. E. *Theoretical and Applied Rheology, Vols 1 and 2* **1992,** 405.

159. Langela, M.; Wiesner, U.; Spiess, H. W.; Wilhelm, M. *Macromolecules* **2002,** 35, 3198.

160. Gupta, V. K.; Krishnamoorti, R.; Kornfield, J. A.; Smith, S. D. *Macromolecules* **1995,** 28, 4464.

161. Okamoto, S.; Saijo, K.; Hashimoto, T. *Macromolecules* **1994,** 27, 5547.

162. Lorthioir, C.; Deloche, B.; Alegria, A.; Colmenero, J.; Auroy, P.; Gallot, Y. *Eur. Phys. J. E* **2003,** 12, 121.

163. Bitsanis, I.; Hadziioannou, G. *J. Chem. Phys.* **1990,** 92, 3827.

164. Bates, F. S. *Macromolecules* **1984,** 17, 2607.

165. Daniel, C.; Hamley, I. W.; Wilhelm, M.; Mingvanish, W. *Rheol. Acta* **2001,** 40, 39.

166. Reimers, M. J.; Dealy, J. M. *J. Rheol.* **1996,** 40, 167.

167. Bockstaller, M. R.; Mickiewicz, R. A.; Thomas, E. L. *Adv. Mater.* **2005,** 17, 1331.

168. Oelschlaeger, C.; Gutmann, J. S.; Wolkenhauer, M.; Spiess, H. W.; Knoll, K.; Wilhelm, M. *Macromol. Chem. Phys.* **2007,** 208, 1719.

169. Massey, J. A.; Winnik, M. A.; Manners, I.; Chan, V. Z. H.; Ostermann, J. M.; Enchelmaier, R.; Spatz, J. P.; Moller, M. *J. Am. Chem. Soc.* **2001,** 123, 3147.

170. Neidhofer, T.; Sioula, S.; Hadjichristidis, N.; Wilhelm, M. *Macromol. Rapid Commun.* **2004,** 25, 1921.

171. Alvarez, F.; Alegria, A.; Colmenero, J. *Phys. Rev. B* **1991,** 44, 7306.

172. Cates, M. E.; Milner, S. T. *Phys. Rev. Lett.* **1989,** 62, 1856.

173. Reinheimer, K.; Massimiliano, G.; Wilhellm, M. *J. Colloid Interface Sci.* **2011**, doi:10.1016/j.jcis.2011.05.002.

174. Capaccioli, S.; Prevosto, D.; Best, A.; Hanewald, A.; Pakula, T. *J. Non-Cryst. Solids* **2007,** 353, 4267.

175. Lin, Y.; Boker, A.; He, J. B.; Sill, K.; Xiang, H. Q.; Abetz, C.; Li, X. F.; Wang, J.; Emrick, T.; Long, S.; Wang, Q.; Balazs, A.; Russell, T. P. *Nature* **2005,** 434, 55.

176. Dyre, J. C.; Schroder, T. B. *Rev. Mod. Phys.* **2000,** 72, 873.

177. Grubbs, R. B. *J. Polym. Sci. Part A: Polym. Chem.* **2005,** 43, 4323.

178. Dyre, J. C. *J. Non-Cryst. Solids* **1986,** 88, 271.

179. Dyre, J. C.; Maass, P.; Roling, B.; Sidebottom, D. L. *Rep. Prog. Phys.* **2009,** 72, 15.

180. Montroll, E. W.; Weiss, G. H. *J. Math. Phys.* **1965,** 6, 167.

181. Dyre, J. C. *J. Appl. Phys.* **1988,** 64, 2456.

Appendix

Technical drawing of the Rheo-Dielectric geometries

I.   Ceramic isolation for the dielectric electrodes

II. Dielectric electrodes

A-A (2 : 1)

n 25,00
n 8,00
3,00
8,00
3,00 2,00
3,00
n 5,20
n 5,40
6,80 6,80

6,80 6,80
M2x0.4 - 6H
M2x0.4 - 6H
M2x0.4 - 6H
7,00

| Maßstab: | | ewicht: | G |
| Material: | nvar | | |

					Datum	ame N	Dielektrik 8mm PP
					Gezeichne 09.05.2011	inz mermann	
					Kontrolliert		
					Norm		

KIT
Karlsruhe Institute of Technology

1
A4

Status nderungen atum amBN

III.   Upper fixture

A-A (1 : 1)

Maßstab:	ewicht:		G
Material:	nvar		

Dielektrik Ares

	Datum	ame	N
Gezeichne	12.05.201		imzmermann
Kontrollier			
Norm			

KIT
Karlsruhe Institute of Technology

1

A4

Status nderungen atum ame

IV.   Lower fixture

19,00

50,00   2,50

5,50   40,00   8,80

A

A

n 20,70   n 20,90

R2,5

6,25

A-A (1 : 1)

7,30

R2,50

7,96   11,47

25°

64,00   13,50

2,74 3,24

90°

15,21   4,68

n 28,50

						Maßstab:	ewicht:	G
						Material:		
			Datum	ame	N			
			Gezeichne	09.05.2011	in mermann			
			Kontrollier					
			Norm					
								1
			KIT					A4
Status	nderungen	atum	am N					

Karlsruhe Institute of Technology

Acknowledgements

Of course, a thesis like the present one is not accomplished by one person working alone. Therefore, I would like to acknowledge the support, helpful discussions, comments and ideas that were contributed from various people.

I am deeply indebted to:

- Prof. Dr. Manfred Wilhelm for the opportunity to work in his group at the Karlsruhe Institute of Technology (KIT), for his continual interest at each stage of my work and for the friendly atmosphere he provided which allowed me to balance both my professional and family life.

- Dr. Bernd Struth and Michael Walther from the Deutsches Elektronen-Synchrotron (DESY, Hamburg, Germany) for providing the opportunity to use the BW1 beam line and for providing guidance throughout the synchrotron Rheo-SAXS experiments.

- Prof. Dr. Kyu Hyun for providing assistance during several of the Rheo-SAXS experiments and for being a good friend to enjoy a chilled Hefeweizen with at the end of the day.

- Dr. Amir Fahmi and his former PhD student Cesar Mendoza from the School of Mechanical, Materials and Manufacturing Engineering at the University of Nottingham for providing the gold-hybrid block copolymer nano-composites.

- Dr. Nico Dingenouts for explaining the many details and interesting phenomena of 2D-SAXS experiments.

- Sabine Weiland for always helping me with unexpected bureaucratic paperwork.

- The whole AK Wilhelm group for offering an inspiring atmosphere to work in. I would especially like to acknowledge Michael Kempf, Ingo Naue, Dr. Christopher Klein, Deepak Ahirwal and Kathrin Reinheimer who have all become good friends that I could count on.

CURRICULUM VITAE

Persönliche Daten

Name: Thomas Meins

Geburtsdatum: 26. Oktober 1979 in Bayreuth

Nationalität: deutsch

Familienstand: verheiratet

Schulausbildung

1986 – 1990   Besuch der Grundschule Neudrossenfeld

1990 - 1998   Übertritt und Besuch des Markgraf-Georg-Friedrich-Gymnasiums Kulmbach

1998 - 2000   Übertritt an das Wirtschaftwissenschaftliche-Mathematisch-Naturwissenschaftliche Gymnasium Bayreuth und Abschluss der Schulausbildung mit dem Abitur

Zivildienst

2000 - 2001   Zivildienst auf der Herzstation am Klinikum Bayreuth

Studium

10/2001 - 09/2004   Universität Bayreuth Studiengang Polymer- und Kolloidchemie

05/2007 - 11/2007   Diplomarbeit unter der Betreuung von Prof. M.Wilhelm mit dem Titel:
„Kombination von dielektrischer Spektroskopie und FT-Rheologie an Blockcopolymeren"

11/2007 - 06/2011   Doktorarbeit am Karlsruher Institut für Technologie unter der Betreuung von Prof. M. Wilhelm mit dem Titel:
„In-situ investigations of the shear-induced alignment of diblock copolymer melts with combined methods"

Beschäftigung

01/2010 - 02/2010 Praktikum bei Partner für Innovation und Förderung, Lahr